A Biosensor-Based Digital Microfluidic System for Neuroanalysis in the Intensive Care Unit

Michelle Louise Rogers

Department of Bioengineering

Imperial College

A thesis submitted for the degree of

PhilosophiæDoctor (PhD)

September, 2011

Imperial College London

The publications arising from this thesis are:

• Rogers M, Leong C, Niu X, deMello A, Parker KH and Boutelle MG (2011) Optimisation of a microfluidic analysis chamber for the placement of microelectrodes, Physical Chemistry Chemical Physics, 13, 5298-5303, DOI: 10.1039/C0CP02810J

• Patel BA, Rogers M, Wieder T, O'Hare D, Boutelle MG (2011) ATP microelectrode biosensor for stable long-term in vitro monitoring from gastrointestinal tissue. Biosensors and Bioelectronics 26, 6, 2890-2896, DOI:10.1016/j.bios.2010.11.033

I thank the co-authors for all their support and declare that the work presented in this thesis is of my own work except where it is otherwise acknowledged.

Michelle Rogers

This thesis is protected by copyright and other intellectual property rights. Copyright in the material it contains belongs to the author unless stated otherwise. No information or quotation from the thesis may be published or re-used without proper acknowledgement.

Abstract

The primary focus of this thesis is the development of a digital microfluidic based system with integrated microelectrode biosensors, designed for the analysis of human brain microdialysate in the intensive care unit. The main aim is to measure the neurochemical effects of spreading depolarisations (SD waves), which have been shown to be detrimental to the injured human brain.

A combined electrode was developed containing working electrodes in the range of 25 to 125 μM, a reference electrode and an auxiliary electrode, within a needle of outer diameter 300 to 500 μm. Glucose, lactate and ATP biosensors were developed with detection limits of 2 to 10 μM and response times of under 10 seconds.

A digital microfluidic system was designed to segment the dialysate at a microdialysis probe outlet, thereby eliminating Taylor dispersion and reducing the time lag between the sample leaving the brain and analysis. Different designs are discussed for the manipulation of droplets for optimal analysis, thus creating a microfluidic toolkit. The analysis chamber was analysed mathematically, the optimal placement of electrodes found and the sensor performance assessed on-chip.

The on-chip glucose biosensor was used *in vivo* in a translational pilot study. The biosensor performance was validated against rapid sampling microdialysis with excellent results. The glucose biosensors successfully monitored concentration changes, in response to stimulations, in the range of 10 to 400 μM. The data shows that during a SD wave, there is a time delay between the increase in potassium and the decrease in glucose, due to the uncoupling of blood flow and metabolism. For the first time, the microfluidic system was used in the intensive care unit, monitoring brain injury patients at the bedside.

Acknowledgements

I would like to thank all those without whom this thesis might not have been written; my supervisor Martyn, for inspiring and guiding me throughout. Everyone in the Department of Bioengineering for the continual assistance and my fellow lab workers, past and present, for all the advice and laughter. But also, my family and friends to whom I am immensely thankful for their perpetual support, inspiration and passion.

Its kinda fun to do the impossible
Walt Disney



Contents

List of Figures **15**

List of Tables **21**

List of Abbreviations **23**

1 Introduction **25**

1.1 The Human Brain . . . 25

1.1.1 Neurons . . . 27

1.1.2 Astrocytes . . . 29

1.1.3 Brain Metabolism . . . 29

1.2 The Injured Brain . . . 32

1.2.1 Focal and Global Ischemia . . . 33

1.2.2 Primary and Secondary Injury . . . 33

1.2.3 Spreading Depolarisation . . . 34

1.2.4 Monitoring the Injured Human Brain . . . 36

1.3 Neurochemical Analysis . . . 38

1.3.1 Microdialysis . . . 38

1.3.2 Rapid Sampling Microdialysis . . . 40

1.3.3 Implanted Biosensors . . . 42

1.3.4 Comparison of Microdialysis and *in vivo* Biosensors . . . 43

1.3.5 A New Paradigm for Microdialysis . . . 46

1.4 Outline of Thesis . . . 48

2 Methods & Materials **49**

2.1 Electrochemistry . . . 49

2.1.1 Cyclic Voltammetry . . . 49

2.1.2 Amperometry . . . 50

2.2 Rapid Sampling Microdialysis . . . 53

2.2.1 Microdialysis Probe . . . 53
2.2.2 Injection Valve . . . 53
2.2.3 Enzyme Beds . . . 55
2.2.4 Radial Flow Cell . . . 55
2.2.5 Data Analysis . . . 55
2.2.6 The Clinical Trolley . . . 56
2.3 Microfluidics . . . 57
2.3.1 Mask: Design and Fabrication . . . 57
2.3.2 Master Fabrication . . . 57
2.3.3 Use of Chips . . . 57
2.4 Materials and Reagents . . . 58
2.4.1 Ferrocene Monocarboxylate . . . 58
2.4.2 Hexaamine Ruthenium (III) Chloride . . . 58
2.4.3 Potassium Ferrocyanide . . . 58
2.4.4 Phosphate Buffer Solution . . . 58
2.4.5 Artificial Cerebral Spinal Fluid . . . 59
2.4.6 Krebs Buffer Solution . . . 59
2.4.7 Substrate Standards . . . 59

3 Development of Microelectrodes 61
3.1 Introduction . . . 61
3.1.1 Working Electrode Material . . . 61
3.1.2 Microelectrodes versus Macroelectrodes . . . 64
3.1.3 Microelectrode Theory: Inlaid Microdisk . . . 65
3.1.4 Microelectrode Theory: Hemispherical Electrode . . . 67
3.2 Cylindrical Electrodes . . . 68
3.2.1 Fabrication of Electrodes . . . 68
3.2.2 Fabrication of Radel Flow Cell . . . 70
3.2.3 Characterisation of Cylindrical Electrodes within a Radel Flow Cell . . . 71
3.3 Needle Electrodes . . . 73
3.3.1 Needle Electrode Fabrication: Working Electrode . . . 73
3.3.2 Needle Electrode Fabrication: Reference Electrode . . . 74
3.3.3 Characterisation of Platinum Disc Electrodes . . . 74
3.4 The Combined Needle Electrode . . . 77
3.4.1 Method of Fabrication . . . 77
3.4.2 Chloridising Reference Electrode . . . 79

3.4.3 Validation . . . 79
3.5 Dual Electrodes . . . 82
3.5.1 Crosstalk . . . 82
3.5.2 Screen Printed Electrodes . . . 85
3.6 Conclusion . . . 86

4 Biosensor Development 87
4.1 Introduction . . . 87
4.1.1 Enzymes . . . 87
4.1.2 Biosensor Classification . . . 92
4.1.3 Biosensor Fabrication . . . 94
4.1.4 Enzyme Kinetics . . . 95
4.2 Investigating Immobilising Films . . . 98
4.2.1 Polymerisation by Cyclic Voltammetry . . . 98
4.2.2 Film Formation: Electropolymerisation . . . 100
4.2.3 Film Selectivity: Flow Injection Analysis . . . 102
4.2.4 Size versus Charge . . . 104
4.2.5 Polymer Selectivity . . . 105
4.2.6 Film Decision . . . 105
4.3 Glucose Biosensor: Radel Flow Cell . . . 106
4.4 Glucose Biosensors: Disc Electrodes . . . 108
4.4.1 Glucose: Beaker Calibrations . . . 108
4.4.2 Glucose: Stability . . . 111
4.4.3 Glucose Biosensor: Beaker Assessment . . . 112
4.5 Lactate Biosensor . . . 114
4.5.1 Lactate Biosensor: Sensitivity and Response Times . . . 114
4.5.2 Lactate Biosensor: Beaker Assessment . . . 115
4.6 ATP Biosensor . . . 117
4.6.1 Stability in the Response to Glucose Concentrations . . . 117
4.6.2 Characterisation of ATP Biosensor . . . 119
4.6.3 ATP Biosensor Conclusion . . . 121
4.7 Conclusion . . . 122

5 A Microfluidic Tool Kit 123
5.1 Introduction . . . 123
5.1.1 Continuous Flow Microfluidics . . . 123
5.1.2 Digital Microfluidics . . . 123

5.1.3 Microfluidics and Microdialysis . . . 124
5.1.4 Chip Fabrication . . . 125
5.1.5 Droplet Generation . . . 125
5.1.6 Carrier Fluid . . . 126
5.2 Initial Investigations . . . 127
5.2.1 Methods: Chip Fabrication . . . 127
5.2.2 Methods: Electrodes . . . 127
5.2.3 Initial Findings: Droplet Generation . . . 128
5.2.4 Initial Findings: Analysis of Droplets . . . 128
5.2.5 Lessons Learnt . . . 131
5.3 Droplet Generation . . . 132
5.3.1 Chip Fabrication . . . 132
5.3.2 Optical Detection . . . 133
5.3.3 Droplet Generation: T junction . . . 134
5.3.4 Droplet Generation: Robotic Head . . . 136
5.3.5 Droplet Frequency . . . 138
5.3.6 Droplet Length . . . 138
5.4 Digital Microfluidics and Microdialysis . . . 140
5.4.1 Laser Induced Fluorescence . . . 140
5.4.2 Microdialysis Probe Recovery . . . 140
5.4.3 Micro Particle Imaging Velocity (microPIV) . . . 145
5.5 Manipulation of Droplets . . . 148
5.5.1 Surface Tension . . . 148
5.5.2 Flow Rates . . . 149
5.6 Analysis Chip . . . 150
5.6.1 Analysis Chip: Design 1 . . . 150
5.6.2 Analysis Chip: Design 2 . . . 155
5.7 Passive Coalescence . . . 157
5.8 General Running of Analysis Chip Design 2 . . . 159
5.8.1 Flow Rate Optimisation . . . 159
5.8.2 Siphoning from the Chamber . . . 159
5.9 Droplet Dosing . . . 162
5.9.1 Dosing using a T junction . . . 162
5.9.2 Dosing using a Side Arm . . . 163
5.9.3 Size of Droplets and Mixing . . . 166
5.9.4 Addition of Enzyme Solutions . . . 167

5.10 Clinical Safety . . . 172
5.11 Conclusion . . . 173

6 On-Chip Sensors 175
6.1 Introduction . . . 175
6.1.1 Optical Analysis on Microfluidic Chips . . . 175
6.1.2 Electrodes in Microfluidic Chips . . . 175
6.1.3 Mass Transport and Diffusion Layers . . . 176
6.2 Electrochemistry in Digital Microfluidics . . . 179
6.2.1 Placement of the Electrodes Relative to the Chamber Ceiling . 181
6.2.2 Electrochemistry in Different Flow Regimes . . . 183
6.3 Dispersion in Continuous and Droplet Flows . . . 186
6.3.1 Optical Measurement . . . 187
6.3.2 Electrochemical Measurement . . . 189
6.4 Placement of Electrodes Along the Length of the Chamber . . . 192
6.4.1 Optical Analysis . . . 192
6.4.2 Mathematical Model of the Chamber . . . 193
6.4.3 Flow Dynamics in the Droplets and the Chamber . . . 197
6.5 Dual Electrode Orientation . . . 203
6.6 Biosensors On-Chip . . . 207
6.6.1 Glucose . . . 207
6.6.2 Lactate . . . 212
6.6.3 Multi-Analyte . . . 215
6.7 Conclusion . . . 216

7 On-Line Analysis of Microdialysate, *in vivo* 219
7.1 Introduction . . . 219
7.1.1 Clinical Background . . . 219
7.1.2 Translational Studies . . . 220
7.1.3 Testing of the Microfluidic System for the Clinic . . . 222
7.2 Animal Studies . . . 223
7.2.1 Methods and Setup . . . 223
7.2.2 Results: Droplet Flow . . . 231
7.2.3 Biosensor Validation . . . 233
7.2.4 Results: Insertion of the Microdialysis Probe . . . 236
7.2.5 Result: Euthanasia . . . 239
7.2.6 Results: Stroke model . . . 243

7.2.7 Results: Spreading Depolarisation's 245
7.3 Human Studies in the Intensive Care Ward 254
7.3.1 Equipment Setup 254
7.3.2 Patient Data 256
7.4 Conclusion 260

8 Discussion **263**
8.1 Overview 263
8.2 Future Work 267

References **271**

List of Figures

1.1 Structure of the human brain 26
1.2 Structure of a neuron 27
1.3 Schematic of a synapse 28
1.4 Spatial organisation of astrocytes and neurons in the cortex 30
1.5 Summary of the key metabolites involved in metabolism 31
1.6 Key pathways involved during injury 32
1.7 Swollen neuron during an SD 35
1.8 Brain injury 36
1.9 Principle of microdialysis 39
1.10 Recovery of microdialysis probes *in vitro* and *in vivo* 41
1.11 Damage upon implantation of a microelectrode and a MD probe . . . 44

2.1 Cyclic voltammetry 50
2.2 Electropolymerisation 51
2.3 Polymerisation of phenol 52
2.4 rsMD schematic 54
2.5 The clinical trolley 56

3.1 Hydrogen peroxide calibration on platinum and gold electrodes 62
3.2 Surface species for hydrogen peroxide oxidation on a platinum surface 64
3.3 Schematic of the diffusion field of electrodes 65
3.4 Schematic of a radel flow cell 68
3.5 CV of a cylindrical electrode 69
3.6 SECM image of the cylindrical electrode 69
3.7 Radel flow cell photographs 70
3.8 Radel flow cell response to alternating Fc and PBS at different flow rates 71
3.9 Photograph of a combined needle electrode 73
3.10 Disc electrode CVs using hexaamine ruthenium (III) chloride 75

3.11 Photograph of needle electrodes 77
3.12 SECM image of a 30G electrode tip 78
3.13 CV showing silver molecules on the working electrode. 80
3.14 CVs using external and internal reference and auxiliary electrodes. . . 81
3.15 Photograph of an integrated needle electrode after exposure to heat . 81
3.16 Photographs of the dual electrodes taken using a microscope 83
3.17 CVs in 1.5 mM Fc showing cross talk of dual electrodes 84
3.18 Possible screen printed electrode design 85

4.1 Structure of glucose oxidase 88
4.2 Structure of lactate oxidase 89
4.3 Structure of horse radish peroxidase 90
4.4 Structure of hexokinase 91
4.5 Schematic of first generation biosensors 92
4.6 Schematic of second generation biosensors 93
4.7 Schematic of third generation biosensors 93
4.8 How inhibition of enzymes affects V_{max} and K_m 97
4.9 The structure of monomers investigated for use as immobilising films 98
4.10 Film polymerisation using cyclic voltammetry 99
4.11 CVs of a bare and an oPD coated electrode 101
4.12 FIA analysis 103
4.13 Wire biosensor in Radel flow cell 107
4.14 Glucose biosensor beaker calibration 109
4.15 Biosensor calibration on day 1 and day 21 111
4.16 Overnight running of a glucose biosensor 112
4.17 Calibration of a lactate sensor 115
4.18 Schematic diagram showing the operation of the ATP biosensor. . . . 117
4.19 Investigating the GOx component of the ATP biosensor 118
4.20 Calibration response of ATP biosensor. 120

5.1 Photograph of the initial chip 128
5.2 Response of 2 mm cylindrical electrode in droplet flow 129
5.3 Response of 50 μm electrodes to hexadecane oil 130
5.4 High speed camera setup 134
5.5 Master of T junction 135
5.6 High speed sequence of droplet generation 135
5.7 The flow within an aqueous droplet 136

5.8 A photograph of the robotic head in a 15 well setup . . . 137
5.9 LIF data of droplets . . . 138
5.10 Recovery of fluorescein in droplet and continuous flows . . . 141
5.11 The difference in recovery between continuous and droplet flow . . . 142
5.12 Comparison of fluorescein recovery in droplet and continuous flows with different tubing lengths . . . 143
5.13 The tracking of a particle in a T junction . . . 145
5.14 Movement of the disperse phase in a T junction . . . 146
5.15 Depiction of droplets in a channel with different wetting properties . 149
5.16 Analysis chip design 1 . . . 150
5.17 Pillar spacing effect on droplets . . . 151
5.18 Design 1: images from a high speed camera . . . 153
5.19 A PDMS chip sealed in glue . . . 154
5.20 Analysis chip design 2 . . . 155
5.21 Design 2: images from a high speed camera . . . 156
5.22 Detailed view of droplet coalescence . . . 157
5.23 A still from a high speed camera showing detailed merging of droplets 158
5.24 Analysis of droplet catching with varying oil flow rates . . . 160
5.25 Siphoning from the analysis chamber . . . 161
5.26 Droplet dosing using a T junction . . . 162
5.27 Droplet dosing using a side arm . . . 163
5.28 Droplet lengths before and after dosing addition . . . 164
5.29 Droplet dosing using a side arm . . . 165
5.30 Mixing in a large droplet . . . 166
5.31 Mixing in small droplets in a serpentine . . . 167
5.32 Droplet dosing: addition of GOx . . . 168
5.33 Enzyme dosed glucose droplets sticking to the channel surface . . . 169
5.34 Glucose droplet baseline . . . 170
5.35 Glucose droplets dosed with GOx on a Duxback treated chip . . . 171
5.36 Schematic of clinical microfluidics . . . 172

6.1 Schematic of electrode diffusion fields on-chip . . . 177
6.2 Photograph of electrode placement affecting chamber design . . . 179
6.3 Photograph of a needle electrode placed on-chip . . . 180
6.4 CVs in continuous and droplet flow . . . 181
6.5 On-chip CVs at different heights in a 100 μm and 250 μm high chambers 182
6.6 CVs in different flow regimes using ferrocene monocarboxylate . . . 183

6.7 CVs looking at ferrocene monocarboxylate and oil 184
6.8 Taylor dispersion in continuous flow 186
6.9 Optical comparison of continuous and droplet flow regimes upon dispersion over 1 m tubing 188
6.10 Coalescence of droplets 189
6.11 Comparison of continuous and droplet flow regimes upon dispersion over a 1 m tubing using different analysis techniques 190
6.12 Processing of high speed videos 192
6.13 Frames of a video of the aqueous solution entering the analysis chamber 194
6.14 Experimental data of dark and light droplets in the chamber 195
6.15 Velocity ratio 197
6.16 Velocity distribution 198
6.17 Simulated dispersion within the chamber 199
6.18 Coalescence at the entrance of the chamber 200
6.19 False colour frames of different coloured droplets within the chamber 202
6.20 Schematic of dual electrodes under flow conditions 203
6.21 CVs showing the collection efficiencies of electrode D4 when placed in different orientations on-chip 205
6.22 CVs of separate needle electrodes in the chamber 206
6.23 Syringe pump flow rate measured with flow sensors 208
6.24 A glucose biosensor on-chip: calibration 209
6.25 A glucose biosensor on-chip in droplet flow: chamber not working . . 210
6.26 A glucose biosensor on-chip in droplet flow 211
6.27 A lactate biosensor on-chip: calibration 212
6.28 Two lactate biosensors on-chip: calibration 213
6.29 A lactate biosensor on-chip: calibration in droplet flow 214
6.30 A glucose and lactate biosensor on-chip: contamination 215

7.1 Setup for animal experiments in MPI, Cologne 225
7.2 Close view of setup of probes in the rat in MPI, Cologne 226
7.3 Close view of the sensors in an analysis chip in a faraday box 227
7.4 Depiction of relative positions of probes and stimuli on the rat cortex 229
7.5 Schematic of animal set-up 230
7.6 Needle prick and cardiac arrest in droplet flow 231
7.7 Glucose biosensor versus rsMD 233
7.8 Glucose biosensor validation with Clarkes grid 234
7.9 Glucose biosensor validation 235

7.10 Laser speckle images of a MD probe insertion 237
7.11 Biosensor and rsMD glucose raw data during a MD probe insertion . 238
7.12 Laser speckle images of a KCl injection 239
7.13 Euthanasia induced by KCl injection 240
7.14 Changes during euthanasia 242
7.15 Visual inspection of the location of the injected macrosphere 243
7.16 Changes upon injection of a macrosphere into the connecting artery. . 244
7.17 Laser speckle images of a cotton bud induced SD 246
7.18 Changes upon application of a cotton bud. 247
7.19 Needle prick: probe measurements 249
7.20 Needle prick: on-chip glucose, potassium and blood flow 251
7.21 Assessment of glucose and potassium changes after a needle prick . . 253
7.22 rsMD and microfluidic setup on the intensive care ward at KCH . . . 255
7.23 On-line glucose recordings from patient at KCH 256
7.24 On-line glucose recordings from a stroke patient at MPI 258

8.1 Glucose and potassium changes 266

LIST OF FIGURES

List of Tables

3.1 Currents expected from inlaid microdisc electrodes 66
3.2 Currents expected from hemispherical electrodes 67
3.3 Flow cell results: T_{90} and current against flow rate 72
3.4 Limiting currents and electrode sizes 75
3.5 25 μm diameter microelectrode intra-current summary 76
3.6 Needle sizes: gauge and diameters 78
3.7 Wire sizes: diameters of coated and uncoated 79
3.8 Collection efficiencies in 1.5 mM ferrocene monocarboxylate 84

4.1 Literature summery of glucose biosensors fabricated with different films 95
4.2 Enzyme kinetics of glucose biosensors: film assessment 101
4.3 FIA results : I / I_{clean} **Mean**±StDev n=4. Charge of the injected specie at pH 7 and relative sizing of the species are also shown 104
4.4 Polymer selectivity 105
4.5 Response of glucose biosensor in the flow cell: current response . . . 106
4.6 Response of glucose biosensor in the flow cell: T_{90} 107
4.7 Responses of glucose biosensors 110
4.8 Assessment of glucose biosensors in a beaker 113
4.9 Responses of lactate biosensors 115
4.10 Assessment of lactate biosensors in a beaker 116
4.11 Comparing enzyme activity (U/mg) and sensitivities ($nAmM^{-1}cm^{-2}$) 116

5.1 Sizes of commonly used tubing and electrode needle compared with the blunted needle used to punch the hole 133
5.2 Approximate length of droplets in FEP tubing compared to aqueous and oil flow rates 139

6.1 Dispersion over 1 m connection tubing: continuous and droplet flows 191

6.2 Collection efficiencies on-chip 204
6.3 Continuous flow on-chip glucose biosensors at 2 μLmin^{-1} 209
6.4 Droplet flow on-chip glucose biosensors at 2 and 5 μLmin^{-1} 211
6.5 Assessment of glucose biosensors on-chip 211
6.6 Continuous flow on-chip lactate biosensors at 2 μLmin^{-1} 213

7.1 Changes in glucose concentration caused by needle pricks 250
7.2 Glucose and potassium changes during a NP 252

List of Abbreviations

5-HT	Serotonin
AA	Ascorbic acid
aCSF	Artificial cerebral spinal fluid
ADP	Adenosine diphosphate
AMP	Adenosine monophosphate
ATP	Adenosine triphoshate
AP	Action potential
BBB	Blood brain barrier
CBF	Cerebral blood flow
CO_2	Carbon dioxide
COSBID	Cooperative study on brain injury depolarisations
CSF	Cerebral spinal fluid
CT	Computerised tomography
CV	Cyclic voltammogram
DA	Dopamine
df	Degrees of freedom
Ea	Activation energy
ECoG	Electrocorticography
EEG	Electroencephalography
EDTA	Ethylenediaminetetraacetic acid
ES	Enzyme-Substrate
EWOD	Electrowetting on dielectric
FAD	Flavin adeninie dinucleotide
Fc	Ferrocene monocarboxylate
FeCN	Potassium ferrocyanide
FEP	Fluorinated ethylene propylene
FIA	Flow injection analysis
FMN	Flavin mononucleotide
fMRI	functional magnetic resonance imaging
GABA	Gamma-aminobutyric acid
GFP	Green fluoresent protein
GOx	Glucose oxidase
GTP	Guanosine triphosphate
H_2O_2	Hydrogen peroxide
HEX	Hexokinase
HPLC	High performance liquid chromatography
HRP	Horse radish peroxidase
ICA	Internal carotid artery
ICP	Intracranial pressure
ISE	Ion selective electrode
KCH	Kings College Hospital
LIF	Laser induced fluoresence
LOC	Lab on chip
LOD	Limit of detection
LOx	Lactate oxidase
LSF	Laser speckle flowmetry
MCA	Middle cerebral artery
MCAO	Middle cerebral artery occlusion
MEMS	Microelectromechanical systems
MD	Microdialysis
mPD	m-phenylenediamine

LIST OF ABBREVIATIONS

MPI	Max Plank Institute
NADH	Nicotinamide adenine dinucleotide
NNF	No net flux
NP	Needle prick
oPD	o-phenylenediamine
PBS	Phosphate buffer solution
PCR	Polymerase chain reaction
PDMS	Polydimethylsiloxane
PEB	Post exposure baking
PEEK	Polyether ether ketone
PET	Polyethylene terephthalate
PSSPL	Poly(sodium-4-styrene-sulfonate) poly(L-lysine-hydrobromide)
Pt	Platinum
QH_2	Cytochrome C reductase
ROI	Region of interest
RSD	Relative standard deviation
rsMD	Rapid sampling microdialysis
RuHex	Ruthenium hexaamine
SD	Spreading depolarisation
sd	Standard deviation
SENT	Sentinel electrode
SOx	Substrate oxidase
T_{90}	90% response time
TBI	Traumatic brain injury
TTX	Tetrodotoxin
UPS	Uninterruptible power supply

Chapter 1

Introduction

1.1 The Human Brain

The human brain is a complex organ, which actively controls most bodily functions. It is similar in structure to that of other mammals, however when comparing to body size, the human brain is three times larger (1). The brain regulates and monitors the body's actions and functions by receiving sensory information via nerve inputs and processes them using many different representations, before giving a response. Different areas of the brain are responsible for different functions, for example the brain stem regulates autonomous functions such as the heart beat, the basal ganglia controls motor output, the cerebellum is used for coordinated movement, the hippocampus for memory and the neocortex brings the signals together and processes them, giving rise to personalities and consciousness. The locations of these brain areas are indicated in figure 1.1. Damage to the brain can have devastating consequences. The most severe is death however, brain injury can have more subtle effects. The most common brain injury is caused by a hit on the head and the external forces involved are most likely to affect the neocortex. Therefore, the processing and the response to external stimuli can change and the personality of the patient can become very obsessive or violent. Whilst there is no obvious disability, this can have a very debilitating effect on the patient and their family.

There are two main components of the brain: white and grey matter. White matter forms the main bulk of the deeper parts of the brain and is composed of myelinated axons. Therefore it can quickly transmit messages to different parts of the brain and to other organs. Grey matter is the area of the brain which processes information. It is composed of neuronal cell bodies and glial cells known as astrocytes. The brain is protected both by the skull, which in humans is more than 1 cm

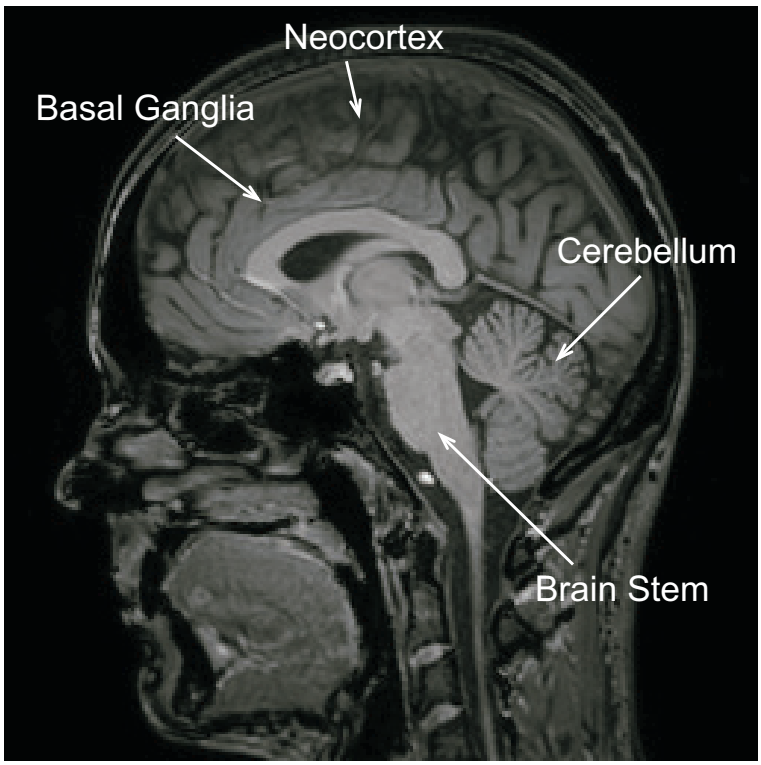


Figure 1.1: Structure of the human brain
Sagittal view of the human brain. Image created using MRI. The brain stem is responsible for autonomous functions, the cerebellum for movement and the cortex for personality and consciousness. The hippocampus is not visible on this mid-line sector.

thick and is cushioned by cerebral spinal fluid (CSF). CSF provides mechanical support so that the brain is not affected by its own weight and acts as a cushion against jolts and injuries (2). The brain is also protected from large molecules and bacteria by the blood brain barrier (BBB). The BBB separates the circulating blood and the extracellular fluid of the brain and is crucial for correct neuronal function (3). It is present along the capillaries and consists of tight junctions which seal together the endothelial cells. The tight junctions restrict the passage of water soluble molecules, and protects the brain from infection and from fluctuations in the composition of fluids in the rest of the body, by forcing molecules to travel via the trans-cellular route across the BBB (4). The BBB also protects molecules that are released by cells in the brain from being washed away in the blood stream, allowing for complex pathways to occur.

1.1.1 Neurons

Neurons have a distinctive structure, as shown in figure 1.2, and form networks, in which information is relayed electrically and chemically. Neurons process information uni-directionally along their length via electrical action potentials (AP) and transmit information to other cells via chemical release at their terminus (5). Dendrites relay electrochemical information from other neurons to the soma, or cell body, and the axons transmit the information away from the soma to other neurons. A neuron only has one axon however it can branch many times and innervate multiple parts of the brain.

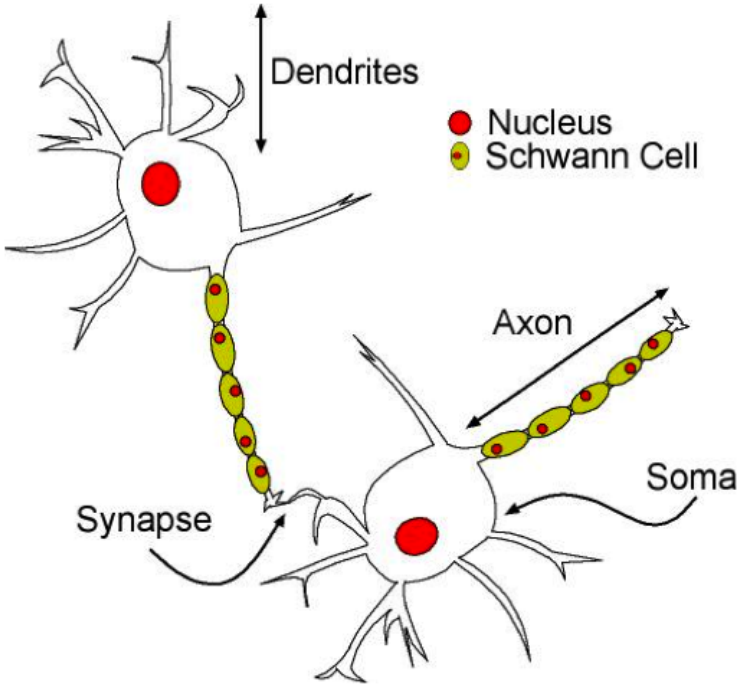


Figure 1.2: Structure of a neuron
The schematic shows two neurons. The soma (cell body), dendrites and axons are indicated. The synapse is the junction which connected an axon of one neuron to the dendrite of another neuron. Schwann cells form the myelin sheath which increase the conduction of electrical messages.

The junction whereby one neuron communicates with another is known as a synapse. A synapse is a specialised junction over which the chemical signal is passed and is shown in figure 1.3. A synapse allows the electrical signal to be converted into a chemical signal, which is passed between neurons (6). The AP propagates along membranes by sodium and potassium channels sequentially depolarising local segments of the membrane, until it reaches the presynaptic terminal. Here, the depolarisation causes voltage-gated calcium channels to open. Calcium floods into

the cells, which triggers synaptic vesicles to dock onto the membrane. The contents (neurotransmitters) are released via a process known as exocytosis. The neurotransmitters diffuse across the synaptic cleft (5 - 50 nm (7)) and some bind to receptor molecules (ligand-gated ion channels) on the postsynaptic cell. This changes the local transmembrane potential causing an AP in the dendrite (8). The generation of the AP depends not only on the receptor stimulation but also on the immediate chemical environment of the postsynaptic cell. Re-uptake pumps may actively pump the excess neurotransmitter back into the cells to prepare the synapse for future stimulations. A poison derived from a pufferfish, known as tetrodotoxin (TTX), locally blocks APs by inhibiting voltage-gated sodium channels and therefore preventing membrane depolarisation (9).

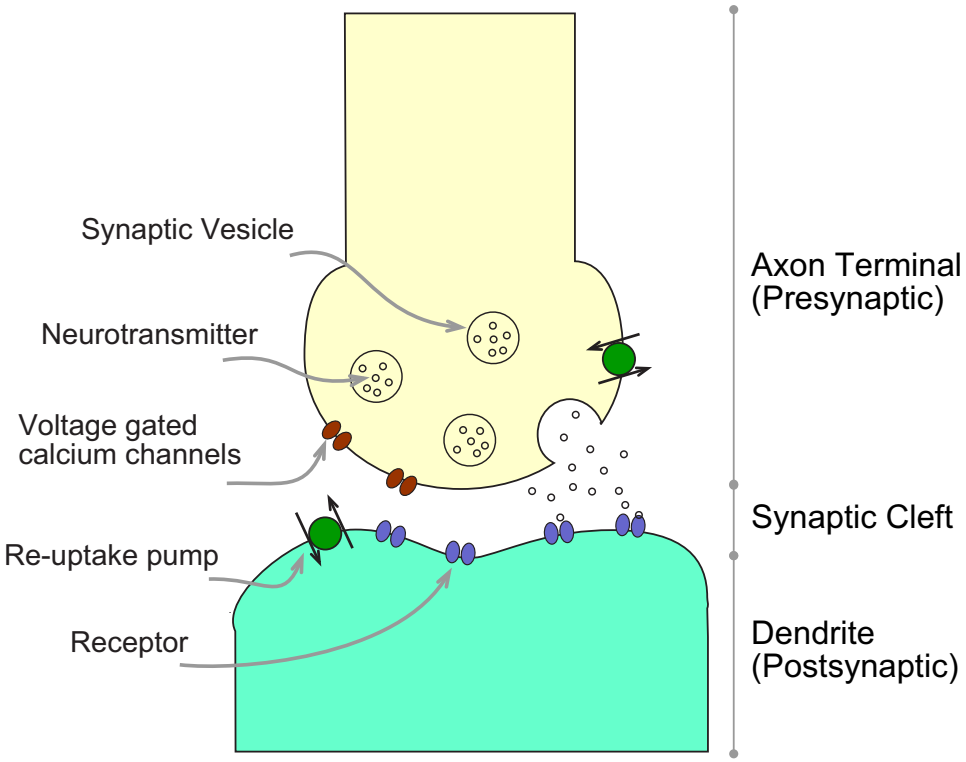


Figure 1.3: Schematic of a synapse
A schematic showing the structure of the junction between two neurons. An AP from the axon stimulates chemical release of neurotransmitters into the synaptic cleft. These diffuse across the gap to the postsynaptic receptors on the dendrite. An AP is then triggered in the second neuron.

1.1.2 Astrocytes

Astrocytes have multiple functions and constitute over 50% of the cell mass of the brain (10). Previously, they were thought to provide only physical support and to perform house-keeping duties for the neurons. This idea originated from the fact that they are electrically non-excitable and therefore could not play a role in signal transmission (11). This has since been challenged and it is now known that their function goes beyond general house-keeping. Astrocytes are indeed involved in regulating the local environment by maintaining ion and pH homeostasis, delivering glucose efficiently, providing nutrition and removing neuronal waste products (11). However, it is now also thought that they can directly regulate neurons and affect their ability to form a synaptic network (11). During embryogenesis they provide molecules that modify the growth of the neuron. Additionally, within the cerebellum and the hippocampus they can form myelin and participate in signal transmission. Astrocytes are star shaped glial cells, which are crucial for clearance of the main excitatory neurotransmitter glutamate from the synaptic cleft, preventing a neurotoxic build up. They also couple this glutamatergic activity to the local supply of energy in the form of glucose and lactate (12).

Spatial Organisation

Astrocytes and neurons are the two main cells of the grey matter. Figure 1.4 shows the spatial organisation of the astrocytes and neurons in the cortex (11). The blood vessels are outlined by the astrocytic end feet which form gap junctions to the endothelial cells. This forms a partial barrier (part of the BBB), which regulates the transmission of water-soluble molecules from the blood to the brain via active transport (13). The gap junctions allow for rapid communication between the astrocyte and the neuron and allow small molecules, such as glucose and lactate, as well as ions to move freely through the network that the astrocytes create (10).

1.1.3 Brain Metabolism

The brain consumes 20% of the energy used by the body even though it represents just 2% of the human body mass (12, 14). Much of the energy required is used for processing information in the form of APs, and more specifically in the re-establishment of ionic gradients post-AP. This is a high energy task, which requires more oxygen and glucose to be taken from the blood for use in metabolism. Glucose can be incorporated into various lipids and proteins and can produce metabolic

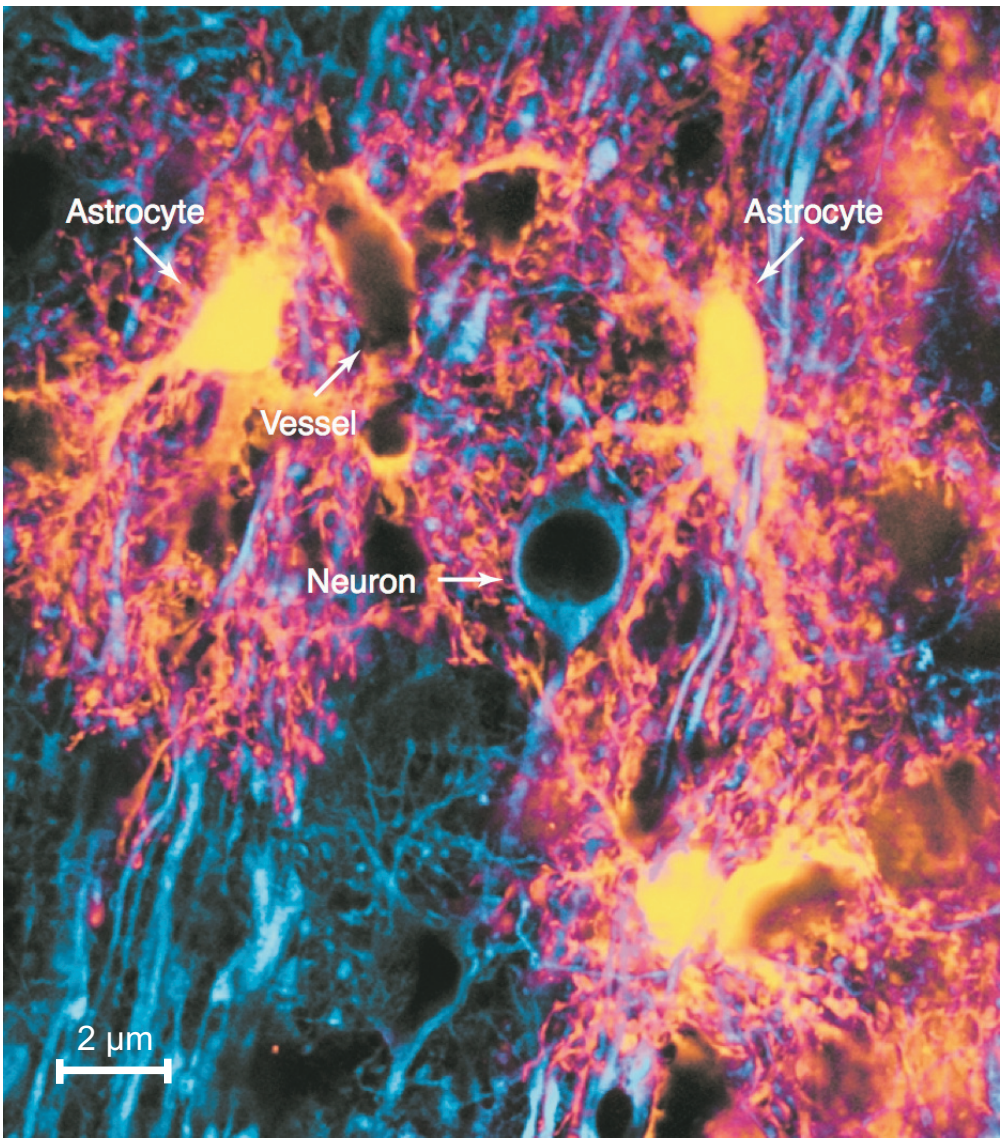


Figure 1.4: Spatial organisation of astrocytes and neurons in the cortex
Neurons are labeled with antibody to microtubule-associated protein 2 (MAP-2; blue), whereas astrocytes are expressing enhanced green-fluorescent protein (eGFP; yellow). A small vessel is outlined by eGFP-positive astrocytic end feet. Image taken from (11)

intermediates. It is the precursor for several neurotransmitters such as GABA, glutamate and acetylcholine. The delivery of metabolic substrates by the blood, is tightly linked to different brain processes, which have different metabolic demands. Metabolism is usually described as three processes: glycolysis, the citric acid cycle and oxidative phosphorylation.

Glycolysis is the pathway which converts glucose into pyruvate and occurs in both aerobic and anaerobic metabolic pathways. In anaerobic conditions, pyruvate

can be converted to lactate. In aerobic conditions, pyruvate is passed into the mitochondria where the citric acid cycle occurs. The products are passed to the membrane where various protein complexes generate ATP by a sequence of redox reactions. A simplified overview of this process is shown in figure 1.5.

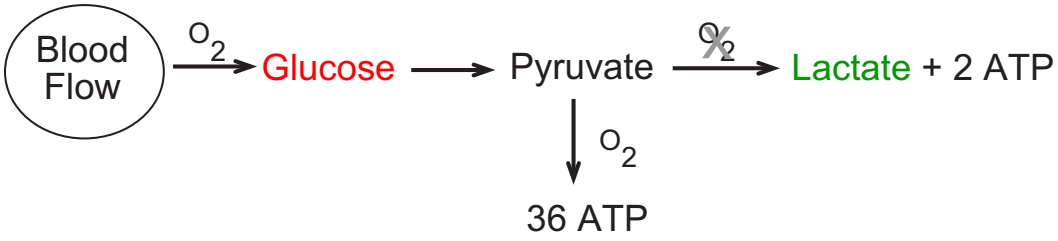


Figure 1.5: Summary of the key metabolites involved in metabolism
Oxygen and glucose are provided by the blood vessels. Glucose is converted to pyruvate during glycolysis. In the absence of oxygen, lactate is formed. In the presence of oxygen, metabolism follows the citric acid cycle and oxidative phosphorylation occurs.

Energy resources stored within astrocytes are in the form of glycogen, which is effectively a type of glucose polymer, however these stores are limited. These glycogen stores are small and the supply of the metabolic substrates (glucose and oxygen) from the blood, is tightly coupled to demand. During periods of higher activity, local blood flow increases. This is known as neurovascular coupling and is the basis of many common imaging methods for brain activity. Initially it was thought that the glycogen was an energy source, for use when glucose was unavailable. However, it has a high turnover rate even when glucose levels are normal, and there is a body of evidence which suggests that glycogen may also play a role in normal brain metabolism (10, 12, 15).

Although glucose is overwhelmingly thought of as being the main energy source for cells, there are many examples of studies showing that lactate is produced and used during aerobic respiration (16, 17, 18, 19), thus supporting a publication in 1953, which stated that *in vitro* brain tissue can utilise lactate to respire (20). Measurements from astrocytes showed that these cells produced lactate from glucose during hypoxic events and that lactate increased during neuronal stimulation (15, 21). An astrocyte-neuron shuttle system has been postulated by many (22, 23, 24, 25) and proved a controversial topic of much discussion (26, 27). In this hypothesis, astrocytes produce lactate from pyruvate and release it into the extracellular fluid. Lactate is then taken up by the neurons and possibly used as a fuel for oxidative metabolism to re-polarise the cell (28).

1.2 The Injured Brain

Traumatic brain injury (TBI) has recently been described as a silent epidemic by the Lancet Neurology journal (29). In the UK, an estimated 238,000 people suffer a TBI each year (30). When compared to breast cancer, which for example has an incidence of approximately 120,000 people annually, the awareness of TBI is very low. Interruption of cerebral blood flow for 10 seconds can result in loss of consciousness and cell damage (31) and after 20 second electrical activity ceases (32). Impairment of the local energy state and of homeostasis develops within minutes and after 5-10 minutes, irreversible cell damage is likely to arise (31). When the tissue is injured, blood vessels are damaged and it has a higher energy demand. It is the combination of these effects that means that the local metabolic demands are often not met. This results in an increase in lactate concentration and a fall in pH. A simplified overview of the key pathways involved is shown in figure 1.6. The majority of head injury's are caused by impacts to the head. This causes local haematoma (bleeding) and swelling. As the brain is a closed box, this increases the pressure in the brain tissue which will most likely result in the breakdown of the local blood supply to damaged tissue. Perfusion to the injured area can be supplied by collateral blood vessels but when this is required long-term, it is often insufficient. Treatment may include increasing blood pressure to push blood through swollen brain tissue, or removing part of the skull to allow the tissue to swell freely. Patient outcome in these cases is hard to predict.

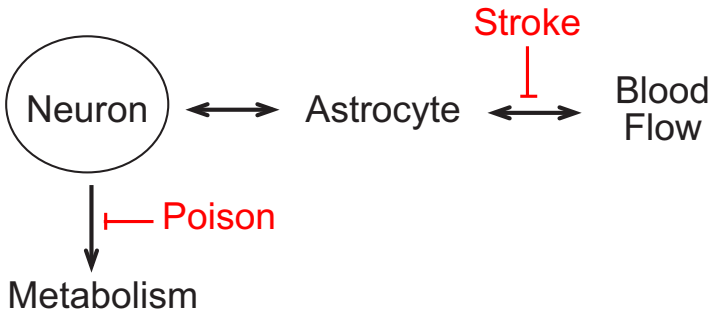


Figure 1.6: Key pathways involved during injury
The neuron, astrocyte and blood flow are tightly coupled. When the tissue becomes injured if one part of the pathway is affected, it can silence the neuron. This means it can no longer communicate and the viability of the cell is affected due to demands on metabolism. A stroke can affect the blood flow by occlusion of vessels. Poisons (toxic chemicals released from neighbouring cells) can directly affect the metabolism.

1.2.1 Focal and Global Ischemia

As discussed, injured brain tissue often becomes ischemic (33). In this case, there is insufficient blood flow to meet the metabolic demands of the tissue and the extracellular fluid can contain high levels of irritant chemicals released from the nearby dead or dying tissue. There are two types of brain ischemia: focal and global. Focal ischemia occurs when there is a localised reduction in blood flow to a specific brain region, normally due to a blood clot. Global ischemia affects the whole brain and the blood supply is limited to all regions. This is most commonly caused by cardiac arrest. Ischemia can cause a variety of symptoms, including lack of sight, loss of coordination or slurred speech, depending upon which area of the brain is affected. These symptoms may only last seconds but can also be permanent if the tissue becomes irreversibly damaged (34).

1.2.2 Primary and Secondary Injury

Primary and secondary injury is used to classify processes that occur during brain injury. Primary injury refers to the initial damage and is the physical result of the trauma. It is irreversible and often occurs before the paramedics arrive at the scene. TBI may take many forms including intracerebral haemorrhage (ICH) where haemorrhage occurs in the brain tissue, subarachnoid haemorrhage (SAH) where blood collects between the arachnoid membrane and the pia mater, cerebral contusion which is a bruise in the brain tissue, and axonal injury which results from rapid acceleration or deceleration of the brain causing lesions in the axons and neuronal death.

Secondary injury refers to the gradual decline of penumbral tissue surrounding the ischemic core (the primary injury site) and may involve an array of cellular processes triggered by the trauma. Secondary injury can develop slowly over days, often whilst the patient is being monitored in intensive care. This type of injury is a large contributing factor in brain damage and death. Approximately 40% of TBI patients deteriorate days after the initial injury (35). Secondary injuries can include ischemia, cerebral hypoxia, cerebral edema (swelling of the brain cells), raised intracranial pressure and neurovascular edema (leakage of the blood plasma into the brain).

1.2.3 Spreading Depolarisation

A spreading depolarisation (SD) is a mass depolarisation of neuronal and glial cells. SDs self-propagate along the cortex surface, like a wave. The depression of the electrical signal, first described by Leao in 1944 (36), coincides with a large increase in extracellular potassium as the neuronal cells depolarise, an increase in blood flow and changes in metabolism (37). The resting potential of a cell is -70 mV and when a threshold of -50 mV is reached, the cell is said to be depolarised. Depolarisation is caused by an influx of cations, for example sodium or calcium. As a result, there is an efflux of potassium into the extracellular space and an influx of chloride ions into the cells. To recover from the depolarisation, the initial intracellular and extracellular ionic gradients must be re-established. This in turn, imposes a high demand for energy (38) and hence challenges the local delivery of glucose and oxygen to the brain. Figure 1.7 shows the mechanisms of a spreading depolarisation in a neuron (39).

SDs have been shown to spontaneously occur in the injured human brain (40, 41, 42). During brain injury and ischemia, the extracellular glucose concentration has been shown to decrease and the concentration of lactate to increase (43, 44). The accumulation of lactate in the extracellular fluid may cause acidosis which could have a deleterious effect (32). The number of depolarisations and the clustering of these events, is associated with the growth of the infarct area (45, 46, 47) and the secondary damage in the injured human brain (48, 49, 50). A schematic is shown in figure 1.8, which is taken from (51). Whilst SDs may occur in the healthy human brain, for example during a migraine with aura, there is unlikely to be damage to the cortex if cerebral perfusion is normal (40).

Clinically, the patient outcome several days after the initial brain injury is characterised by a set of covariates recorded on admission, such as age, pupil abnormalities, level of hypoxia and motor score. However, a study by Murray et al showed that these commonly used covariates only explain 30% of the variance in TBI outcome (52). Results obtained by the Co-Operative Study on Brain Injury Depolarisations (COSBID) group, suggest that the number and frequency of spreading depolarisations are a better indicator of patient outcome than any of the currently used factors. Therefore the technology described in this thesis is aimed at characterising these waves chemically.

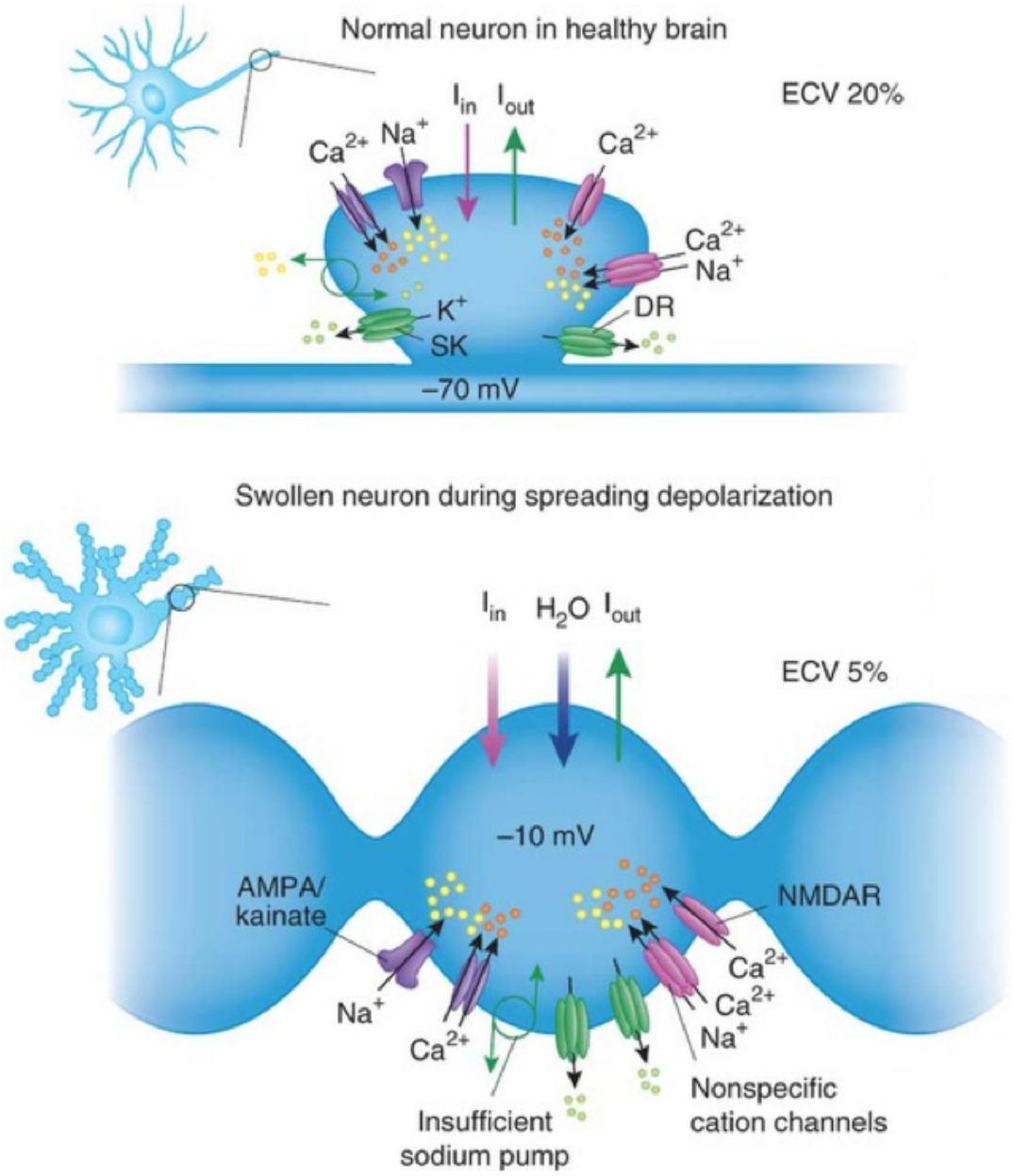


Figure 1.7: Swollen neuron during an SD

In the top diagram a healthy brain cell is shown. In the bottom diagram a swollen cell during a SD is shown. If the influx of sodium and calcium is more than the outflux of potassium, there is a near-complete loss of electrochemical energy, passive ion distribution across the membrane, intracellular hyper-osmolality with cellular swelling and distortion of dendritic spines and extracellular hypo-osmolality with extracellular volume (ECV) shrinkage. The hallmark of this process is near-complete sustained depolarisation from ∼70 to ∼10 mV. (39)

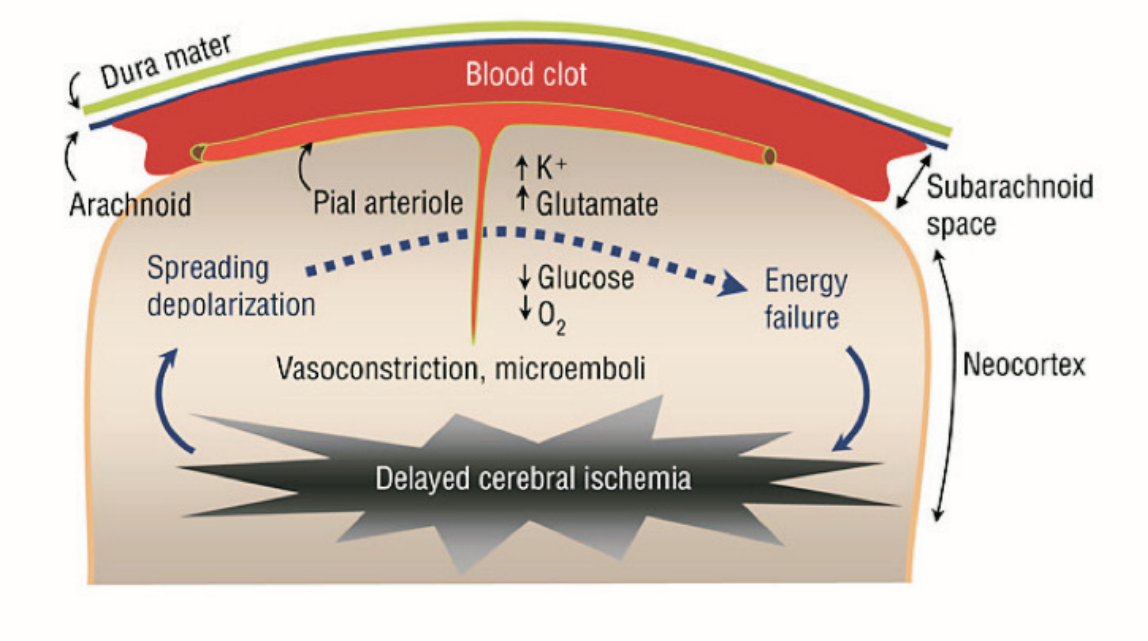


Figure 1.8: Brain injury

Schematic of brain injury taken from (51). Delayed cerebral ischemia may result from a complex chain of events. SDs could precipitate brain damage by imposing additional metabolic stress on the energy-depleted brain and by worsening the oxygen and glucose deficits.

1.2.4 Monitoring the Injured Human Brain

The underlying pathophysiological mechanisms of an injured brain are complex. At present there are a variety of methods that are used in hospitals to monitor the injured brain. Computerised tomography (CT) and functional magnetic resonance imaging (fMRI), can provide useful information by constructing an image of the brain, however it does not provide continuous or bedside monitoring. In fact, most TBI patients have at best two CT scans and no MRI scans during a five day stay in the intensive care ward. There are a variety of methods to monitor brain injury at the bedside which can include intracranial pressure (ICP), changes in brain oxygenation using jugulous venous oxygen saturations or a LICOX probe, brain tissue monitoring via microdialysis, brain electrical activity using electroencephalogram (EEG) or electrocorticography (ECoG) and cerebral hydrodynamics using transcranial doppler flowmetry and near infrared spectroscopy.

To investigate the underlying mechanisms of brain injury, and specifically spreading depolarisations, the electrical and chemical signals should be identified. During the SD event, the tissue is under sustained depolarisation and hence the electrical activity is suppressed due to the neurons being unable to fire (39). Monitoring this

suppression and identifying SD waves, will aid in the assessment of the health of at-risk tissue. It has also been shown that the local glucose and lactate concentrations have a clear response to an SD wave (53). Glucose has been shown to decrease and local lactate levels to increase. These molecules are also associated with energy metabolism in the tissue and may help identify underlying pathways, which lead to tissue deterioration. Therefore, simultaneously monitoring glucose and lactate, as well as electrical activity, will provide further assessment of the health of the tissue.

1.3 Neurochemical Analysis

We have had the opportunity to work with clinicians at King's College Hospital, London, to monitor at the bedside of brain injury patients on the intensive care ward. During surgery, a microdialysis probe, ECoG strip electrode and ICP probe are implanted into the at-risk tissue during surgery allowing the recording of neurochemical changes, brain electrical activity and brain pressure respectively.

Microdialysis sampling coupled with *ex vivo* analysis is one of two main approaches to neurochemical analysis, the other being the implantation of a biosensor directly into the tissue for *in vivo* analysis. An overview of each method will now be given.

1.3.1 Microdialysis

Microdialysis (MD) was originally used to measure the neurotransmitter concentrations within the rat brain in 1974 by Ungerstedt and Pycock (54) and was first used in the human brain in 1990 (55). It is now used in a wide variety of experiments in animals (44, 56) and in human studies (53, 57).

Technique

Microdialysis is a popular method of tissue sensing and uses a semi-permeable membrane to mimic a blood capillary, as shown in figure 1.9. A MD probe consists of a double lumen concentric tube. Buffer that is ionically similar to the extracellular fluid of the tissue, is steadily perfused through the inner tube to the tip of the probe and flows back via the outer tube. At the tip there is a membrane with a molecular weight cut off that can range from 5kDa to 100kDa. This prevents large molecules and cells from entering the dialysate sample. Small molecules, that can diffuse across the membrane, follow their concentration gradients into the probe. The analyte of interest is collected in the dialysate that emerges at the outlet of the probe for *ex vivo* analysis.

Recovery

Microdialysis is a sampling tool and the amount of analyte that diffuses across the semi-permeable membrane into the dialysate, is dependent upon a variety of factors. Recovery (R) can be calculated using equation 1.1.

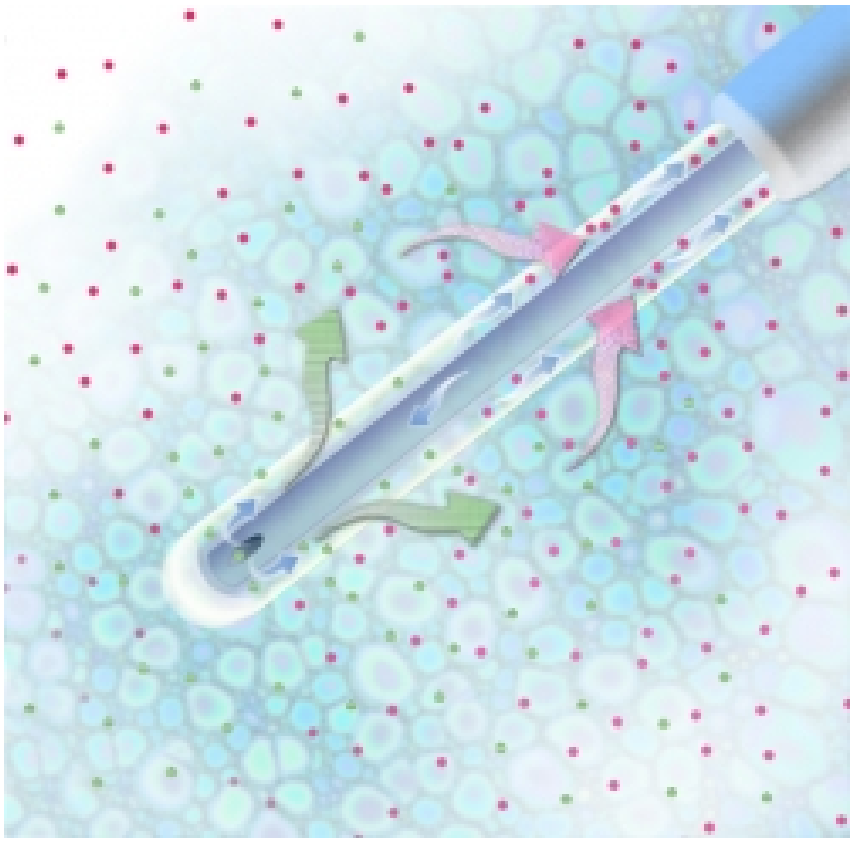


Figure 1.9: Principle of microdialysis
A diagram showing the main principles of microdialysis. Solution flows in through the inner tube and washes over the tip. The tip is a semi-permeable membrane allowing small molecules to diffuse from the tissue into flowing solution. This flow is then carried out of the tissue by the outer tube for analysis. Image from CMA Microdialysis.

$$R(\%) = \frac{C_{out}}{C_{ext}} \times 100 \tag{1.1}$$

C_{out} is the concentration of analyte at the probe outlet and C_{ext} is the *in vivo* analyte concentration. Probe recovery is dependent upon the length of the probe membrane, the external diameter and thickness of the membrane, the perfusion flow rates, the temperature and pH, along with the shape and charge of the analyte. Diffusion through the extracellular space, *in vivo* cellular re-uptake and capillary exchange between the tissue and blood can also affect recovery (58).

Calibration and quantification methods of *in vivo* recovery are controversial, as *in vivo* recovery is dependent on both active and passive effects (7, 59, 60). These include active uptake and release processes, tortuous diffusion paths and excluded volumes (where the cells take up space through which the molecules cannot pass).

The concentration gradients *in vivo* are therefore not principally across the membrane but across the tissue. This is indicated in figure 1.10 which is adapted from (61). In general, *in vivo* recovery is lower than *in vitro* recovery, and *in vitro* recovery should not be used to estimate tissue levels. Tissue levels can be estimated using a no-net-flux (NNF) experiment (7, 62). However, in humans this is not possible and true concentrations are estimated by setting the *in vivo* recovery to 100%. This is achieved by using long membrane lengths and low perfusion flow rates (61).

Detection Method

Analysing neurochemical samples requires high sensitivity and time resolution. The sensitivity of the detection method must allow accurate assessment of concentrations within the physiological range and be able to detect small variations in fast concentration changes. This can be done in a wide variety of ways including optical, electrochemical methods and separation techniques such as mass spectrometry or electrophoresis. Currently, neurochemical analysis on the clinical ward is achieved by combining a microdialysis probe with electrochemical detection.

1.3.2 Rapid Sampling Microdialysis

Classical microdialysis involves hourly sample collection followed by batch-wise analysis using separation techniques, such as HPLC, electrophoresis and mass spectrometry. This has a number of drawbacks within a clinical setting. The low flow rates involved means that a long time is required to collect a large enough volume of dialysate for analysis. Hence, there is a low temporal resolution, due to hourly collection of samples. This has been greatly improved with on-line techniques, such as rapid sampling microdialysis (rsMD), which allows for the collection of samples every 30-60 seconds using flow injection analysis (FIA) (63). Results from both animal (44, 56, 64) and human brain studies (53, 57, 63) indicate that rapid, large changes in neurochemicals occur on these timescales, which can only be recorded by this sampling technique. Therefore, separation techniques such as mass spectrometry or electrophoresis are not ideal for on-line monitoring. The small sample volumes require not only a fast but also a sensitive technique as the samples contain a small number of molecules. By flowing more quickly, the fall in probe recovery with higher flow rates, challenges sensitivity.

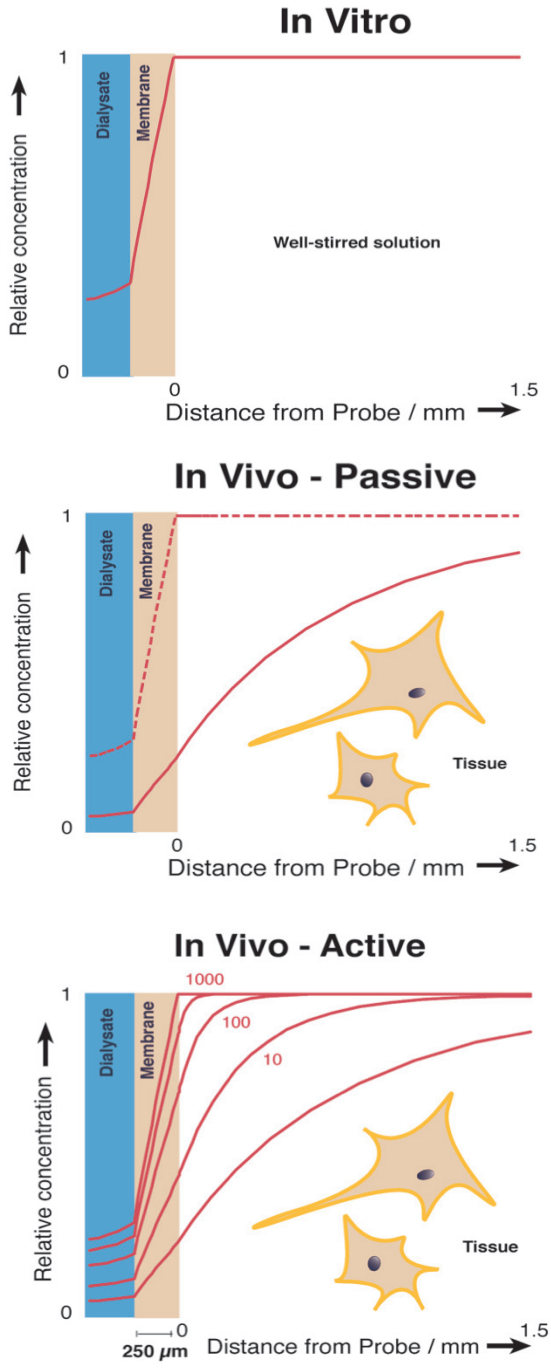


Figure 1.10: Recovery of microdialysis probes *in vitro* and *in vivo*
In *in vitro* recovery the dialysate concentration is limited by the diffusive flux across the membrane and internal flow rate. In *in vivo* recovery there are passive effects such as excluded volumes and tortuous diffusion paths and active effects such as cellular uptake and release rate to the local extracellular fluid concentration. Adapted from (61).

1.3.3 Implanted Biosensors

An alternative to MD sampling is to implant a biosensor directly into the tissue. Microelectrodes are often employed due to the fast time responses and small sizes, 10 ms and 10 s of μm^3 respectively (7).

Electroactive Neurochemicals

A small number of neurochemicals are inherently electroactive, the most important being the neurotransmitter dopamine. Changes in the dopamine concentration at the 100's of nM level, can be detected by fast cyclic voltammetry at carbon fibre electrodes (65). The high voltage scan rates that are used, give both sensitivity and selectivity, as only the kinetics of dopamine oxidation are fast enough for detection.

Non-electroactive Neurochemicals

For non-electroactive neurochemicals, biosensors are used. A biosensor consists of two parts: a molecular recognition component, such as an enzyme, and a signal transducer, for example an electrode. Typically, biosensors operate amperometrically at a constant potential, so a given analyte concentration gives an oxidation flux of the enzyme that is reflected in the current produced by the electrode. This has very good sensitivity. When fabricating a biosensor, the enzymes need to be in close conjunction with the electrode to provide good sensitivity and stability of the biosensor.

Interference

The basal levels of glucose and lactate in the brain have been recorded using implanted biosensors, to be 300 and 100 $\mu molL^{-1}$ respectively (43, 62). The big problem for biosensors studying neurochemicals is interference from other molecules, which may also be present in the sample solution. There are more than 200 neuroactive compounds within the brain (7) and this places a strong requirement for selectivity on any chemical sensor. As many biosensors are operated with a large overpotential, interference from other electroactive species, such as the oxidation of ascorbic acid, is a major problem for measuring glucose and lactate levels in the brain. The concentration of ascorbic acid in the brain is typically 250 to 400 $\mu molL^{-1}$ (66), and hence the current produced by ascorbate can obscure any signal from the analyte of interest. Different approaches to improve selectivity include adding an enzyme filter layer with ascorbate oxidase, as well as using size- and charge-selective polymer films (43). Selectivity can also be achieved by using a sentinel electrode

where the electrodes are self-referencing. Gerhardt developed a glutamate electrode using microfabrication techniques, which had two recording sites, only one containing glutamate oxidase (67). A simple subtraction calculation eliminates background effects and interferences from unwanted molecules.

Calibration

Similar to a MD probe, *in vivo* calibration is a challenge due to tortuous diffusion paths. The majority of groups rely on post experiment calibration. However, neurotransmitters and other proteins may foul the electrode surface, reducing the performance of the biosensor over time. Therefore the calibration of the sensor once it has been removed from the tissue may not be representative of the sensor at the time of recording. These are major challenges and need to be considered when applying biosensors to an *in vivo* environment.

1.3.4 Comparison of Microdialysis and *in vivo* Biosensors

The two main approaches to neurochemical analysis will now be compared in terms of important criteria for accurate and reliable measurements.

Damage

Many neuroanalytical animal studies involve using an *in vivo* sensor to target specific regions of the brain. This is achieved with great accuracy due to their small size. The damage caused upon implantation of a microelectrode is less than that of implanting a MD probe (68, 69), and due to the lower consumption of molecules, sensors do not affect the local dynamics of the environment as much as a MD probe could do. Both an *in vivo* sensor and a MD probe are invasive and the extent of damage occurring upon implantation into the tissue depends upon the dimensions, material sterility, and the perfusion fluid (7). The tracks of a microelectrode and a MD probe, 7 days after initial implantation are shown in figure 1.11 (taken from (69)). It is clear to see that the MD probe (figure 1.11b) causes much more damage to the surrounding tissue than an implanted microelectrode sensor (same position in figure 1.11a).

Blood flow and glucose metabolism decrease immediately after implantation but given time this does recover (7). Initial damage from implantation may result in disruption to the blood brain barrier however resealing usually occurs within 1-2 h. Implantation can next initiate an acute inflammatory response, where cells and proteins of the immune system migrate to the sensor or probe and release reactive

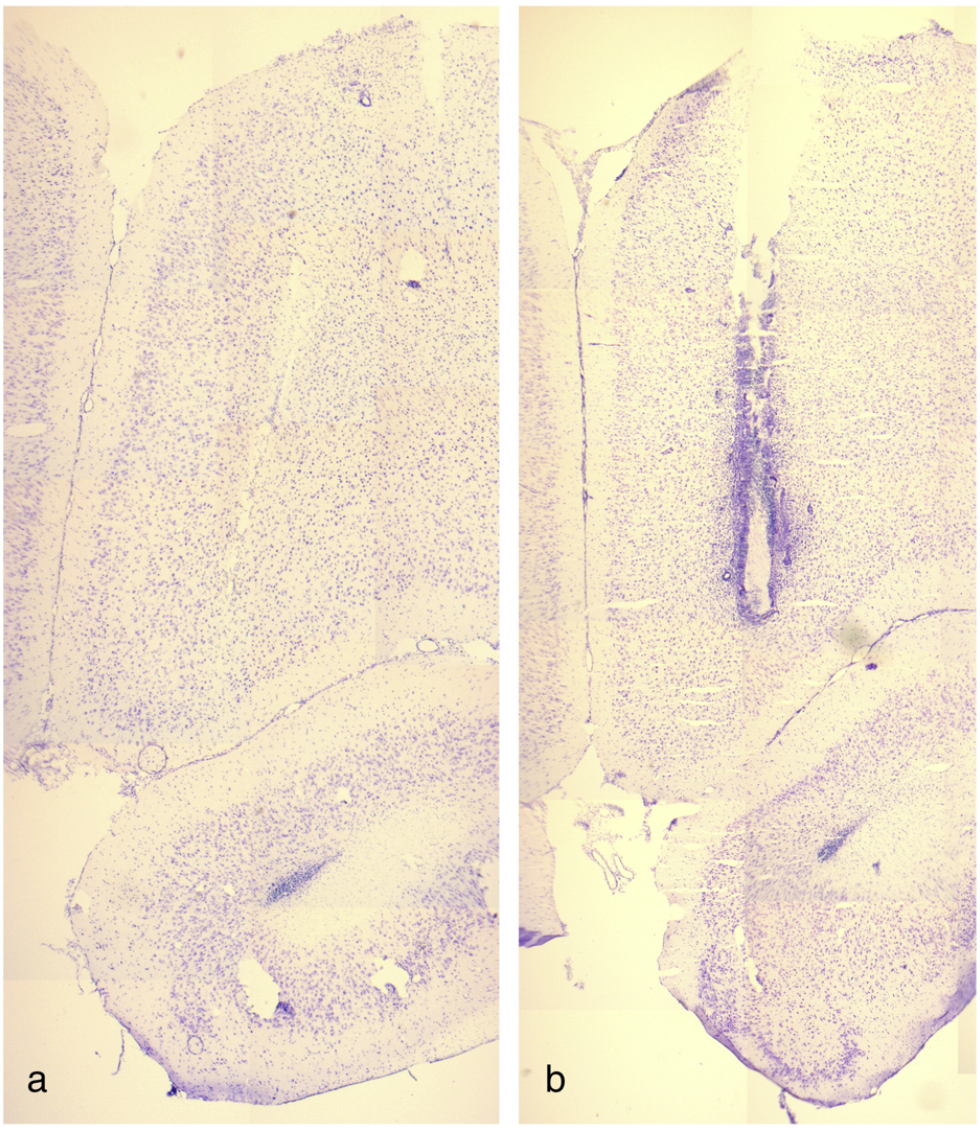


Figure 1.11: Damage upon implantation of a microelectrode and a MD probe
Microelectrode and MD probe placements verified with cresyl violet staining, 7 days following implantation. A: a minor track produced by the microelectrode. B: a pronounced track produced by the MD probe. Taken from (69)

oxygen species and enzymes that adsorb to the surface and lower sensitivity. The acute immune response can last up to three days, and the formation of a fibrotic capsule can block the sensor off from the environment. Use of biomolecules as the molecular recognition element may also induce an immune mediated response, as can the texture of the sensor. Fouling of the sensor or probe is due to reversible or irreversible protein adsorption onto the sensor surface. This conditioning layer endures and mediates all further interactions that occur at the surface (70). To

eliminate the effect of fouling, different polymers applied to the biosensor have been tested for compatibility (64, 71, 72) and a sentinel electrode is often employed (73).

Infection also creates a huge problem when inserting probes or sensors directly into the tissue. Foreign body reactions of the tissue to the biomaterial of the sensor can affect the recordings (71). Kelly Drew found that implanting a MD probe into a tissue caused up to 1.4 mm of damage surrounding the probe using light and electron microscopy (74). Adrian Michael reported that the damage caused by a microsensor is too small to be detected with a light microscope (75). The difference was put down to the significant size difference, however, it was mainly due to infection, as the microdialysis probe had been in the tissue for several months.

Sensitivity

Although implanted sensors have great sensitivity, they are often hindered by noise. As discussed, the sensors are sensitive to other chemicals in the tissue, although much has been done to exclude the interference signals. At very low concentration levels, the signal of the analyte can disappear into the background noise, at which point not much can be done to improve it. Due to the nature of MD sampling, it can be coupled to many other analytical techniques such as HPLC, mass spectrometry or electrophoresis. This allows the collection of samples, which increases the volume analysed, and hence the number of molecules. This improves the sensitivity of the assay and allows multiple neurochemicals to be measured.

Time Resolution

The time resolution of microdialysis is often poor. Classical microdialysis involves the hourly collection of samples. Here, the fast neurochemical changes cannot be identified, only the overall trend. This has been improved upon by rsMD, which analyses samples every 30-60 seconds on-line. However, it still does not compare to the sub-second time resolution of an implanted sensor.

Spatial Resolution

MD has a spatial resolution of 100 μm^3 (7). This is clearly much larger than individual synapses, so MD levels reflect the responses within a local brain area. Microelectrodes often see hot-spots and can have a spatial resolution down to 10 μm^3 (7).

Calibration

There is no good method for calibrating *in vivo* in either microdialysis or implanted sensors. The MD probe is dependent upon the recovery of molecules across the membrane and the surrounding tissue. As the MD probe causes more damage than an implanted sensor, the local tissue environment may change over time and have an effect on the recovery rates of the probe. Calibrating an implanted sensor is also difficult. Many rely upon an *ex vivo* calibration after the experiment, however issues of fouling and interference from unexpected or unknown molecules may affect the interpretation of such a calibration.

Human Use

In human studies an *in vivo* sensor cannot be directly implanted into the brain due to compatibility issues. The biosensors contain many substances (enzyme, immobilising films etc.), which may be toxic and immunogenic. These molecules must be proven to cause no adverse reaction in the tissue before use, which is a difficult task. Therefore, many use a microdialysis probe, as it is already FDA approved and is easily sterilised. To date, no implantable sensor has been approved for clinical use. Examples of sensors designed for monitoring the human brain include carbon fibre monitoring of dopamine (76, 77), and biosensors for glutamate sensing (78), proving that this method is exceptionally difficult to implement.

1.3.5 A New Paradigm for Microdialysis

At present, for clinical monitoring we are restricted to using microdialysis. With on-line microdialysis, the only format to give higher time resolution, there is often a significant length (typically 1 m) of low volume connection tubing. At the low flow rates used in microdialysis, this length results in a time lag between dialysate leaving the brain and analysis, typically ten minutes. The flow rate is limited due to pressure upon the membrane and is set at a compromising flow rate (between time lag and recovery) of 2 μLmin^{-1} in the intensive care unit. A major problem is Taylor dispersion, (79) which acts in continuous flows and is described in more detail in chapter 6. Dispersion of molecules reduces the signal amplitude and broadens the signal of transient changes, increasing the difficulty of analysis. The microdialysis equipment and particularly the associated analysis instrumentation, is not suitable for mounting on the animal or patient. The clinical rsMD system is described in detail in chapter 2 and within clinical use, it is placed on a trolley behind the patients

bed. Miniaturisation of the system would be preferable and may lead to a wearable device that allows monitoring of patients not only at the bedside but as they recover and begin to move around.

Whilst rsMD had improved the time resolution from classical microdialysis, a continuous measurement of concentration levels would increase the time resolution further. The small volumes involved with using microdialysis must be analysed accurately and with an easily measurable output. The use of microelectrode-based biosensors allows a fast response time with great sensitivity in the physiological range within these small sample volumes. Coupling biosensors to microdialysis would therefore be of great advantage, allowing rapid changes in metabolites to be seen. This method would be highly translational between animal and clinical studies, as biosensors could be combined with microdialysis to analyse the dialysate continuously for several days due to the ability to frequently calibrate the biosensors *ex vivo*. In this thesis, glucose and lactate biosensors have been combined with microdialysis.

A method to address all of these problems could be the implementation of a microfluidic platform. Lab-On-Chip (LOC) devices aim to miniaturise a full chemical laboratory onto a small device. Within the device all the manipulations and chemical reactions for appropriate analysis takes place. This idea was first introduced by miniaturising chemical electrophoresis onto a chip (80). Here, the channels were micromachined using microphotolithographic techniques and samples were injected, separated and detected on-chip.

The flexibility of design and usefulness in many different areas, from pharmaceuticals and biotechnology, to defence and agriculture, has enabled microfluidics to become very successful. Continuous flow microfluidic platforms have had great success in use for kinetic studies (81, 82), on-chip polymerase chain reaction (PCR) (83, 84, 85), diagnostics (86, 87) and cell studies (88, 89) due to the inherent advantages of very small sample volumes, faster analysis times and low cost.

The aim in this thesis is to use a microfluidic chip, not only to miniaturise the system, but also to remove many problems facing microdialysis users. Namely, those caused by the long connection tubing that is often required: Taylor dispersion and long time delays before analysis. More information on microfluidics can be found in chapter 5.

1.4 Outline of Thesis

The current clinical analysis system, rapid sampling microdialysis (rsMD), is described in detail together with common methods and materials in chapter 2.

To improve the time resolution, a microelectrode-based biosensor is proposed which will allow for continuous analysis of the microdialysate. The development of small, integrated electrochemical cells using microelectrodes for the placement within small flow channels is discussed in detail in chapter 3. Using these electrodes, key biosensors, such as glucose, lactate and ATP, are fabricated. The performance of the biosensors is discussed in chapter 4.

Digital microfluidics has been developed for use with a microdialysis probe to eliminate the Taylor dispersion seen in the long lengths of connection tubing necessary in a clinical ward. Chapter 5 discusses the implementation of a microfluidic toolkit. This starts with a T Junction, which is used to generate droplets of microdialysate in oil. The droplets are transferred to a second microfluidic chip for analysis. Digital microfluidics reduces the time lag (the time taken for the sample to leave the probe in the brain and reach the analysis system) by using a fast flowing oil stream and propelling the droplets to the analysis. This not only allows real time analysis of the microdialysate but has the added advantage of allowing the perfusion rate to be lowered, which in turn increases the recovery of the probe, without affecting the time lag. Further manipulations of droplets, such as dosing with standards and enzymes, are also discussed. Placement of electrodes within an analysis chamber, designed to collect droplets and remove the oil, and the performance of biosensors on-chip is described in chapter 6.

In chapter 7, the microfluidic system is tested in a pilot animal study using a glucose biosensor in continuous flow. Here the glucose biosensor is validated against rsMD glucose levels. Models of ischemia were used to investigate brain physiology in a translational study and laser speckle was used to monitor blood flow whilst glucose, lactate and potassium levels were also measured. Finally, the thesis ends with proof of concept clinical data and a discussion about implementation and validation of the microfluidic system in the clinical ward.

Chapter 2

Methods & Materials

2.1 Electrochemistry

Electrochemistry is the study of reactions that occur at the surface of an electrode. It involves the exchange of electrons between the electrode surface and the solution and it is generally dependent upon the potential applied to the electrode. The transfer of the analyte towards the surface of the electrode occurs by diffusion down a concentration gradient (the concentration being small at the electrode surface due to consumption during the reaction). In transport limited conditions the movement of electrons between the solution and the electrode can be measured as current, which is proportional to the bulk concentration of reacting species. Electrochemical methods offer good spatial and temporal resolution and a continuous monitoring of the analyte.

2.1.1 Cyclic Voltammetry

Cyclic voltammetry (CV) is a widely used electrochemical method and involves linearly scanning the potential applied to the working electrode, up and down at a constant rate, to oxidise and reduce the species at the surface of the electrode. When a potential is reached where a reaction can occur, an increase in current is seen. A typical waveform and CV is shown in figure 2.1. This can be used to study the reversibility of the reaction, the analyte concentration and can provide some detail of the surface and the geometry of the electrode. The CV in figure 2.1B, was obtained using a cylindrical electrode (diameter 125 μm) in 1.5 mM ferrocene monocarboxylate (Fc), recipe shown in section 2.4.1. As the potential is scanned more positive, Fc is oxidised to Fc^+ and Fc is depleted from the electrode surface

creating a concentration gradient. The peak current can be related to the diffusion coefficient, the number of electrons exchanged, the electrode surface area, the analyte bulk concentration and the scan rate, by the Randles-Sevcik equation. Upon the reversal of potential, Fc^+ is reduced back to Fc, due to the reaction being reversible. Standard redox couples such as, Fc, Hexaamine ruthenium (III) chloride (RuHex) and potassium ferrocyanide (FeCN), are commonly used to assess the electrode surface prior to biosensor fabrication. In this thesis, the electrodes were connected in a three electrode cell, to a potentiostat which is controlled using EChem software.

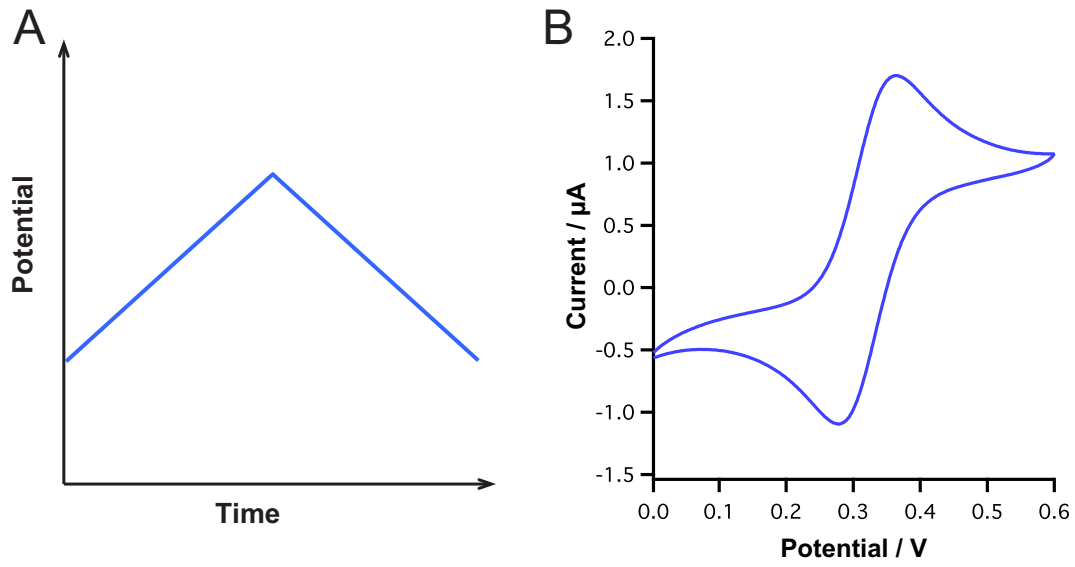


Figure 2.1: Cyclic voltammetry
A: shows a typical waveform used in cyclic voltammetry B: A typical CV produced using a platinum electrode (125 μm diameter, 2 mm long) in 1.5 mM ferrocene monocarboxylate.

2.1.2 Amperometry

Amperometry is another commonly used electrochemical technique. Here, the electrode is held at a constant potential and the current is monitored over time. In this thesis, two common methods use this technique: electropolymerisation and biosensor characterisation. These methods will now be described.

Electropolymerisation

Electropolymerisation involves the application of a fixed potential to an electrode, which triggers the polymerisation of monomers within the solution to join together. More information on the electropolymerisation of immobilising films is given in chapter 4.

A typical electropolymerisation trace is shown in figure 2.2. Electropolymerisation is particularly well suited to non-conducting films as growth of the polymer is self-limiting and produces a relatively thin film.

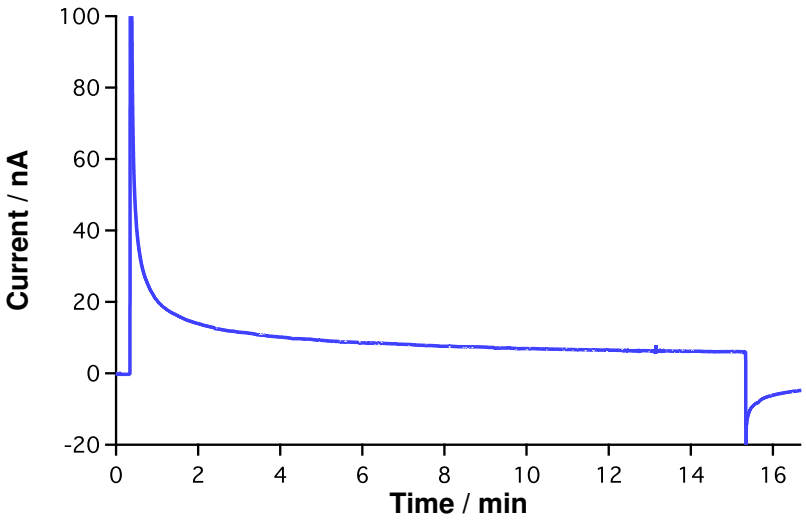


Figure 2.2: Electropolymerisation
The typical trace seen during electropolymerisation of a film to the electrode surface. 50 mM phenol in PBS pH 7. 0 V for 20 seconds, 0.9 V for 15 minutes, 0 V until end.

Unless otherwise stated, the biosensors used in this thesis, contain an electropolymerised poly(phenol) film to entrap the enzymes close to the surface of the electrode. The schematic of the polymerisation of phenol is shown in figure 2.3 (Image taken from (90)). The oxidised phenol molecule creates a radical that couples to a second phenol molecule creating a para-linked dimer radical. This can occur repeatedly to form a polyphenol film. Once formed, if a high potential is applied to the electrode, hydroxyl radicals can be formed and can mechanically break up the polyphenol film (90).

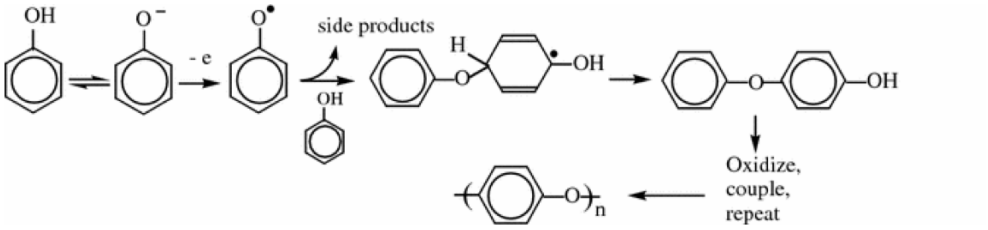


Figure 2.3: Polymerisation of phenol
A schematic of the polymerisation of phenol. Image taken from (90). The phenol molecule is oxidise to form a phenoxy radical which couples to other phenol molecules forming a polymer film.

Biosensor Characterisation

The biosensors were assessed using standard amperometric techniques, in an electrochemical cell with a silver silver chloride (Ag|AgCl) reference and Pt wire auxiliary electrode, unless an integrated electrode was used (discussed in chapter 3). Experiments were carried out using an in-house potentiostat. All measurements were performed at +0.75 V vs. Ag|AgCl in buffer (PBS pH 7.2, Krebs pH 7.4). For calibrations, aliquots of substrate were added using a glass Hamilton syringe, under stirred conditions. The step changes in current corresponded to the concentration of substrate added.

The biosensors were placed in the flow cell (Radel or PDMS) and calibrated using a syringe switcher to perfuse the electrodes with varying concentrations. The biosensor was held at 0.75 V and connected to using an in-house potentiostat to measure current. On-chip characterisation is discussed more in chapter 6.

2.2 Rapid Sampling Microdialysis

Rapid sampling microdialysis (rsMD) is the current clinical analysis system used to monitor dialysate from brain injury patients. A microdialysis (MD) probe is inserted during surgery and is linked to a mobile bedside rsMD system via a 1 m length of low volume FEP connection tubing. The dialysate stream was fed into the rsMD valve, which alternates injections between enzymatic beds of glucose and lactate, at 30 second intervals. Details of all the equipment used in rsMD will now be given and a schematic is shown in figure 2.4.

2.2.1 Microdialysis Probe

A MD probe (CMA70, CMA Sweden) was inserted during a craniotomy, into the area of tissue estimated to be the ischemic penumbra, on the basis of Xenon CT scans. The probe was perfused using sterile aCSF (CMA Sweden) at 2 μLmin^{-1}.

2.2.2 Injection Valve

The MD probe outlet was connected to 1 m FEP tubing (Thames-Restek, Bucks). At the other end, a needle (22 gauge, 0.75 inches, Hamilton, Switzerland) is used to connect the tubing into a port on the injection valve. The custom-made 6 port valve (Valco Instruments, Schenkon, Switzerland, USA) has a 0.2 μL dual internal loop. Standard solutions used for calibration are manually injected into the valve using a Hamilton glass syringe.

The six ports are in pairs, one pair is the inlet and outlet of dialysate. Another pair connects a Fc stream to a glucose enzyme bed reactor. And the final pair of ports connects a Fc stream to a lactate enzyme bed reactor. As the valve switches position, a sample of dialysate is injected into the Fc stream and carried to the reactor.

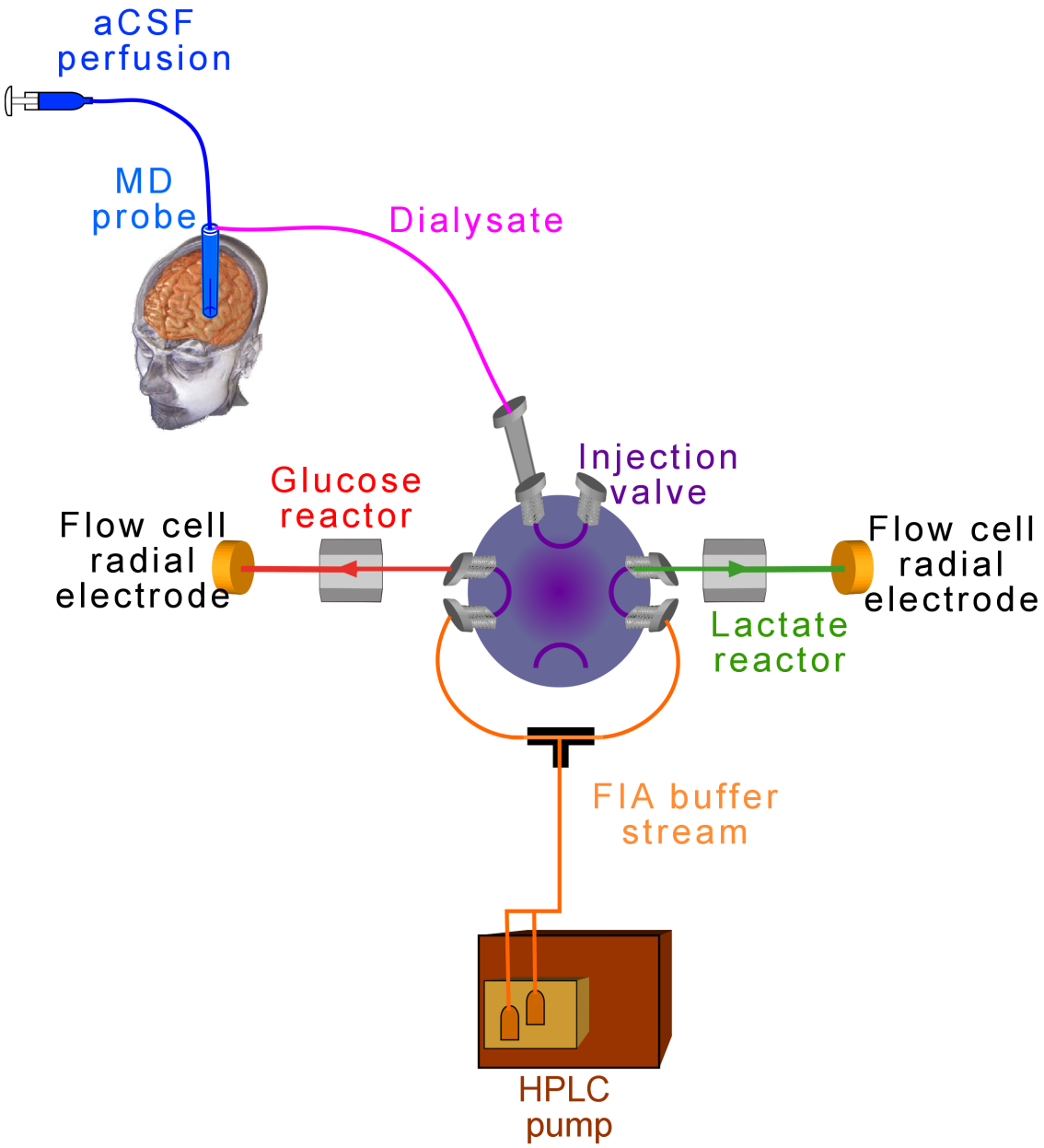


Figure 2.4: rsMD schematic

The rapid sampling on-line clinical analysis system. aCSF is perfused through a MD probe, which is placed during surgery in the at-risk penumbral tissue. The dialysate is transferred via approximately 1 m low volume connection tubing to the injection valve, which switches every 30 seconds. This injects a sample of dialysate into a FIA buffer stream containing Fc. The sample passes through either a glucose or a lactate reactor and the radial flow cells contain electrodes used to detect the reaction products.

2.2.3 Enzyme Beds

Enzyme beds consist of membranes (6 mm discs) that are loaded with enzyme. Reactors hold these membranes in place and are made from biocompatible filter components with three sections - stainless steel body and two PEEK end fittings.

To load to the membranes with enzyme, the enzyme was dissolved in ferrocene buffer and filtered several times through a 25 mm filter holder (Swinnex, Millipore, UK) containing a mixed cellulose ester membrane (0.025 μm pore, 25 mm, Millipore UK). A ring was placed in the filter holder to create a seal so that the enzyme must pass through the membrane. When successful the membrane turns a yellowy colour, as intensive filtering adsorbs the enzyme in the filter. Several membranes of 6 mm diameter were then punched from the original using a hole punch. To prevent drying, the membranes were stored in Fc solution in the fridge. Two membranes, one containing the substrate oxidase (SOx) and the other HRP, were sandwiched in the reactors. SOx must be the first membrane, in the direction of flow, to ensure the biochemical reaction takes place.

2.2.4 Radial Flow Cell

The electrodes used in conjunction with rsMD were housed in a radial flow cell (BAS, USA). The flow from the enzyme reactors passes through a stainless steel jet auxiliary. A 3 mm glassy carbon working, is embedded in the radial flow cell, as is a Ag|AgCl reference electrode. The working and auxiliary electrodes are separated using a 16 μm teflon gasket.

2.2.5 Data Analysis

When the injected sample is detected at the electrode, changes in current are seen as peaks. The amplitude of the peaks is related to the concentration of substrate in the dialysate. A calibration curve is formed from injections of known standards directly into the valve. The peak heights are then compared to the calibration curve for conversion into concentration. The raw data is processed using Matlab where algorithms are used to remove common noise artefacts such as spikes, ripples and baseline drift (91).

2.2.6 The Clinical Trolley

The clinical trolley is used to hold all the equipment necessary for bedside monitoring. The clinical trolley is shown in figure 2.5. The trolley consists of several shelves to hold the electrical equipment: HPLC and syringe pumps, powerlabs and an uninterruptible power supply (UPS). The solutions are held in a side tray in bottles. The moveable arm contains the flow injection valve and enzyme beds in the front compartment (open in the photograph) and the potentiostats are contained in the back.

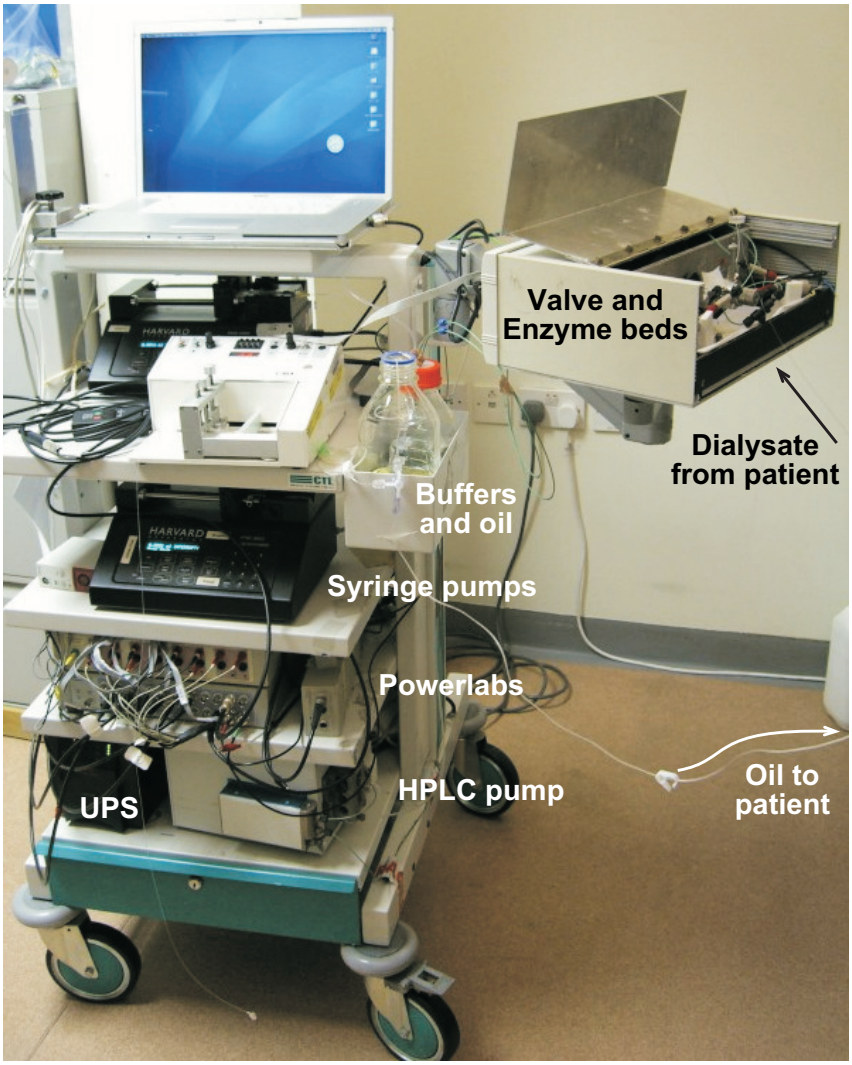


Figure 2.5: The clinical trolley
The trolley houses all the equipment required for rsMD monitoring at the patients bedside.

2.3 Microfluidics

2.3.1 Mask: Design and Fabrication

In collaboration with Dr Xize Niu, several designs to generate and rejoin the droplet of dialysate were generated. The designs were drawn out using AutoCad (AutoDesk) and a thin dark-film mask printed (Circuit Graphics). The mask is transferred to glass layered with chromium, after which it can be used multiple times to create a master. The channel designs are discussed in more detail in chapter 5.

2.3.2 Master Fabrication

A negative master is generated using 1:1 contact photolithography. Photolithography uses light to create a pattern in a photoresist, and involves a series of chemical treatments to engrave or deposit the pattern. A commonly used photoresist is SU-8. This is a negative photoresist, which becomes insoluble when exposed to UV light, due to cross-linking of long molecular chains. It is popular due to its excellent adhesion to silicon, high stability, formation of near vertical walls giving high resolution and its biocompatibility.

The masters used in this thesis are fabricated by spin coating SU8-2025 negative photoresist (Microchem) onto a silicon wafer (3-inches diameter, Compart Technology) at 3000 rpm and baking at 65 °C for 5 minutes, followed by 30 minutes at 90 °C. The glass mask is placed firmly on top and is exposed to UV light for 20 seconds and then baked for 1 minute at 65 °C and for 5 minutes at 90 °C. This is known as post exposure baking (PEB). The master is then placed in a developing solution (SU8 developer) for 2 minutes and blown dry using nitrogen gas. Silanization occurs for 30 minutes, which changes the surface chemistry of the master so that it is chemically inert, which allows the microfluidic chip to peel easily away from the surface once cured.

2.3.3 Use of Chips

FC-40 oil was used as the carrier fluid in the experiments (unless stated otherwise) and was motivated using precision syringe pumps (PHD2000 Harvard Apparatus). A high-speed camera (Phantom V) attached to an inverted microscope, was used for video acquisition and Matlab and ImageJ were used to analyse the recorded images.

2.4 Materials and Reagents

2.4.1 Ferrocene Monocarboxylate

Ferrocene monocarboxylate (Fc) was used in rsMD to mediate the reaction occurring in the enzyme beds. It was regularly made to avoid contamination and is kept in the fridge. Fc was also used in some electrochemical techniques as a redox couple, such as cyclic voltammetry, to assess the surface of the electrodes.

It was composed of sodium citrate (0.1 M, Sigma), ferrocene monocarboxylate (1.5 mM, Fluka), EDTA (1 mM, Fluka), and sodium chloride (150 mM, BDH laboratory supplied). The pH was adjusted to pH 7.0 using 1 M hydrochloric acid. If the solution was for use at the hospital, 0.5 ml of 5-chloro-2-methyl-4-isothiazoline-3-one (Kathon CG, Rohms and Hass) was added as an antibacterial agent, and the solutions were filtered with membrane filters (0.1 μm and 0.02 μm 47 mm Anodisc, Whatman International Ltd) to avoid blocking of the small bore tubings.

2.4.2 Hexaamine Ruthenium (III) Chloride

Hexaamine ruthenium (III) chloride (denoted in this thesis as RuHex) was used a redox species in electrochemistry to assess the performance of the working electrodes. 1 or 10 mM RuHex (Sigma) was dissolved in 0.1 M or 1 M potassium chloride (Sigma) respectively ($Ru(NH_3)_6Cl_3$). Before use the solution was de-oxygenated by purging with nitrogen gas for 20 minutes.

2.4.3 Potassium Ferrocyanide

Potassium ferrocyanide (denoted in this thesis as FeCN) was also used as a redox species in electrochemistry to assess the electrode performance. 1 or 10 mM FeCN (Sigma) was dissolved in 0.1 M or 1 M potassium chloride respectively ($K_3Fe(CN)_6$).

2.4.4 Phosphate Buffer Solution

Phosphate buffer solution (PBS) was used during biosensor calibrations. It was composed of 150 mM sodium chloride and 100 mM di-sodium hydrogen orthophosphate 2 hydrate (Sigma). The pH was adjusted to 7.2 using 0.1 M sodium hydroxide.

2.4.5 Artificial Cerebral Spinal Fluid

Artificial cerebral spinal fluid (aCSF) was used as the dialysate in brain injury microdialysis. It consisted of a physiological saline with the following concentrations. 150 mM sodium chloride, 3 mM potassium chloride, 2.5 mM calcium chloride and 1.8 mM magnesium chloride.

2.4.6 Krebs Buffer Solution

Experiments involving ATP biosensors were carried out using Krebs buffer solution. Krebs composition consisted of 117 mM sodium chloride, 4.7 mM potassium chloride, 2.5 mM calcium chloride, 1.2 mM magnesium chloride, 1.2 mM sodium dihydrogen phosphate, 25 mM sodium bicarbonate and 11 mM glucose. pH was adjusted to pH 7.4

2.4.7 Substrate Standards

Standard solutions of glucose, lactate and ATP (all from Sigma-Aldrich) were dissolved into PBS for biosensor calibrations. For animal and clinical studies, standards were dissolved into aCSF and for ATP studies, into Krebs solution.

Chapter 3

Development of Microelectrodes

3.1 Introduction

The aim of this thesis is to develop a microfluidic system with incorporated electrochemical sensors for the continuous measurement of dialysate from brain injury patients. The electrochemical cell was changed in design to improve both the biochemical measurements and for incorporation on the microfluidic analysis chip. This chapter will focus only on the development of the electrodes used throughout this thesis.

3.1.1 Working Electrode Material

As a sensing element of a biosensor, the electrode material must be sensitive to the reaction of interest. Biosensors are described in detail in chapter 4, but the molecule that the electrode will detect (a product of the enzymatic reaction) is hydrogen peroxide (H_2O_2) and this will be discussed in this section.

Whilst there are many potential materials to use for an electrode the fabrication process limits the choice by material and size. Easily fabricated electrodes could include carbon fibre, gold and platinum. Carbon fibre electrodes are often used to study neurochemistry. Neurotransmitters are easily oxidised and therefore easily measured on a carbon fibre electrode which are frequently used to monitor molecules such as dopamine (92, 93, 94).

The ability of the electrodes to respond to H_2O_2 was characterised by the step changes in current following the addition of increasing concentrations of H_2O_2 over time. A calibration curve was thus obtained. It is known that carbon fibre and gold do not oxidise H_2O_2 at a useable rate at a low potential and figure 3.1 compares the response at a platinum and a gold electrode. Indeed, platinum exhibits a good response with higher sensitivity towards H_2O_2 as compared to gold. Platinum was therefore selected as the material of choice for the working electrodes, which are used in this thesis.

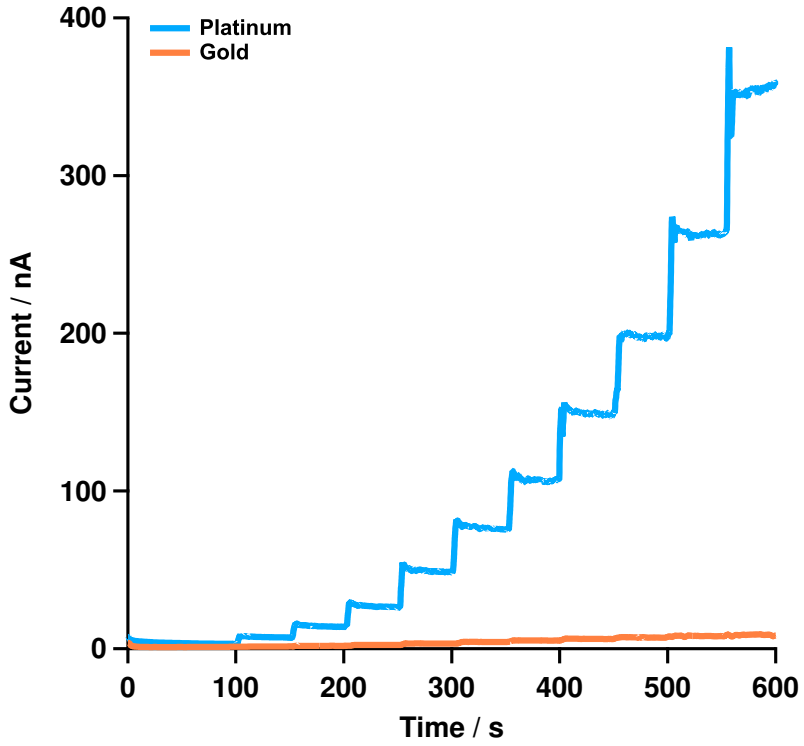


Figure 3.1: Hydrogen peroxide calibration on platinum and gold electrodes
0.5 mM, 1 mM, 2.5 mM, 5 mM, 7.5 mM, 10 mM, 15 mM, 20 mM, 30 mM, 50 mM step changes in H_2O_2 concentration occurring every 50 s. The response of a 50 μm electrode is recorded.

H_2O_2 is oxidised by platinum at a low potential and the electrons transferred to the electrode produce a measurable current. The reaction of H_2O_2 at the surface of the platinum electrode is an adsorption controlled mechanism (95). The overall reaction is shown in equation 3.1.

$$Pt + H_2O_2 \longrightarrow Pt + 2H^+ + 2e^- + O_2 \tag{3.1}$$

This is a two step process. When a potential of 0.7 V is applied to a platinum electrode the reaction, shown in equation 3.2, occurs. When hydrogen peroxide is present the reaction, shown in equation 3.3, occurs as soon as possible.

$$Pt + 2H_2O \longrightarrow Pt(OH)_2 + 2H^+ + 2e^- \tag{3.2}$$

$$Pt(OH)_2 + H_2O_2 \rightleftharpoons Pt + 2H_2O + O_2 \tag{3.3}$$

This cyclic reaction constantly supplies two electrons to the platinum surface for as long as hydrogen peroxide is available. The reaction can also be broken down into an absorption step (equation 3.4) and a reduction step (equation 3.5).

$$Pt(OH)_2 + H_2O_2 \rightleftharpoons Pt(OH)_2.H_2O_2 \tag{3.4}$$

$$Pt(OH)_2.H_2O_2 \longrightarrow Pt + 2H_2O + O_2 \tag{3.5}$$

This mechanism is therefore analogous to a Michaelis-Menten enzyme mechanism and hence surface availability (in the form of $Pt(OH)_2$ sites), which catalyses the conversion of hydrogen peroxide to water can limit the rate of reaction. If the sites are saturated with hydrogen peroxide then the rate of reaction is at its maximum, known as V_{max}. This leads to complications such as competition for the reaction sites, which could potentially lead to fewer points where the hydrogen peroxide can be detected, ultimately leading to a lower sensitivity, as seen in figure 3.2. One such competing reaction is shown in equation 3.6. This removes the active $Pt(OH)_2$ sites but does not produce the inactive Pt species. Hence, the overall reaction cannot occur and sensitivity is low. Another competing reaction is shown in equation 3.7. At low hydrogen peroxide concentrations this is not a problem as the concentration of $Pt(OH)_2.H_2O_2$ is low. However when the level of $Pt(OH)_2.H_2O_2$ increases, production of the protonated complex can occur. This species cannot undergo the reaction step and the current signal is lost.

$$Pt(OH)_2.(hydroxidegroups) + O_2 \rightleftharpoons Pt(OH)_2.O_2 \tag{3.6}$$

$$Pt(OH)_2.H_2O_2 + H^+ \leftrightharpoons Pt(OH)_2.H_2O_2.H^+ \tag{3.7}$$

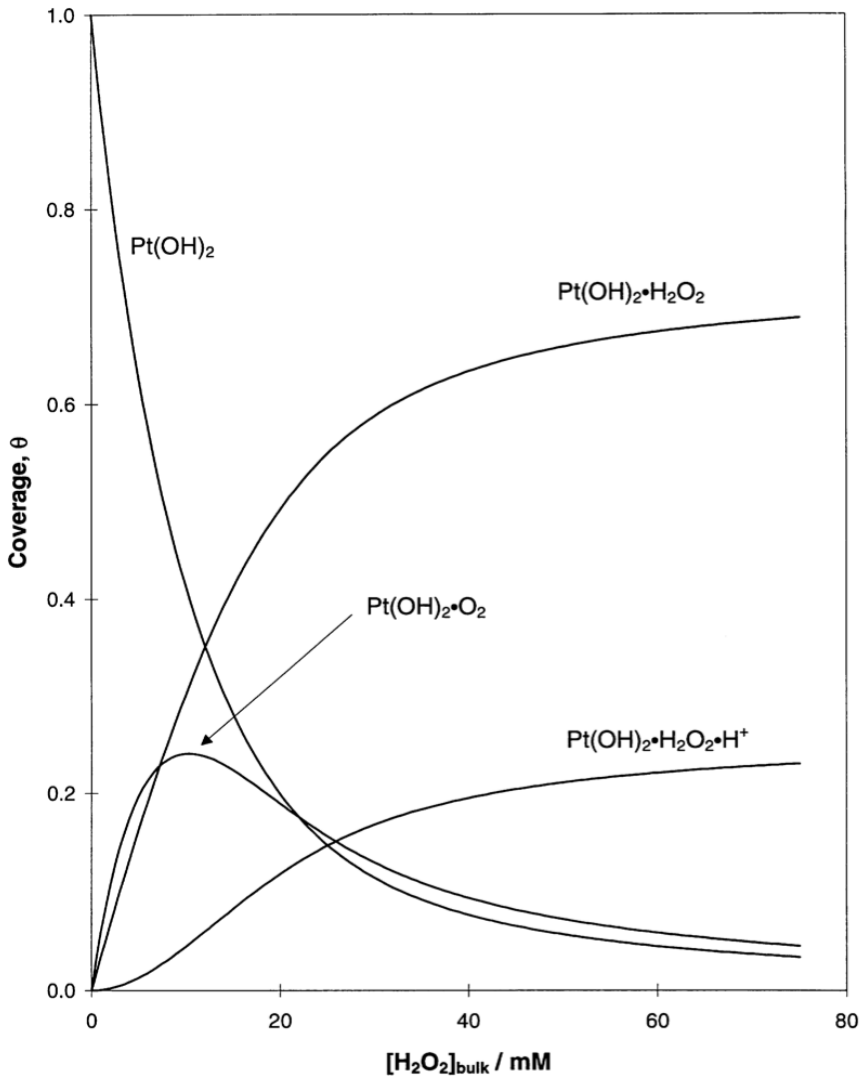


Figure 3.2: Surface species for hydrogen peroxide oxidation on a platinum surface
Figure taken from Hall et al (95). Concentration of different species on the surface of a platinum electrode are shown as the bulk concentration of hydrogen peroxide increases.

3.1.2 Microelectrodes versus Macroelectrodes

Microelectrodes and macroelectrodes are defined by their dimensions (micrometre and millimetre respectively). The currents seen at a microelectrode are typically pA or nA, and are several orders of magnitude smaller than the currents passed at a macroelectrode. The difference in size causes differences in diffusional mass transport. At a macroelectrode the diffusion of molecules to and from the surface is planar. Reducing the size to a microelectrode means that the enhanced edge effects

transform the diffusion field into a hemispherical shape and the dimensions of the diffusion field around a microelectrode, exceed the dimensions of the electrode itself. Subsequently the flux of molecules to the electrode surface is significantly higher than the flux to a macroelectrode. This efficiency of mass transport allows steady-state observations at low scans rates during cyclic voltammetry.

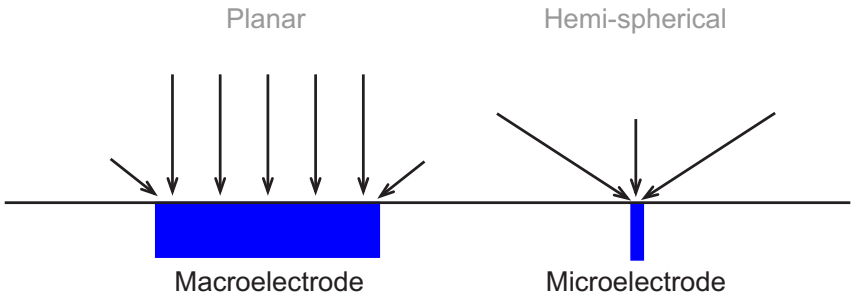


Figure 3.3: Schematic of the diffusion field of electrodes
The electrodes are shown in blue and the diffusion of molecules to the surface of the electrode is indicated by the arrows. Diffusion to a macroelectrode is planar whereas the diffusion field to a microelectrode is hemispherical.

3.1.3 Microelectrode Theory: Inlaid Microdisk

At a sufficiently long time the solution to the convective diffusion equation for an inlaid micro disc electrode is given by equation 3.8.

$$I = 4nFDrC \tag{3.8}$$

Where n is the number of electrons transferred, F is the Faraday constant (96487 $Cmol^{-1}$), D is the diffusion coefficient, r is the radius of the microelectrode and C is the concentration of the species involved.

The diffusion coefficient for ferrocene monocarboxylate (Fc) used, was 5.73 x 10^{-10} m^2s^{-1} found in Bartlett and Pratt 1995 (96), which experimentally finds the diffusion coefficient for FeCOOH for cyclic voltammetry and ring disk experiments. The diffusion coefficient for hexaamine ruthenium (III) chloride (RuHex), used is 7.7 x 10^{-10} m^2s^{-1} from Beriet and Pletcher, 1994 (97) and for potassium ferrocyanide (FeCN), 6.5 x 10^{-10} m^2s^{-1} also taken from (97). As hydrogen peroxide will be detected at the electrode surface this too is included here. The process involves a two electron transfer with a diffusion coefficient of 1.3 x 10^{-9} m^2s^{-1} (98).

A summary of the current expected at different sizes of electrodes for these different species is shown in table 3.1, based on equation 3.8.

Table 3.1: Currents expected from inlaid microdisc electrodes

Electrode Diameter / μm	Concentration / mM	Current / nA
Ferrocene monocarboxylate		
125	1.5	20.7
50	1.5	8.3
25	1.5	4.2
125	1	13.8
50	1	5.5
25	1	2.8
Hexaamine ruthenium (III) chloride		
125	1	18.6
50	1	7.4
25	1	3.7
Potassium ferrocyanide		
125	1	15.7
50	1	6.3
25	1	3.1
Hydrogen peroxide		
125	1	62.7
50	1	25.1
25	1	12.5

3.1.4 Microelectrode Theory: Hemispherical Electrode

If the electrode is not flat, but curved in shape, it is said to be hemispherical in geometry. The equation to find the current (I), which is expected when using a hemispherical electrode, is given by equation 3.9.

$$I = 2\pi FDrC \tag{3.9}$$

Where F is the Faraday constant (96487 $Cmol^{-1}$), D is the diffusion coefficient, r is the radius of the electrode and C is the concentration of the species used. Using the diffusion coefficients from before, table 3.2 has been created to indicate how much current would be expected from a hemispherical disc electrode. These theoretical currents have been used in this thesis to assess the results obtained from characterising the electrodes in table 3.4, section 3.3.3.

Table 3.2: Currents expected from hemispherical electrodes

Electrode Diameter / μm	Concentration / mM	Current / nA
Ferrocene monocarboxylate		
125	1.5	32.5
50	1.5	13.0
25	1.5	6.5
125	1	21.7
50	1	8.7
25	1	4.3
Hexaamine ruthenium (III) chloride		
125	1	29.2
50	1	11.6
25	1	5.8
Potassium ferrocyanide		
125	1	24.6
50	1	9.9
25	1	4.9
Hydrogen peroxide		
125	1	49.2
50	1	19.7
25	1	9.9

3.2 Cylindrical Electrodes

The first approach, of incorporating microelectrodes into the clinical system for analysis of low volume and low flow rate dialysate, was to use a wire in a fine bore tube. This created a cylindrical electrode within a flow cell and a schematic is shown in figure 3.4.

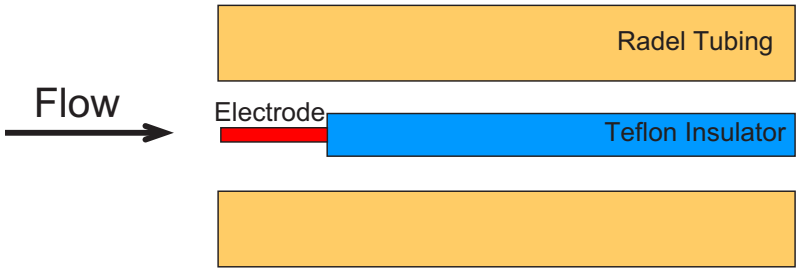


Figure 3.4: Schematic of a radel flow cell
The schematic shows a cross section through a Radel tubing flow cell. The walls of the tubing are shown in yellow. The electrode is threaded inside with the exposed surface (red) close to the entrance of the flow cell. The insulation is shown in blue.

Cylindrical electrodes have the advantage of a large surface area, which gives an easily measurable current. The electrodes were arranged into a flow cell designed to attach to the rsMD outlet. This was to achieve a continuous recording of glucose and lactate levels using biosensors, described in chapter 4.

3.2.1 Fabrication of Electrodes

Platinum/iridium wire (Advent) insulated with Teflon (125 μm diameter) and platinum wire (A-M Systems Inc) insulated with Teflon (50 μm diameter) were used to create working electrodes. The insulation was removed either by cutting the insulation with a scalpel or by melting the insulation with a lighter. This exposed the wire to create a cylindrical electrode, which was then cut to size. The insulation was removed from the opposite end and an IC socket (RS components) was soldered on as a connector. The silver wire (50 μm, Advent) was chloridised using potassium dichromate solution (BAS Inc USA) to produce a Ag|AgCl reference electrode. To assess the electrode prior to use, cyclic voltammetry was used which investigated properties such as CV shape, peak height and peak separation. Figure 3.5 shows a typical CV of a cylindrical wire in 1.5 mM Fc.

The main problem of electrode fabrication was the precise exposure of electrode surface by removing the Teflon insulator. The main method used was scraping the

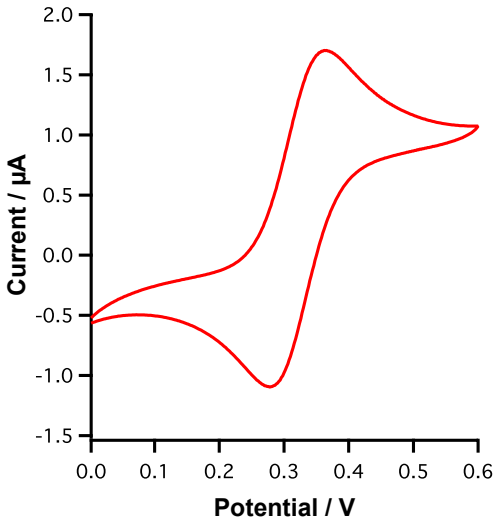


Figure 3.5: CV of a cylindrical electrode
The potential is scanned from 0 V to 0.6 V at a rate of 100 mVs^{-1} at a 2 mm long cylindrical wire electrode of diameter 125 μm, in a solution of 1.5 mM ferrocene monocarboxylate.

Teflon off with a scalpel. However, SECM images of the wires showed that this can scratch the surface of the electrode and can also stretch and tear the Teflon, figure 3.6. Therefore, later versions were created by shrinking the Teflon via heat, to expose the wire. The wire was then cut to a specific length under a microscope. The average limiting current for the 2 mm cylindrical electrodes with a diameter of 125 μm is 2.21 $\pm$ 0.57 μA (n=62). The majority of the error in this reading, comes from the scratching the surface and reproducibly cutting to 2 mm in length.

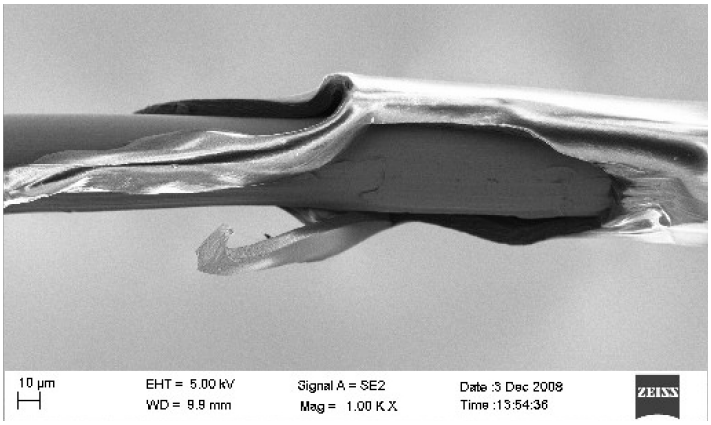


Figure 3.6: SECM image of the cylindrical electrode
SECM was used to image the electrode surface and Teflon insulator, after exposing the surface using a scalpel. Note the scratches on the surface and the stretching and tearing of the Teflon.

3.2.2 Fabrication of Radel Flow Cell

Radel tubing was used for multiple reasons. The outer diameter is 1/16", which is compatible with HPLC fittings used in the rsMD system. This makes attachment to the rsMD system easy. The tubing is also transparent, so any bubbles forming on the electrode can be seen. Furthermore, it allows for the easy placement of the wires within the tubing.

A flow cell containing the three electrodes was fabricated using RadelTM tubing (UpChurch Scientific) in a conformation optimal for electrochemical measurements, figure 3.7. In this way a dialysate stream was passed through the flow cell and perfused the electrodes. There were two configurations for the incorporation of the reference electrode. Initially the reference electrode was wound into a ball using 125 μm diameter wire and placed outside the flow cell. Later, the reference electrode was fabricated from a thinner wire (50 μm) and placed within the flow cell itself.

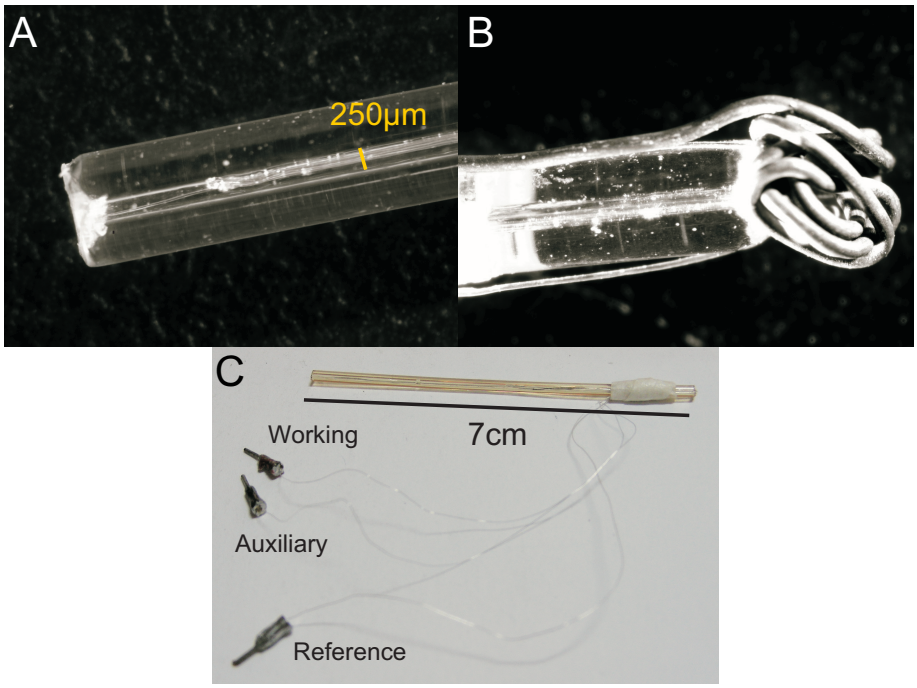


Figure 3.7: Radel flow cell photographs
A: A close up of the 2 mm long cylindrical working electrode within 0.03" radel tubing. B: In the first design of the flow cell, the reference electrode was curled into a ball at the outlet of the tubing. Later it was incorporated within the lumen of the radel tubing using a 50 μm wire. C: The complete radel flow cell, with all three electrodes within the tubing. Note that for all photographs, the direction of flow is from left to right.

3.2.3 Characterisation of Cylindrical Electrodes within a Radel Flow Cell

The electrode placement was tested under flow conditions using a bare platinum cylindrical electrode and a common redox species, Fc. Perfusion solution alternated between PBS and 1.5 mM Fc using a syringe switcher. The electrodes were connected to a potentiostat and the working electrode was held at a potential of 0.75 V to oxidise the Fc. The current was recorded as the solutions changed. The response of the flow cell at different flow rates is shown in figure 3.8.

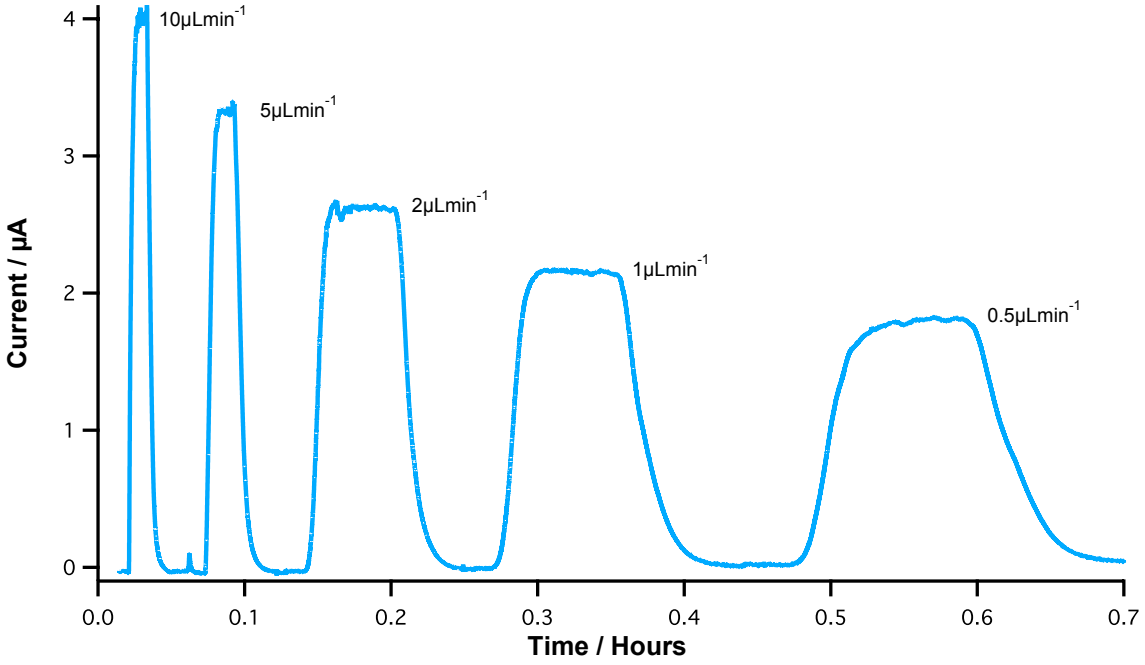


Figure 3.8: Radel flow cell response to alternating Fc and PBS at different flow rates
A 2 mm long bare platinum electrode (diameter 50 μm) was assembled into a flow cell, which was perfused with buffer solution. The electrode was held at 0.75 V and the solution was switched to 1.5 mM Fc. The change in current was recorded. The flow rate of both the PBS and the Fc solution was changed. Flow rates used were 10, 5, 2, 1 and 0.5 μLmin^{-1}.

As expected the results depended upon the flow rate. With larger flow rates, the 90 % response time (T_{90}) is smaller and the current detected is larger. This is due to the mass transport of Fc being enhanced by the higher convective flow. At a higher flow rate, the change in solution occurs more quickly and molecules are being supplied to the surface of the electrode at a faster rate, increasing the current. However for use with microdialysis, a problem occurs. At faster flow rates, the microdialysis probe has a lower recovery and in the clinic a compromising flow

rate of 2 μLmin^{-1} is used. By considering the flux (J) delivered by the flow, the theoretical current that is produced at varying flow rates can be calculated and compared to the experimental data (equation 3.10).

$$I = nFJ \tag{3.10}$$

For 1.5 mM ferrocene monocarboxylate, at a flow rate of 1 μLmin^{-1}, the flux to the electrode is given by equation 3.11.

$$Flux(J) = \frac{1.5 \times 10^{-3}}{10^{6}} \times \frac{1}{60} = 2.5 \times 10^{-11} \tag{3.11}$$

Table 3.3 shows the theoretical and experimental current response seen upon perfusing 1.5 mM Fc solution at varying flow rates. At 0.5 μLmin^{-1}, the oxidation of Fc at the electrode gives the maximum current predicted by our calculation. However, at a flow rate of 10 μLmin^{-1}, only a sixth of the maximum current is being recorded. This is due to the convection flow carrying away the molecules before they can be detected by the electrode. In the intensive care ward, the flow rate used is 2 μLmin^{-1}, and at this rate the sensor only records half of the possible current.

Table 3.3: Flow cell results: T_{90} and current against flow rate

Flow rate / μLmin^{-1}	T_{90} / s	Theoretical I / μA	Experimental I / μA
10	13	24.12	4.05
5	23.4	12.06	3.36
2	46.4	4.82	2.66
1	76.2	2.40	2.16
0.5	153	1.21	1.61

Although the currents produced are large (μA), which allows for easy recording, the response time is long at the slower flow rates. At 2 μLmin^{-1}, the T_{90} is 46.4 s. This would be too slow to resolve the dynamic changes expected. The slow responses are due to a volume effect at the electrode. The volume surrounding the electrode (250 μm diameter tubing, 50 μm diameter 2 mm length wire) is 0.375 μL. At 0.5 μLmin^{-1}, this would take 45 s to fill. This is too large a volume for the range of flow rates required. However, it would be extremely difficult to make it smaller using the same approach. Therefore, microfabrication of disc electrodes and flow cells was used to create smaller volumes.

3.3 Needle Electrodes

A second approach was to use a microdisk electrode. Smaller electrodes were desirable to take advantage of the benefits of using a microelectrode - namely the enhanced sensitivity due to the geometry of the electrode. Disc electrodes were created using a method developed by the O'Hare group (99). These disc electrodes are held by epoxy resin within a blunted needle, which can be polished to give a smooth surface. A photograph of a needle electrode is shown in figure 3.9.

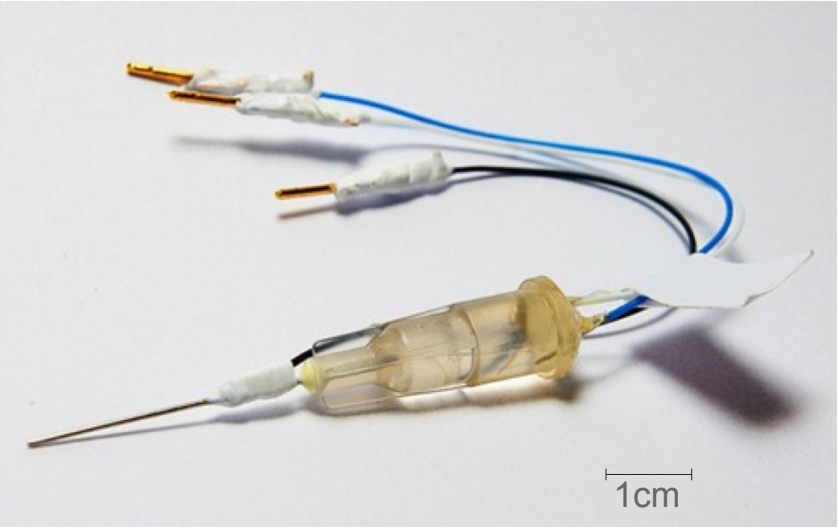


Figure 3.9: Photograph of a combined needle electrode
27 gauge hypodermic needle. Contains a platinum wire (diameter 50 μm) and a silver wire (diameter 50 μm) threaded through, sealed in with glue. Tip is polished flat to give a disc electrode. Once cured needles can also be bent for easier placement in flow cells.

3.3.1 Needle Electrode Fabrication: Working Electrode

Teflon insulated platinum wires (A-M Systems Inc., US) were threaded through a hypodermic needle. The wires were stripped of their insulator using a lighter to expose the metal. The platinum wire and an electrical wire were either soldered together within a glass capillary or glued together using a conductive silver epoxy glue (RS Components). Epoxy resin (Robnor resins, CY1301 and HY1300) was used to fill the internal volume of the needle and secure the wires in place. The two solutions of the epoxy resin, were mixed thoroughly together and a desiccator was used to remove any bubbles formed in the mixing process. The needles were connected by a piece of tubing to a second hypodermic needle, which was used to fill

the internal space and fix the wires in place. The two connected needles were secured in an upright and level position. This prevented the epoxy resin from leaking out. The needles were left to cure at room temperature for two days.

Once the epoxy had cured, the sharp end of the needle was cut using a diamond saw (Buehler) to expose the platinum microelectrodes. The ends were polished using alumina slurries. First, a 1 μm slurry was used. The electrode was held flat against the polishing pad and moved in a figure of 8. This was repeated 25 times and then the needle rotated by 90 °. This whole process was repeated 4 times. The electrode tip was cleaned in distilled water in a sonicator to remove any particle of the slurry, which may be stuck to the surface. The tip was then polished using 0.3 μm alumina slurry in the same way. Finally, 0.05 μm alumina slurry was used. Cyclic voltammetry was used to assess the surface of the electrode and the electrode was re-polished until a satisfactory CV was achieved. Different sized platinum wires could be threaded though the hypodermic needles to create different diameter disc electrodes. Three sizes were commonly used, 125 μm, 50 μm and 25 μm diameter platinum wire.

3.3.2 Needle Electrode Fabrication: Reference Electrode

Reference electrodes were also fabricated in the same way, using silver wire instead of platinum. Once polished flat using all three grades of alumina slurries, the silver disc was chloridised by placing in Chloridising Solution (BAS) for 5 seconds, to create a Ag|AgCl reference electrode.

3.3.3 Characterisation of Platinum Disc Electrodes

The platinum working electrodes were characterised using cyclic voltammetry. The stainless steel shaft of the hypodermic needle was used as an auxiliary electrode and the reference electrode was a Ag|AgCl created in a second hypodermic needle. Figure 3.10 shows CVs conducted in a beaker, from disc electrodes of various sizes.

10 mM RuHex was bubbled with nitrogen to purge the solution of oxygen. CVs were formed by scanning from 0 V to -0.4 V, where the direction was reversed to bring the potential back to 0 V. The shapes produced are characteristic of disc electrodes. The smallest electrode (25 μm diameter) gives a tighter shape as it reached a steady state more quickly than a larger electrode.

Table 3.4 gives an overview of the average currents obtained from different sized electrodes in both Fc and RuHex. For comparison to the theoretical currents for an

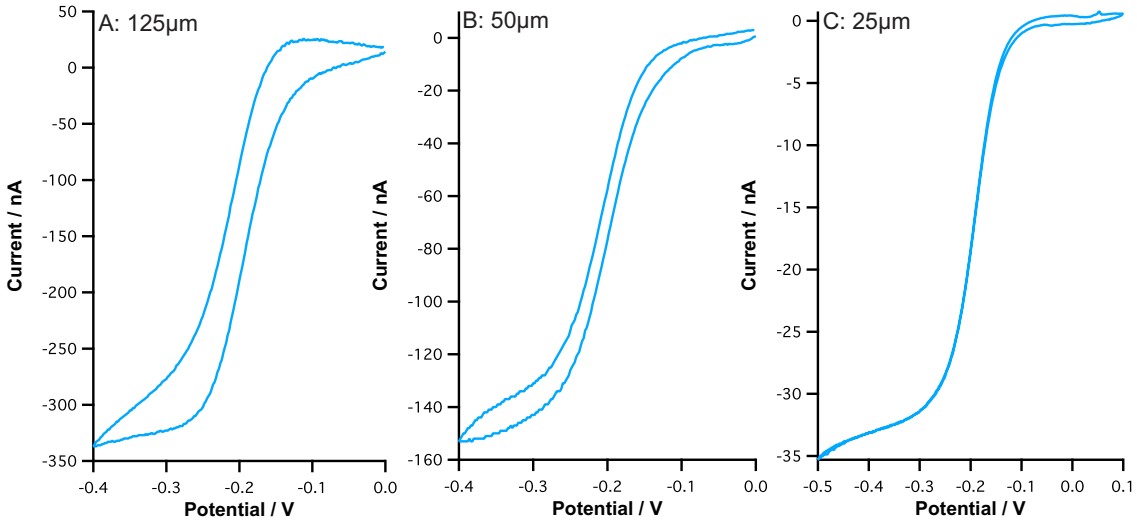


Figure 3.10: Disc electrode CVs using hexaamine ruthenium (III) chloride
10 mM Hexaamine ruthenium (III) chloride in 1 M KCl. 10 mVs^{-1} scan rate. A: 125 μm platinum disc electrode B: 50 μm platinum disc electrode C: 25 μm platinum disc electrode.

inlaid microelectrode see table 3.1 and for the predicted currents of a hemispherical electrode see table 3.2. The currents seen at a 125 μm disc electrode are larger than the predicted value of an inlaid microelectrode of this size. The values obtained using RuHex suggest that the polishing of the electrode was not producing a flat disc but a hemispherical disc. Overtime, my polishing technique got better and the currents became closer to the value expected, as indicated by the smaller standard deviation of the CVs performed in Fc. A hemispherical electrode can be produced by applying more pressure to the edges of the needle, most likely due to tilting the angle of the needle on the polishing pad. This means that the edges are polished more than the middle, thereby creating a dome shaped end.

Table 3.4: Limiting currents and electrode sizes

Redox species	Electrode diameter/μm	Current ± sd / nA
Fc / 1.5mM	125	24.5 ± 5.2 (n=10)
Fc / 1.5mM	50	10.9 ± 2.9 (n=62)
Fc / 1.5mM	25	6.3 ± 1.7 (n=125)
RuHex / 10mM	125	343 ± 56.9 (n=4)
RuHex / 10mM	50	83.1 ± 39.1 (n=6)
RuHex / 10mM	25	44.3 ± 9.2 (n=22)

The 50 μm disc electrode produced currents between the expected currents for an inlaid disc and a hemispherical electrode. This may be due to polishing the needle at an angle producing a flat end but an oval shaped electrode. Therefore the surface area increases but not to the same extent as a hemispherical electrode.

The 25 μm disc electrode were extremely hard to polish as the needle tip is so fine and easily bent. The currents produced indicate that a hemispherical electrode geometry was created. Table 3.5 shows an overview of the limiting currents obtained at six 25 μm needle electrodes in 1.5 mM ferrocene monocarboxylate. In between each CV, the electrodes were used during an experiment and re-polished. As a reminder: the current expected at an in-laid 25 μm disc electrode is 4.2 nA and with a hemispherical geometry 6.5 nA. Four out of the six electrodes gave currents of that expected from a hemispherical electrode geometry. One electrode gave a higher current but it had a large variability, indicating that the fabrication of the electrode was not particularly good. One electrode consistently gave a lower current than the others. However, the current is still higher than that expected at an in-laid microdisc and closer to that of a hemispherical electrode.

Table 3.5: 25 μm diameter microelectrode intra-current summary

Electrode	Current ± sd / nA
1	6.7 ± 1.1 (n=20)
2	6.6 ± 1.2 (n=14)
3	8.5 ± 4.1 (n=7)
4	6.4 ± 1.5 (n=16)
5	5.7 ± 1.4 (n=24)
6	6.4 ± 1.4 (n=12)

In conclusion, the 125 μm electrode was not used a great deal due to the need for miniaturisation of the electrodes. These electrodes were mainly used for practising the construction of the syringe needles and my polishing technique. The 50 μm electrodes were easier to polish to a flat disc than the 25 μm electrodes due to the size and strength of the larger sized hypodermic needle used. Most of these electrodes produced currents that are expected of a hemispherical electrode.

3.4 The Combined Needle Electrode

To save space and create a smaller electrode system for placement in a flow cell, a combined needle electrode was created. This includes all three electrodes for an electrochemical cell, the working (Wrk), the reference (Ref) and the auxiliary (Aux) electrode; a photograph is shown in figure 3.11.

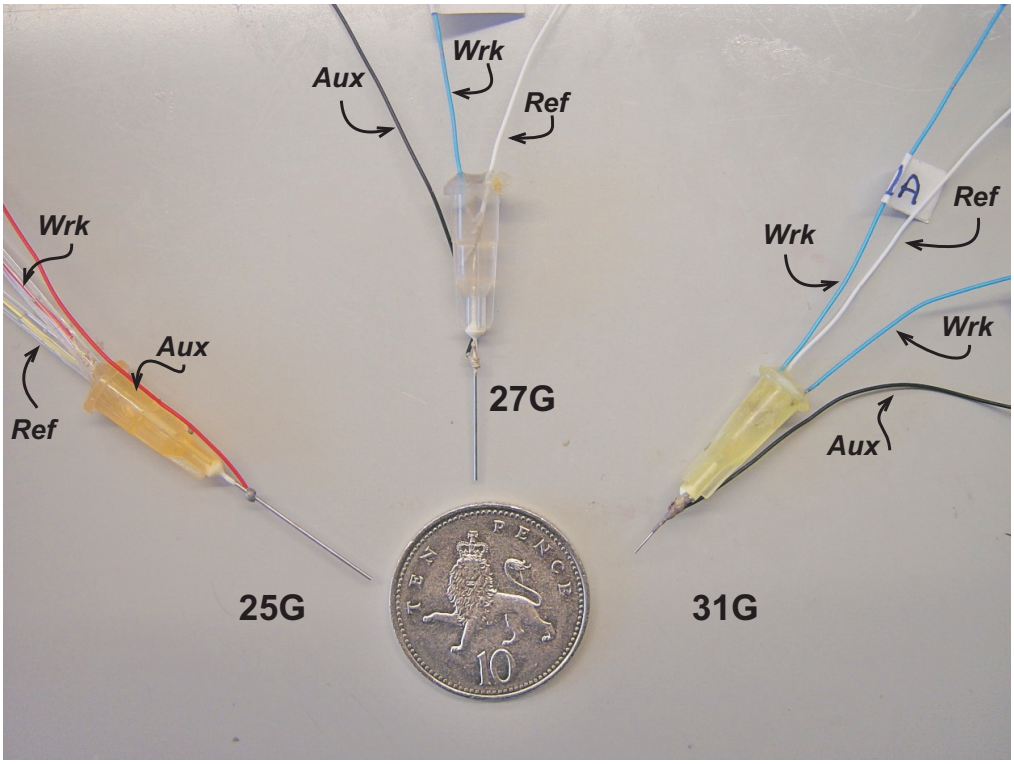


Figure 3.11: Photograph of needle electrodes
Combined needle electrodes in 3 different sizes. The 25 gauge needle contains a 125 μm Pt wire and 125 μm Ag wire. The 27 gauge needle contains a 50 μm Pt wire and a 125 μm Ag wire. The 30 gauge needle contains two 25 μm Pt wires and a 50 μm Ag wire.

3.4.1 Method of Fabrication

Both the silver wire and the platinum wire were threaded through the hypodermic needle. As the wires were so fragile and the syringe needle so small, the connections could no longer be soldered in glass capillaries to be sealed. Therefore, they were individually glued together using a silver loaded epoxy adhesive (RS Components), which is a conductive glue and was cured at 65 °C for 4 hours. The connections were then glued to the inside of the syringe needle using Araldite glue before the epoxy resin sealed all the wires in place.

This was to ensure that there was no connection between the wires, which would cause a short circuit. Once cured, the electrodes were prepared using the same method as before. Figure 3.12 shows an SECM image of a needle electrode tip containing both a silver and a platinum wire, polished flat to give a disc.

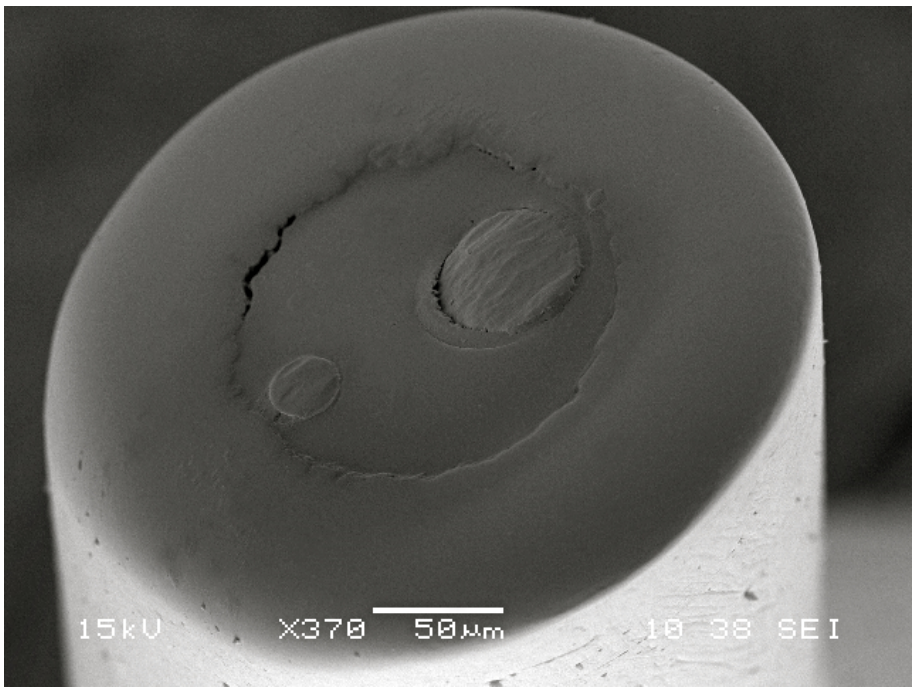


Figure 3.12: SECM image of a 30G electrode tip
30 gauge needle electrode (outer diameter 311 μm) with a 50 μm silver disc (coated diameter 75 μm) for use as a reference and a 25 μm platinum electrode (coated diameter 27 μm) used a working electrode.

Table 3.6 provides the hypodermic syringe needle sizes (gauge and internal and external diameters) used in this thesis. Table 3.7 gives information on the wires used (diameters of coated and uncoated wires shown) in the fabrication of needle disc electrodes.

Table 3.6: Needle sizes: gauge and diameters

Needle / G	Internal / μm	External / μm
25	260	514
27	210	413
30	159	311

Table 3.7: Wire sizes: diameters of coated and uncoated

Material	Insulator	Coated diameter / μm	Bare diameter / μm
Pt/Ir	Teflon	200	125
Pt/Ir	Teflon	75	50
Pt	Isonel	27	25
Ag	PTFE	235	200
Ag	Teflon	177	125
Ag	Polyester	75	50

3.4.2 Chloridising Reference Electrode

The main problem of combining the electrodes within one needle was how to chloridise the silver wire to form the reference electrode, without affecting the other electrodes. The potassium dichromate solution used for chloridising the silver wire, also oxidised the working and auxiliary electrode. Therefore, both of these needed to be cleaned after the chloridisation and before use. I could not re-polish, as this removes the chloridised layer on the silver electrode. Therefore, I dipped the construct into diluted hydrochloric acid (1 in 10 dilution). This removed the oxide layer from the working and the auxiliary electrodes but not from the reference electrode. However, if the electrodes were in the acid solution for too long the stainless steel shaft could be eroded. The needle was rinsed thoroughly with water before use.

Some of the combined electrodes exhibited a previously unseen peak at $\pm$ 0.1 V, seen in figure 3.13. This is a result of some silver atoms transferring to the platinum working electrode during polishing. I have found that subsequent sonication can remove these atoms to give a clean CV. However, the reference electrode needs to be re-chloridised and the acid cleaning process repeated.

3.4.3 Validation

To check whether using a combined electrode in this conformation is viable, CVs in Fc were conducted using external reference and counter electrodes, Figure 3.14. These scans were then compared to the CVs obtained using the combined electrode.

A problem found with these constructs is that heat cannot be applied to electrode after it has been cured, for example to solder on a connection. Heat causes any air bubbles left in the epoxy resin to expand, deforming and cracking the epoxy resin. This can potentially break the fine wires used. Figure 3.15 shows an example of

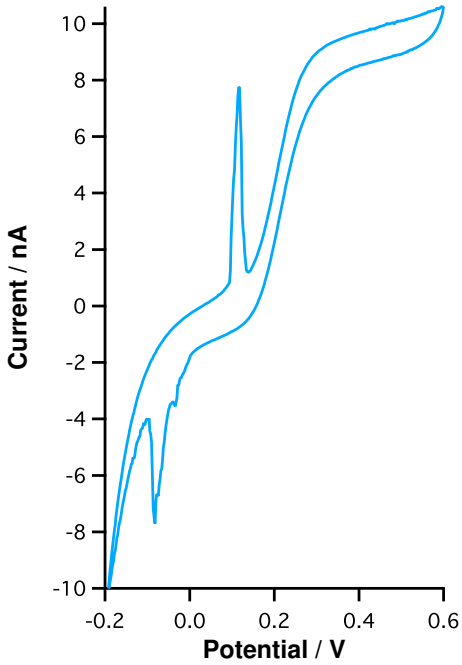


Figure 3.13: CV showing silver molecules on the working electrode.
50 μm platinum disc in 1 mM potassium ferrocyanide in KCl, using an external reference and auxiliary electrode. Scan rate 10 mVs^{-1}. The peaks at $\pm$ 0.1 V indicates silver on the working electrode.

this. After soldering on a connection lead to the stainless steel shaft of the needle to create the auxiliary electrode, the epoxy glue deformed and pushed out from the needle. The silver wire can still be seen at the tip, indicating the wire has snapped. Any connections made after curing the epoxy resin, were therefore created using silver epoxy (RS Components), which is a conductive glue that can be left at room temperature to cure.

The combined electrode is an effective method of incorporating all three electrodes into one construct, which is easy to place in a flow channel. Using the stainless steel shaft as the auxiliary and a chloridised silver disc as the reference has been tested and compared to external electrodes. The CVs were very similar, indicating that this is a good method of miniaturisation.

The method of fabrication has been optimised so that now, 30G syringe needles can be used with a 25 μm platinum disc as a working electrode. This allows optimisation of the flow cell used, which is described in chapter 5.

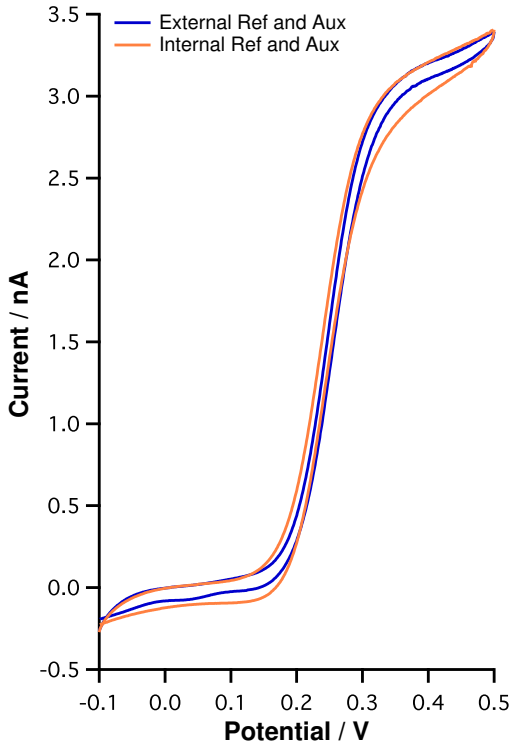


Figure 3.14: CVs using external and internal reference and auxiliary electrodes. 1.5 mM ferrocene monocarboxylate. Scan rate 10 mVs^{-1}. 25 μm platinum disc electrode.

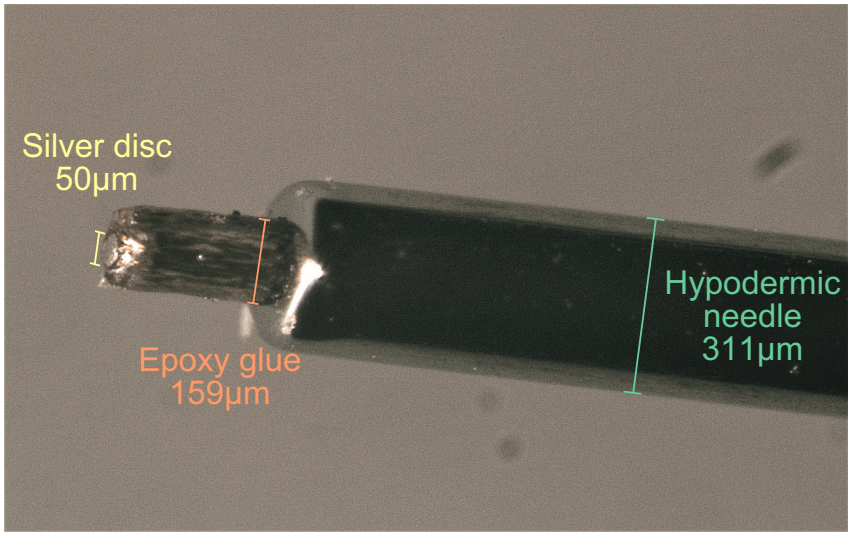


Figure 3.15: Photograph of an integrated needle electrode after exposure to heat A soldering iron was used to solder a connection onto the end of the electrode wires. Due to the heat expanding any air in the epoxy glue, the filling including the electrodes has been pushed out from the needle.

3.5 Dual Electrodes

To increase the number of potential recordings, dual electrodes were fabricated. This involved placing two platinum wires (25 μm) and one silver wire (50 μm) into the syringe needle (30G) and following the same procedure that was used to create the previously discussed versions of the needle electrodes.

3.5.1 Crosstalk

The dual electrodes were assessed using cyclic voltammetry in 1.5 mM Fc. Whilst each electrode produced a satisfactory CV individually, cross talk between the electrodes was found to occur when run simultaneously, affecting the current seen at each electrode. This is due to the inter-electrode distance being small enough for the diffusion fields of each electrode to overlap. Figure 3.16 shows photographs of dual electrodes taken using a microscope and a schematic of the diffusion field overlap, which leads to cross talk. Each electrode is a 30G syringe needle with an outer diameter of 311 μm.

As the relative positioning of the working and reference electrodes within the needle cannot be controlled, each electrode made was individually assessed. This involved photographing each electrode under a light microscope so the relative positions are known and characterising each electrode in terms of cross talk using cyclic voltammetry. The combined dual electrodes were placed in a beaker of 1.5 mM Fc and the potential at one electrode was scanned from -0.1 V to +0.5 V at a scan rate of 1 mVs^{-1}. The second electrode was held at 0 V. The currents at both electrodes were recorded simultaneously. Figure 3.17 gives an example of the CVs from a dual electrode assessed in this way and table 3.8 shows the collection efficiencies derived from the dual electrodes.

Both working electrodes show a response, even though one electrode is held at 0 V. As the potential at the scanning electrode becomes more positive, the ferrocene is oxidised to produce Fc^+. This gives the characteristic CV. At the same time, however, the second electrode also exhibits a negative response. This is because the product of the scanning electrode, Fc^+, diffuses to the second electrode where it can be reduced back to Fc at 0 V. Therefore a reduction curve is seen. The percentage of product that the fixed potential electrode picks up compared to the current seen at the scanning electrode, is known as the collection efficiency.

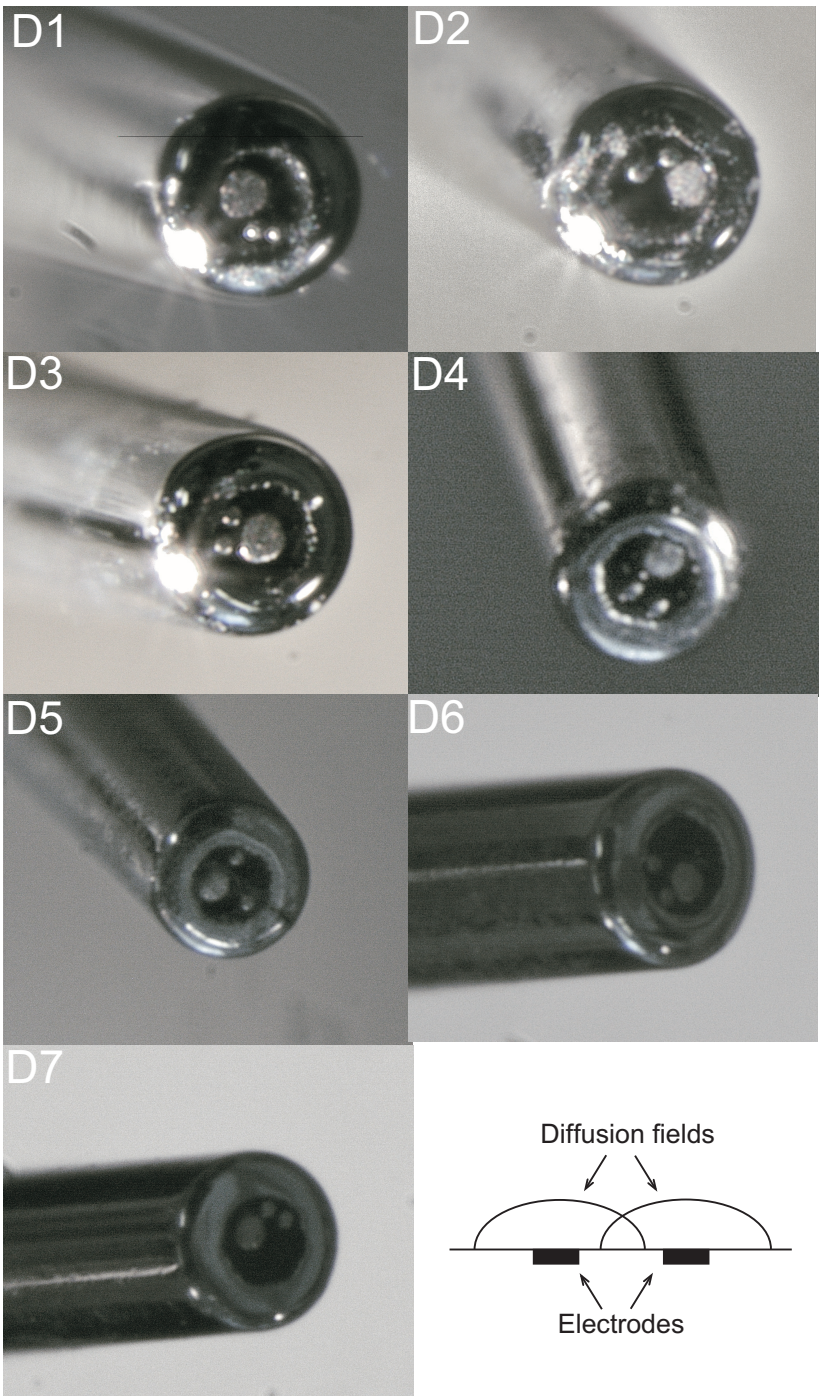


Figure 3.16: Photographs of the dual electrodes taken using a microscope
Each electrode contains two 25 μm platinum working electrodes and one 50 μm silver electrode. The stainless steel shaft of the 30 G syringe needle is used for the auxiliary. The schematic illustrates two electrodes with the diffusion fields overlapping. This leads to cross talk when the electrodes are run simultaneously.

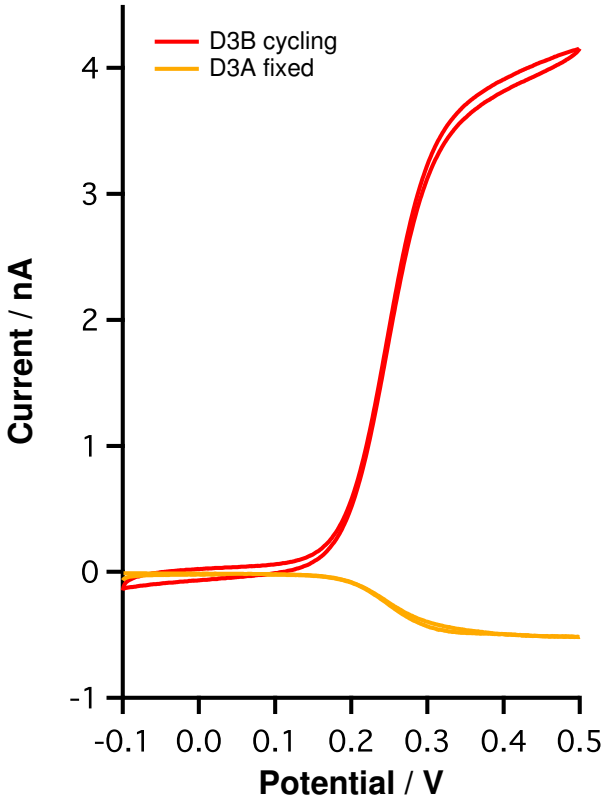


Figure 3.17: CVs in 1.5 mM Fc showing cross talk of dual electrodes
Dual electrode, D3, in 1.5 mM Fc. D3A (orange) is held at 0 V through the experiment. D3B (red) has a ramped potential applied at a scan rate of 1 mVs^{-1}. Cross talk is seen by the response at the electrode held at a constant potential.

Table 3.8: Collection efficiencies in 1.5 mM ferrocene monocarboxylate

Electrode	A_{Scan}:$B_{Collect}$	B_{Scan}:$A_{Collect}$
D1	21.86	21.88
D2	9.22	10.51
D3	12.04	12.62
D4	12.74	11.56
D5	2.76	4.17
D6	9.15	9.57
D7	20.62	21.18

The collection efficiency of each electrode is different due to the different geometries. When the two electrodes are close together, the collection efficiency is greater, as seen in electrode D1 or D7, which show approximately 20 % collection efficiency. However, when the two electrodes are at further distances from each other, such as

the electrodes in electrode D5, the collection efficiency is less because there is less overlap of the two diffusion fields. Even when the two electrodes are at opposite sides of the syringe needle, such as electrode D5, there is still cross talk between the electrodes (approx. 3 %). This suggests that this design is not optimal for multi-analyte detection. The percentage of cross talk when in a flow cell is described in section 6.5 and a summary is shown in table 6.2.

3.5.2 Screen Printed Electrodes

Another option in the design of electrodes for multi-analyte detection is to screen print electrodes. These could be implemented with a flow cell described later in this thesis in chapter 5. The electrochemical cell setup was designed using AutoCAD and is shown in figure 3.18. The working electrodes could be separated by an auxiliary electrode. This will act as a shield as it can remove the species responsible for the cross-talk before it can reach the other working electrode. However, due to an analysis of the microfluidic chip, as discussed in chapter 6 section 6.4.3, the screen printed electrodes were not used.

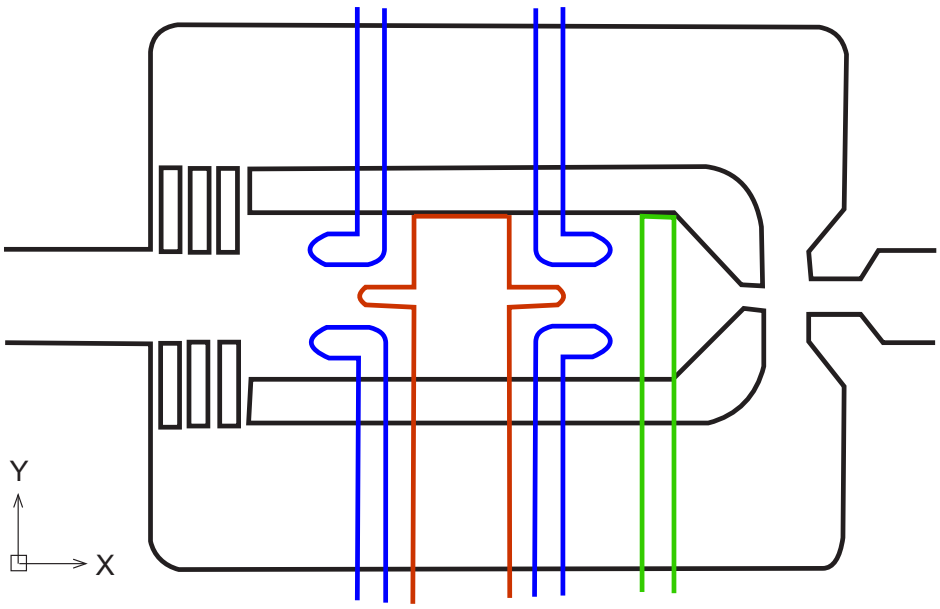


Figure 3.18: Possible screen printed electrode design
Black lines indicate flow channel design (described in more detail in chapter 5) Blue lines indicate the working electrodes, the red indicates the geometry of the proposed auxiliary electrode and the green indicates the reference electrode.

3.6 Conclusion

Electrodes contained within a flow cell, for continuous analysis of microdialysate was proposed, to improve the time resolution of the clinical monitoring system. Cylindrical electrodes were first investigated and were used within a custom made Radel flow cell. The Radel flow cell has the advantage of easily integrating with rsMD and allowing placement of electrodes with a larger surface area. This gives more current, which is easier to detect. However, it was found that the response time of such a flow cell was too slow to accurately measure the dynamic changes expected in the microdialysate, due to a large volume surrounding the electrode. The design was impractical to miniaturise and hence, needle electrodes were fabricated for placement within a microfluidic chip.

The development of syringe needle electrodes has been described and the inlaid micro-disc electrodes characterised using cyclic voltammetry. Miniaturisation was continued by using smaller gauge needles and smaller platinum wires. The integration of the auxiliary and reference electrodes produced an effective combined syringe needle electrode with an outer diameter of 311 μm. This allows placement within a micro-fabricated device, which is described in more detail in chapter 5.

Whilst the combined electrode works well, it was very difficult to control the organisation of dual electrodes within the syringe needle. Even when the electrodes are at opposite sides of the syringe needle, there is still some crosstalk between the electrodes, and hence they were not used for multi-analyte detection.

Chapter 4

Biosensor Development

4.1 Introduction

Biosensors combine the specificity of a biological agent such as an enzyme, with a detection mechanism such as an electrochemical electrode. Biosensors are typically small in size with adequate sensitivity from millimolar concentrations of glucose (62) to micromolar range (66, 100) of glutamate. In this chapter, I will focus on the fabrication of biosensors for use with microdialysis.

4.1.1 Enzymes

Enzymes are an important component of biosensors and they provide a specific reaction, which relates to the concentration of analyte. Enzymes are proteins, which act as catalysts in the biological world. They have an active site, which is responsible for the specificity of the chemical transformations. The substrate briefly (and non-covalently) binds to the enzyme creating an enzyme-substrate (ES) complex. Most of the interactions between the enzyme and substrate are weak and include ionic bond, hydrogen bonds and hydrophobic interactions. Successful formation of the ES complex therefore requires the two molecules to be in close proximity and have a large amount of complimentarily. This provides the basis of the high specificity the enzyme has for its substrate. This section will now give some information on all the enzymes used in this thesis.

Glucose Oxidase

Glucose oxidase (GOx) is an oxido-reduction enzyme, which catalyses the reduction of glucose. Naturally, it is produced by some insects as an anti-bacterial and anti-fungal agent (101), due to the production of hydrogen peroxide, which causes oxidative stress (especially if the intended target doesn't produce scavengers of H_2O_2 such as catalase). In industry, GOx is used in food preservation, diagnostic glucose biosensors are widely used to monitor diabetes, and in bioreactors glucose levels are monitored during fermentation. The structure of GOx is shown in figure 4.1. It is a homodimeric protein (each subunit is 80kDa) and is normally isolated from *Aspergilus niger*. The active site of the enzyme is situated within a deep pocket and for catalysis to occur, two flavin adenine dinucleotide (FAD) cofactors are required as electron carriers (102). The dimensions of GOx are 6.75 x 6.75 x 21.54 (nm) and the molecular weight is 65.69 kDa (103).

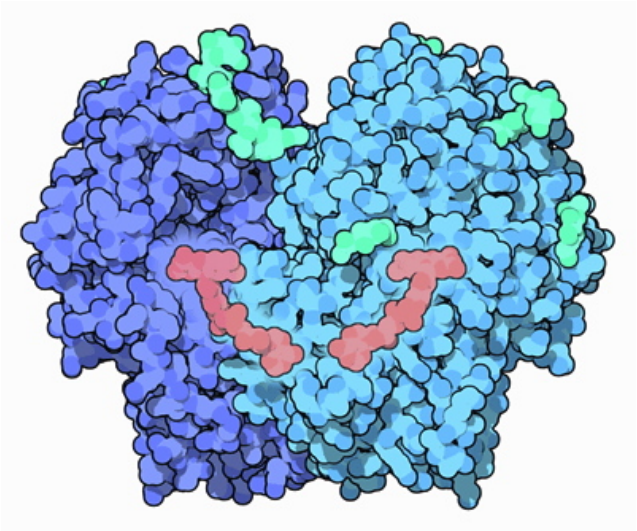


Figure 4.1: Structure of glucose oxidase
The two identical subunits are shown in light and dark blue. FAD molecules are shown in pink. Taken from Wong et al (104).

The proposed mechanism of GOx is shown in equation 4.1 (105).

$$\begin{aligned} E_{ox} + S &\rightleftharpoons E_{ox}S \rightharpoonup E_{red} + P \\ E_{red} + O_2 &\rightharpoonup E_{ox} + H_2O_2 \end{aligned} \tag{4.1}$$

where E_{ox} and E_{red} are the oxidised and reduced form of the enzyme respectively, S is the substrate, P is the product and $E_{ox}S$ is the ES complex.

Glucose oxidase catalyses D-glucose to D-gluconolactone and hydrogen peroxide. This reaction is shown in equation 4.2.

$$C_6H_{12}O_6 + O_2 \longrightarrow C_6H_{10}O_6 + H_2O_2 \tag{4.2}$$

Hydrogen peroxide is easily measured electrochemically and its formation is directly related to the glucose concentration in the sample. For complete enzymatic catalysis, the enzyme requires an electron donor (glucose) and an electron acceptor. Naturally, oxygen acts as the electron acceptor, however other molecules may do so. Cass et al in 1984 described the basis of a glucose biosensor using a ferrocene mediated enzyme electrode (106), which showed improved sensitivity. GOx has an isoelectric point of 4.2 (107) and therefore at pH 7, will have a net negative charge.

Lactate Oxidase

Lactate oxidase (LOx) is a member of the flavin mononucleotide (FMN)-dependent α-hydroxy acid-oxidising enzyme family and crystal structures have revealed the location of the active site at the FMN (108, 109). LOx is obtained from *Aerococcus viridans* and has the dimensions of 11.73 x 13.47 x 18.56 nm and a molecular weight of 330.99 kDa (108). It has an isoelectric point at pH 4.6 (110).

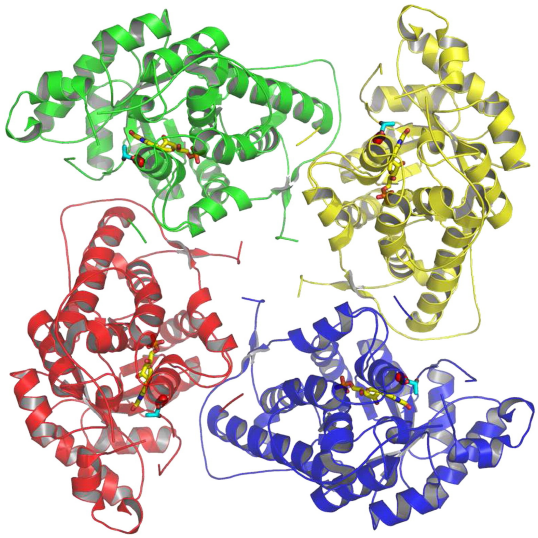


Figure 4.2: Structure of lactate oxidase
Ribbon representation of lactate oxidase. The LOx tetramer complexed with d-lactate with each monomer depicted in a different colour. LOx has fourfold symmetry. Taken from Furuichi et al (108).

LOx catalyses the reaction of lactate to pyruvate and hydrogen peroxide as shown in equation 4.3.

$$C_3H_5O_3 + O_2 \longrightarrow C_3H_3O_3 + H_2O_2 \tag{4.3}$$

The mechanism is complex and has been extensively studied. It is described detail in (111). The first half of the reaction is a reduction of the enzyme to convert lactate to pyruvate. The second half of the reaction, is an oxidation of the enzyme by the electron carrier, oxygen, to form hydrogen peroxide.

Horse Radish Peroxidase

Horse radish peroxidase (HRP) is often used in biochemistry to amplify small signals and increase the sensitivity of an assay. HRP is a haem-containing enzyme with dimensions of 4.28 x 6.75 x 11.7 nm and a molecular weight of 34.52 kDa (112)



Figure 4.3: Structure of horse radish peroxidase
Ribbon representation of HRP. The iron heme is in the centre of the enzyme shown in black with the iron atom as the red sphere. The two calcium atoms are black spheres and lie within the helical regions of the enzyme, with one in the distal region and one in the proximal region. Image taken from RCSB Protein Data Bank.

HRP catalyses the oxidation of many substrates and the overall equation is shown in equation 4.4 (113).

$$H_2O_2 + S_{red} \longleftarrow HRP \longrightarrow 2H_2O + S_{ox} \tag{4.4}$$

In this thesis, HRP is used in the clinical FIA system, developed previously by the group. This involves second generation biosensors in which HRP is used to enhance the signal by mediating glucose and lactate enzyme beds with ferrocene monocarboxylate, as discussed in common material and methods in chapter 2.

Hexokinase

Hexokinase (HEX) is used in conjunction with GOx to create an ATP sensor, described in more detail in section 4.6. There are four important mammalian hexokinases. HEX I is a housekeeping enzyme, HEX II is present in many cancers and little is known about HEX III. These three enzymes have a very high affinity for glucose even at low concentrations. HEX IV is also known as Glucokinase and has an important role in metabolism. It is obtained from *Saccharomyces cerevisiae* and has dimensions of 14.48 x 7.88 x 6.19 nm and a molecular weight of ~50kDa (114). A representation of the structure is shown in figure 4.4. In this thesis, HEX IV is used and will be denoted as just HEX.

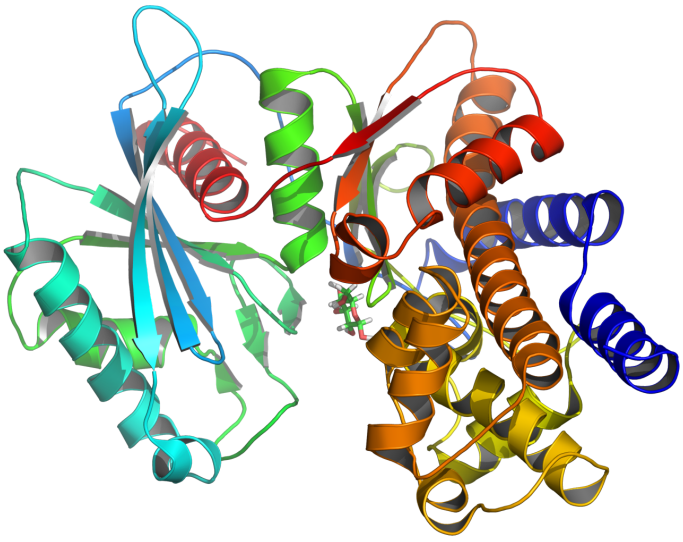


Figure 4.4: Structure of hexokinase
Ribbon representation of HEX. The enzyme structure is made up of mainly alpha helixes and beta sheets. Image taken from RCSB Protein Data Bank.

HEX is required for the first step in glycolysis to phosphorylate glucose to glucose-6-phosphate, and maintain a downhill gradient to facilitate glucose into the cells. The addition of a phosphate group to a molecule traps the glucose inside the cell as hexose phosphates cannot easily cross cell membranes. Glucose-6-phosphate is also an allosteric inhibitor. The reaction is shown in equation 4.5.

$$Glucose + ATP \longrightarrow Glucose6phosphate + ADP \tag{4.5}$$

4.1.2 Biosensor Classification

Biosensors can be described in terms of three generations based upon their operation. The biosensors described in this chapter are first generation sensors.

First Generation

First generation biosensors detect the natural product or reactant of the enzyme at an electrode, as shown in figure 4.5. Hydrogen peroxide is produced as the enzyme catalyses the reaction of substrate to product. The current produced from the oxidation of hydrogen peroxide at the electrode surface is therefore directly related to the concentration of the substrate. This model requires a constant supply of oxygen but it is less sensitive to oxygen than if oxygen was detected directly. This is because the hydrogen peroxide recycles as a natural mediator. The main problem in this design is interference by other electro-active redox species found in the sample.

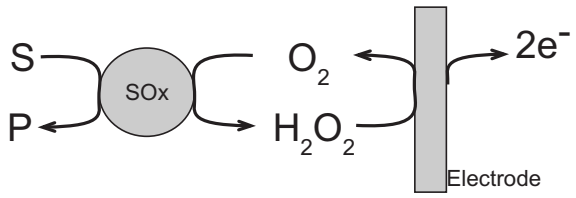


Figure 4.5: Schematic of first generation biosensors
First generation biosensor, where S = substrate P = product, SOx = substrate oxidase. The electrode detects a natural product of the enzymatic reaction.

Second Generation

Second generation biosensors use a synthetic mediator, such as ferrocene monocarboxylate (Fc), to shuttle electrons, which replaces the need for oxygen, shown in figure 4.6. Synthetic mediators are often incorporated to increase the sensitivity of

the assay and reduce the interference from other naturally occurring molecules to some extent. Fc is in a much higher concentration (1.5 mM) than oxygen (200 μM) and the electrochemistry involved with Fc is faster. However, the mediator needs to be in close proximity to the enzyme and electrode surface and have a high turn-over rate with both the enzyme and the electrode. The enzyme beds used in rsMD are second generation sensors.

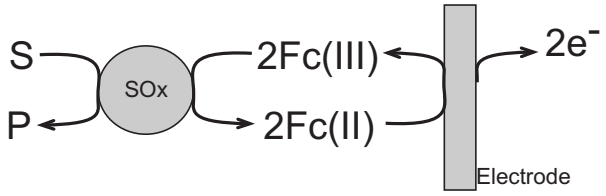


Figure 4.6: Schematic of second generation biosensors
Second generation biosensor, where S = substrate P = product, SOx = substrate oxidase, Fc = ferrocene monocarboxylate. A synthetic mediator is used to shuttle electrons to the electrode.

Third Generation

Third generation biosensors transfer electrons directly from the enzyme to the electrode. This eliminates interference, however reproducibility is poor. Redox proteins that have the active site at the surface are well suited to this type of sensor. However in GOx, for example, the flavin molecules are 20 nm from the protein surface (115). This is too far for effective electron transfer and attempts to improve this, such as wiring, may result in damaging the enzyme. A schematic is shown in figure 4.7. Recently, the direct attachment of laccase onto functionalised carbon electrodes (116) and the immobilisation of GOx onto carbon nanotubes (117), have been successfully investigated and allows for fast electron exchange and a good biosensor performance.

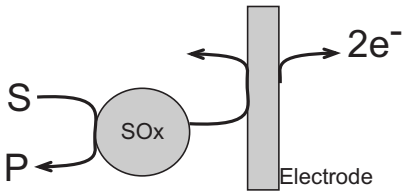


Figure 4.7: Schematic of third generation biosensors
Third generation biosensor, where S = substrate P = product, SOx = substrate oxidase. Electrons are directly transferred to the electrode.

4.1.3 Biosensor Fabrication

An amperometric biosensor requires the enzyme to be in close proximity to the electrode surface. Immobilisation of enzymes onto the surface of an electrode, without affecting the catalytic activity and biological selectivity is fundamental to the production of a successful biosensor. Once they arrive at the electrode surface, enzymes can be physically adsorbed to the surface of the electrode by the hydrophobicity of the enzyme core and possibly hydrogen bonds depending upon the electrode surface. There is little chemical modification of the enzymes but a major disadvantage is leakage of the enzyme from the electrode surface. To reduce desorption, covalent bonding to the electrode surface via functional groups can be induced, but this potentially damages the enzyme. Cross-linking enzymes involves covalently bonding the enzyme molecules together and this method is commonly used by Gerhardt (67). However this technique requires very careful optimisation otherwise it may reduce the stability and functionality of the enzymes.

An alternative is to encapsulate the enzymes into a gel, which is easily fabricated, porous and stable. The gel is a matrix in which coupled reactions can take place, improving the performance of the sensor and allows fast access of the analytes.

The formation of polymer films can entrap enzymes to the electrode surface. Deposition of a film such as nafion (118, 119) has been widely reported however there are problems with the reproducibility and the thickness of the film. Electropolymerisation builds a mesh-like framework of polymers, by monomer units joining together to form a chain (120, 121). Deposition of the polymer film occurs in the exact location where the appropriate potential is applied, so that on an electrode array, individual electrodes can be coated independently of each other, opening up a wide range of possibilities. Many factors influence the growth, properties and morphology of the polymer film, such as concentration of monomers within the diffusion zone, electrode potential, temperature and properties of the solvent used. Also, some films such as polyphenol, are self-limiting in growth, producing thin, insulating and hydrophobic films (122). Commonly used polymers are pyrrole (123, 124), phenols (125) and phenylenediamines (126).

This report focuses on three commonly used films to entrap glucose oxidase. Poly o-phenylenediamine (o-PD) is reported to be approximately 10 nm thick, stable and strongly adherent (127). Polyphenol is said to have a significant effect on blocking interference, the reproducibility is said to be good and the response rapid and relatively stable (128). Poly m-phenylenediamine (m-PD) is thought to be relatively thin at approximately 10-30 nm, with a rapid response time, however the

sensitivity significantly decreases after 7 days in storage (118). A literature overview of the main characteristics of glucose biosensors formed using these three films is shown in table 4.1. The references used to create this table are; oPD (126, 127, 129), mPD (118, 130, 131, 132) and phenol (125, 128, 133, 134, 135).

Table 4.1: Literature summery of glucose biosensors fabricated with different films

Characteristic	oPD	mPD	Phenol
Sensitivity	440 nA.mM^{-1}.cm^{-2}	99 nA.mM^{-1}.cm^{-2}	1200 nA.mM^{-1}.cm^{-2}
Stability	20hrs continuous use	Sig. drop after 7 days	After 7 days, falls by 25%
T_{90} / s	< 2 s	< 1 s	< 4 s
LOD	3 μM	50 μM	20μM
Thickness	10 nm	10 - 30 nm	3nm, 7.5nm with enzyme

4.1.4 Enzyme Kinetics

During the development of the biosensors used in this thesis, the enzyme kinetics were assessed. Enzymes are very effective catalysts because they lower the activation energy (Ea or $\Delta G‡$) of the reaction. As a result, the reaction rate is increased and products are formed faster. The enzyme may be affected by a variety of factors, including concentration of substrate, temperature, pH of solution and the presence of inhibitors.

The majority of enzymes follow the Michaelis-Menten kinetics. The reaction rate is the number of reactions per second that are catalysed per mole of enzyme. The reaction rate increases with increasing substrate concentration [S], asymptotically approaching the maximum rate, V_{max}. V_{max} is therefore the maximum catalytic rate that can be achieved by a particular enzyme. K_m is the Michaelis-Menten constant and is defined as the substrate concentration at which the reaction rate is half its maximum speed. It inversely represents the enzymes affinity for the substrate and is a measure of how stable the enzyme-substrate complex is. The K_m for glucose oxidase is reported to be in the low 20 mM range at pH 7 (102, 136, 137). The expected K_m of lactate oxidase is 0.7 mM as recorded on the Genzyme data sheet.

The Michaelis-Menten formula is shown in equation 4.6.

$$V = \frac{V_{max}[S]}{K_m + [S]} \tag{4.6}$$

where V is the reaction rate, V_{max} and K_m are as previously described and [S] is the substrate concentration.

Inhibition of the enzyme can change its performance and hence the V_{max} and K_m values, an overview of which is shown in figure 4.8. There are two types of inhibition, competitive and non-competitive.

Competitive inhibitors compete with the substrate to bind to the enzyme's active site. Therefore more substrate is required to reach the same velocity that it would do with no inhibitor present. Hence, the same V_{max} can be reached albeit at a higher substrate concentration, resulting in a larger K_m. Application of a polymer film to the surface of the electrode could have the same effect on K_m, for a different reason, by reducing the diffusion to the electrode surface. At a high enough substrate concentration, the same V_{max} is reached, but at the lower concentrations, diffusion is limiting the current, resulting in a larger apparent K_m.

Non-competitive inhibitors bind to a part of the enzyme molecule that is not the active site. The viability of the enzyme is then compromised and its efficiency reduced. This results in a lower V_{max} as there are less enzyme molecules to process the substrate, however as the active site of the viable enzymes is not impaired, the K_m remains the same. This effect could be seen if the orientation of the enzymes entrapped in polymer films is such that the substrate cannot be processed by the enzyme. The V_{max} would be reduced as the number of enzymes processing the substrate is reduced, but the functionality of the active site is not affected.

If at lower substrate concentrations there was no inhibition, the biosensor calibration curve would start by following the red line in figure 4.8. If, at a certain threshold the substrate acts as a non-competitive inhibitor, then the calibration curve would switch to the green line. A scenario that could produce this effect is if the higher concentration of substrate altered the polymer film such that some of the enzymes could no longer function. This results in a lower V_{max} and a lower than expected K_m.

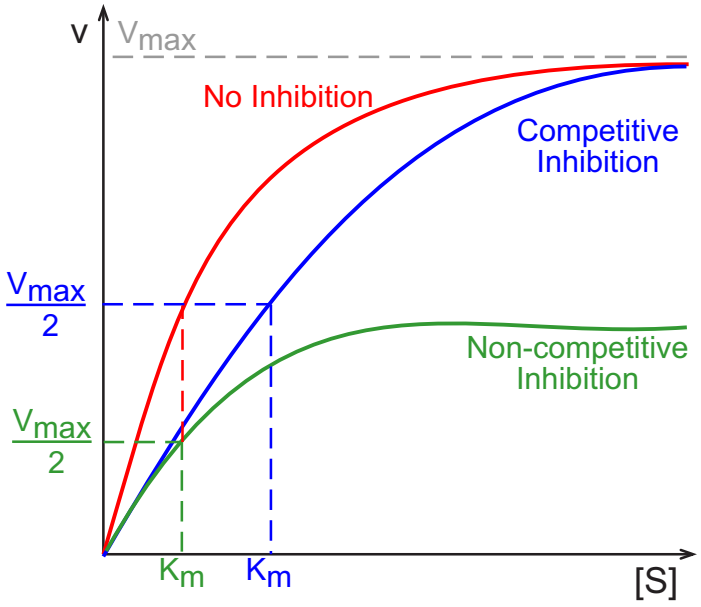


Figure 4.8: How inhibition of enzymes affects V_{max} and K_m
Competitive and non competitive inhibition are assessed in terms of Vmax and the K_m. x axis is increasing velocity, y axis is increasing substrate concentration.

Sometimes the binding of a ligand or molecule can enhance the binding of subsequent ligands by changing the enzyme conformation and increasing the binding affinity at the other vacant sites. This is known as cooperative binding, which was quantified by Archibald Hill. The Hill coefficient provides a quantification of the degree of cooperative binding. A well known example of this is the sigmoidal binding curve of oxygen to haemoglobin. The Hill equation is shown in equation 4.7 (138).

$$I = \frac{V_{max}}{1 + (K_m/[glucose])^{\alpha}]} \tag{4.7}$$

Where I is a measure of the rate of enzymatic reaction and α is a measure of the deviation from the ideal Michaelis-Menten behaviour.

The Hill equation is widely used to study the enzyme kinetics of biosensor calibration curves as often there is a deviation from linearity at both lower and higher substrate concentrations. It is often used when describing allosteric enzyme biosensors where there can be several allosteric binding effectors (139).

4.2 Investigating Immobilising Films

Following table 4.1, three immobilising films were tested using glucose oxidase. A potential can be applied to an electrode to polymerise a film in two ways: a fixed potential (electropolymerisation) or a ramping potential (cyclic voltammetry). The films were assessed using both methods and the monomers investigated are shown in figure 4.9 and were:

- o-phenylenediamine (oPD)
- m-phenylenediamine (mPD)
- Phenol

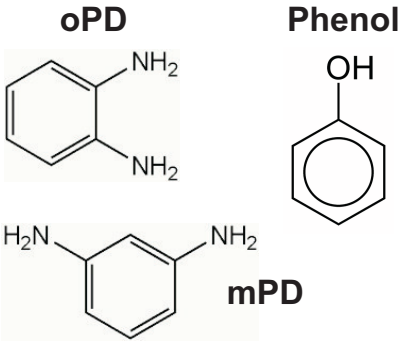


Figure 4.9: The structure of monomers investigated for use as immobilising films
The chemical structures of three monomers, o-phenylenediamine, m-phenylenediamine and phenol, which are investigated for use as immobilising films, are shown.

4.2.1 Polymerisation by Cyclic Voltammetry

Electrodes (2 mm cylindrical or disc electrode) were placed in a solution containing 50 mM of the monomer. For all films, the solution is purged with nitrogen for 20 minutes before the potential is scanned at 50 mV/s over a suitable range (oPD and mPD: 0 V to 1 V. For phenol: 0 V to 1.5 V). For phenol only, the experiment is also repeated without purging the solution. The current is recorded as the potential is scanned, producing a CV.

Figure 4.10A shows the resulting CV of oPD polymerisation, using a 2 mm long 125 μm diameter electrode. There are two peaks in the polymerisation process, one at 0.65 V and the second at 0.75 V. The majority of the monomers are polymerised during the first scan seen easily as the large decrease in current intensity.

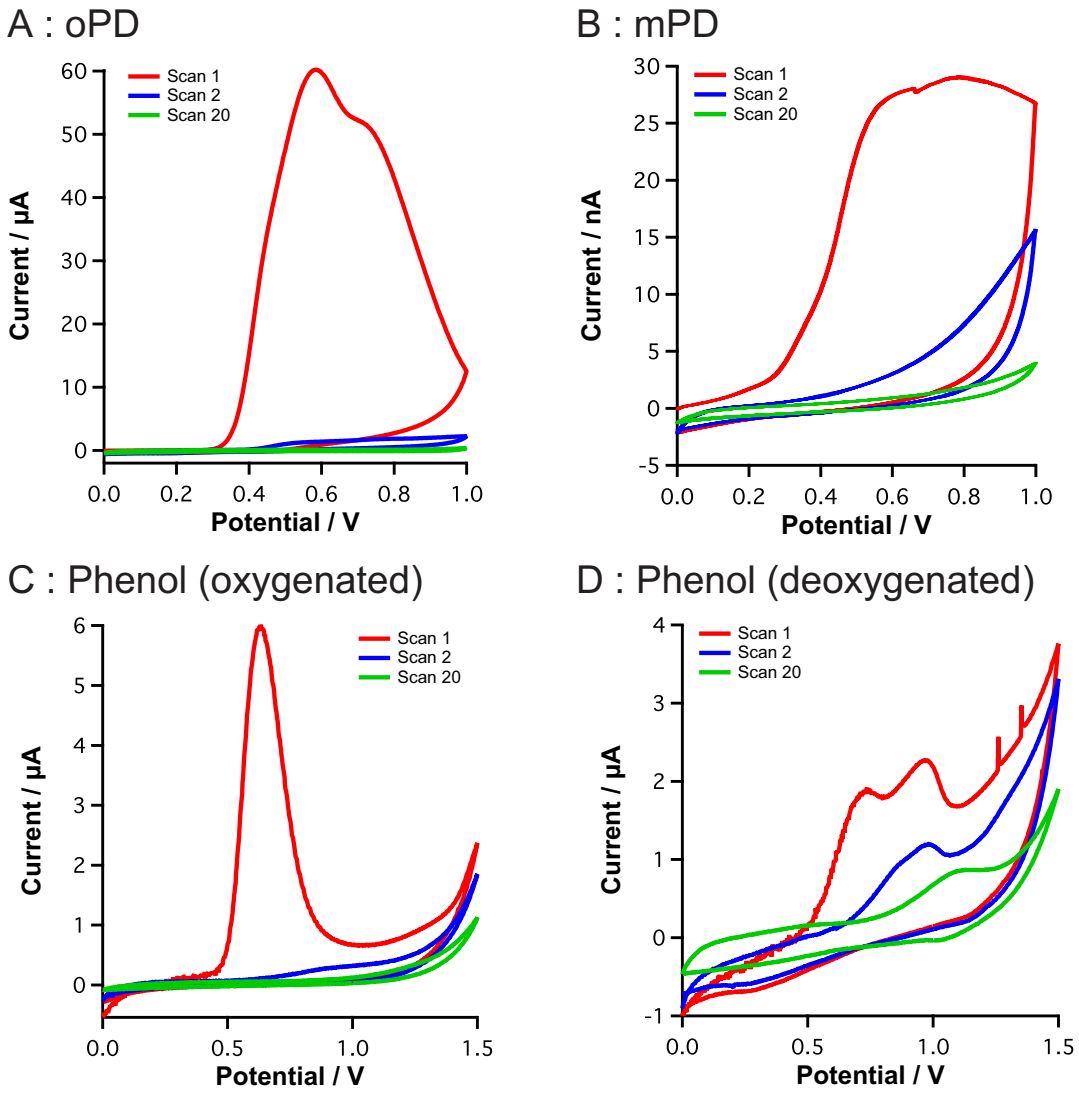


Figure 4.10: Film polymerisation using cyclic voltammetry
A: 2 mm long 125 μm diameter cylindrical electrode in 50 mM oPD in PBS. Potential scanned from 0 to 1 V at a scan rate of 50 mV/s in deoxygenated solution. B: 125 μm disc electrode in 50 mM mPD in PBS. Potential scanned from 0 to 1.5 V at a scan rate of 50 mV/s in deoxygenated solution. C: 2 mm long 50 μm diameter cylindrical electrode in 50 mM phenol in PBS (oxygenated solution). Potential scanned from 0 to 1.5 V at a scan rate of 50 mV/s. D: 2 mm long 50 μm cylindrical electrode in 50 mM phenol in PBS (deoxygenated solution). Potential scanned from 0 to 1.5 V at a scan rate of 50 mV/s

Figure 4.10B shows the CV resulting from the polymerisation of mPD, using a 125 μm platinum disc electrode. Again, after the first scan there is a large drop in current indicating that a large part of the film is formed quickly. By the 20th scan the CV shows no peaks indicating a fully formed film.

Figure 4.10C and figure 4.10D shows the polymerisation of phenol in oxygenated and deoxygenated solutions respectively. In both cases, a 2 mm long, 50 μm diameter cylindrical platinum electrode was used. In oxygenated solutions the electrochemistry looks much simpler as there is only one peak at 0.63 V and the majority of the film is again formed within one scan. For deoxygenated solutions, the CVs show two clear peaks at 0.7 V and 0.95 V. After the first scan, the peak at 0.7V disappears but the second peak remains. This second peak can still be seen in the 20th scan. Oxygenated solutions were therefore chosen as the electrochemistry was simpler and the film was fully formed after the 20th scan.

4.2.2 Film Formation: Electropolymerisation

The biosensors used in this thesis were fabricated using electropolymerisation. The electrode was placed in 50 mM film monomer and 4 mg/mL enzyme. The pH of the solution was buffered to pH 7.2. The electrode was placed in the enzyme solution for 10 minutes. This is the stabilisation time. The working electrode was held at 0 V for 20 s, polarised to the required potential for 15 minutes for electropolymerisation of the film and then held at 0 V for 20 s. The potential applied was 0.75 V, 1 V and 0.9 V for oPD, mPD and phenol respectively. Following electropolymerisation, the biosensor was gently rinsed with de-ionised water and stored dry overnight at 4 °C before use. Exceptions in this thesis include, the quantity of LOx used (halved to 2 mg/ml) and for the ATP biosensor, 40 mg/ml HEX and 10 mg/ml GOx was used.

Cyclic voltammetry was used to check for successful film polymerisation after biosensor fabrication. CVs of a bare and a coated electrode are shown in figure 4.11.

Enzyme kinetics were investigated to assess the functionality of GOx in the films. Aliquots of glucose was added to a stirred beaker in a step-wise fashion. The V_{max} and K_m were found by plotting the change in current against concentration and fitting the points with the Hill equation in a graphing software (Igor Pro). An overview of 4 sensors of each film is shown in table 4.2. Note, the expected K_m of GOx is reported to be in the low 20 mM range at pH 7 (102, 136, 137).

oPD has the lowest K_m value, indicating that the functionality of the enzyme is good, and the enzyme has a strong affinity for for glucose. The current, however, is low with an average V_{max} of only 7.6 nA. This means that the sensitivity of the sensors will be low and small concentrations of glucose will be very difficult to see. Phenol coated sensors have the highest V_{max}, indicating that the turnover of substrate is highest and the sensors will have the best sensitivity and the K_m is similar to the reported K_m of glucose oxidase.

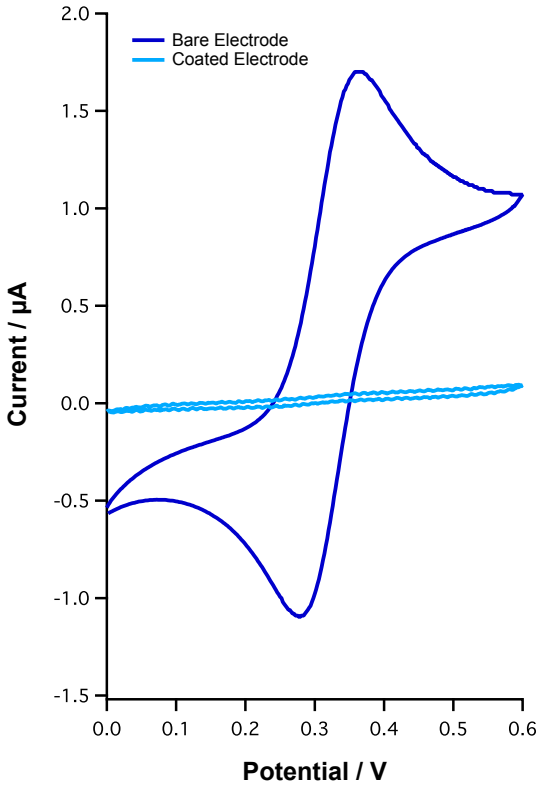


Figure 4.11: CVs of a bare and an oPD coated electrode
The potential is scanned from 0 V to 1 V and back again at 50 mV/s and the change in current recorded. A 125 μm diameter, 2 mm long, cylindrical platinum electrode in 1.5 mM Fc, was assessed before and after an oPD film was electropolymerised on the surface.

Table 4.2: Enzyme kinetics of glucose biosensors: film assessment

Film	K_m / mM	V_{max} / nA
oPD (n=4)	20 ± 5.4	7.6 ± 1.6
Phenol (n=4)	26.5 ± 1.29	19.25 ± 11.03
mPD (n=4)	39.37 ± 3.6	14.72 ± 10.1

Although mPD coated sensors have a reasonable V_{max}, the K_m of the enzyme is high at approximately 40 mM. This indicates that the enzyme has been damaged during the polymerisation of the film.

4.2.3 Film Selectivity: Flow Injection Analysis

Each film was assessed for its ability to reject unwanted signals from other electroactive species that may be present in the analytical sample. For these selectivity measurements, flow injection analysis (FIA) was carried out comparing a coated electrode and a bare electrode.

To test the three films against the common interferents, an in-house flow cell was produced, using a silicone elastomer, as described previously by Anastassiou et al (140). The flow cell was connected to a quaternary HPLC pump (HP1050, Aligent), used to change solutions. The flow rate was set at 1 $mLmin^{-1}$ and baseline current was collected by pumping potassium chloride buffer solution. The pump was then changed to a solution, which contained various interferents, for the duration of 20 s, after which potassium chloride was again perfused. This was repeated four times. The responses of unmodified 50 μm platinum electrodes were compared to the coated 50 μm platinum electrodes. Both the unmodified and coated electrodes were simultaneously assessed for selectivity, in the presence of 1 mM ascorbic acid (AA), 1 mM dopamine (DA), 10 mM FeCN and 10 mM RuHex. The potential applied to the electrode was +0.75 V, +0.75 V, +0.6 V and -0.4 V respectively. The responses to hydrogen peroxide were also deduced from a separate standard calibration. The results are shown in table 4.3.

An example of the responses seen at a phenol coated electrode compared to a bare electrode is shown in figure 4.12. The responses to the injected species is greatly attenuated by the application of a polymer film to the electrode surface. RuHex is the only species where a response is clearly seen at the coated electrode, however the response is clearly reduced.

A reading was taken at the peak of the signals at both electrodes, and compared to the baselines. The ratio of the change in current at the coated electrode (I) to the change in current seen at the unmodified electrode (I_{clean}) is an indicator of the permeability of the film, and the results are shown in table 4.3.

All species are attenuated by the films implying that the films have introduced a diffusion barrier to the electrode surface. H_2O_2 is the easiest to pass through all of the films. This is ideal because this is the product of the enzymatic reaction, which the electrode is detecting. The ability of H_2O_2 to permeate the films is one of the qualities of why these three films are so commonly used in first generation biosensor designs.

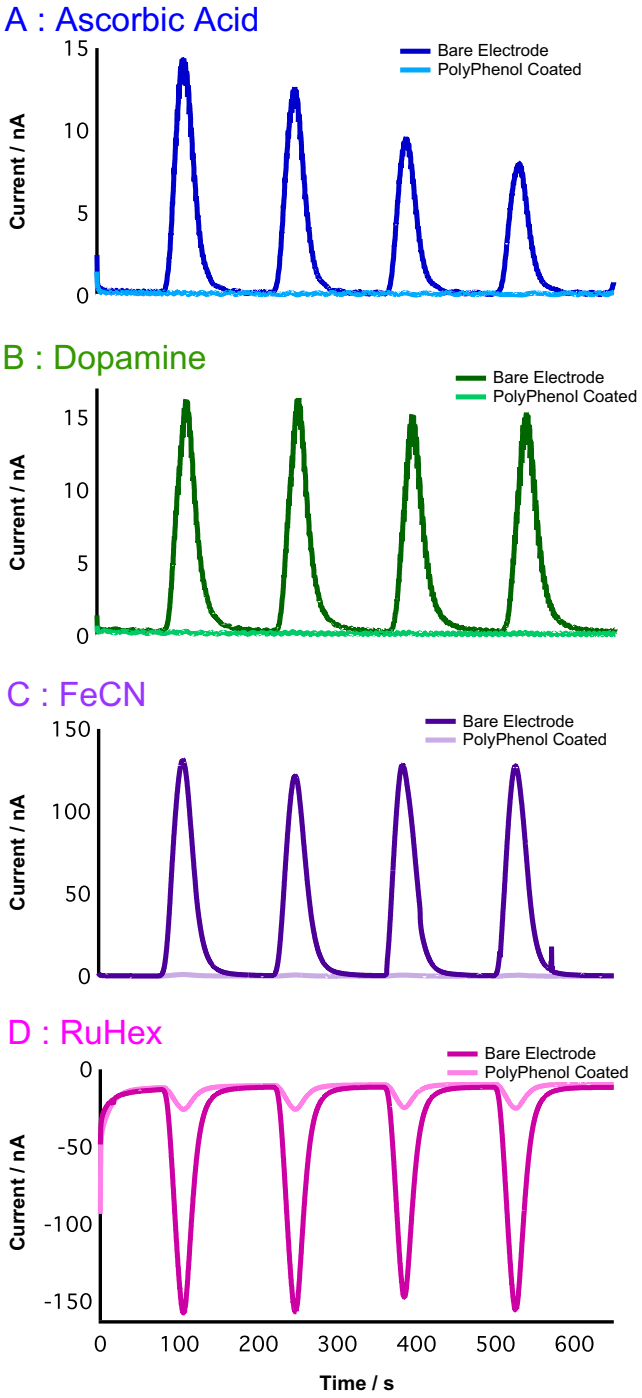


Figure 4.12: FIA analysis

50 μm Pt disc electrode. A: 1 mM AA (blue), B: 1 mM DA (green) C: 10 mM FeCN (purple) D: 10 mM RuHex (pink). 20 s injection pulses were carried out against a background solution of potassium chloride at 1 mLmin^{-1} for the four different molecules. Measurements from both electrodes were carried out simultaneously.

Table 4.3: FIA results : I / I_{clean} **Mean**±StDev n=4. Charge of the injected specie at pH 7 and relative sizing of the species are also shown

Film	H_2O_2	AA	FeCN	RuHex	DA
Phenol	**0.72**±0.16	**0.0027**±0.0001	**0.0077**±0.0005	**0.12**±0.006	**0.0053**±0.0008
oPD	**0.51**±0.014	**0.12**±0.002	**0.0043**±0.0002	**0.25**±0.5	**0.06**±0.028
mPD	**0.72**±0.01	**0.59**±0.073	**0.037**±0.0068	**0.057**±0.1	**0.29**±0.021
Charge	Neutral	Negative	Negative	Positive	Positive
Size	Small	Medium	Large	Large	Medium

Looking at the $\frac{I}{I_{clean}}$ ratio for each polymer film, the order for the most excluded specie to the least excluded specie is:

* **Phenol**: AA, DA, FeCN, RuHex, H_2O_2
* **oPD**: FeCN, DA, AA, RuHex, H_2O_2
* **mPD**: FeCN, RuHex, DA, AA, H_2O_2

4.2.4 Size versus Charge

The size and charge of molecules may have an effect on its apparent permeability through a film. The oPD film looks to be excluding molecules on the basis of size, with the exception of RuHex. The oPD film excludes the medium sized AA and DA less than the larger FeCN molecule. This shows that there is no effect of charge as AA and DA are similarly excluded but are positively and negatively charged at pH 7, respectively. This could be related to the Debye length being sufficiently small that the charges have little effect. The mPD film also looks to be excluding molecules on the basis of size, similar to the oPD film, but here RuHex fits the trend. The phenol responses indicate that the film is not excluding species based on either the charge or the size. Whilst no concise conclusion can be determined over the permeation properties, this was not investigated further as the poly(phenol) film gave the best exclusion of AA and DA, than either oPD or mPD.

4.2.5 Polymer Selectivity

Polymer selectivity was further assessed by calculating the percentage of interference of AA in the H_2O_2 detection. Polymer selectivity can be calculated using equation 4.8 (141).

$$S\% = \frac{I_{AA}}{I_{HP}} \times 100 \tag{4.8}$$

Where, S=polymer selectivity, AA=ascorbic acid and HP=hydrogen peroxide. The optimal value of S%, as defined here, is zero for biosensor applications. The selectivity of each film was assessed by applying this equation to the results from the FIA experiment. The results are shown in table 4.4. mPD has the highest S% out of the three films. It is three times larger than oPD, again suggesting that film formation is not as good. The S% for oPD is still large, indicating that there will be interference from ascorbic acid. The S% for phenol is very small and close to zero, indicating that phenol is a good barrier to interferences from other electro-active species.

Table 4.4: Polymer selectivity

Film	S%
Phenol	0.37 ± 0.08
oPD	23.58 ± 3.9
mPD	82.47 ± 10.3

4.2.6 Film Decision

Poly(phenol) is reported to be 3 ± 1.2 nm thick and with glucose oxidase 7.4 ± 0.8 nm thick (134). The growth of the phenol films is self-limiting and as a consequence is thin and free of defects such as pinholes (142). Poly(phenol) is a good insulator, which prevents interference from unwanted species by blocking them from the electrode surface, and minimise fouling. This is all represented in the permeability and selectivity data shown. The best film to use is phenol because the permeability and selectivity is superior to oPD and mPD. The K_m and V_{max} of the glucose biosensors fabricated using phenol gave the best sensitivity and a similar K_m to that reported in the literature. Therefore the biosensors used in this thesis will be fabricated using a phenol film, electropolymerised at 0.9 V, to entrap the enzyme to the electrode surface.

4.3 Glucose Biosensor: Radel Flow Cell

Electropolymerisation of 50 mM phenol at 0.9 V was used to entrap glucose oxidase (4 mg/mL) on the electrode surface. The electrode and flow cell construction was detailed in the previous chapter. The biosensor was placed in a beaker containing PBS, which is highly stirred, at 0.75 V. Aliquots of a concentrated glucose solution were added to the PBS to create known step changes in concentration. Wires were all 2 mm in length but different diameters were used and the sensitivity of the biosensors was characterised on the different electrode sizes.

In a beaker, the 50 μm diameter cylindrical biosensor had a sensitivity of 1.95 $\pm$ 0.64 x 10^7 nAmM^{-1}cm^{-2} and a 90 % response time (T_{90}) of 3.0 s $\pm$ 1.5 (n=10). The 125 μm diameter biosensor had a similar sensitivity of 1.45 $\pm$ 0.18 x 10^7 nAmM^{-1}cm^{-2} but a longer T_{90} of 6.8 $\pm$ 1.4 (n=10).

The glucose biosensors were designed for a Radel flow cell, which was to be placed after the valve on the rsMD trolley. The Radel flow cell design and construction was described in chapter 3. Here, a glucose biosensor fabricated on a cylindrical electrode was placed inside and solutions perfused the flow cell at a flow rate of 1 μLmin^{-1}. The solutions were alternated between aCSF and glucose in varying concentrations using a syringe switcher. Figure 4.13 shows a typical trace for a cylindrical glucose biosensor placed in a Radel flow cell.

Table 4.5 shows that the current for a particular glucose concentration is independent of flow rate for all normal microdialysis flow rates (0.1 to 10 μLmin^{-1}). Such performance is more than sufficient to detect glucose continuously *in vivo*.

Table 4.5: Response of glucose biosensor in the flow cell: current response

[Glucose] / μM	I / nA @ 8.8μLmin^{-1}	I / nA @ 1μLmin^{-1}
1000	17.2	19.9
500	7.98	7.15
250	3.62	3.75

The limit of detection (LOD), calculated as 3 standard deviations of baseline noise 30 seconds before the addition, of this flow cell for glucose is 6 μM. The average LOD for a 50 μm wire is 5.3 $\pm$ 1.6 μM (n=10). Glucose responses were routinely recorded for low glucose concentrations such as 50 μM. As expected the 90 % response time, T_{90}, for the flow cell varies with dialysate flow rate, see table 4.6.

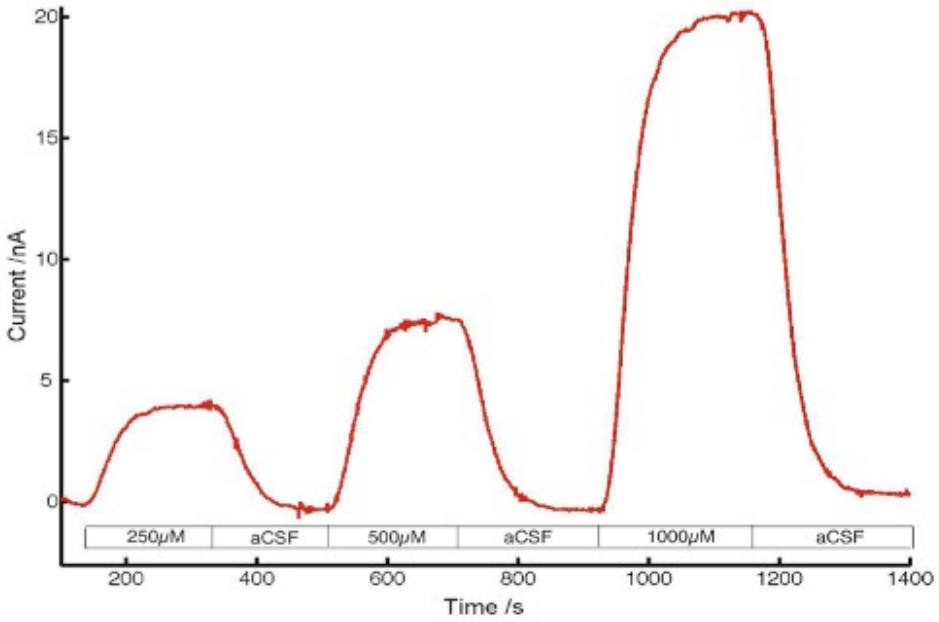


Figure 4.13: Wire biosensor in Radel flow cell
In vitro calibration of the radel flow cell for glucose. Wire size 50 μm diameter, 2 mm length. Flow rate 1 μLmin^{-1}. Solutions were switched between aCSF and varying concentrations of glucose. Glucose concentrations are 250, 500 and 1000 μM.

Table 4.6: Response of glucose biosensor in the flow cell: T_{90}

Flow rate / μLmin^{-1}	T_{90} / s
1	77
2	39
8.8	20.5

Although the sensitivity of the biosensor is good, the response time when in the flow cell is too slow to detect the fast changes seen in the brain. Although efforts were made to make the volume of the flow cell smaller, the bore of the tubing must be sufficient to fit three wires inside and hence it was still too large to achieve the fast response times required. Therefore, further work involving microfabrication of the flow cells was done and designs discussed in chapter 5. For electrochemical measurements in the smaller flow cells, needle electrodes were developed (as discussed in chapter 3). These disc electrodes will now be assessed as biosensors.

4.4 Glucose Biosensors: Disc Electrodes

Glucose biosensors were fabricated on disc electrodes by entrapping glucose oxidase to the electrode surface using electropolymerisation of polyphenol. The structure of the electrodes was described in chapter 3. The biosensors were characterised in a beaker, in the same fashion as the cylindrical biosensors, which is described here. The sensors were also used on-chip, which will be discussed later, in chapter 6.

4.4.1 Glucose: Beaker Calibrations

The biosensors were characterised in a beaker containing PBS, which is highly stirred. Aliquots of a concentrated glucose solution were added to the PBS using a glass hamilton syringe, to create known step changes in concentration in the bulk media. Figure 4.14 shows a typical calibration in a beaker using a 25 μm glucose biosensor. The sensitivity of the biosensors, the response times and the enzyme kinetics were characterised on different electrode disc sizes, 125 μm, 50 μm and 25 μm diameter discs.

The glucose biosensors were typically calibrated up to 80 mM. This is to assess the functionality of the enzyme trapped on the surface. At the high millimolar concentration the sensor should be approaching V_{max} and the K_m of the enzyme can also be assessed by calculating the glucose concentration at half V_{max}. Figure 4.14A shows a graph of the change in current at increasing glucose concentrations using a 25 μm glucose biosensor. Here V_{max} is seen as a plateauing of the trace and K_m is the glucose concentration at half V_{max} as indicated on the graph. The curve has been fitted with the Hill equation in IgorPro. The coefficient values $\pm$ one standard deviation of the fitted line in figure 4.14A are: V_{max} = 218.8 $\pm$ 9.7 pA, K_m = 20.1 $\pm$ 1.4 mM.

The reported K_m of GOx should be about 24. Overall, the K_m of the biosensors varied. The average K_m for 25 μm disc biosensors (n=28) was 20.2 $\pm$ 14.5 mM. Upon closer examination, there were three populations, sensors with the expected K_m (24.2 $\pm$ 4.0 n=8), sensors with lower K_m (11.1 $\pm$ 3.3 n=12) and sensors with a higher than expected K_m (39.2 $\pm$ 6.5 n=7). There was no way of predicting which group the biosensor will fall into before calibration.

The sensor shown in figure 4.14 responds well to glucose and has a high V_{max}. The V_{max} also varied greatly between sensors, the average V_{max} for 25 μm disc biosensors (n=28) was 162.2 $\pm$ 113.5 pA. The large variability in the enzyme kinetics was not limited to only the smaller electrodes but was seen across all sizes of

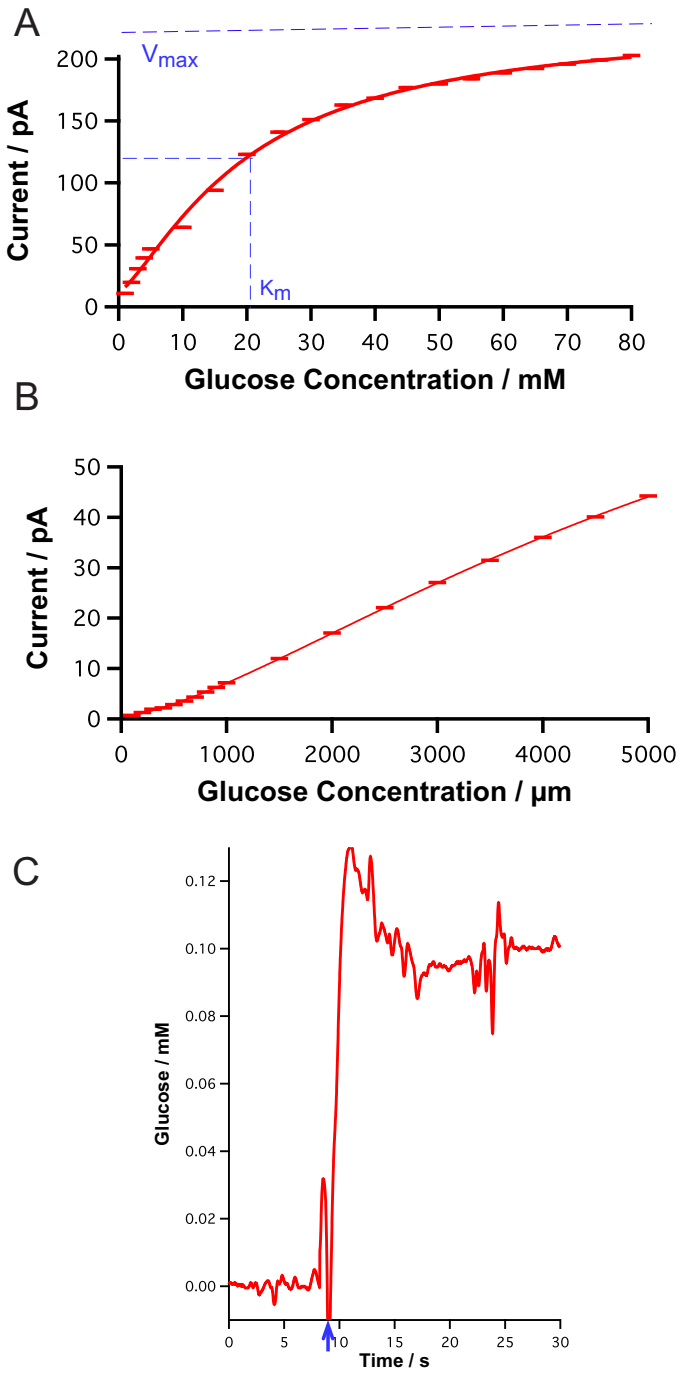


Figure 4.14: Glucose biosensor beaker calibration

Calibration of a glucose biosensor (25 μm) in a beaker. Biosensor was held at a constant potential of 0.75 V. A: Calibration up to 80 mM glucose concentration. V_{max} and K_m values shown on graph are used from the curve fitting in IgorPro. Mean ± standard deviation of measurement shown. B: Calibration up to 5 mM. This is is the physiological range. C: Raw data trace of a step change in concentration from 0 to 100 μM glucose. The arrow indicates the timing of addition.

biosensor. This indicates that the functionality of the enzyme influences the overall performance of the biosensors greatly. However, this is the the part of the process of which there is least control.

Figure 4.14B shows a closer view of the calibration in the physiological range (up to 5 mM). Here you can see a lag in the response to glucose at very low concentrations. This is often seen with glucose biosensors and therefore instead of the Michaelis-Menten curve, the Hill equation has been used to fit the calibrations, as it allows for this initial lag (138). The biosensor was quick to respond to the addition of glucose and the T_{90} of this sensor is 1.8 s. This is in-line with the literature reports, which state the response time as under 4 s (125).

Even though the current is in the pA range, a clear change is observed at the addition of 100 μM glucose, which is shown in figure 4.14C. The change in current is 6 pA and the LOD is 1.5 μM. The initial rise to above 100 μM before settling down is likely to be due to the addition of the concentrated glucose solution creating a localised high concentration before mixing into the bulk solution. The larger diameter disc electrodes gave maximum current in the nA range. All electrode sizes gave LOD in the low μM range, which is less than the reported literature LOD value of approximately 20 μM (135).

Overviews of the sensitivity and the response times for multiple glucose biosensors on different sized disc electrodes, are shown in table 4.7. The development of the electrodes coincided with the testing of the biosensors and therefore as the design of the electrodes was optimised for the flow cell (which decreased in size) the larger electrodes were less used.

Table 4.7: Responses of glucose biosensors

Electrode size / μm	Sensitivity / nAmM^{-1}cm^{-2}	T_{90} / s
125 (n=4)	3.1 ± 0.4 x 10^5	7.17 ± 2.9
50 (n=15)	3.9 ± 0.6 x 10^3	3.1 ± 1.3
25 (n=70)	3.1 ±1.3 x 10^3	5.18 ± 4.1

The sensitivity decreases with the size of the electrode. The enhanced diffusion, due to greater edge effects at smaller electrodes, does not seem to be helping the sensitivity of the sensor. This is probably because, not only is the glucose more likely to diffuse to the enzyme but also hydrogen peroxide is also more likely to diffuse away from the surface of the electrode and into the bulk media without being detected.

The response times of the sensors are all in the order of seconds. The 50 μm diameter disc biosensors have a faster time response than the 125 μm disc electrodes (P value = 0.00052, df = 17) and the time response is also, surprisingly, faster than the 25 μm disc electrode (P value = 0.054, df = 83). Furthermore the 25 μm electrodes are more sensitive to noise and as indicated by the large standard deviation. The magnitude of the change in current is much smaller and the addition of concentrated glucose solution using a Hamilton glass syringe, causes noise that is much greater than the change seen in the signal. When there is little noise upon the addition the response times are approximately 1 to 2 seconds.

4.4.2 Glucose: Stability

A glucose biosensor was fabricated on a 125 μm disc electrode and calibrated in a beaker the day after fabrication (day 1). After three weeks of storage in the fridge, the same biosensor was calibrated again and it responded to glucose with a much lower sensitivity, shown in figure 4.15.

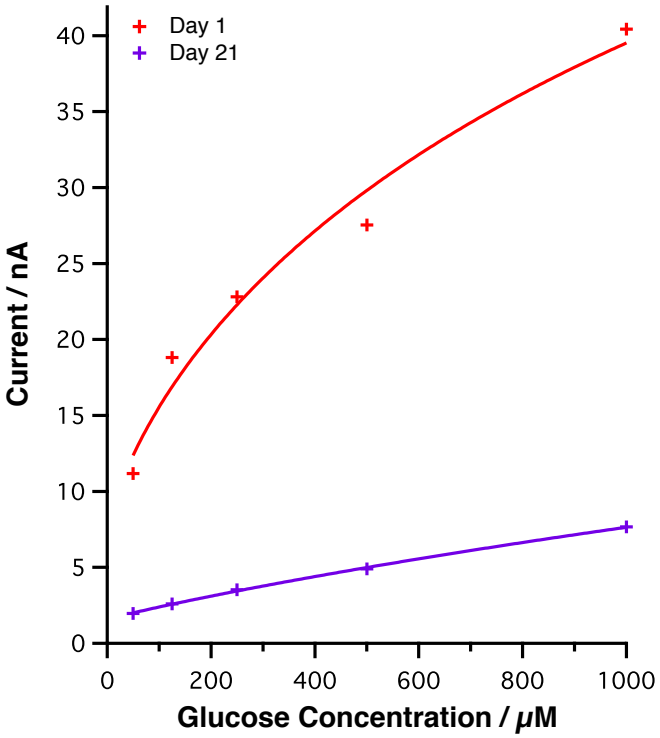


Figure 4.15: Biosensor calibration on day 1 and day 21
in vitro calibration of a glucose biosensor (125 μm) in a beaker on the day of fabrication (day 1) and 3 weeks later. Both calibrations were run at a constant potential of 0.75 V.

The sensitivity on day one is 3.3x10^5 nAmM^{-1}cm^{-2}, whereas three weeks later that has decreased to approximately 20% of that value to 6.24x10^4 nAmM^{-1}cm^{-2}. This indicates that biosensors do not store well and need to be fabricated before each experiment to achieve the best sensitivity.

A newly made 50 μm diameter glucose biosensor was tested for stability by continuously running overnight in a beaker containing 1 mM glucose. The overnight trace is shown in figure 4.16. The sensor is stable in the presence of glucose for 12 hours, with some fluctuations due to a change in the speed of stirring around 450 minutes. This shows that the sensors are stable enough for continuous monitoring in an intensive care unit.

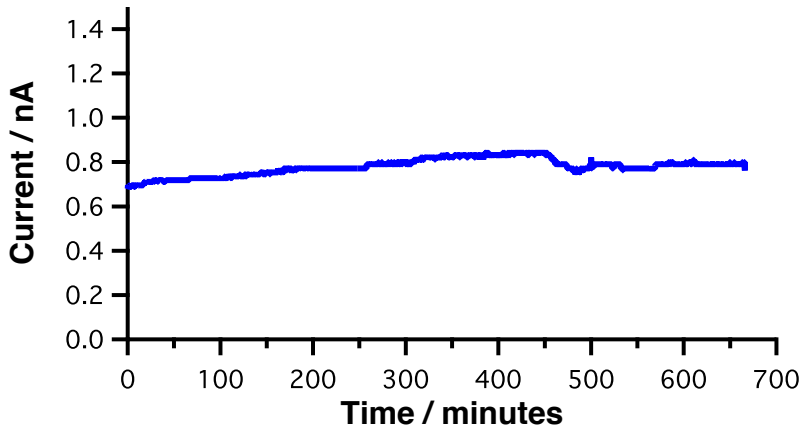


Figure 4.16: Overnight running of a glucose biosensor
A glucose biosensor (50 μm) was run at 0.75 V in a beaker containing 1 mM glucose, a day after fabrication.

4.4.3 Glucose Biosensor: Beaker Assessment

Glucose biosensors of various sizes were assessed in a beaker using step changes of concentration. This section will now discuss whether these sensors are fit for purpose to be placed within a flow cell. Table 4.8 assesses the sensors in terms of electrode size for the key factors. The sensitivity, LOD and response time were assessed and it was found that all sizes performed well. Whilst the 125 μm had far greater sensitivity it was found that placement on-chip was very difficult due to its size. The 25 μm sensor was very sensitive to noise and disruption and gave the lowest sensitivity. Therefore the 50 μm electrode was more focused upon when placed on-chip in chapter 6 as it had a slightly better sensitivity and a better signal

to noise ratio than the smaller size allowing for more accurate recording, and a needle size smaller than 125 μm made for easier use on-chip.

Table 4.8: Assessment of glucose biosensors in a beaker

Electrode size	Sensitivity	LOD	T_{90}
125	✓✓	✓✓✓	✓✓
50	✓✓✓	✓✓✓	✓✓✓
25	✓✓	✓✓✓	✓✓

4.5 Lactate Biosensor

Lactate biosensors were fabricated by soaking the combined needle electrode in a solution containing 2 mg of lactate oxidase per mL of 50 mM phenol in PBS, pH 7.2. The phenol was electropolymerised by applying a potential of 0.9 V for 15 minutes, as previously described. The sensors were characterised in a stirred beaker, discussed here, before placement on a microfluidic chip described in later chapters.

4.5.1 Lactate Biosensor: Sensitivity and Response Times

The lactate biosensors were mainly fabricated on two different sizes: 125 μm and 50 μm. Aliquots of lactate were added to the PBS as described in the glucose biosensor section. The expected staircase trace was seen and upon addition of the lactate there was noise in the form of large spikes. This was either noise from movement close to the electrode due to the addition or to a localised high concentration of lactate being sensed before it is dispersed into the bulk solution. This also occurred in the calibration of the glucose sensors and is an artefact of the method. Figure 4.17 shows a calibration curve of a 50 μm disc lactate biosensor in a beaker. The change in current is plotted against the concentration of lactate and the data points were fitted with the Hill equation using IgorPro.

The expected K_m value using LOx is 0.7 mM (as stated on the Genzyme data sheet). The average K_m for the 50 μm disc biosensors is 0.5 $\pm$ 0.2 mM (n=8) and for the 125 μm disc biosensors is 0.8 $\pm$ 0.6 mM (n=8). An overview of the sensitivity and the response times of lactate biosensors on two different sizes of electrode, are shown in table 4.9. Whilst fit for purpose, the overall sensitivity could be improved. The current responses for lactate sensors are in the pA range even though the larger disc electrodes are used. The glucose biosensors fabricated on the same size electrodes gave responses that are in the nA range. This could be due to using 2 mg/mL of enzyme instead of the 4 mg/mL used of GOx. This was reduced to conserve enzyme stocks. Another reason for lower sensitivity could be that the activity (U/mg) of LOx is much less that of GOx (20-60 U/mg and >250 U/mg respectively). Therefore it is unsurprising that that the sensitivity is lower and further work could be done to increase loading of the enzyme to the electrode surface. Despite this, the LOD of all lactate sensors of all sizes was approximately 10 μM.

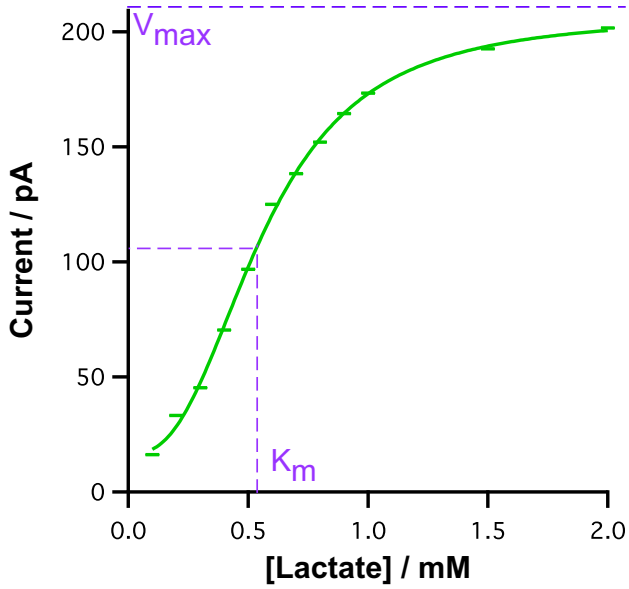


Figure 4.17: Calibration of a lactate sensor
Aliquots of lactate were added to a beaker of stirred solution and the current responses recorded. The lactate biosensor was held at a constant potential of 0.75 V throughout. A typical calibration curve of a 50 μm lactate biosensor is shown. Mean ± standard deviation of measurement shown. V_{max} = 207 ± 3.3 pA, K_m = 0.56 ± 0.01 mM.

Table 4.9: Responses of lactate biosensors

Electrode size / μm	Sensitivity / nAmM^{-1}cm^{-2}	T_{90} / s
125 (n=8)	2.7 ± 1.5 x 10^3	5.5 ± 3.3
50 (n=8)	1.8 ± 0.6 x 10^3	6.9 ± 3.9

4.5.2 Lactate Biosensor: Beaker Assessment

The lactate biosensors have been assessed in a beaker for two different sized electrodes. The 25 μm disc electrode was not tested as the sensitivity of the larger two electrodes was much lower than that seen for the glucose sensors. A 25 μm electrode provides a lower current and further work to optimise the signal must be done. This section will now discuss whether the lactate sensors tested, are fit for purpose to be placed placed within a flow cell. Table 4.10 assesses the sensors in terms of electrode size and the key factors are investigated and awarded ticks.

Table 4.10: Assessment of lactate biosensors in a beaker

Electrode size	Sensitivity	LOD	T_{90}
125	✓✓	✓✓✓	✓✓
50	✓✓	✓✓✓	✓✓

Whilst the lactate biosensors do not perform as well as the glucose biosensors, they do perform well enough for use to monitor lactate changes associated with brain injury.

The method of fabrication was optimised for glucose and it is possible that the differences in the enzyme may affect how well the same method fabricates a different biosensor. Table 4.11 assesses the sensitivity of glucose and lactate sensors in terms of electrode size and enzyme activity (with 4 mg used for GOx and 2 mg used for LOx). A smaller electrode will increase the flux of substrate towards the surface due to the diffusional field. If the sensitivities were scaled just by area, the expected sensitivity using a 50 μm disc electrode, compared to a 125 μm disc electrode, would increase. For the glucose sensors this is true, but for the lactate sensors a clear decrease in sensitivity is seen. This suggests that the lactate sensors would benefit by increasing the enzyme loading on the electrode surface. This could be done by increasing the concentration (and using a smaller volume) of the enzyme and phenol electropolymerising solution.

Table 4.11: Comparing enzyme activity (U/mg) and sensitivities ($nAmM^{-1}cm^{-2}$)

Enzyme	Activity	125 μm	50μm
GOx	250	3.1 x 10^3	3.9 x 10^3
LOx	60	2.7 x 10^3	1.8 x 10^3
$\frac{GOx}{LOx}$	8.33	1.14	2.17

Therefore the method of fabrication could be optimised for lactate, with particular attention paid to the enzyme loading on the surface of the electrode to improve the sensitivity.

4.6 ATP Biosensor

As a continuation of the work done on the glucose biosensor, an ATP sensor was created. The sensor was was developed and tested at Imperial College by an undergraduate student (Talia Wieder) under my instruction. In collaboration with Dr Bhavik Patel, Ms Wieder used the sensors to investigate ATP release from ileum tissue. This work has been published in the journal Biosensors and Bioelectronics.

The ATP sensor has the same basis as the glucose biosensor and uses the needle electrode construct. The difference between a glucose biosensor and an ATP biosensor, is the addition of a second enzyme, hexokinase (HEX). The detection of ATP on the biosensor is based on a competing reaction of HEX with GOx, shown in figure 4.18.

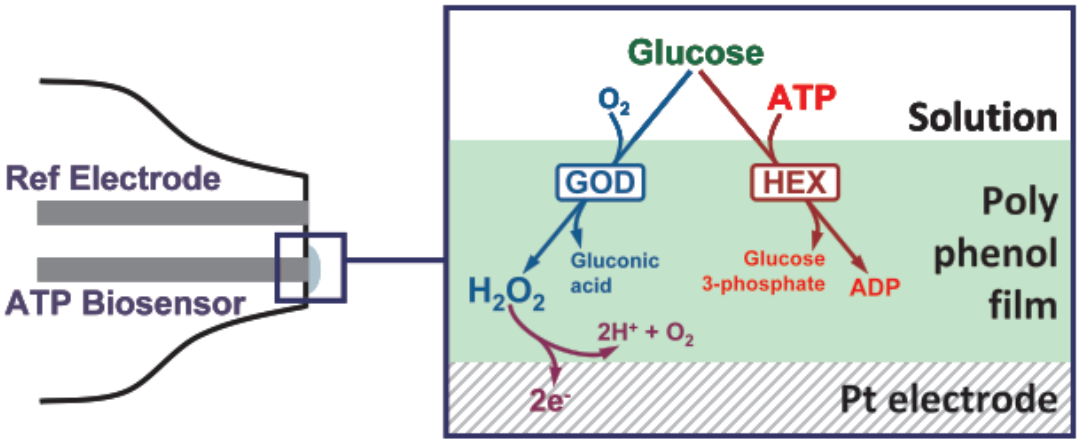


Figure 4.18: Schematic diagram showing the operation of the ATP biosensor. The ATP electrode is fabricated on a needle electrode, using a combination of HEX and GOx entrapped in a polyphenol film.

4.6.1 Stability in the Response to Glucose Concentrations

Due to the competing nature of the biosensor, GOx must provide a stable and reproducible response. In figure 4.19A a typical calibration of glucose on a 50 μm ATP biosensor is shown. The biosensor is responding well to glucose, indicating that the function has not been affected by the addition of the second enzyme.

The method of fabrication was investigated further to try and optimise the sensitivity. The stabilisation time allows for the enzyme in solution to adsorb to the electrode surface before electropolymerisation of the polyphenol film. Periods of 5, 10 and 30 minutes were investigated and results are shown in figure 4.19B.

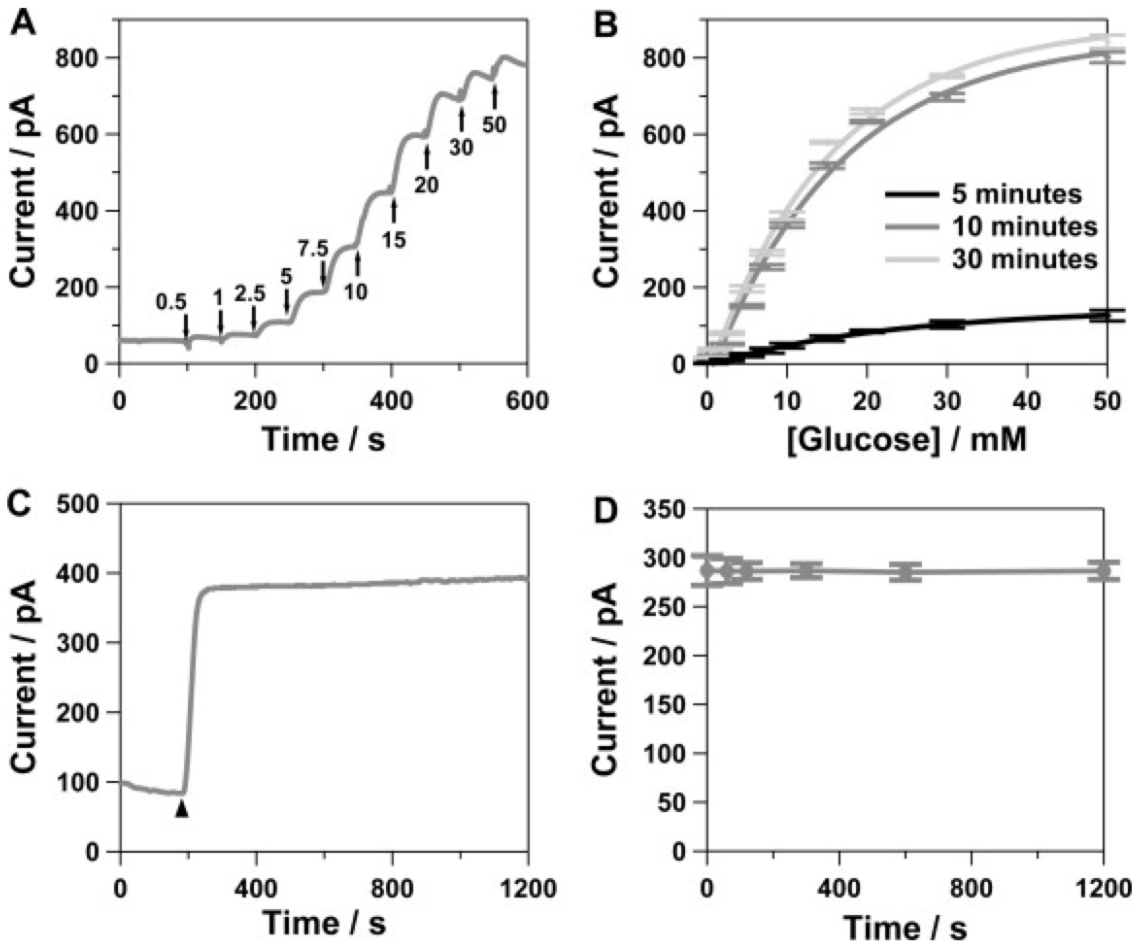


Figure 4.19: Investigating the GOx component of the ATP biosensor
A: A typical glucose calibration response on the ATP biosensor. B: the influence of stabilisation prior to electropolymerisation of the film, responses are shown as mean ± SD (n = 6). C: a typical experimental response of the ATP biosensor when exposed to 11 mM glucose. D: the overall drift between 10 sensors, responses are shown as mean ± SD and n = 10 for 11 mM glucose. All experiments are carried out in Krebs buffer pH 7.4, at 0.75 V vs. Ag|AgCl.

The V_{max} was used as an indicator of the effectiveness of longer stabilisation times. The V_{max} for 10 minutes stabilisation time was 853.56 ± 7.8pA (n=6) and was significantly greater than that at 5 minutes (144.54 ± 30.7 pA, p<0.001, n=6). However, there was no difference when the stabilisation time was further increased to 30 minutes (825.69 ± 19.5 pA, p=0.24, n=6). A stabilisation time of 10 minutes was chosen for the fabrication of the ATP biosensor.

Figure 4.19C shows a typical response to an addition of 11 mM glucose. This concentration of glucose was used as it is present in Krebs buffer, which is utilised for *in vitro* biological recordings. The response from multiple ATP biosensors is shown in figure 4.19D and shows a stable recording for all 10 biosensors used over a period of 20 minutes. There was no significant difference between the currents post stimulus for 20 minutes, showing excellent stability. Between electrodes there was a percent relative standard deviation (%RSD) of 5.27% to the same stimulus, indicating good reproducibility in the fabrication of the ATP biosensors.

Overall the ATP biosensor showed excellent stability and reproducibility for the detection of glucose, thus making it suitable for the monitoring of ATP. There was minimal drift in the signal, which is essential to assure accurate responses of ATP are obtained during in situ and *in vitro* measurements.

4.6.2 Characterisation of ATP Biosensor

The response to additions of ATP in the presence of 11 mM glucose, is shown in figure 4.20A. The ATP electrode shows a stable current when 11 mM glucose was added alone. There are then systematic decreases when aliquots between 0.25 μM and 2 μM ATP are added.

Following the addition of ATP, approximately 45 s is required to resolve the ATP concentration. This is better than some ATP biosensors (143) but is slower than other ATP electrodes, where response times in the order of milliseconds have been achieved (144, 145). However, for the biological areas of interest within this study, the ATP biosensor is fit for purpose.

A typical calibration curve for the ATP biosensors is shown in figure 4.20B. There is a good linear relationship between 0.25 and 4 μM and the limit of detection (LOD), defined as the concentration equivalent of 3 times the standard deviation at the y-intercept, was 9.9 ± 3.2 nM, with a sensitivity of 45.8 ± 1.22 pAμM^{-1} (n=8). Such sensitivity is essential to study small fluctuations in ATP release during biological measurements.

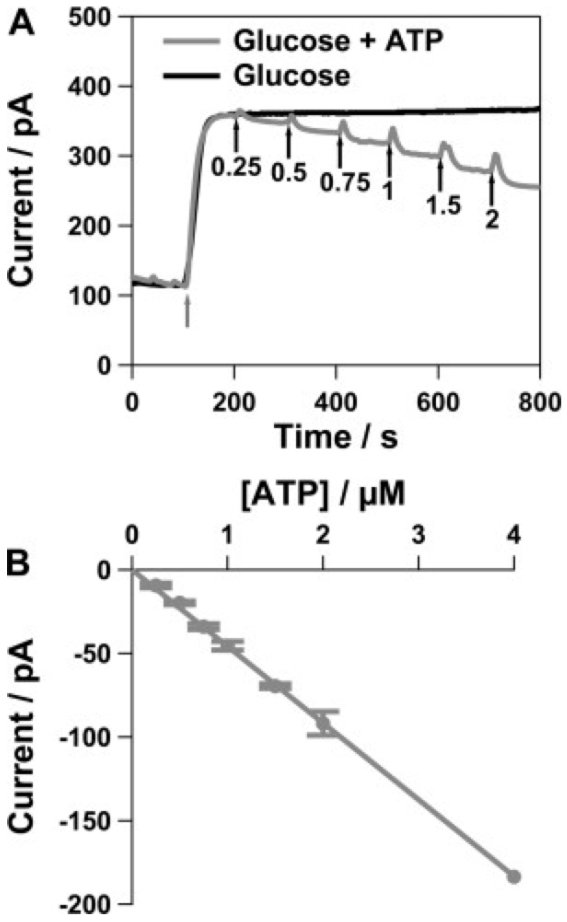


Figure 4.20: Calibration response of ATP biosensor.
A: ATP biosensor responses are shown. All sensors were exposed to 11 mM glucose (grey arrow) and ATP concentrations in the μM were added. B: The difference in the current from the 11 mM glucose response (black trace) and the ATP response (dark grey trace) was obtained and plotted as function of ATP concentration. All experiments are carried out in an amperometric mode at 0.75 V in Krebs buffer pH 7.4. Data shown as mean ± SD where n=8.

The LOD is at least between 10 and 100 times greater than all other sensors developed utilising the same GOx/HEX scheme in the literature, as the size of our electrode is far smaller that of previous studies (143, 144, 146, 147, 148).

4.6.3 ATP Biosensor Conclusion

The ATP biosensor was then used in an *in vitro* study in collaboration with Dr Patel. The sensor was used for the detection of mucosal released ATP from ileum tissue and the results are shown in the published work.

An ATP biosensor with exceptional sensitivity, long-term stability and selectivity from common biological interferents has been developed. The biosensor was shown to have sensitivity and limit of detection, suitable for *in vitro* biological monitoring. The ATP biosensor was stable under biological conditions and was able to conduct long term biological recordings from *in vitro* ileum tissue without any signal attenuation. The biosensor was used to detect variations in ATP release from isolated ileum and colon tissue successfully.

4.7 Conclusion

Biosensors were developed to measure key metabolites in the brain microdialysate. Glucose was initially studied and the method of fabrication was optimised. Three immobilising films were tested for suitability for entrapping GOx close to the electrode surface. The electropolymerisation of phenol was chosen to fabricate biosensors, as the selectivity against common interferents, such as dopamine and ascorbic acid, were far superior to the other two films tested. Glucose biosensors were then fabricated upon cylindrical electrodes and placed within a Radel flow cell. Although the sensitivity of the sensors was good, the response times were too slow for the dynamic changes expected in brain dialysate. This was attributed to the large volume of the flow cell and further miniaturisation was required. The microfabrication of flow cells is discussed in the next chapter.

Glucose biosensors were assessed on needle disc electrodes. Here, the glucose biosensors showed good sensitivity to glucose in the beaker, with fast response times. Surprisingly, the sensitivity at the smallest electrode was less, but this could be due to the enhanced diffusion of hydrogen peroxide away from the electrode. The stability of the biosensors in storage was not sufficient and the biosensors were therefore made fresh for each experiment. However, continuous usage of a newly made biosensor was satisfactory over a 12 hour period, which is sufficient for clinical monitoring. After assessment, it was concluded that the 50 μm electrode size had the best chance of giving an accurate and reliable signal when placed on-chip.

Lactate biosensors were also fabricated for the analysis of lactate levels in the dialysate. The method used for the glucose sensors was followed, substituting GOx for LOx. Whilst the LOD was good, and the 90% response was satisfactory, the sensitivity was low. The process of fabrication could be optimised to improve this aspect of the lactate sensors, and this is required if these sensors are to be used in the intensive care ward.

ATP biosensors were a development of the glucose biosensor and included a second enzyme, HEX. The ATP biosensor showed excellent reproducibility and stability to the glucose response and good sensitivity to ATP. When used *in vitro* to measure ATP release from colon and ileum sections, the ATP biosensor performed well. The *in vitro* work was a collaboration with Dr Patel, and the biosensor development and the *in vitro* results have been published.

Chapter 5

A Microfluidic Tool Kit

5.1 Introduction

Microfluidics has been incorporated into this thesis, as a platform to miniaturise the current clinical analysis system, and also to address problems many microdialysis users face. These are primarily Taylor dispersion (more discussion found in chapter 6) and long time delays from the sample leaving the microdialysis probe and being transferred to analysis. Some background on microfluidics followed by the development of a microfluidic toolkit, designed for use in conjunction with microdialysis, will be described.

5.1.1 Continuous Flow Microfluidics

Continuous flows involve nanolitre volumes of continuous liquid flow within microfabricated channels. An external pressure, such as a mechanical pump or an integrated micro-pump, propels the liquid flow through the system. Whilst this type of microfluidic device will miniaturise the analysis system and has proved successful in areas such as on-chip electrophoresis (80, 149) and polymerase chain reaction (PCR) (84, 85), it does not address the problem of dispersion and time delays associated with microdialysis.

5.1.2 Digital Microfluidics

An important recent advance in microfluidics has been the use of an immiscible carrier fluid to break the analytical flow stream into discrete segments or droplets. This area is becoming known as digital microfluidics. The advantage of digital microfluidics is that droplets are easily manipulated and independently controlled.

Droplets can be merged together (150, 151, 152), thoroughly mixed (153, 154), split (155, 156), sorted (157, 158) and incubated (159), followed by analysis on-chip (160, 161). Droplets can also be manipulated by geometry of the channels alone, which removes the need for moving parts (such as valves or pumps (162)).

Digital microfluidics provides reproducible operations using low volume reactors and the high control and rapid mixing in droplet-based systems has decreased reaction times and provided a high throughput platform. The advantage of this is a low cost device, with minimum interference from the user, for many applications.

5.1.3 Microfluidics and Microdialysis

The first on-line biosensor for microdialysis used tubular electrodes (163) and the first miniaturised device incorporating microdialysis sampling with on-chip chemical analysis of glucose and lactate, was described in 1997 (164). Whilst successful, it was a complicated multiple layer system designed for plasma analysis, which typically has much higher concentrations of glucose and lactate. There are examples of using on-line microdialysis coupled to amperometric analysis (164, 165), but the majority of studies are conducted in animals. Clinically, as previously discussed, only rsMD has been used, but this too has problems. All of these studies are conducted in continuous flows and hence ignore the problems of dispersion and the time delay before analysis.

In the clinical environment, microfluidic devices have been used only in laboratories, but development is moving towards point-of-care testing (166, 167, 168, 169). The low volumes and easy manipulations make this an attractive idea. Using microfluidics on-line to measure continuously from a patient at the bedside, is a new concept and combining microfluidics and microdialysis has many advantages. The use of digital microfluidics can eliminate Taylor dispersion, cross-contamination, dilution of samples and evaporation due to compartmentalisation of reagents (170) within the carrier fluid.

It is my view that microdialysis is in many ways the killer application that benefits from microfluidics. Using a faster flowing oil stream, the aqueous dialysate droplets can be quickly propelled down the connection tubing reducing the time lag between sampling at the MD probe tip and analysis. Hence, the microdialysate flow rate through the probe can be reduced, achieving a higher analyte recovery, without compromising on the transit time. As the dialysate droplets are segmented in an immiscible fluid, there is no mixing between successive droplets and hence no smearing of sharp concentration changes due to the Taylor dispersion seen in continuous

flows. This will greatly improve temporal resolution and allow monitoring of fast analyte changes.

The group of Kennedy et al were the first to interface digital microfluidics to microdialysis analysing the signals optically via laser induced fluorescence (171). Whilst in a research environment optical analysis is a good solution and is easy to implement in a two-phase system, it is inappropriate for use in an intensive care ward due to the large and expensive equipment. The development of novel techniques to manipulate and analyse the droplets will introduce a potentially beneficial system for all microdialysis users and I aim to integrate digital microfluidics and microdialysis with electrochemical analysis. With good design, droplets can be easily manipulated and the improvement in fabrication techniques provides the opportunity to fabricate an on-chip electrochemical detector.

5.1.4 Chip Fabrication

The methods of fabrication initially started with photolithography using silicon, as the technologies were well-developed from the semi-conductor industry. Due to increased popularity of LOC devices, specific characteristics were more in demand, such as optical transparency and biochemical compatibility. This led to the advancement of technology for a wider range of materials including glass, metals and plastics. Soft lithography is the method of fabrication used to create structures in polydimethylsiloxane (PDMS) (172), a popular material of choice. PDMS is easily moulded and cured and it is optically transparent down to a wavelength of 300 nm. PDMS is durable with a good chemical stability and has a low interfacial free energy (22 dyn/cm) (172). PDMS is naturally hydrophobic with a water contact angle of 112 °, is gas permeable and chemically inert (173). The drawbacks of PDMS include swelling of cured PDMS and shrinking (of about 1%) of the polymer upon curing ((172)). The softness of the elastomer limits the aspect ratio of microstructures that can be fabricated without pairing or sagging, which lowers accuracy. Delamarche et al (174) show that the aspect ratio must be between 0.2 and 2 to obtain defect free stamps.

5.1.5 Droplet Generation

By use of an immiscible fluid such as oil, aqueous solutions can be segmented into droplets, due to the liquid-liquid interfacial tension and shear force between the two phases. These droplet compartments are well-defined and reproducible and can act

as reaction cells in which kinetic parameters can be extracted (175). Multiphase flows are most commonly generated by the use of T junctions (176) and flow focussing geometries (176, 177, 178, 179). A T junction is where an inlet channel containing the disperse phase joins perpendicularly to a continuous phase (170). Induced shear forces within the two phase system causes the head of the disperse phase to be elongated into the main channel until the neck thins to a point where it breaks. The characteristics of the droplets formed can be tightly controlled through relative flow rates, viscosities, surface tension and geometry (153). Flow focusing is where both phases are forced through a narrow gap and the droplets are formed by symmetric shearing. This geometry is harder to implement. In this thesis a T junction is used to generate droplets.

5.1.6 Carrier Fluid

The carrier fluid (the fluid with the higher wettability on the channel surfaces) is most often oil in digital microfluidics. An alternative is air, thus removing the potential safety problems oil causes on a clinical ward. Here, a flow focussing method provides better stability of droplet formation and droplets could be produced faster. However, a much higher flow rate is needed (20 μLmin^{-1} plus) and ideally a vacuum pump or gas cylinder would be used to propel droplets. When tested, the droplet generation was unstable and it was harder to manipulate the droplets due to the compressibility of air. Evaporation of water from the droplets is a problem in air resulting in a false analysis due to the concentration of analytes changing. Also, droplets could come in contact with the channel surfaces, resulting in cross contamination of samples due to adherence of proteins. Oil has the advantage of a mechanical force to manipulate the fluids and wet the surface of the channels, removing cross-contamination and evaporation issues. Therefore, in this thesis oil is used. Initial experiments used hexadecane, a hydrocarbon with a chain of 16 carbon atoms. However, the majority of work was conducted using FC-40, a perfluorocarbon, which has high stability to various chemicals, excellent lubricity and dielectric properties, and is non-toxic.

5.2 Initial Investigations

The first test was to create a droplet flow stream. Oil and water were perfused through a crude T junction fabricated by hand. Once droplets were formed, the next question was how to analyse the contents of the droplets. A second chip was fabricated and droplets of ferrocene monocarboxylate (Fc) were generated. Electrodes housed in Radel tubing (as described in section 3.2.2) were placed in the droplet stream.

5.2.1 Methods: Chip Fabrication

A crude chip was cast to create a T junction and generate droplets. A second chip was created using the same method and electrodes inserted into the droplet stream. The method was as follows:

Polyester resin and activator (Robnor resins, RX771C/NC and Ardour hardener HY1300GB) were mixed in a ratio of 3:1, poured into a polydimethylsiloxane (PDMS) mould consisting of a single channel (width 500 μm and depth 250 μm) and heated at 60 °C for 10 minutes. A slide made of PET was treated in a plasma chamber for 12 seconds. The cast was placed on the PET and returned to the oven at 80 °C for 1 hour. Drilling through the side of the cooled chip created a T junction. Radel tubing of inner diameter 750 μm (1/16" OD), was used as connection tubing and glued into place using epoxy resin. The second chip, used Radel tubing to house the electrodes, which were also glued into place. Oil was connected to the inlet at a flow rate of 176 μLmin^{-1} and Fc was connected to the T junction inlet, with flow rates varying from 1.5 μLmin^{-1} to 2 μLmin^{-1}. Figure 5.1 shows a photograph of these chips.

5.2.2 Methods: Electrodes

Two working electrodes were tested in the initial chip: a cylindrical working electrode , diameter 50 μm length 2 mm, and a 50 μm disc electrode. These electrodes were tested using both a bare electrode and an electrode coated with poly(sodium-4-styrene-sulfonate) poly(L-lysine-hydrobromide) (PSSPL) (Sigma-Aldrich). A dip coating method was used with PSSPL to create a hydrophilic layer on the working electrode. To do this, first the clean working electrode was dipped into 25 mM polystyrene sulfonate for 30 seconds. The electrode was then left vertically to dry with the tip pointing up, for 30 minutes. The electrode was then dipped into poly-lysine solution for 30 seconds and left, vertically, overnight to dry at room temperature.

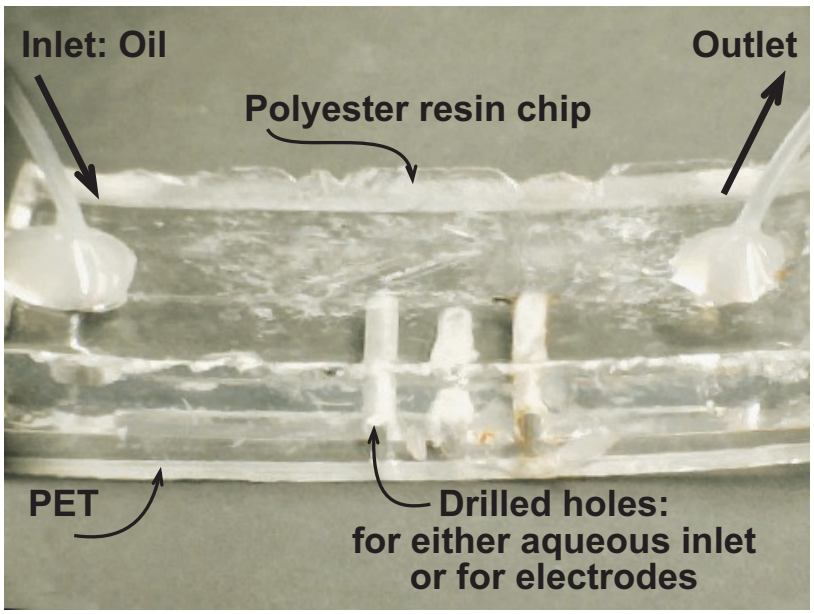


Figure 5.1: Photograph of the initial chip
A simple straight channel was cast into polyester resin and sealed to a glass slide. Perpendicular channels were drilled to create either a T junction or channels in which electrodes are inserted. The above photograph has three perpendicular channels, one each for the working, auxiliary and reference electrodes. Connections at the inlet and outlet were made using epoxy glue (Araldite).

5.2.3 Initial Findings: Droplet Generation

Generation of droplets within this crudely made chip was surprisingly easy. However, although high flow rates were used the droplets were very long in length. This was due to the large geometry of the channels and hence large volumes used. Using this method of fabricating the chips, it is very difficult to make the channels smaller by hand and hence a better technique is required. Later versions of the microfluidic chips were fabricated using soft lithography.

5.2.4 Initial Findings: Analysis of Droplets

Two main issues arose from placing the electrodes directly into the droplet stream. It was found that the electrodes must be contained within the same droplet for analysis of its contents. If one electrode is within the oil or within another droplet then the circuit is broken and a reliable reading cannot be taken. This was not a problem here as the droplet length was very long. Also, if the electrode came in contact with the oil, the oil fouled the electrodes by wetting the surface and blocked out the aqueous signal, see figure 5.2.

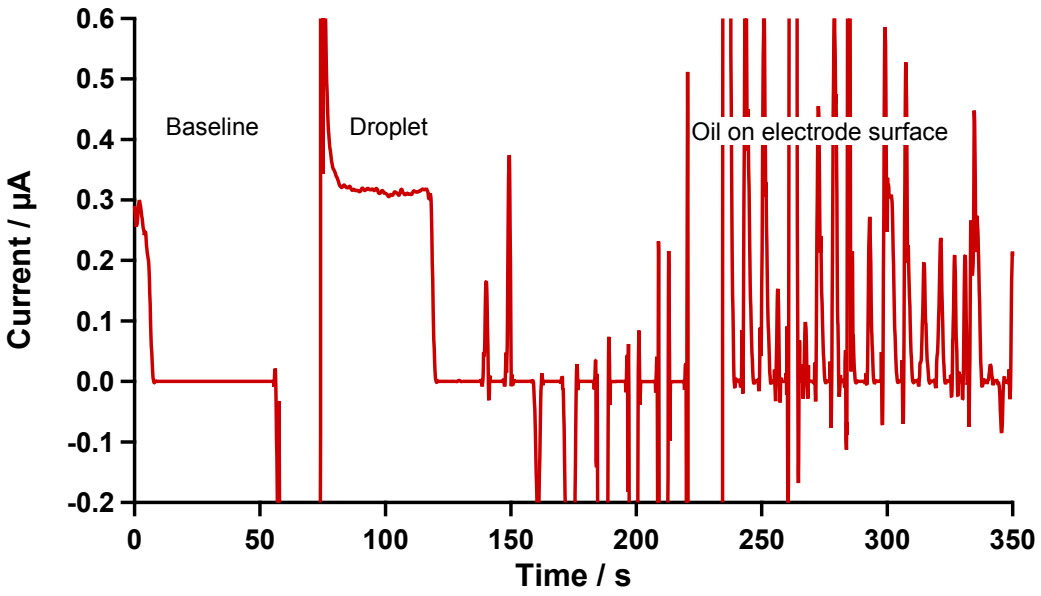


Figure 5.2: Response of 2 mm cylindrical electrode in droplet flow
The working electrode was held at a constant potential of 0.5 V vs Ag|AgCl and the current recorded in a droplet stream of ferrocene monocarboxylate and hexadecane oil.

To investigate this further, a 50 μm disc electrode was moved between hexadecane oil and ferrocene solution in a beaker and the electrochemical response recorded, shown in figure 5.3. The electrode functioned well after dipping in the oil for 1 s, figure 5.3B. However, if the surface is exposed to the oil for a longer time period, the aqueous signal is lost due to surface fouling, figure 5.3C.

To overcome the fouling, a hydrophilic PSSPL film was applied to the surface of the electrodes using a dip coating method. Application of PSSPL stabilised the signal of droplets even after repeated long exposure to oil. PSSPL allows wetting of the electrode surface by the aqueous solution and therefore the oil passes by without covering the surface. Looking at the responses of a bare electrode compared to a PSSPL electrode there is a reduction from approximately 10 nA to 0.8 nA in current when run at a potential of 0.5 V, figure 5.3D . Hence, there is a trade-off between stability of the electrode in a multiphase flow and the signal recorded. If this film was subsequently used on a biosensor this would severely impair the sensitivity of the sensor, rendering it useless for monitoring ischemia.

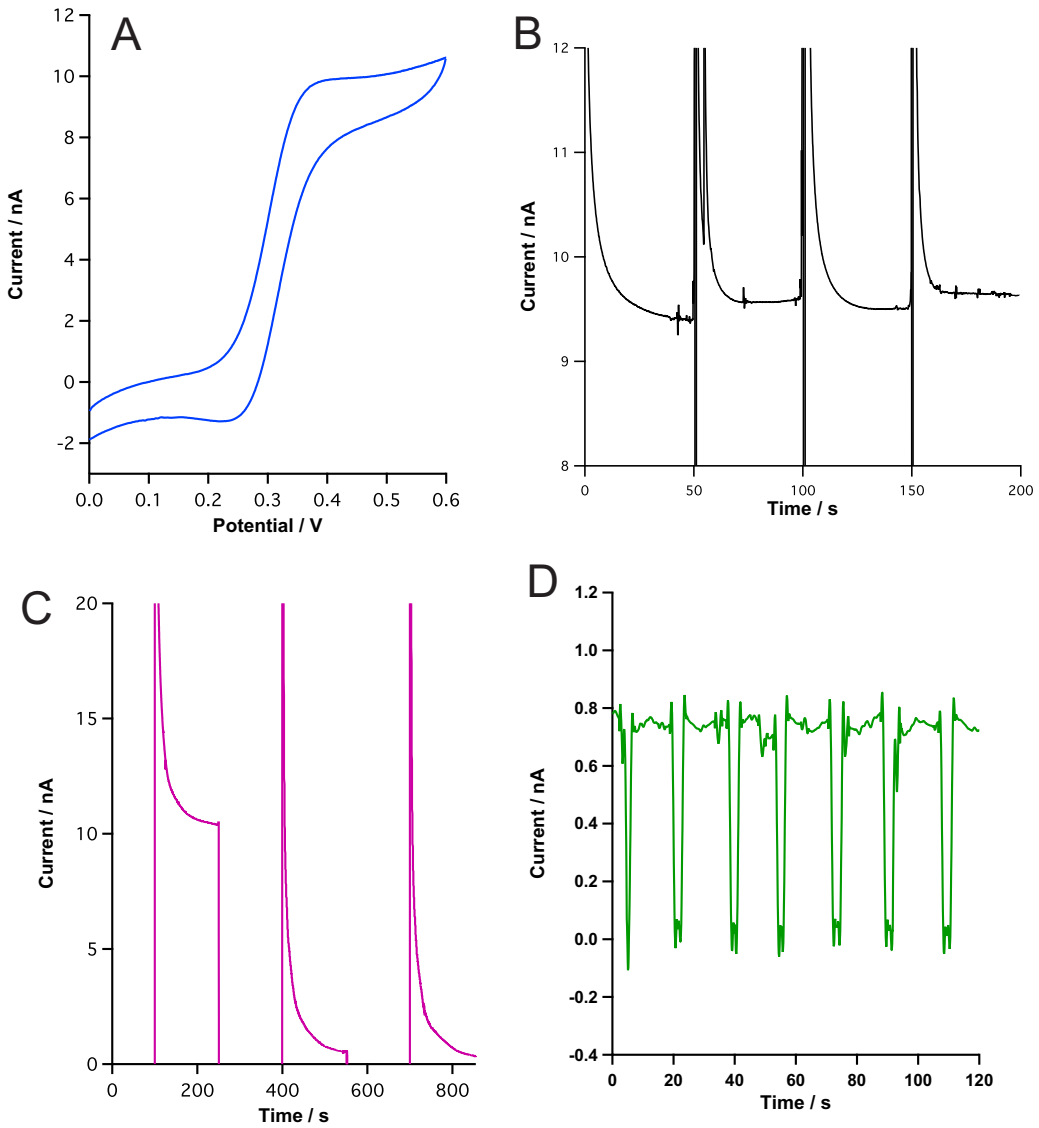


Figure 5.3: Response of 50 μm electrodes to hexadecane oil
A: Cyclic voltammogram in a beaker of 1.5 mM ferrocene monocarboxylate versus Ag|AgCl. Scan rate 50 mV/s B: The working electrode was held at 0.5 V and the electrode repeatedly dipped in hexadecane for 1 s periods. C: The working electrode was held at 0.5 V and was repeatedly transferred to the oil for 150 s before being moved back to the ferrocene solution. D: PSSPL coated 50 μm electrode on chip in a droplet stream of 1.5 mM ferrocene monocarboxylate and hexadecane.

5.2.5 Lessons Learnt

Whilst we were able to make droplets easily using a polyester drilled T junction, the end product was messy and inflexible. The main channel was formed using a master made by curing PDMS over a wire. There is a limit on the size of wire that can be used to do this reproducibly and to a good enough standard. As the inlet for the aqueous phase was made by drilling, the surface of the channel walls were not very smooth. Also this channel was much larger than the main channel. Hence, large droplets were formed with short spacings of hexadecane oil. Due to this ratio, the overall flow rate of the droplet stream was not as fast as we had hoped. The connections to the inlet and outlet were very difficult to make successfully and permanent once glued in placed. This led to problems when trying to optimise the system as more flexibility was required. These issues were addressed by using PDMS chips.

5.3 Droplet Generation

PDMS was used to give more flexibility in chip and channel design. George Whitesides first used rapid prototyping to create microfluidic systems in PDMS (180). Whitesides also used PDMS to create complex three dimensional structures, which he describes as basket weaves (181). This section will look at the T junction fabricated using soft lithography in PDMS, which is used throughout this thesis.

5.3.1 Chip Fabrication

The method of fabricating the mask and master is defined in chapter 2. Once a master is created, it can be re-used to fabricate chips several times. This step is described here.

The PDMS chip is made by thoroughly mixing 25 g PDMS base and 2.5 g curing agent (Sylgard 184 elastomer) (10:1 ratio by weight) in the open laboratory. Approximately 90 % of the mixed PDMS is poured over the master, which has been cleaned by blasting with nitrogen. The extra 10 % is poured into a clean petri dish and kept to one side for use later as the base. PDMS casting either took place in a chemistry clean room or in the fume cupboard of a wet lab. The master PDMS is degassed using a desiccator attached to a vacuum pump. If after 10 minutes there are still bubbles on the surface, a pasteur pipette was used to pop them. The master PDMS is baked for 1 hour at 65 °C on a hot plate. Once cured, the PDMS is peeled from the master, cut into chips using a sharp scalpel and holes punched for connection tubing, using a blunted needle tip (see table 5.1 for details). The extra PDMS in the petri dish, is now placed on a hot plate (65 °C) for 12 minutes. The base PDMS is semi-cured and is tested by lightly touching the surface with a fully cured piece of PDMS, and the two should stick together. The texture should be such that only a light imprint of the fully cured PDMS is left on the surface. If the base is not cured enough then the chip will sink and the channels will fill up, and if it is too cured then the two halves will not stick together. The chips are placed channel side down onto the semi-cured PDMS base and sealed together by baking at 65 °C for at least 4 hours but preferably overnight.

Table 5.1: Sizes of commonly used tubing and electrode needle compared with the blunted needle used to punch the hole

Electrode size / Gauge	Hole punch size / gauge
25	20
27	22
31	22
Tubing OD / μm	Hole punch size / gauge
780 (FEP)	20
1090 (Portex)	18
610 (Portex)	20

5.3.2 Optical Detection

Droplets in the PDMS chip were visualised using several optical methods. A USB microscope (VHM-004, Discovery, Veho) was found to be sufficient to check the microfluidic chips in detail when in use in the wet laboratory. Here, coloured dyes were often used in the aqueous flow for contrast. This USB microscope had the added advantage of coupling the video to the data acquisition software used for the electrodes (Chart, ADInstruments). A high speed video camera was also used to gain videos of droplets through the PDMS chips. An inverted optical microscope (IX71, Olympus) served both as light source and detector. To collect images and videos, a CCD camera (Phantom Miro 3, Vision Research) was connected to the microscope, shown in figure 5.4. Fluorescent measurements were also taken when using droplets of fluorescein (Sigma-Aldrich). This involves Laser Induced Fluorescence (LIF), which is discussed in section 5.5.1 and the method involved using the optical microscope in epifluorescence mode. A mercury lamp (U- LH100HG, Olympus) was used for wide-field illumination and images collected by using the same objective (UPlanFL N 10x/0.30, Olympus). The fluorescence emission and the illumination were separated using fluorescence mirror sets (U-MF2, U-MWIG3, Olympus). To acquire the emission light, an EM-CCD camera (iXon+, Andor Technologies) was used and analysed with the accompanying software.

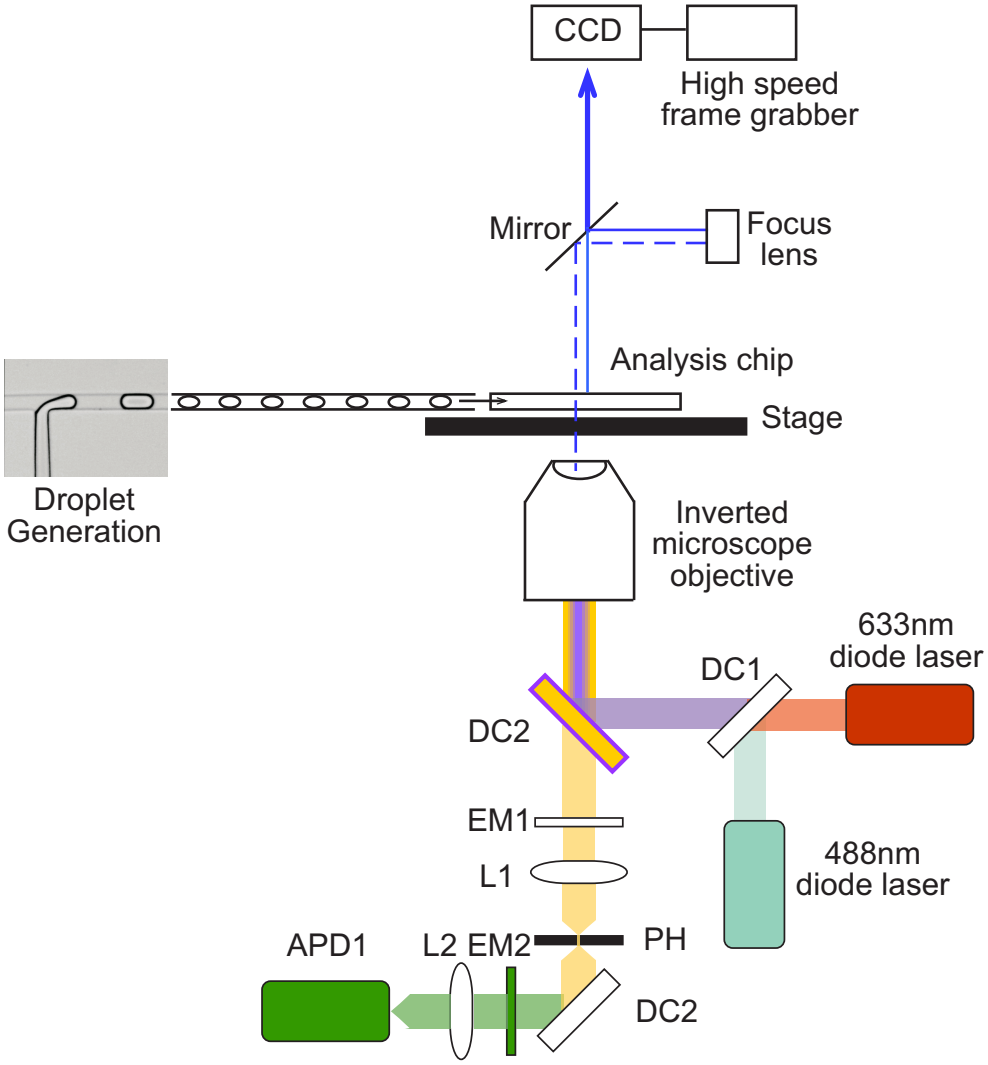


Figure 5.4: High speed camera setup
The experiments were conducted using an inverted microscope coupled with a high speed CCD camera. Droplets were generated using either a T junction in a microfluidic chip or using a robotic head, both of which are described in the following sections.

5.3.3 Droplet Generation: T junction

To form a droplet flow, a T junction was fabricated using PDMS. This consists of a main channel, in which the carrier phase flows, and a second perpendicular channel containing the disperse phase. Figure 5.5 shows the master used. An extensive evaluation of the effect of geometry on droplet size and stability was carried out by Dr Xize Niu for this project. The best results were obtained using the design shown.

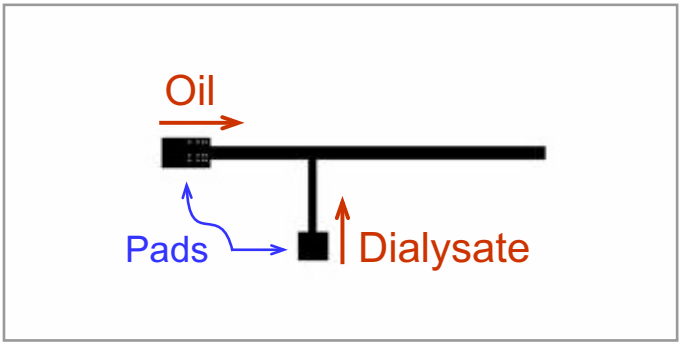


Figure 5.5: Master of T junction
The master is used to fabricate PDMS chips. The square pads contain square pillars and were designed as filters for dust or large particles in the solutions. To avoid droplet break up, this feature was omitted at the outlet.

At the junction where the two immiscible fluids interact, droplets spontaneously form. The aqueous phase pushes into the main channel and the flow of the oil drags it down the channel. The neck of the aqueous flow will thin until it is unstable and it breaks, forming a droplet. This is shown clearly in figure 5.6 and in Video 1 on the associated DVD. The size and frequency of the droplets formed is very tightly controlled by the geometry of the channels, the flow rate ratio and the relative viscosities of the liquids used. Due to the immiscibility of the two phases, the droplets remain separate. Although droplets do not mix together, the solution within one droplet is well mixed. There is a no-slip condition at the walls but at the interfaces of aqueous solution and oil the velocity is equal to the convective velocity of the droplet.

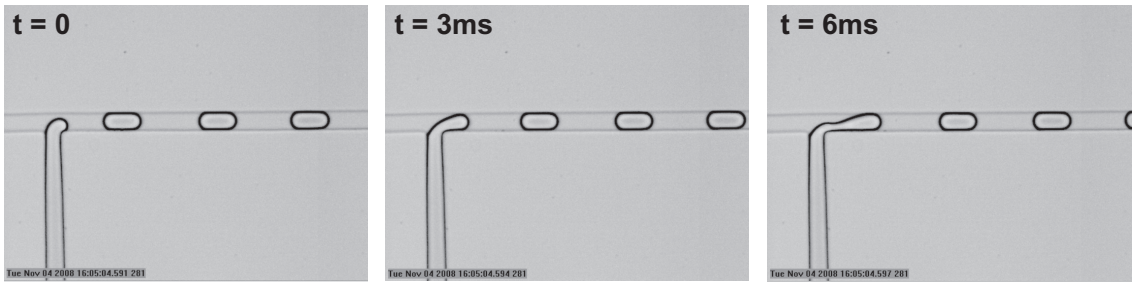


Figure 5.6: High speed sequence of droplet generation
A high speed camera was used to record the generation of droplets in a PDMS T junction. Hexadecane oil and water were pushed into the chip using syringe pumps at 225 and 150 μLmin^{-1} respectively. The width of the channels is 100 μm. A frame is shown every 3 ms.

This difference results in a flux of fluid in a strong circulatory, secondary flow within the droplet i.e. the solution is dragged to the back of the droplet and circles back to the front by passing through the middle, figure 5.7. Therefore each droplet has rapid and thorough mixing and homogeneous concentration profiles.

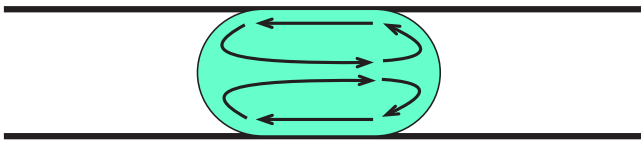


Figure 5.7: The flow within an aqueous droplet
A schematic indicating the movement of solution within an aqueous drop due to the no-slip condition at the walls. As the droplet moves down the channel, the solution is pushed towards the back of the droplet and circles back through the middle.

5.3.4 Droplet Generation: Robotic Head

Droplets were also formed using a robotic head designed by Dr Xize Niu (Drop-Tech). This allows the aqueous solution to change with great precision. The tubing is attached to the robotic head and the end of the tubing is positioned at the interface between oil and sample. Suction is applied and the robotic head moves up and down, moving the tubing end across the interface. The initial version allowed for two different aqueous solutions and a newer version of the robotic head now exists, allowing for fifteen different aqueous solutions and is programmable using Labview. The fifteen well robotic head is shown in figure 5.8.

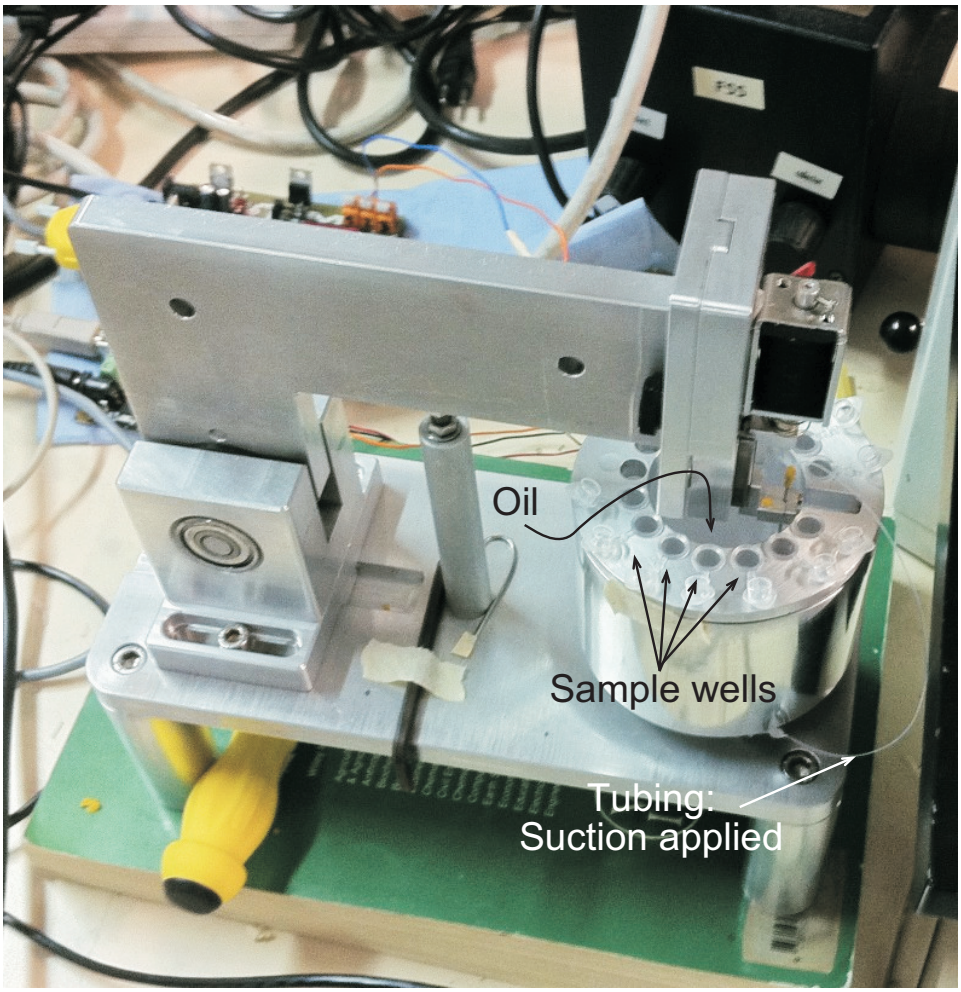


Figure 5.8: A photograph of the robotic head in a 15 well setup
15 sample wells are arranged in a circle above a large well filled with oil. The 15 samples rotate around and the tubing is moved up and down between the oil and the aqueous solution.

5.3.5 Droplet Frequency

LIF was used to investigate the effect of flow rate on the droplet frequency and size, figure 5.9. The oil was pumped through the system at a constant rate of 10 μLmin^{-1}. The aqueous flow rate was changed from 2 μLmin^{-1} to 4 μLmin^{-1}. The number of droplets produced increased with aqueous flow rate, as expected.

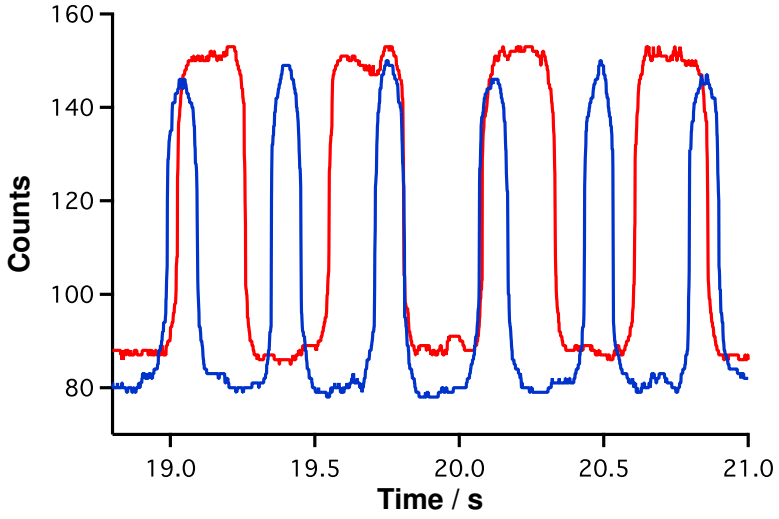


Figure 5.9: LIF data of droplets
LIF used to detect fluorescein droplets at different flow rates. The red trace has an aqueous flow rate of 2 μLmin^{-1} and the blue trace has an aqueous flow rate of 4 μLmin^{-1}. The oil was pulled through the system at a flow rate of 10 μLmin^{-1} in both cases.

5.3.6 Droplet Length

A sequence of droplets containing fluorescein was recorded using LIF, figure 5.9. The resulting trace was analysed by calculating the relative standard deviation (%RSD) of the length of the droplet at half height. Generation of a droplet every 3 seconds gives a %RSD of 0.63 (n=25). At a generation rate of 1 droplet every 1.5 seconds the %RSD = 1.39 (n=25). These numbers indicate that the droplet generation is very stable in terms of length, and hence volume, of the droplets produced. The easiest way of changing the length of the droplets, and hence the volume, during operation is to change the ratio of flow rates.

Table 5.2 summarises the findings from manipulating the flow rates of the aqueous and oil phases. The length of the droplets in the FEP tubing connected to the

outlet of the microfluidic chip, was measured using a ruler and therefore is an approximate reading. Another way of changing the volume of the droplets is to change the geometry of the channels however, this requires new designs and re-fabrication.

Table 5.2: Approximate length of droplets in FEP tubing compared to aqueous and oil flow rates

Aqueous / μLmin^{-1}	Oil / μLmin^{-1}	Droplet length / mm
2	10	3
2	7	4
2	5	5
2	2	6
2	1	7
1	4	4
2	4	6
5	4	10
7	4	very near continuous

5.4 Digital Microfluidics and Microdialysis

5.4.1 Laser Induced Fluorescence

Laser Induced Fluorescence (LIF) is a spectroscopic measurement used for detection and analysis of molecules. The laser used is a diode laser. The species to be visualised are excited by a laser beam using a particular wavelength. When the species de-excites, a larger wavelength than the excitation wavelength is emitted. This is detected and the species is said to fluoresce. A laser was aligned and focused on the microfluidic analysis chip. Droplets of fluorescein were pushed through the chamber and the resulting emittance was recorded and analysed. Excitation wavelength of fluorescein is 490 nm.

5.4.2 Microdialysis Probe Recovery

A recovery experiment was conducted to test the application of digital microfluidics for a microdialysis system. This involved placing a microdialysis probe (Animal probe: CMA12, membrane length 2 mm, CMA Microdialysis) in the vortex of a vigorously stirred fluorescein solution [1 μM]. The probe was perfused with buffer solution at varying flow rates. The outlet of the microdialysis (MD) probe was connected to a T junction chip via FEP tubing of varying lengths (approximately 10 cm, 1 cm and 0 cm). When required droplets were formed using FC-40 oil. The dialysate was transferred to an analysis chip where fluorescence measurements were taken. LIF was used to record the level of fluorescein in the dialysate as the perfusate flow rate was changed. 100 % recovery was recorded by perfusing the analysis chip with 1 μM fluorescein. Recovery in continuous and droplet flow regimes were tested and was calculated using equation 5.1.

$$Recovery(\%) = \frac{(FluorescenceIntensity)_{Dialysate}}{(FluorescenceIntensity)_{PureFluorescein}} \times 100 \qquad (5.1)$$

The recovery results using 3 different connection tubing lengths are shown in figure 5.10. As expected, the recovery largely depends upon flow rate. At lower flow rates there is a higher recovery due to the solution within the probe having longer to equilibrate with the external solution.

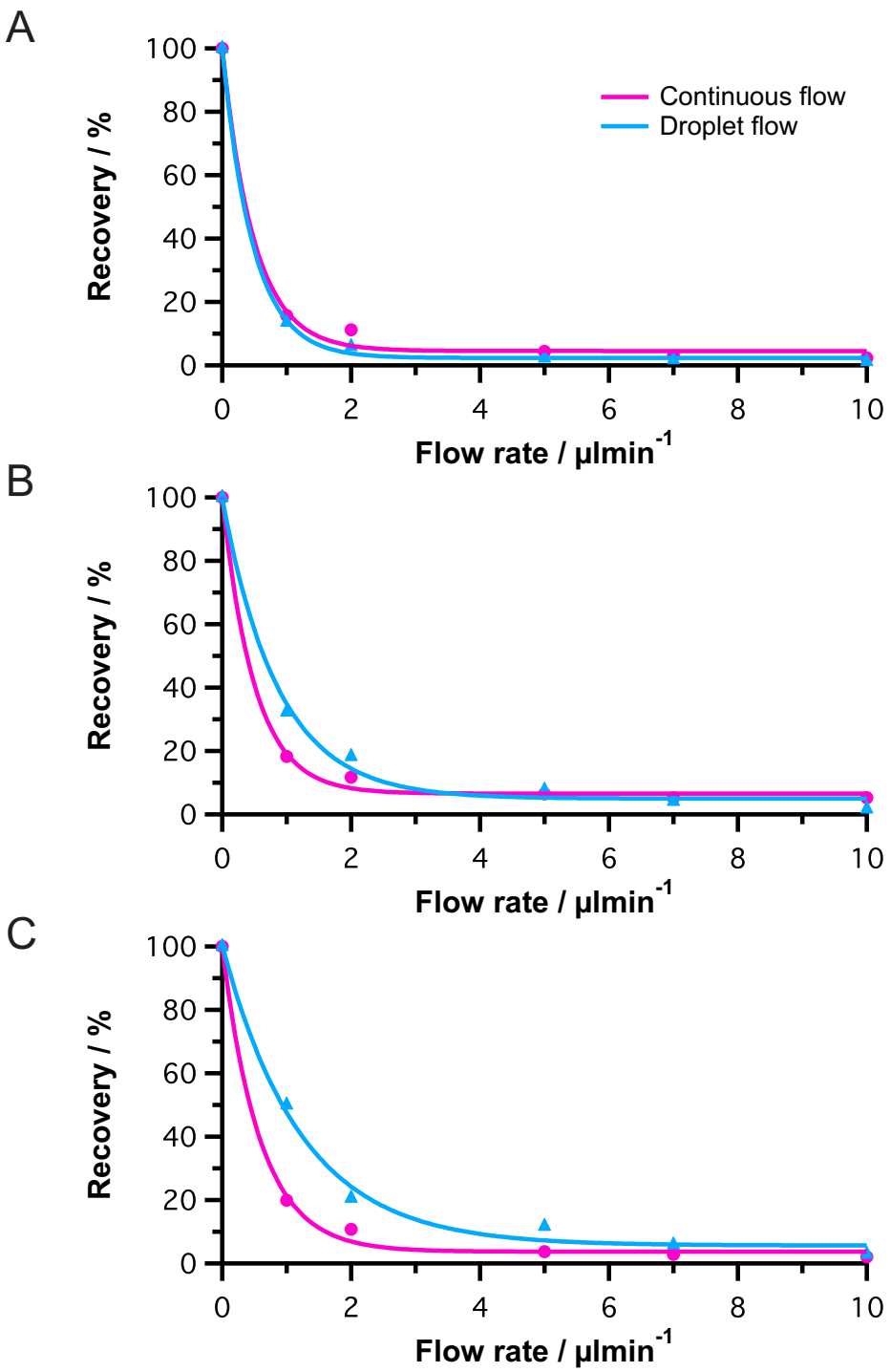


Figure 5.10: Recovery of fluorescein in droplet and continuous flows
The figure compares the recovery in continuous and droplet flow. A: Continuous and droplet flow recoveries using approximately 10 cm connection tubing length. B: using approximately 1cm tubing length C: the outlet of the MD probe is attached directly onto the T junction.

With approximately 10 cm of FEP tubing between the probe outlet and the T junction (figure 5.10A), there is little difference between the recovery seen in the continuous and discrete flow regimes. Unexpectedly, when a shorter tubing length is used, approximately 1 cm, there is a slight difference in the recoveries at lower flow rates (figure 5.10B).

The average difference in recovery levels between droplet and continuous flow are displayed in figure 5.11 for a low (1 μLmin^{-1}) and a higher flow rate (7 μLmin^{-1}). Two connection tubing lengths, 1 cm and 10 cm, are also displayed. A student t-test was conducted on each group (n=3) to see if the discrepancy is significantly different from zero. Only one group was statistically significant; 1 cm connection tubing at 1 μLmin^{-1} had a P value of 0.049. The other three groups were not significant.

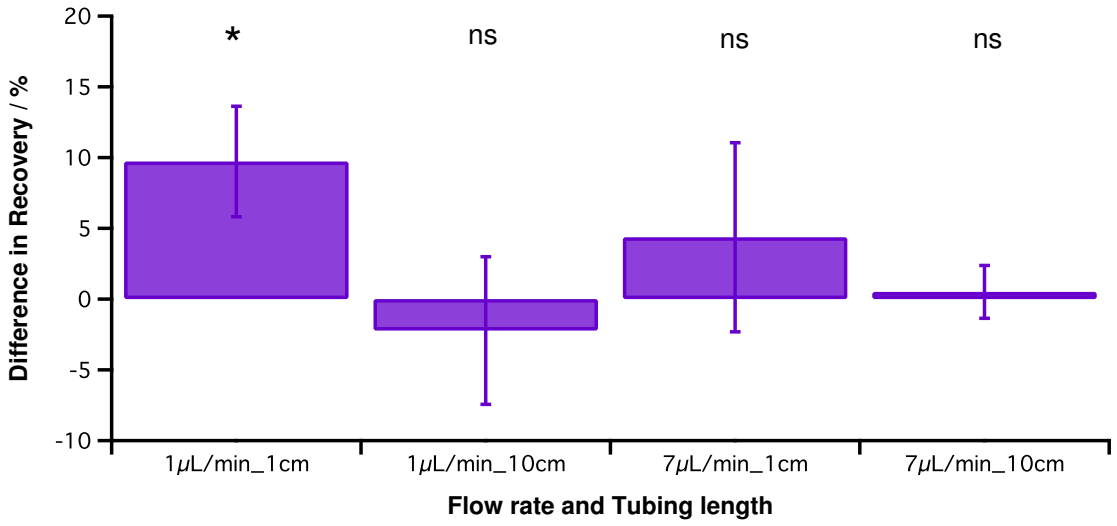


Figure 5.11: The difference in recovery between continuous and droplet flow
Average differences and standard deviation shown. Two lengths of tubing are shown for both a low (1 μLmin^{-1}) and high (7 μLmin^{-1}) flow rate.

This was investigated more closely with an experiment that specifically looked at the effect of tubing length on recovery, at a low perfusion flow rate. The recovery experiment was conducted as before, however only a perfusion flow rate of 1 μLmin^{-1} was used. A small connection tubing of approximately 1 cm was used to connect the outlet of the MD probe to the T junction. Droplet and continuous flow regimes were tested in this setup. The connection tubing was then changed to a longer length, of approximately 10 cm, and the recovery in both regimes tested. The small tubing was then replaced and the experiment repeated. Figure 5.12 shows the results.

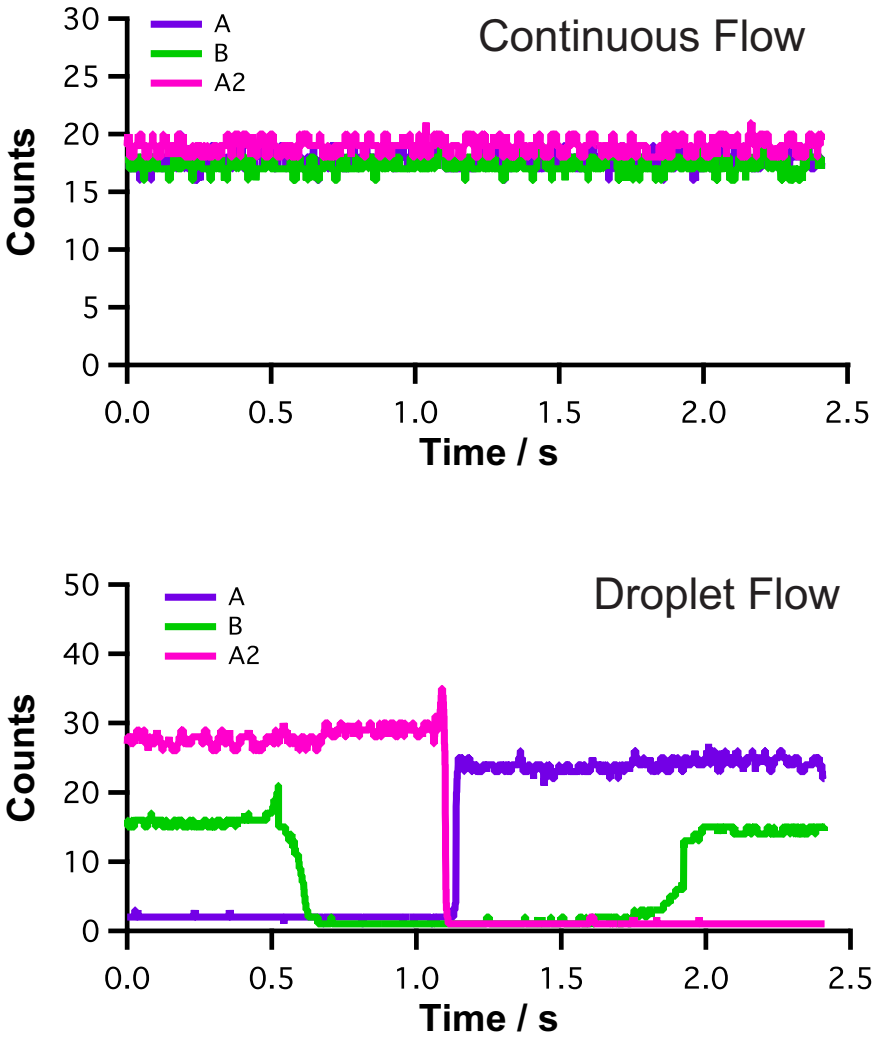


Figure 5.12: Comparison of fluorescein recovery in droplet and continuous flows with different tubing lengths

Trace A (purple) uses approximately 1 cm of connection tubing between probe outlet and T junction. Trace B (green) uses approximately 10 cm tubing. Trace A2 (pink) is a repeat of A. Continuous flow regime shown in the top graph, droplet flow in the bottom.

The level of fluorescein seen in the continuous flow regime did not change over the course of the experiment. This suggests that it is not to do with back pressure in the system. However, in droplet flow, variable levels of fluorescein are seen. The upper levels of the traces indicate the aqueous flow and the lower levels the oil. When a longer tubing (trace B, green) is used, the level of fluorescein is similar to that in continuous flow. However during droplet flow, the level of fluorescein increases by about 50 %.

For confirmation, the outlet of the microdialysis probe was attached directly onto the microfluidic T junction. Figure 5.10C shows the recovery results. The microfluidic chip was heavy in comparison to the probe and balancing the chip on the outlet was, practically, very difficult to achieve (NB the tip of the probe had to be in the vortex, so the positioning of all components was very tricky). There is an enhanced recovery at lower flow rates, with the recovery at 1 μL/min^{-1} increasing by 30 % in absolute terms.

From visual inspection of the intersection at the T junction, the flow of the dispersed phase momentarily stops as the neck of the droplet breaks off. If this effect propagates back to the fluid in the probe, then it could enhance recovery in the microdialysis probe by allowing the fluid in the probe more time to equilibrate. This would account for the higher recoveries found in droplet flow compared to continuous flow. The approximate length of these droplets was measured in FEP and found to be 3 mm equating to a volume of 0.034 μL. The volume of the membrane at microdialysis probe tip is 0.4 μL and therefore at any one time would contain the volume for approximately 12 droplets of dialysate. So, if the stop-start motion generated at the T junction did propagate back to the solution at the tip, it is feasible for the recovery to be affected. However, this effect can only be harnessed if the T junction can be placed close to the MD probe membrane. Clinically approved probes used in the study of brain injury have an outlet tubing, which is too long for this effect to make a difference.

5.4.3 Micro Particle Imaging Velocity (microPIV)

To look more closely at the flow at the T junction, fluorescent microspheres (F8834 Molecular Probes) were perfused through a T junction during droplet generation at a flow rate of 2 μLmin^{-1}. FC-40 oil was used as the carrier fluid at a flow rate of 2 μLmin^{-1}. The T junction was visualised using a USB microscope (VMS-004, Discovery, Veho) and the resulting videos analysed using a particle tracker plugin in ImageJ, figure 5.13.

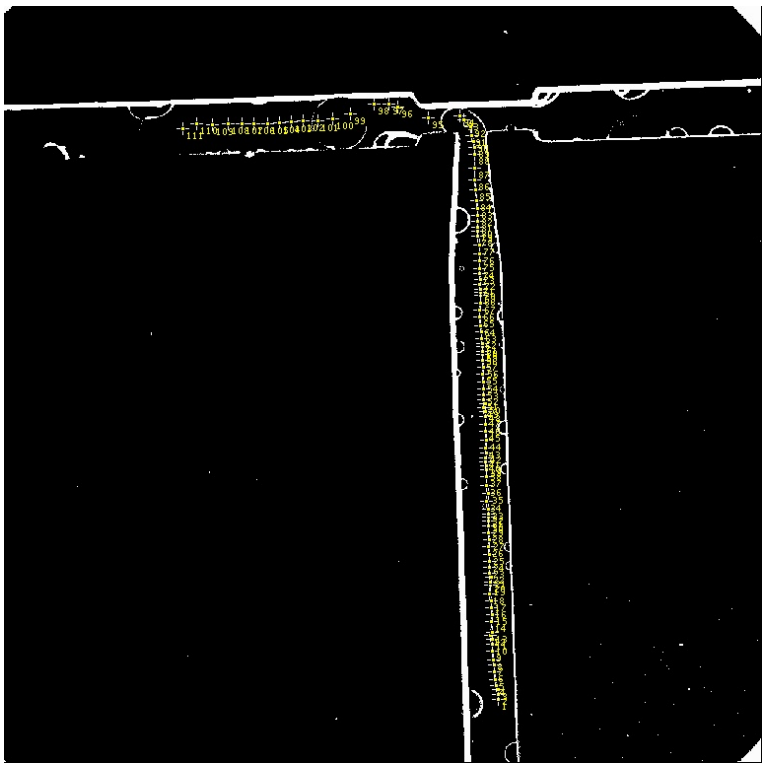


Figure 5.13: The tracking of a particle in a T junction
The image shows the positions of a fluorescent microsphere at each frame of the video as it is carried through the T junction in the disperse phase. Note that the spacing is not even between the positions of the microsphere as it travels down the perpendicular channel.

The velocity changes as each droplet is generated. When the disperse phase pushes into the main channel the velocity increases as it gets carried by the flow of the oil. When a droplet breaks off into the oil phase, the velocity in the aqueous channel decreases. This affects the distance that the microspheres move as they are carried in the aqueous solution, figure 5.14A.

The motion in the aqueous flow during segmentation was also investigated by using a pressure driven pump with integrated flow sensors. The fluids were controlled and driven by pressure created using a gas cylinder. The flow sensors were integrated to monitor the flow rate of the fluids. The flow rate of the aqueous phase during segmentation is seen in figure 5.14B. When a droplet breaks off into the oil flow, the flow rate decreases rapidly before returning to a steady level as a new droplet begins to form.

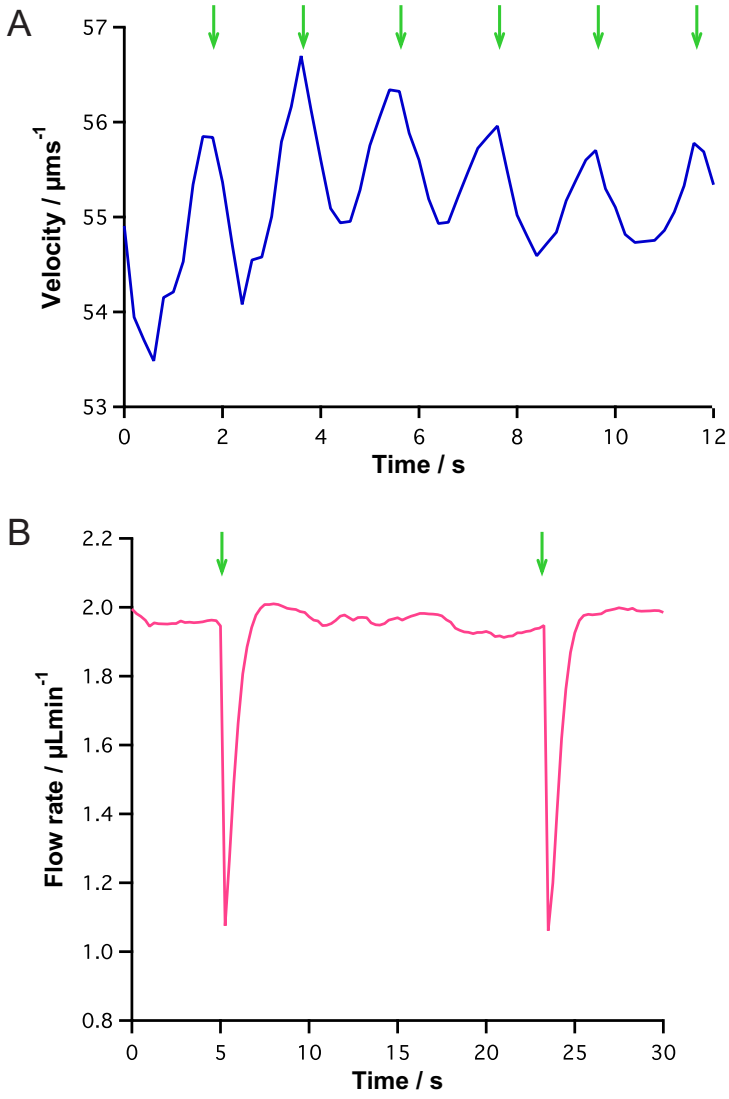


Figure 5.14: Movement of the disperse phase in a T junction
A: The velocity of a microsphere within the aqueous solution, as it moves down the channel, is shown. Velocity was calculated using a particle tracker plugin in ImageJ. B: Flow sensors were used to measure flow rate within a pressure driven droplet generation system. Green arrows indicate the segmentation of droplets.

Overall, when the T junction was connected to the outlet of the animal MD probe, either directly or with 1 cm of connection tubing, an enhancement in the recovery rates were seen. This is an interesting effect, which is likely to be due to the stop-start motion of the aqueous phase at the T junction, seen in the microPIV study. This stop-start motion could be propagated back to the solution at the membrane, allowing more time for the analytes to diffuse across the membrane. However, this would only occur when the connection length is sufficiently small, presumably due to the ability of the plastic syringes and connection tubing to swell slightly and accommodate the changes in flow. Therefore this effect would not be seen in a clinical probe due to the long lengths of tubing required for the outlet. In future research, combining the MD probe with droplet generation may be beneficial and a more thorough study would be needed.

5.5 Manipulation of Droplets

Ultimately digital microfluidics will be applied in the clinical environment. Here, I describe some parameters, which can and will be changed when the droplet stream is introduced.

5.5.1 Surface Tension

Surface tension can be altered by the addition of surfactants to the oil. The ability of a liquid to wet a surface depends upon the adhesive and cohesive forces acting upon the interaction. In a straight microfluidic channel the wetting of the channel walls depends upon the hydrophobicity of the surface and of the liquids. In figure 5.15A, the oil wets the surface. This is the case with PDMS as it is a hydrophobic material and the adhesive forces acting between the PDMS surface and the oil are stronger than the cohesive forces acting within each. The aqueous solution has stronger cohesive forces and tries to avoid contact with the PDMS surface. When surfactants are added to the oil, the interfacial tension between the oil and the aqueous phase is reduced. Surfactants are amphiphilic, containing both a hydrophobic region (the tails) and a hydrophilic region (the heads). At a T junction, the ability of the aqueous phase to push into the oil channel is controlled by the interfacial surface tension. Surfactants sit at this interface, lowering the surface tension, making it easier for the aqueous phase to push into the oil. Therefore longer droplets are formed when surfactants are added to the oil as the neck of the droplet can be stretched thinner. The surfactants can also sit at the interface between the oil and the PDMS channel walls. The surface, therefore loses its hydrophobicity, and the aqueous solution may wet the surface, as seen in figure 5.15B. Here, there are oil droplets forming in the aqueous solution.

For the purpose of my work, it is essential that oil wets the surface of the channels, as this eliminates mixing between the droplets. If surfactants are required then the PDMS surface must be modified to create a super-hydrophobic surface, for example by the use of Duxback. Duxback is commonly used to treat car windows to repel rain water, however, can also be applied to PDMS with the same effect.

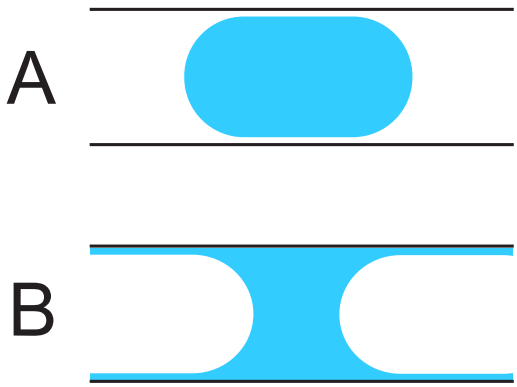


Figure 5.15: Depiction of droplets in a channel with different wetting properties
The aqueous solution is shown in blue. A: the oil is wetting the surface of the channel so the aqueous droplet has convex edges. B: The aqueous solution wets the surface of the channel producing a concave edge effect and oil droplets.

5.5.2 Flow Rates

As previously described, the flow rates of both the oil and the dialysate will affect droplet formation. In the clinical environment however, it can also be used to reduce the lag time. At 2 μLmin^{-1}, with a connection tubing of length 1 m, the time lag between the analyte leaving the probe and reaching the assay for analysis is approximately 10 minutes. Although this is better than offline measurements, such that traditional microdialysis, it is still not real-time. As we are proposing that fast changes in metabolites through events, such as spreading depolarisations (SDs), are detrimental to the overall outcome of the patient, it is our goal to measure the events as close to when they happen as possible. Digital microfluidics is a great way of propelling the dialysate to analysis. By using a fast flowing oil stream, the droplets can be propelled over 1 m of connection tubing without the recovery of the probe being affected. In fact, it has the additional advantage of enabling the dialysis flow rate to be lowered without increasing the time lag. This will increase the recovery of the probe without losing the time resolution needed.

5.6 Analysis Chip

As seen from preliminary studies with electrodes and oil, fouling of the electrode surface is a big issue. A coating (PSSPL) applied to the electrode surface was tested and although it stopped the oil wetting the surface, it resulted in low sensitivity. Therefore, a second analysis chip was designed that could remove the oil and rejoin the droplets into a continuous flow. The aim was for the analysis chip to be placed away from the patient, after the 1 m of necessary connection tubing, and for it to contain all the electrodes required for analysis. In this section I describe two chip designs using the general approach of passive coalescence. A more detailed discussion of passive coalescence follows in section 5.7

5.6.1 Analysis Chip: Design 1

The first design of the analysis chip, to separate the oil and aqueous flows is shown in figure 5.16. The droplet stream approaches a set of pillars, which separates two outlet channels. The oil is filtered through the pillars into a secondary channel. Meanwhile, the aqueous droplets rejoin to form a continuous flow in a main outlet channel. Within this channel, sensors can be placed on-chip for analysis and the continuous dialysate path can be connected to rsMD for validation. Also the solution can be collected and used in traditional microdialysis analysis techniques.

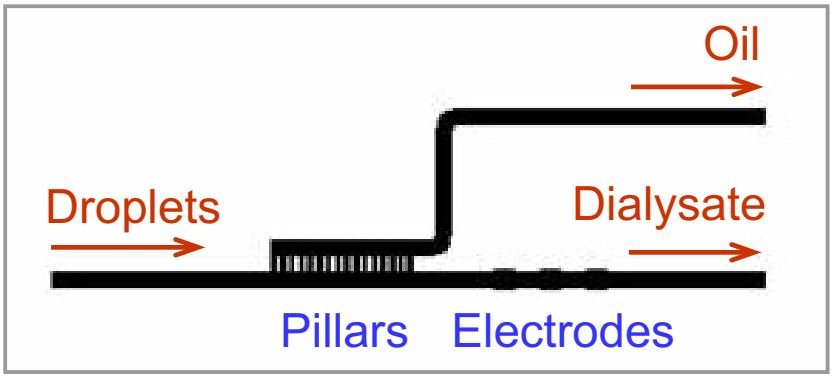


Figure 5.16: Analysis chip design 1
An outline of the mask used to fabricate the analysis chip. Pillars separate the two channels and act as a filter to remove the oil. The varicosities on the dialysate outlet arm are to contain the analysis electrodes. Channel width is 100 μm.

This analysis chip was designed to run under suction. The oil is pulled through the system using a syringe pump placed at the oil outlet in figure 5.16, from a bottle at the oil inlet at the T junction, which precedes this chip. The aqueous phase is both pushed into the T junction and pulled at the dialysate outlet on the analysis chip using syringe pumps. The dialysate push and pull flow rates are equal (typically 2 μLmin^{-1}) and the oil flow rate is defined by the oil suction (typically 5 μLmin^{-1}). This has the advantages of independently controlling the oil and aqueous flow rates and lowering the back pressure in the system. This is particularly important when a microdialysis probe is used, as back pressure can cause the membrane to rupture or can influence recovery.

Figure 5.18 shows a droplet entering the analysis chip and the two phases separating. A video of the droplets joining in design 1 (Video 2) can be found on the associated DVD. In figure 5.18A the oil is being pulled through the pillars at 5 μLmin^{-1}, the rejoined dialysate is moving at 2 μLmin^{-1} and the incoming droplets are moving at a combined flow rate of 7 μLmin^{-1}. Due to the droplets moving faster, the incoming droplet catches up with the rejoined dialysate. The oil continues to deplete through the pillars, shown in figure 5.18B.

Additional free energy is required for a droplet to pass through the pillars. This is defined by the surface tension. During a given time interval, the change in aqueous volume between the pillars as the droplet passes, is the same irrespective of the size of the pillar spacing. However, the shape of the aqueous solution is different when comparing pillars, which are close together and those which are far apart, figure 5.17.

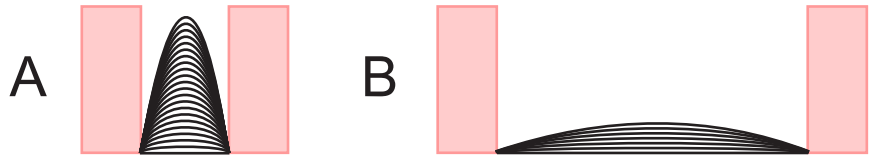


Figure 5.17: Pillar spacing effect on droplets
Pillars are represented by the peach rectangles. A: shows pillars closely spaced. The walls are hydrophobic so the aqueous solution forms a highly curved structure B: shows pillars with large spacing in between them. The same amount of volume if now spread over a wider area.

This leads to the surface area being much larger when the pillars are close together. As the surface energy depends upon the surface area and surface tension, the additional free energy at pillars, which are close together is much larger than when the pillars are spaced far apart. Therefore it is harder for the aqueous droplets to pass between pillars that are closer together. The surface tension of water is 0.072 Jm^2, whereas the surface tension of FC-40 is 0.016 Jm^2 (182). The lower surface tension of the oil allows it to pass more easily through the pillars, and as the channel walls are hydrophobic, the oil wets the surface, making it easier still.

The pillars are spaced such that the droplet is unable to flow between the pillars. It passes straight along and joins the rest of the dialysate, shown in figure 5.18C.

A problem with this design is highlighted in figure 5.18D. Once the droplet has joined the rest of the dialysate, the aqueous phase blocks off the oil channel. As a result, the oil flow rate tends to zero, and both the droplet and the dialysate flow rate is now 2 $\mu Lmin^{-1}$. If this effect is propagated back to the generation of the droplets at the T junction, then both the generation and the rejoining will have to be synchronised. In practice, this is difficult to achieve and the setup took a couple of hours but, once balanced, the separation of the two phases worked spontaneously.

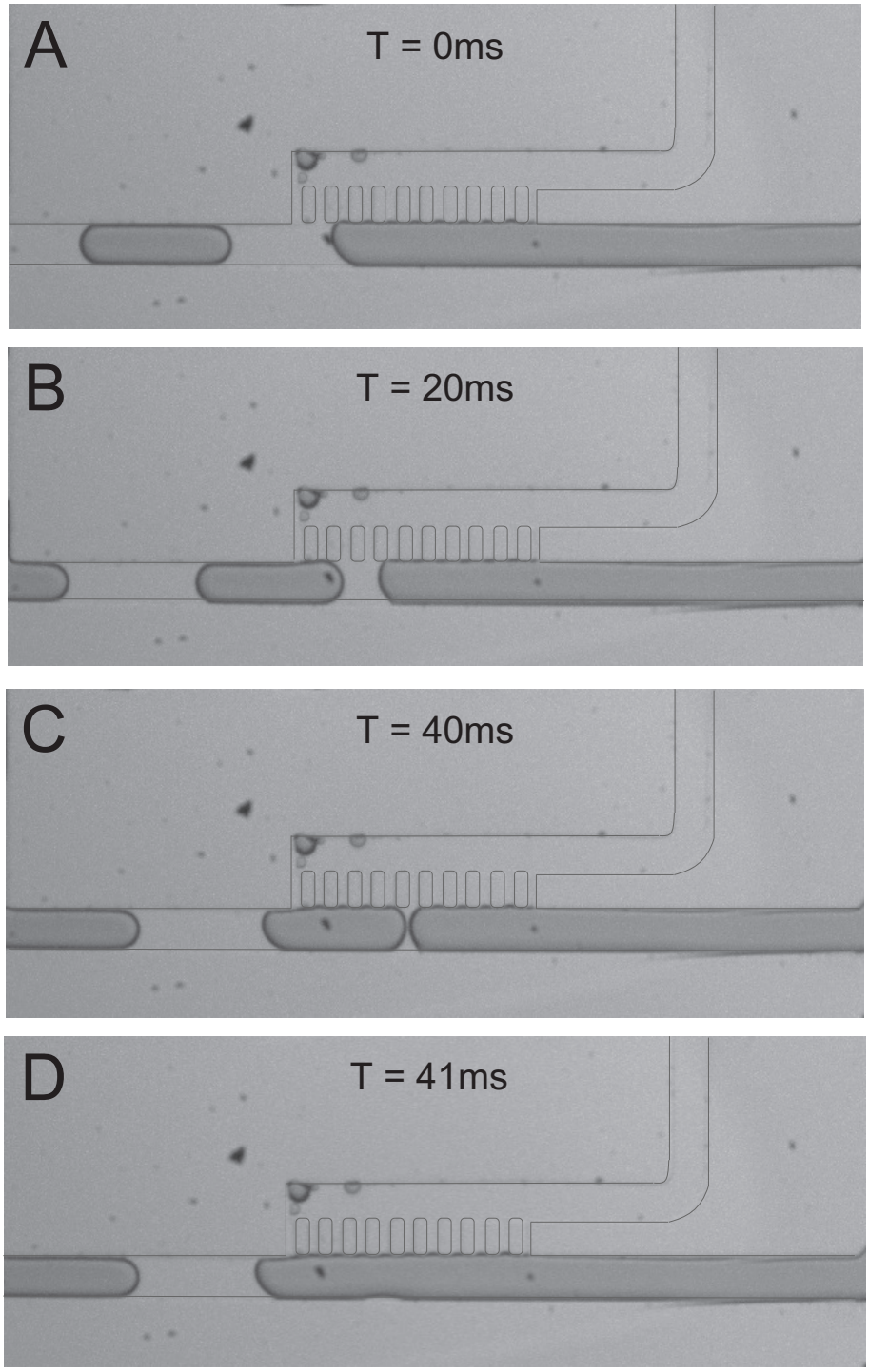


Figure 5.18: Design 1: images from a high speed camera
The chip was videoed using a high speed camera. Channel walls have been outlined for clarity. Frames were cut from a video and show the droplet stream entering left to right. The aqueous droplet phase is dark and the oil phase is transparent. A, B and C are 20 ms apart and D is 1 ms later.

The application of constant suction, at the oil and dialysate outlets, resulted in air bubbles forming in the channels. The air could be pulled from either the FC-40 oil, as FC-40 oil has an oxygen solubility of 15.1 $molm^{-3}$ at 25 °C (183), from the aqueous solution or through the PDMS, which is well known to have a high gas permeability (184). These air bubbles caused many problems by stretching and compressing, resulting in changes to the relative flow rates of the three flows (droplet, oil and aqueous). In this situation the oil and aqueous flows were not separated.

To try and stop air being pulled through the PDMS, I sealed the chip in an epoxy resin glue (Robnor resins, RX771C/NC and Aradur hardener HY1300GB 1:2.5), figure 5.19. The glue did not seal to the tubing used for inlet and outlet connections so once cured I could easily remove and change the tubings when required. However, it was not sufficient and air was still being pulled into the chip. Therefore it was concluded that the air was being drawn from the solutions and a change in design was required.

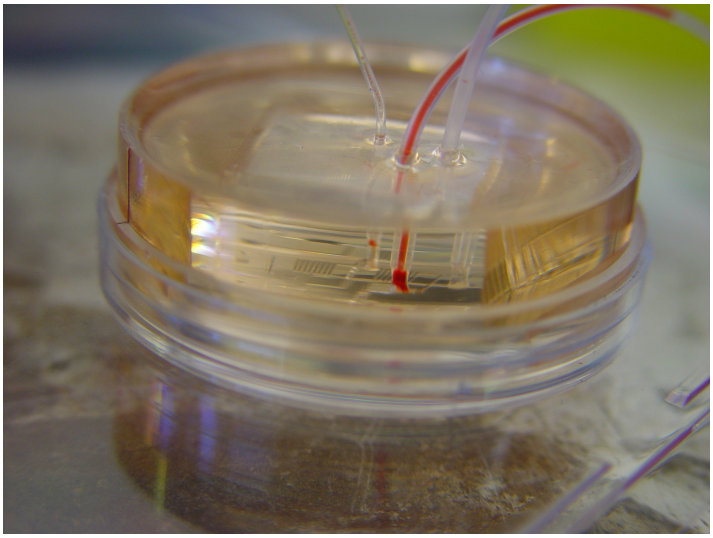


Figure 5.19: A PDMS chip sealed in glue
The objective was to stop air permeating through the PDMS and forming air bubbles in the channel. The PDMS chip was sealed in epoxy glue.

5.6.2 Analysis Chip: Design 2

In response to the problems seen in design 1, a second design was fabricated, figure 5.20. Here, the oil can be filtered through two side channels in either direction, about an analysis chamber. The dialysate droplets coalesce within this chamber, which is 1360 μm x 500 μm. With a wall height of 100 μm the chamber will hold 68 nL of dialysate. The design also contains a T junction to generate droplets on the same chip and a dosing arm, which is discussed later in section 5.9. If any of these channels were unwanted during a specific experiment, then the chip was first flooded with oil and the inlets to the unwanted channels blocked.

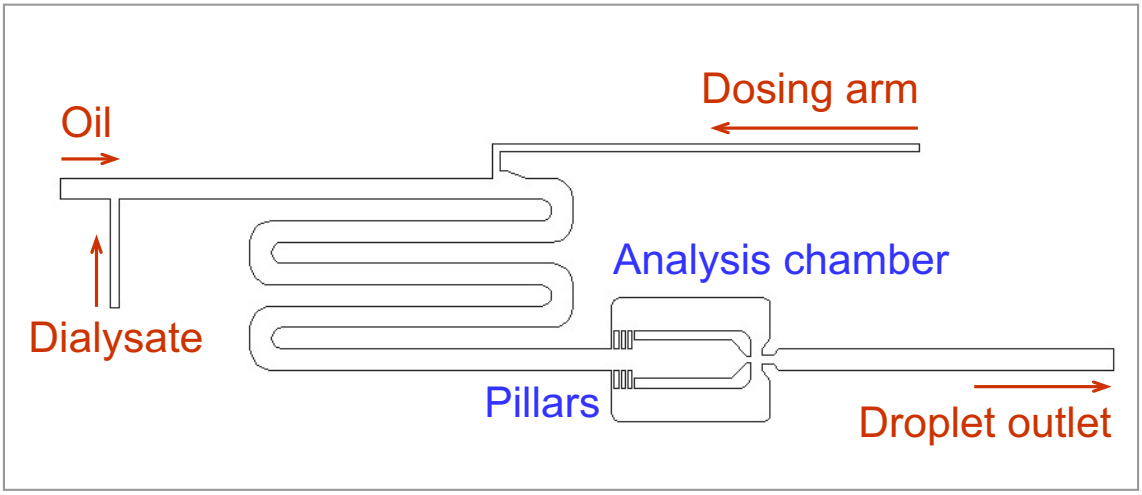


Figure 5.20: Analysis chip design 2
An outline of the mask, which is used to fabricate the analysis chip is depicted. Pillars separate the two phases about an analysis chamber where the electrodes for analysis are placed. The design also contains a T junction for droplet generation and a dosing arm for addition of reactants such as enzyme or calibration solutions of known standards (see section 5.9). Main channel width is 250 μm.

Figure 5.21, shows frames from a high speed video (Video 3 on the associated DVD), in which a droplet enters and emerges from the chamber. The oil phase rejoins the aqueous phase after the chamber and recreates the droplet flow. The aqueous droplets join together in an analysis chamber, which creates a constant aqueous environment with sufficient dimensions to place two integrated needle electrodes. The symmetrical extraction of oil, and the recreation of the droplet flow reduces the formation of disruptive air bubbles. Suction now only needs to be applied to one outlet, rather than two individual outlets as in design 1. Therefore the flow rates do not need to be balanced by the user as the suction applied in design 2 will affect all three flow paths (the oil, the aqueous flow and the droplet flow).

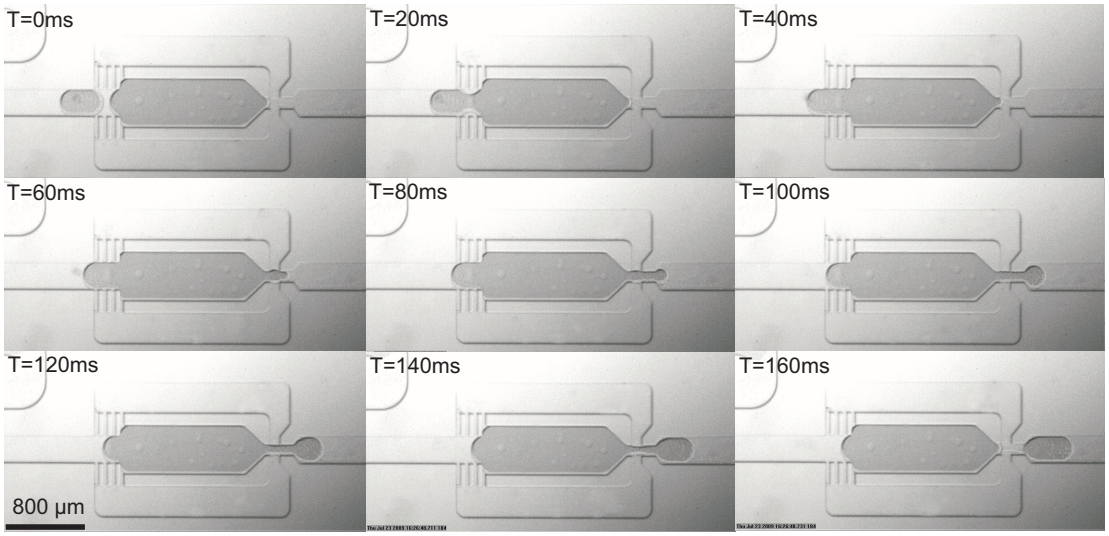


Figure 5.21: Design 2: images from a high speed camera
The frames are cut from a video recorded using a high speed camera and show the progression of a droplet as it passes through the analysis chamber. Each frame is 20 ms apart, the oil is transparent and the water droplets are dark.

5.7 Passive Coalescence

The geometry of the channels and pillars filter out the oil without any moving parts and the separation occurs spontaneously via passive coalescence. The spaces between the pillars are such that they are smaller than the width of the chamber outlet and smaller than the representative droplet diameter. This ensures that the aqueous droplets do not enter the side channel as either a whole droplet or as sister droplets. The incoming droplet flattens against the stationary chamber droplet and the interstitial oil is depleted. The two interfaces interact via Van de Waals forces and the droplets merge. Detail of the coalescence of droplets in design 1 is shown in figure 5.22A and in design 2 in figure 5.22B.

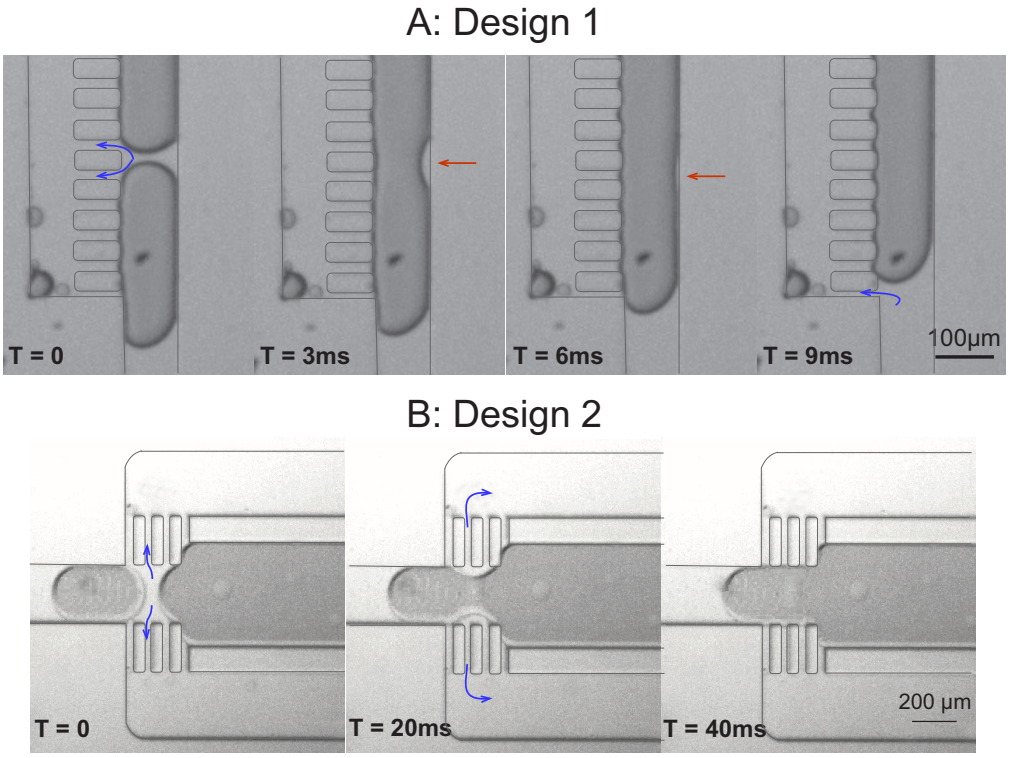


Figure 5.22: Detailed view of droplet coalescence
The frames are cut from a high speed video and the chamber walls have been outlined for clarity. A: shows the progression of a droplet joining the aqueous channel as the oil is filtered into a secondary channel through the pillars in design 1. Each frame is 3 ms apart. Note at 3 ms there is a collection of oil on the side of the droplet furthest from the pillars, which is still seen at 6 ms. B: shows the progression of a droplet joining the aqueous solution within the analysis chamber in design 2. The symmetrical design solves the problem of trapped oil by allowing access to a second side channel.

To investigate the merging of droplets closer, a high speed video was recorded with a frame rate of every 2 ms. Figure 5.23 shows a still from the video. Even at this frame rate it was not enough to capture the coalescence of two droplets, but a hybrid photograph is seen. The frame rate is not fast enough to distinguish either state and shows the droplet both separated and merged with the chamber solution. Bremond et al show a snapshot of two droplets merging together (151). Capturing a frame every 0.1 ms allowed them to see the formation of two nipples in the contact area, after the droplets had flattened against each other and had pulled apart slightly. They speculate that these nipples allow the coalescence to occur.

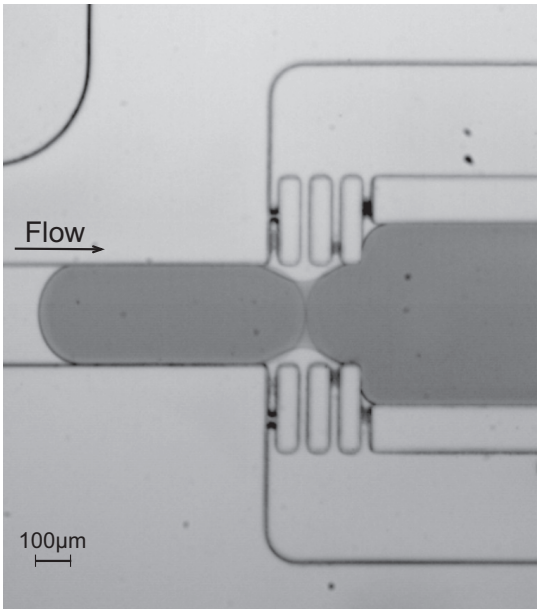


Figure 5.23: A still from a high speed camera showing detailed merging of droplets
Frame rate is 2 ms. The shadow is where the frame rate is not fast enough to catch either state. The image shows both the separated and joined droplets.

5.8 General Running of Analysis Chip Design 2

5.8.1 Flow Rate Optimisation

To look at which flow rates were optimal, the oil flow rate was varied whilst the aqueous flow rate was kept constant at 2 μLmin^{-1}. This altered the size and frequency of the droplets and hence altered the way they interacted at the chamber. Figure 5.24 shows the results. At a distance of 0 μm, the edge of the aqueous solution held within the chamber is in line with the beginning of the wall, as indicated by the orange dotted line. Once a droplet has entered the chamber it stops briefly, whilst the oil between it and the next droplet is removed. At this point a measurement is made from the edge of the chamber solution to the zero line. A positive reading indicates that the chamber is full and the aqueous solution is protruding into the channel, and a negative reading indicates that the chamber is not full enough.

When the oil flow rate is close to the aqueous flow rate there is a great deal of variability in the measurement. Closer inspection of the videos show that the chamber does not function very well. The oil sometimes flows through the chamber, inhibiting the coalescence of the droplets. At very large flow rates the chamber again does not function very well. Here the droplets are too small and they do not join together properly, allowing oil through the chamber. Droplets are seen to bundle together before coalescing. Within the range of 5 to 15 μLmin^{-1}, the chamber works very well, with the spread of reading being much tighter. It is within this range that the oil flow rate should be. The most reliable flow rate is 5 μLmin^{-1}, because the distance is most consistent and close to zero (hence close to the chamber area where the sensors can be placed) and this flow rate was most often used.

5.8.2 Siphoning from the Chamber

The ability to pass the dialysate to rsMD after on-chip analysis, was required to validate the microfluidic system. In design 2 the outlet of the chip cannot be directly connected to rsMD as was initially intended with design 1, as the droplet flow is reformed. Whilst the solution can be collected and allowed to separate into two phases for traditional analysis, online rsMD was still desired. During fabrication a small hole can be punched in the chamber into which tubing can be inserted. If suction is applied at a very slow flow rate (typically < 1 μLmin^{-1}), then an aqueous stream can be formed by drawing out the solution from the chamber. The flow rate must be low, so that the chamber does not become void of aqueous solution. There

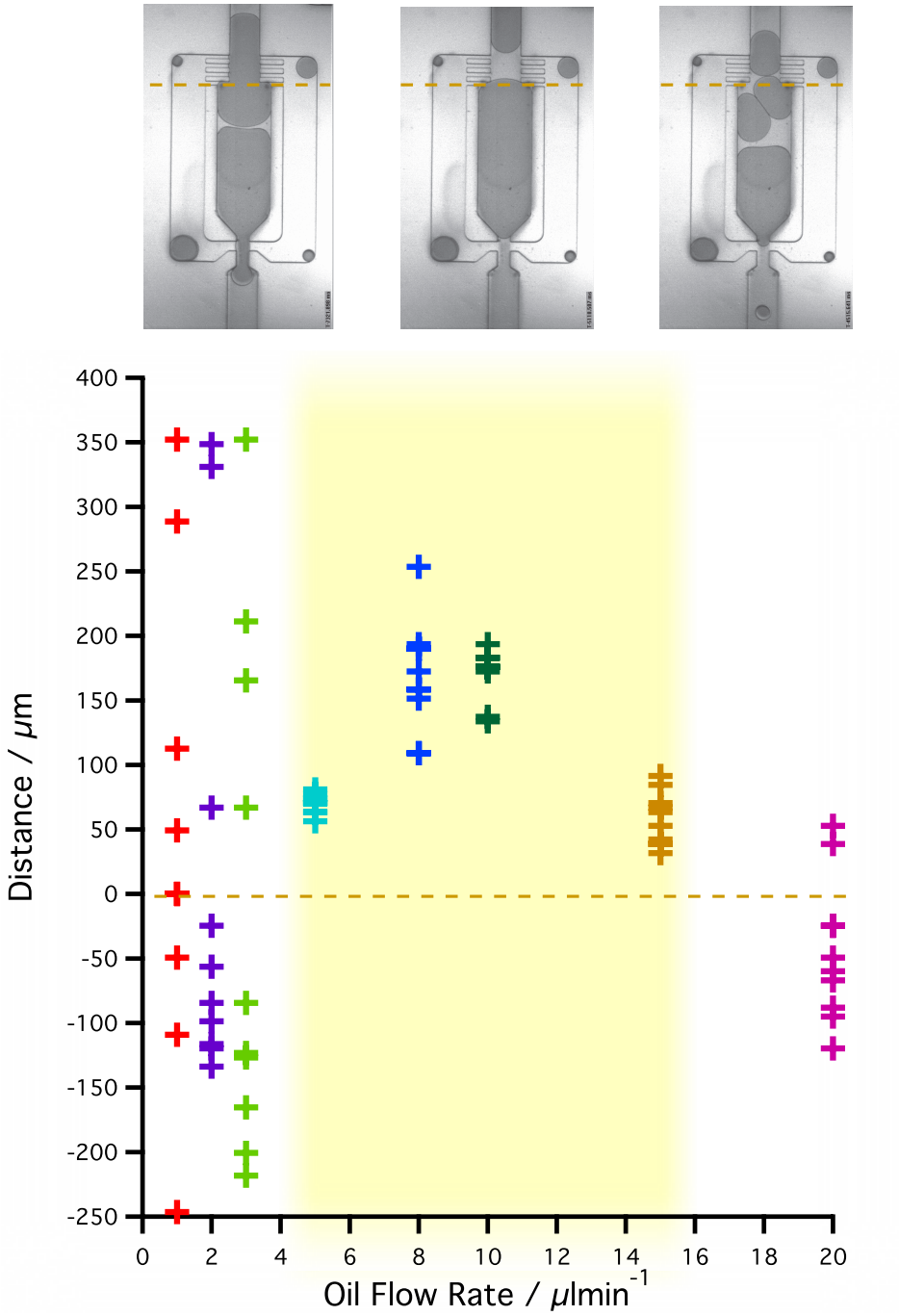


Figure 5.24: Analysis of droplet catching with varying oil flow rates
Aqueous flow rate constant at 2 μLmin^{-1}. Oil flow rate was varied from 1 to 20 μLmin^{-1}. Zero distance is indicated by the dotted orange lines. Chamber droplet size measured from this line when aqueous solution inside was still. A positive distance is towards the pillars and a negative distance is inside the chamber itself. Photographs are stills from high speed videos.

will be some dispersion in the continuous aqueous flow, which is unavoidable, but this may be reduced if the chip was connected to the valve using a small length of low bore connection tubing. Figure 5.25 and Video 4 on the associated DVD, shows the chamber siphoning. The main problems which occurred were ensuring the valve connections were air tight and that the frequency of droplets was such that the chamber did not empty. This was very difficult to do, even with the connection tubing hard-wired into the rsMD machinery. For this reason, this procedure was not employed during the animal and clinical work described in this thesis. However, there is the possibility of optimising this procedure for future work.

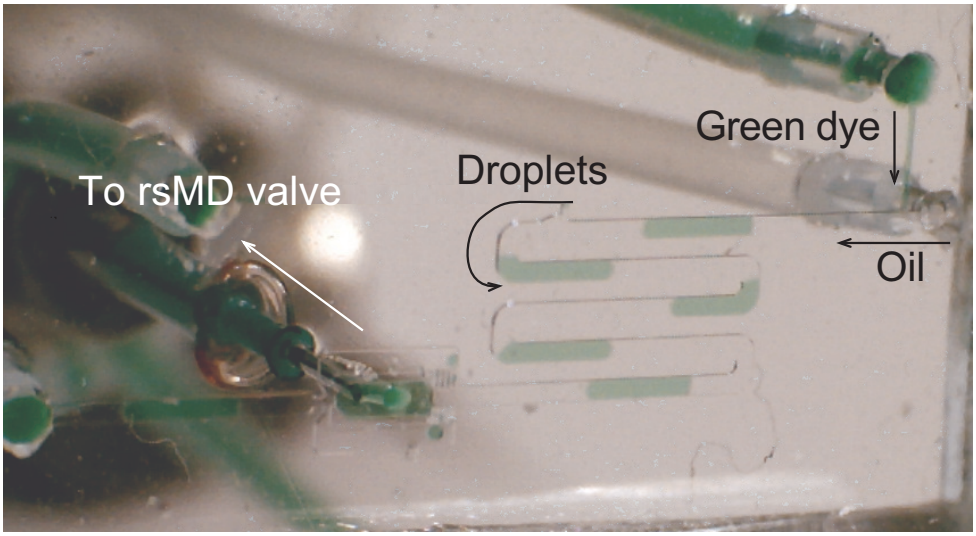


Figure 5.25: Siphoning from the analysis chamber
The still from a video is annotated showing droplets of green food dye being formed using a T junction, passed through a serpentine and then a continuous aqueous stream being pulled from the chamber at a very low flow rate for analysis via rsMD.

5.9 Droplet Dosing

The ability to control and manipulate droplets on-chip led to the idea of dosing droplets. This involves the addition of a known solution to each droplet before analysis. The solution added could be a variety of options, including reagents for reactions, such as enzymes or reaction mediators, or standards for calibrating on-chip sensors. The addition of reagents is an important aspect of chemical and biological analysis. Reliable and precise addition is difficult and many designs have been postulated in the literature. Two designs were tested in this thesis: a T junction and a specially designed side arm channel.

5.9.1 Dosing using a T junction

Instead of flowing oil through the main channel and segmenting an aqueous flow, the T junction can be used to add an amount of solution to a passing droplet stream. A droplet stream is pushed through the oil channel and the dosing solution is pushed through the perpendicular channel. This is shown in figure 5.26 and Video 5 on the associated DVD. Here, coloured dye has been added to water to demonstrate the addition. Yellow droplets are entering from right to left and blue water is added to each droplet as it passes, turning it green.

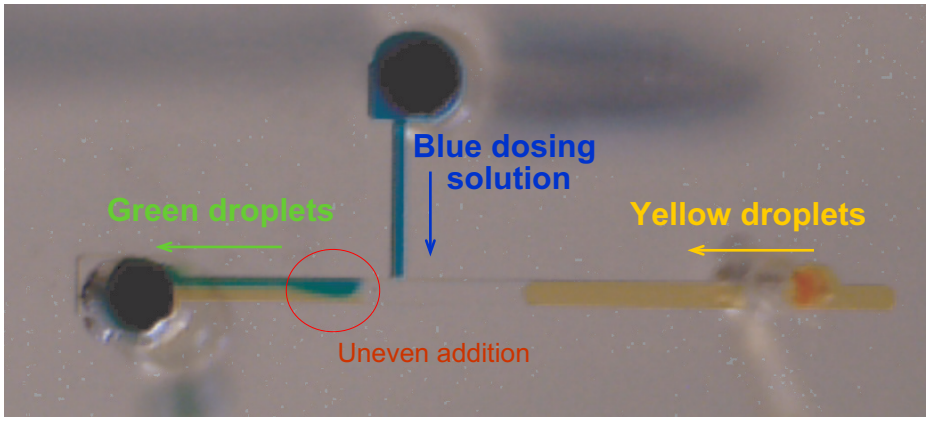


Figure 5.26: Droplet dosing using a T junction
Yellow droplets have already been generated (aqueous 2 and oil 5 μLmin^{-1}) and are being pushed through the oil channel of the T junction. Continuous blue solution is being pumped in the perpendicular channel (0.5 μLmin^{-1}). Green droplets are created due to the addition of the blue solution to the yellow droplets.

Dosing using a T junction was first reported by Henkel et al (185). Addition of reagents via a T junction is said to be efficient as it forces the solution around a sharp bend. This causes a directional change in flow, giving rise to a perpendicular secondary flow that improves mixing of the two solutions (186, 187). However, these reports are within continuous flows. Within the droplet literature, it is reported that there asymmetric shear stresses at the inlet boundary disrupting the dosing (154, 188, 189). This is seen in figure 5.26 where the blue solution is not evenly added to the yellow droplets. That is, the blue solution is added as a thin layer to the yellow droplet until the end of the droplet where a larger volume is added. Whilst, there are ways to thoroughly mix the droplets through design, such as serpentines, the uneven addition may give rise to an error in the volume of blue solution added. Synchronisation was also problematic with extra droplets being formed in between the incoming droplet stream. This too has also been widely reported (185, 188, 190). Therefore the geometry of the chip was altered and a specifically designed side arm was introduced.

5.9.2 Dosing using a Side Arm

A side channel was included in the design of the analysis chip (seen in design 2, figure 5.20). The junction where the dosing arm joins the droplet channel has been altered from a T junction to include room for the incoming solution to expand into. This is displayed in more detail in figure 5.27 and Video 6 on the associated DVD.

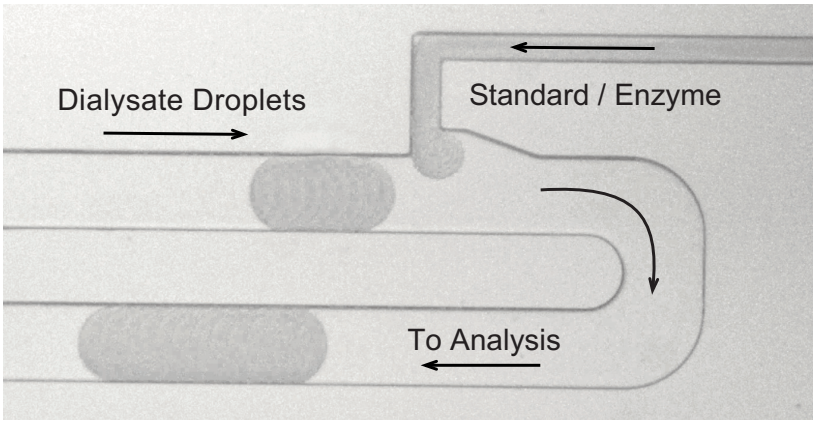


Figure 5.27: Droplet dosing using a side arm
A still from a video showing a solution which is added to each droplet as its passes the side arm. The solution could be enzymes, to analyse the contents of the droplets or standards to calibrate the system at specific time points. The flow rate of the oil was 30 μLmin^{-1}, the aqueous solution was 5 μLmin^{-1} and the dosing solution was 0.5 μLmin^{-1}.

The coalescence of the dosing solution and the droplet is spontaneous and the graph in figure 5.28 shows the mean length of the droplet before the dosing channel and after the dosing channel by analysis of the high speed video in ImageJ (n=4). The volume of each droplet before dosing is approximately 5 nL and the additional volume from the dosing channel is approximately 3.6 nL.

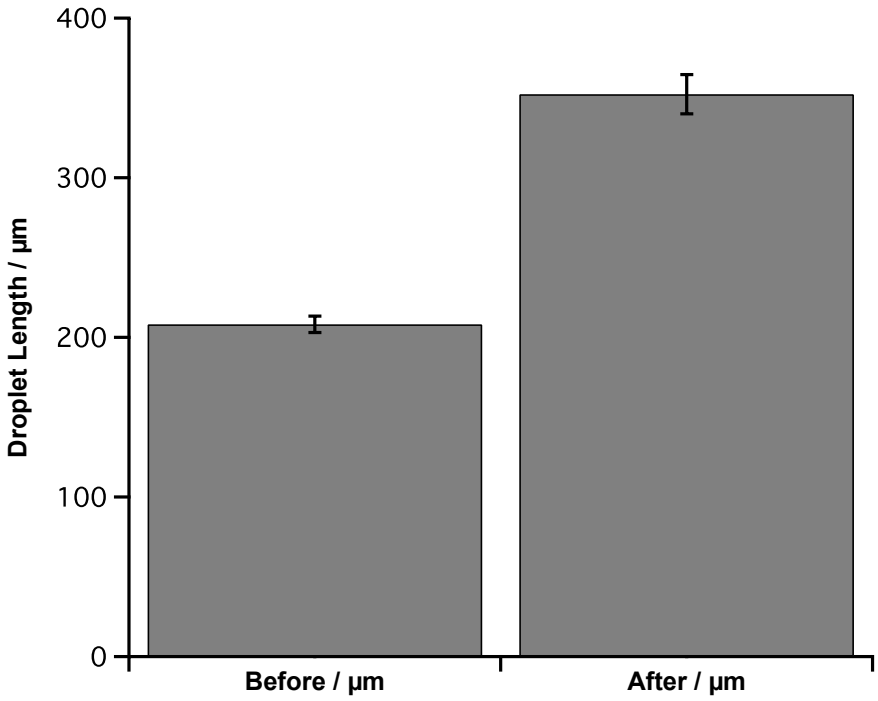


Figure 5.28: Droplet lengths before and after dosing addition
This graph displays the length of the droplets before and after an addition. The flow rate of the oil was 30 μLmin^{-1}, the aqueous solution was 5 μLmin^{-1} and the dosing solution was 0.5 μLmin^{-1}. The length of the droplets were measured in ImageJ. The mean length is shown with standard deviation error bars; n=4.

The %RSD of droplet length before addition was calculated to be 2.46% and after addition to be 3.49%. This will include some error in the measurement of length, which was calculated directly from the video using ImageJ. The dosing of the droplets has increased the error, however the %RSD value is still low.

Instead of joining the main channel at right angles, the perpendicular dosing arm has a ramp on the downstream wall. This angle creates room for the dosing solution to expand into and avoid a pressure build-up as it will no longer occupy the full channel width. The idea of allowing the dosing solution more room to expand has also been seen in the literature, however a different design was used (188). This creates an addition that is evenly spread through the droplet, as seen in figure 5.29. It also reduces the possibility of extra droplets forming (188) as it delays the forward motion of the dosing solution. A serpentine was included to mix the droplets thoroughly by chaotic advection before analysis within the chamber.

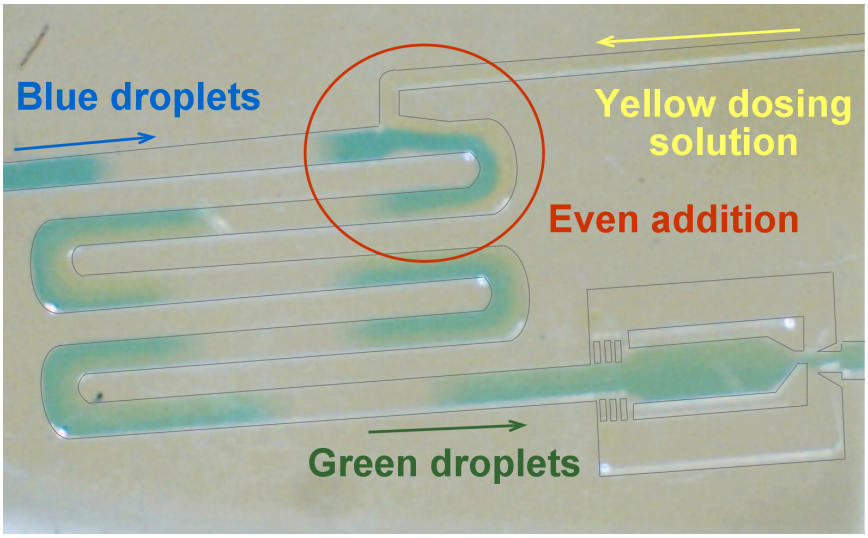


Figure 5.29: Droplet dosing using a side arm
Blue droplets have already been generated (aqueous 2 μLmin^{-1} and oil 8 μLmin^{-1}) and are being pushed through the main channel. Continuous yellow solution is being pumped into the perpendicular channel (1 μLmin^{-1}). Green droplets are created.

Droplet dosing has the possibility of allowing for a primitive form of self calibration, which is required for all clinical instrumentation. A standard could be added to the droplets to calibrate the sensors. This could be automated to occur every few hours so that the performance of the sensor can be tracked during the course of monitoring and any changes in sensor sensitivity can be accounted for in analysis.

5.9.3 Size of Droplets and Mixing

During preliminary investigations a coloured food dye was often added to the water to watch the droplet dosing more easily. After the junction where the dosing channel meets the main droplet channel, a serpentine (An S shaped channel) was employed. The serpentine passively stretches and folds small droplets, which yields chaotic mixing in an otherwise laminar flow. Using food dye to visualise the droplets, it was discovered that if the droplets were too large, then the serpentine was not sufficient for total mixing. Here, mixing occurs upon diffusion alone, and the mixing time scales are therefore very long. This is seen clearly in figure 5.30 where the two solutions remain distinct within the droplet even when within the analysis chamber.

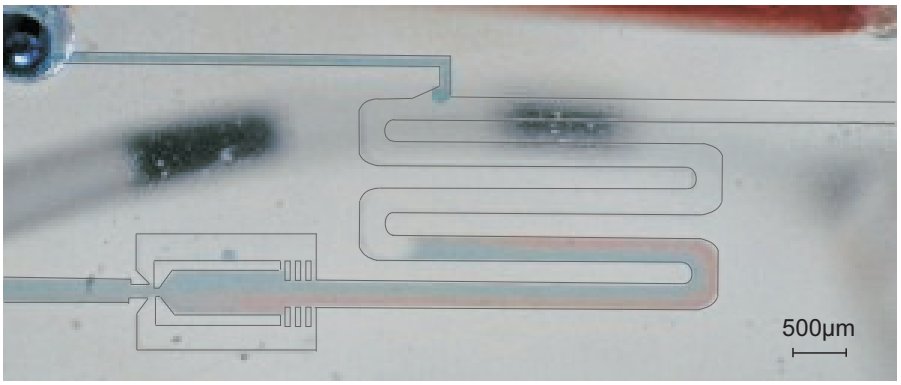


Figure 5.30: Mixing in a large droplet
This photograph shows a droplet stream of coloured water and FC-40 oil (2 μLmin^{-1} and 5 μLmin^{-1} respectively). The T junction used to generate droplets is just out of shot, top right. Red droplets are made at the T junction. Blue water is added to the droplet using a dosing arm (1 μLmin^{-1}). Due to the long length of the droplet there is not sufficient mixing and the two colours remain separate in the droplet. At the analysis chamber, the two colours are still distinct.

In the literature there are many accounts of thorough and rapid mixing in smaller droplets and many report using serpentines. In a straight channel there is convection in each half of the droplet. However, in a serpentine channel, the two halves are reorientated and striations occur, promoting mixing. This is due to chaotic advection which repeatedly stretches and folds the droplets. This is seen in figure 5.31, which is taken from (191). Therefore, if this technique were to be integrated into the clinical system for automated additions of calibration standards, then the system must take droplet length into account and be designed accordingly.

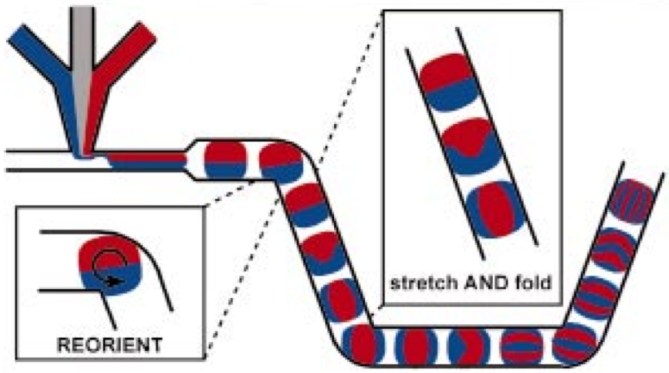


Figure 5.31: Mixing in small droplets in a serpentine
This figure is taken from (191). Mixing by chaotic advection is shown. As a droplet passes through a winding channel it is stretched and folded as it is reorientated. This facilitates diffusion and thoroughly mixes the contents of the droplet.

5.9.4 Addition of Enzyme Solutions

Another way of using the dosing capabilities of microfluidics is to dose in enzyme solutions. The serpentine would thoroughly mix the enzyme with the dialysate. This could allow for an exhaustive reaction between the substrate and the enzyme, provided that the channel length is such as to allow for a complete reaction between enzyme and substrate. This may increase the sensitivity of the sensors. The first attempt is shown in figure 5.32. 1 mM glucose droplets were made at a T junction with FC-40 oil at 2 μLmin^{-1} and 5 μLmin^{-1} respectively. The droplets were passed to the analysis chip which had a dosing channel filled with 4 U/ml GOx. Within the analysis chamber was a 125 μm platinum electrode with external reference and auxiliary electrodes. The flow in the dosing channel was initially off until a baseline current was recorded. The dosing flow was turned then on at a flow rate of 2 μLmin^{-1}.

The change in current seen as enzyme-dosed-droplets pass, is much larger than that seen using a glucose biosensor on the same size electrode. As the flow rates of the glucose and the enzyme solutions were set to the same (2 μLmin^{-1}), each droplet contained 0.5 mM glucose and 2 U/mL of GOx. This gives rise to a sensitivity of 4.9 x 10^5 nAmM^{-1}cm^{-2}, higher than that seen using a disc electrode (see table 4.7 for reference). However, the effect did not last long as the droplets containing the enzyme started sticking to the surface of the channels as shown in figure 5.33. Note, that when only buffers are used during dosing, this effect is not seen. However, once the enzyme is added, the aqueous solution wets the PDMS surface.

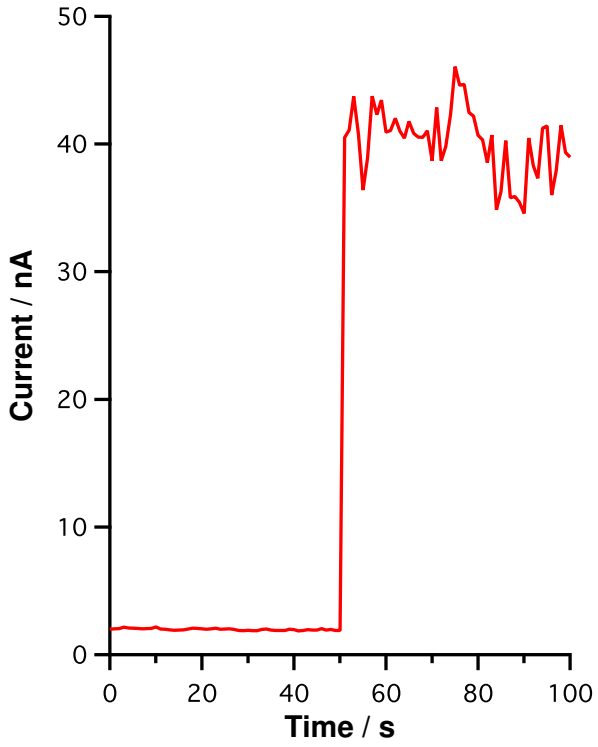


Figure 5.32: Droplet dosing: addition of GOx
Droplets of 1 mM glucose were run through the analysis chip. Current from a 125 μm Pt disc electrode with external reference and auxiliary electrodes, placed in the analysis chamber, was recorded. GOx (40 mg dissolved in 10 mL aCSF) was added by turning on the flow in a dosing channel. Flow rates were 5 μLmin^{-1}, 2 μLmin^{-1} and 2 μLmin^{-1} for FC-40 oil, glucose and GOx respectively.

Once the PDMS surface was covered with aqueous solution, droplets no longer formed. The chips were rinsed with distilled water and the experiment was repeated. To get a baseline 1 mM glucose droplets were run without the enzyme dosing. It was noticed that the baseline had shifted upwards and fluctuations were occurring, figure 5.34A. Using the USB microscope linked to the Chart (ADI) recording software, the timings of these fluctuations in current were investigated. When a glucose droplet enters the chamber the current increases. Once the droplet has passed the current falls. It is most likely to be that some enzyme has stuck to the PDMS during the previous experiment. As the glucose droplets pass through the channels, there is some reaction, forming hydrogen peroxide, which is detected at the electrode.

Figure 5.34B is a zoom of the baseline in figure 5.32, which it at the very beginning of the experiment before any enzyme had been perfused through the chip. The fluctuations are not seen here. In general, the movement of the dialysate through

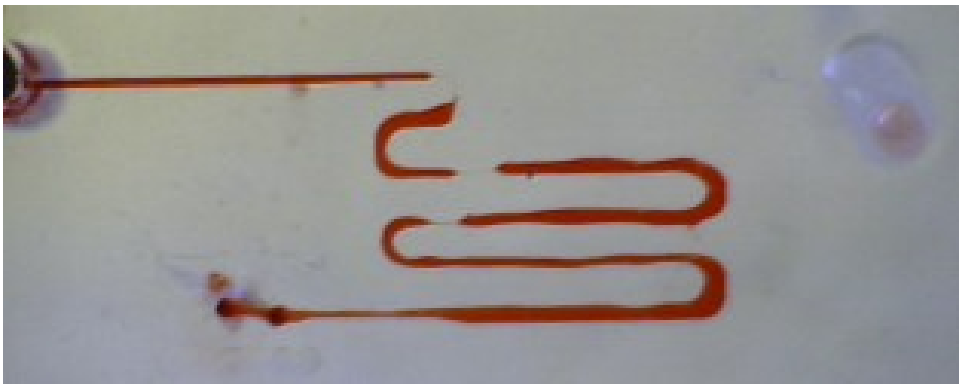


Figure 5.33: Enzyme dosed glucose droplets sticking to the channel surface
Droplets of 1 mM glucose were dosed with GOx solution dyed red with food dye. After one droplet passed, subsequent droplets wet the PDMS channel surface.

the chamber is not seen by the electrode, and hence it can be concluded that the enzyme is stuck somewhere within the channels.

The concentration of the enzyme in the dosing solution was initially high, and to try and reduce the amount of enzyme sticking to the PDMS channels, the concentration was reduced to 1 U/mL. However the same problem of the enzyme sticking to the channel surface still occurred and disrupted the droplet structure.

To try and stop the enzyme sticking to the PDMS, the channels were treated with Duxback. Duxback makes the surface super-hydrophobic. A small amount of Duxback was injected through the channels and the chip was heated on a hot plate at 80 °C for 5 minutes to evaporate the solution. The chip was then primed with oil before the experiment. A poly(phenol) coated 125μm diameter disc electrode was placed in the chamber on a Duxback treated chip. 1 mM glucose droplets were continuously generated (Glucose flow rate was 2 μLmin^{-1}, FC-40 flow rate was 4 μLmin^{-1}) and pushed through the chip. The pump containing the enzyme syringe was turned off and on (at a flow rate of 2 μLmin^{-1}) to dose the droplets with 1 U/mL GOx.

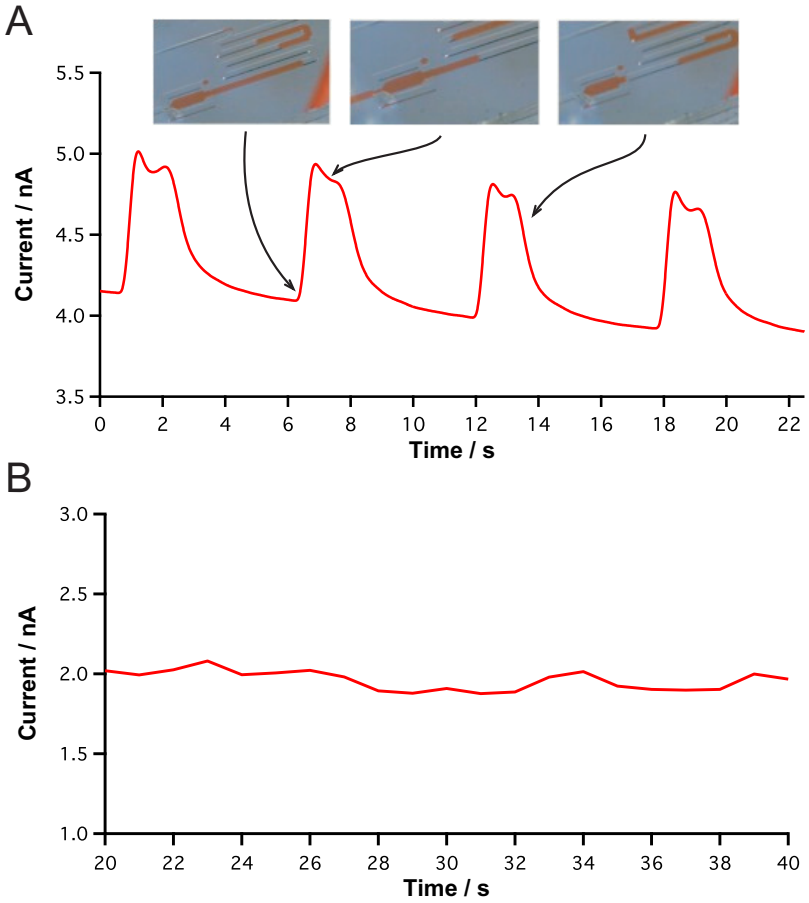


Figure 5.34: Glucose droplet baseline

A: Droplets of 1 mM glucose were pumped over a previously used chip. Fluctuations in baseline are shown using a 125 μm Pt disc electrode placed in the analysis chamber. B: Baseline from figure 5.32 shown in detail and on the same scale as A.

The result is shown in figure 5.35. Whilst this worked for a while, the effect was not long lasting and eventually the enzyme attached to the surface of the PDMS and disrupted the droplet flow as before.

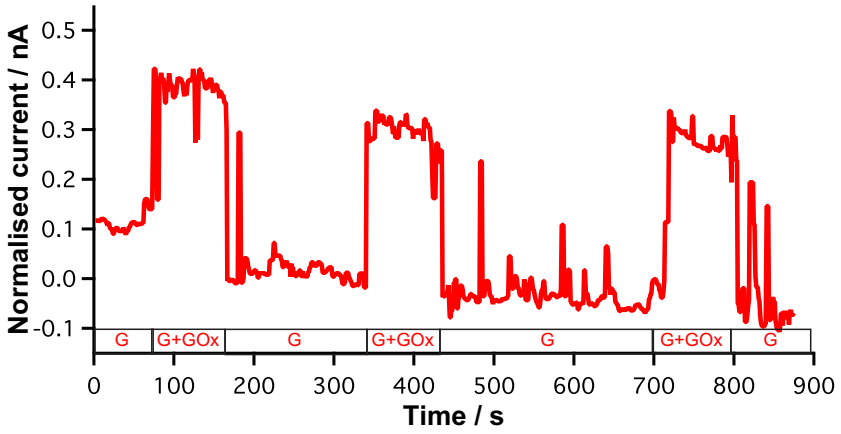


Figure 5.35: Glucose droplets dosed with GOx on a Duxback treated chip
1 mM droplets were flowing through the chip throughout the whole experiment (denoted G). The glucose droplets were dosed with GOx and the current increased (denoted G+GOx). The electrode is a 125 μm poly(phenol) coated electrode.

It is possible that this method could produce a sensitive assay, however the properties of the enzyme, the PDMS, and the oil surfactant need to be thoroughly investigated and optimised. Leach et al used a 1 % solution of bovine albumin for one hour prior to enzyme measurements, to reduce enzyme adhesion to the PDMS channels (192); it would be possible to investigate these methods for future work.

5.10 Clinical Safety

For the application of digital microfluidics into a clinical environment, the system must be fool-proof and safe at all times. The oil was of great concern, as a reversal of flow would push the oil towards the patient. This could cause non-sterile fluid to enter the patient and increase risk of infection and adverse effects. To make the system safe, the oil was sucked throughout the whole system from an open bottle placed lower than the head of the patient, using a syringe pump placed after the analysis chip. This way if any pump failed or if there is a blockage at any point throughout the system then the easiest path for the fluid to flow is to the open bottle and not back through the MD probe. See figure 5.36. Using suction at the end of the system also reduces the back pressure on the microdialysis probe compared to conventional microdialysis.

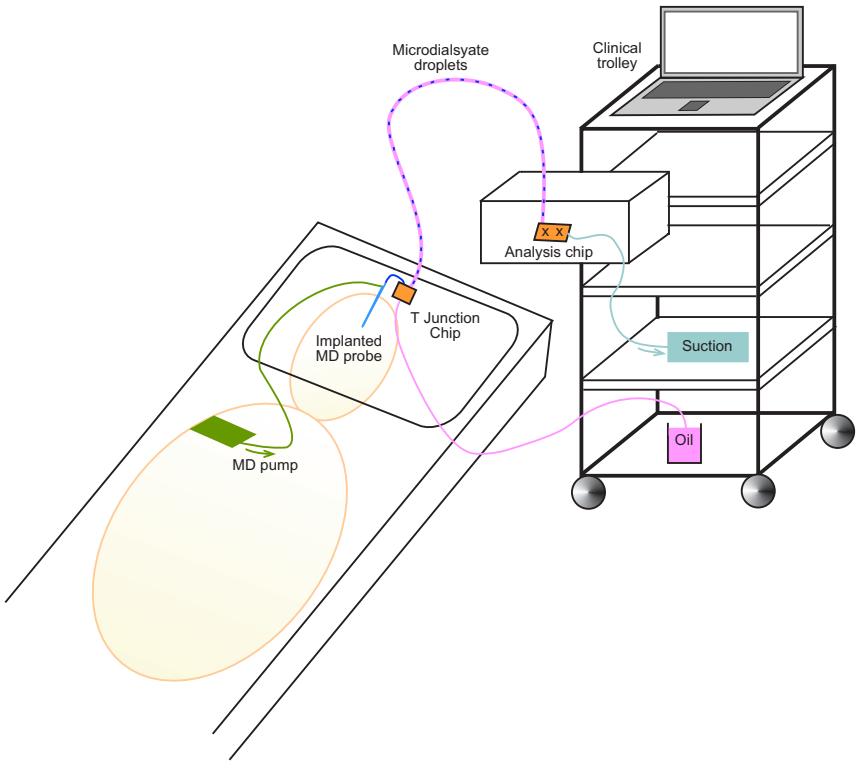


Figure 5.36: Schematic of clinical microfluidics
Schematic showing the setup for use of microfluidics on a clinical ward. The oil is in an open beaker placed below the head of the patient. The oil is pulled through the system by suction from a syringe pump placed on the clinical trolley. The dialysate is pushed through the system using a small microdialysis pump attached to the patient.

5.11 Conclusion

To miniaturise the clinical system and create a low volume flow cell to house electrodes, microfabrication was used. This led to the development of a microfluidic tool kit for microdialysis users. It was decided that digital microfluidics would significantly improve the clinical system by eliminating Taylor dispersion and reducing the time lag of transferring the sample of dialysate from the brain to analysis, a problem for all microdialysis users.

A T junction was fabricated, to high quality, to produce a robust and precise method of droplet generation. Optical methods were used to investigate the properties and the manipulation of droplets. Droplet frequency, length and volume can be altered by varying the channel geometry, the relative flow rates and the surface tension. The compatibility of digital microfluidics and microdialysis was tested using an animal MD probe. Recovery of fluorescein was evaluated using LIF. Surprising results were found, with higher recoveries in droplet flow when the outlet of the probe is connected directly onto the T junction. This was investigated further, using microPIV, with the result that the stop-start motion at the T junction changed the flow of dialysate at the semi-permeable membrane. This may have a consequence when combining the MD membrane and droplet generation into one device. However, for the purposes of clinical microdialysis, where the clinical probe has a long outlet, this has little consequence.

Once droplets of dialysate were reproducibly created, a method of analysing the droplets contents with biosensors was required. The evolution of an analysis chip, designed to be situated away from the patient, with two designs for electrode placement, was discussed. Although design one successfully separated the oil and dialysate into two separate channels using suction, the system was inherently high pressure and the balance of flow rates was hard to fine-tune. Separation did not occur if the system was unbalanced at any point. As well as unsuccessful separation, the high pressure also pulled air through the PDMS and air bubbles formed in the channels, creating further problems. These bubbles blocked the flow and caused difficulties, due the ability of air to stretch and compress. The second design, with a symmetrical separation, was therefore developed. To maintain balanced pressures, the droplet flow was recreated, after an analysis chamber. The oil was filtered into two side channels about the chamber, which was designed to house needle electrodes for analysis. Optimal flow rates were discussed, as well as the collection of droplets for traditional analysis. The creation of a continuous aqueous flow via slow suction from the chamber is preferable, as this allows for comparison of results against rsMD.

This however, needs to be hard-wired into the system and at present it too is prone to air being drawn through the system.

Droplet dosing was investigated by the use of a T junction and a dosing side channel. A serpentine was included in the analysis chip design to mix the droplets after an addition from this side channel. This could be used as a form of self-calibration in the hospital, by standard additions of substrates. However, it was difficult to synchronise the flow from the dosing arm and the incoming droplet flow. Addition of enzymes was also investigated, however further problems of surface wetting occurred, which disrupted the droplet form. This has been successfully reported in the literature and so a more thorough investigation is required. Possible parameters to look at are; the properties and concentration of the enzyme solution, the PDMS surface hydrophobicity and the use of a surfactant to balance the change in surface tension, which the enzyme may introduce.

Clinical safety is utmost and a method of incorporating and running the digital microfluidic tool kit in a fail-safe mode, with no danger to the patient, was described. The system is now ready to incorporate electrodes and biosensors for on-chip analysis of dialysate.

Chapter 6

On-Chip Sensors

6.1 Introduction

This chapter brings together the electrodes from chapter 3, the biosensors from chapter 4 and the microfluidic platform from chapter 5. Here the optimisation of the placement of the electrodes and biosensors within the analysis chamber will be discussed and the characterisation of biosensors on-chip is shown.

6.1.1 Optical Analysis on Microfluidic Chips

The most popular analysis technique of multiphase flow is LIF (171). In LIF, low optical path length is compensated for by high intensity illumination and the high sensitivity detection, possible as the excitation and detection wavelengths differ. Whilst there are many research applications in which LIF is appropriate, it is not technically possible in many situations, such as online detection on a clinical ward or on a wearable device. There have been reports of incorporating optical fibres and LED light source to miniaturise the device (193, 194) with analysis via colorimetric enzyme assays (195, 196). However, the use of external bulk optics is still seen to be preferable.

6.1.2 Electrodes in Microfluidic Chips

Electrochemical microelectrodes are an attractive alternative to optical methods, due to their high sensitivity, small size, low noise and simple electronics. Electrodes were originally assembled into channel electrodes where the fluid path was defined using a gasket. Consideration of the convective-diffusion equation for these systems allowed initially analytical descriptions (see (197, 198) for reviews) and more recently

numerical descriptions (198, 199) of common electrochemical techniques coupled to homogeneous solution reactions. The use of fast flow rates and the fabrication of microelectrodes by microlithographic techniques, allowed the development of flow cells to study ultra-fast kinetics (200, 201).

The advancement of microlithographic techniques allowed the construction of microelectrodes in channels, in either band or array (202) formations. Recently developments in the fabrication of microchannels, has allowed flexible control over both the electrode size and channel dimensions and the possibility of miniaturisation of systems for lower flow velocities. Flow profiles within such microchannels have been simulated (203). Theoretical descriptions for a microelectrode array placed in a flow channel under steady state conditions for flow and concentration, have been used to analyse the effects of flow on coupling between electrodes (204) and to determine the flow profile (205). An analysis of the temporal response of a microband electrode placed in the inlet of a channel has been used to determine the dimensions of the microchannel (206). Reports of microelectrodes analysing multiphase flows are few. One report analyses electrochemical processes at a continuous flowing phase boundary (207), but others concentrate on incorporating electrodes for manipulation of droplets (157), electroporation (208), enzyme kinetics (209) and electrophoretic separations (210) rather than analysis.

A major problem for the chemical analysis of droplets is that the carrier oil can coat the electrode surface, thus degrading the interface between the electrode and the droplet sample. To solve this difficulty, we have created a droplet coalescence chamber, into which only the aqueous phase enters. This was described in chapter 5.

6.1.3 Mass Transport and Diffusion Layers

Different positions of the electrode in relation to the channel ceiling affects the CV because diffusion to the electrode surface becomes inhibited and the diffusion fields become altered.

Kinetics of an electrochemical reaction at an electrode surface depend upon the diffusion of the reactants to the surface and diffusion of the products away as both determine the surface concentrations. If the electrode is flush to the top wall of a channel, the diffusion layers are determined by the electrode shape and size as well as the geometry of the flow cell. When the electrode is recessed, the walls will also affect the diffusion to and from the electrode surface. Therefore a relationship exists

between the relative sizes of the electrode and the height of the chamber walls, which effects the electrode diffusion layer.

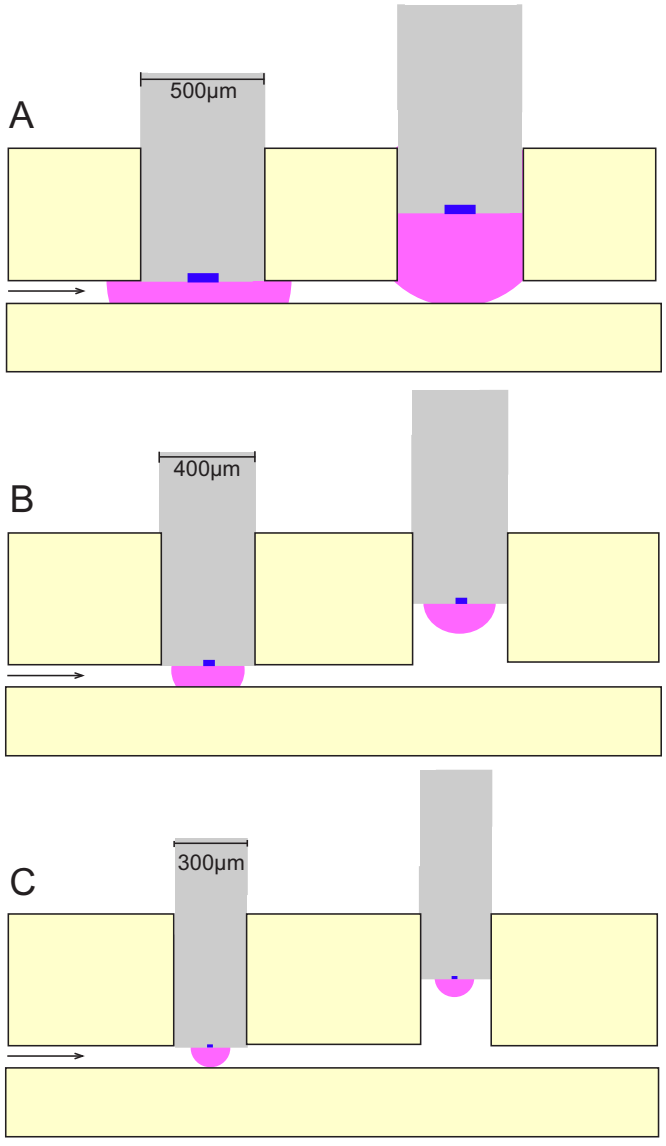


Figure 6.1: Schematic of electrode diffusion fields on-chip
A: 125 μm in a 25G needle, B: 50 μm electrode in a 27G needle, C: 25 μm in a 30G needle. Arrow represents fluid path. Disc electrode indicated in blue. Relative size of diffusion field shown in pink, taken as 5 times the radius (211). Channel height 100 μm.

Figure 6.1 shows a schematic of different electrode sizes placed on-chip in two positions, flush to the ceiling and recessed. The sizes are in the correct scale and the channel height is 100 μm. Figure 6.1A indicates the diffusion field for a 125 μm disc electrode in a 25G needle. The diffusion field is clearly affected in both positions. Figure 6.1B shows the diffusion field for a 50 μm disc electrode in a 27G needle.

When placed flush with the ceiling the diffusion field is inhibited by the floor of the channel. When recessed the diffusion field looks unaffected, however the analyte has to diffuse up towards the electrode before reaching the diffusion field. Also, it is unlikely that the electrode will sit in the middle of the electrode and therefore is likely to be affected by the walls. Figure 6.1C indicates the diffusion field of a 25 μm disc electrode in a 30G needle. In both positions the diffusion field seems unaffected. However when recessed the performance of the electrode will be affected due to the reason just stated. In theory, the best electrode to place on-chip, is the 25 μm electrode, flush to the ceiling. However, using this size to fabricate biosensors with a good performance is much harder.

This chapter will now discuss the placement of needle electrodes on-chip, firstly by investigating electrode performance using cyclic voltammetry. The effect of segmenting the aqueous flow upon the signal seen at the electrode is discussed. Optimal placement of the electrodes along the length of the chamber, at a height relative to the chamber ceiling and for the case of dual electrodes, the orientation to the direction of flow is also assessed. Finally, biosensors were placed on-chip and calibrated. Experiments assess the viability of the sensors for monitoring dynamic changes seen in the brain.

6.2 Electrochemistry in Digital Microfluidics

The placement of the electrodes on-chip can make a lot of difference to the response seen. It very quickly became apparent that if the electrode holes were punched too close to the walls of the chamber then problems would occur with the chip design. It is very tricky to punch the holes correctly; the most common mistake was holes being punched over the wall of the chamber leading to an opening into the oil side channels. The electrode constructs are very large and rigid, compared to the PDMS chamber, so if the holes are punched too close to the exit of the chamber, the electrodes can distort the design by deforming the PDMS. This opened up the exit of the chamber and the chamber could no longer filter the oil out into side channels. An example of each of these problems is shown in figure 6.2. To avoid the deformation of the PDMS chip design, the holes for the needle electrodes were punched towards the pillars, avoiding the exit of the chamber.

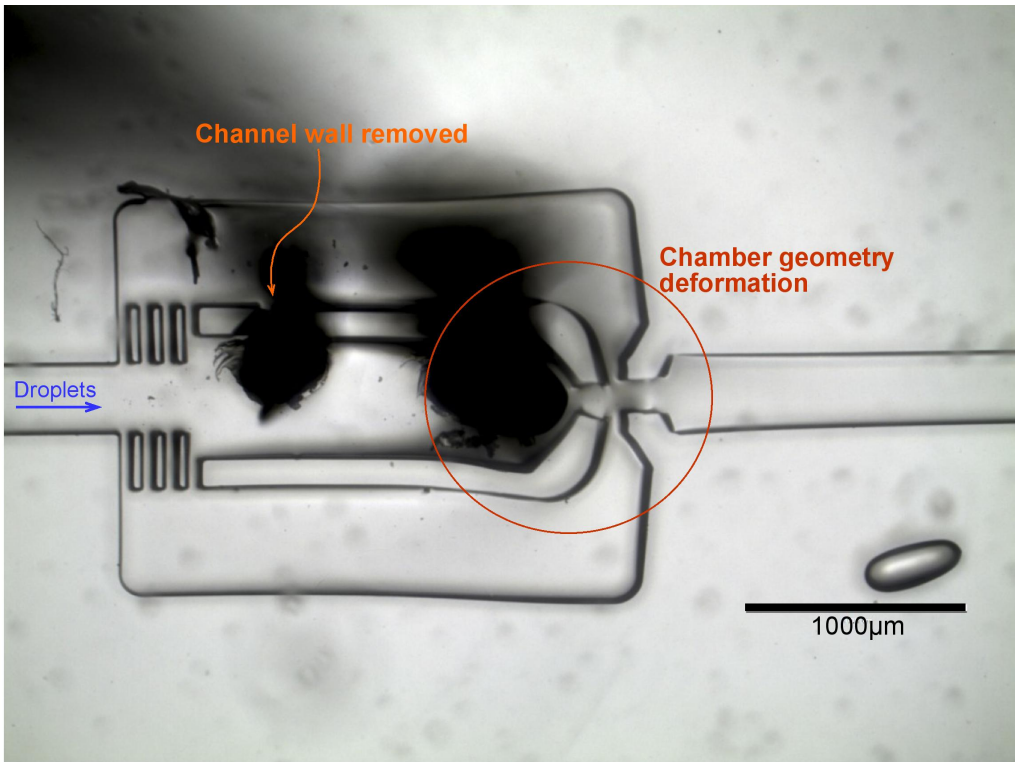


Figure 6.2: Photograph of electrode placement affecting chamber design
There are two holes for electrodes. The left-hand side electrode hole is punched over the chamber wall creating a path between the chamber and the side channel. The right-hand side electrode clearly deforms the chamber design. If droplets were run through this chip the design would not catch the droplets within the chamber.

The first validation of the sensors in segmented flows was conducted using electrochemistry and standard redox couples, RuHex and Fc. The sensors were placed on-chip (figure 6.3) through which the redox species were perfused, and the applied potential scanned to produced a CV. From this trace any problems with the chip and the sensors can be determined.

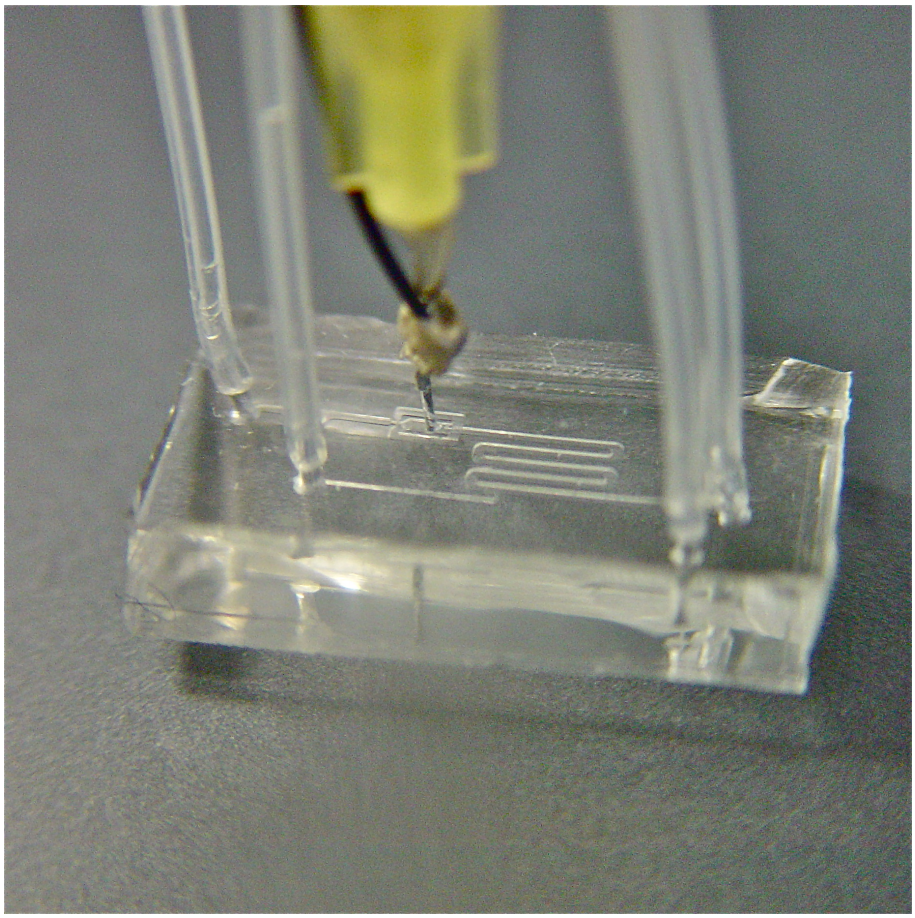


Figure 6.3: Photograph of a needle electrode placed on-chip
The 300 μm tip of the integrated needle sits in the collection chamber of the analysis chip design 2. This one needle contains a 25 μm platinum working, 50 μm Ag|AgCl reference electrode. The stainless steel shaft is used as the auxiliary. The PDMS chip is approximately 2 cm across.

Figure 6.4 compares the CVs using 125 μm and 50 μm disc electrodes under three conditions: in a beaker, on-chip in continuous flow and on-chip in droplet flow. The limiting currents of both sized electrodes, in a beaker, indicate that the geometry of the electrode is hemispherical (as discussed in chapter 3). When placed on-chip in continuous flow, the 125 μm electrode shows a small decrease in peak height compared to the 50 μm disc electrode. When comparing continuous and droplet flows, there is another decrease in the limiting current, seen at both electrode sizes.

However, a satisfactory CV is recorded in droplet flow, with no interruptions or noise from the movement of the droplets merging in the chamber. Therefore, there will be a clear, continuous signal recorded when using biosensors to analyse the contents of the droplets.

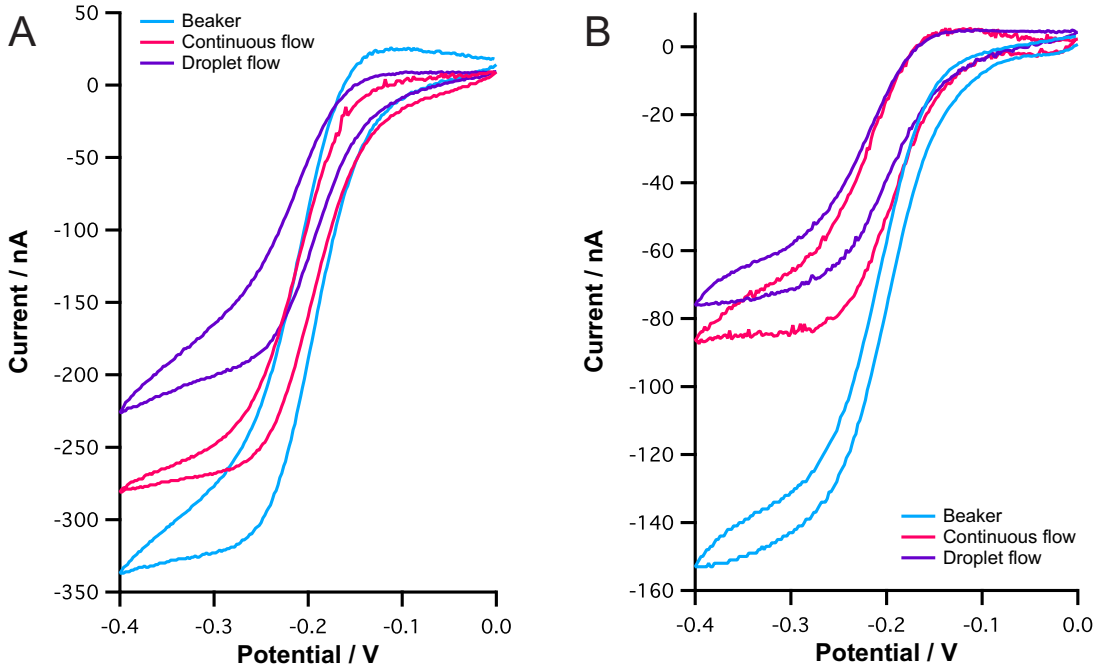


Figure 6.4: CVs in continuous and droplet flow
10 mM RuHex in 1 M KCl used as the redox couple. 10 mVs^{-1} scan rate. Blue line indicates the CV conducted in a beaker, the pink line in continuous flow on-chip and the purple line in droplet flow. A: shows the CV using a 125 μm platinum disc electrode. B: shows the CVs using a 50 μm platinum disc electrode.

6.2.1 Placement of the Electrodes Relative to the Chamber Ceiling

It was found experimentally that there was a lot of variation in the response of the electrode when placing the electrode on-chip. The position of the electrode, in relation to the floor and ceiling of the chamber, was investigated further using electrochemistry.

CVs were performed on-chip in a continuous flow of Fc, at different electrode positions within the PDMS chip. Figure 6.5A shows the results in a 100 μm high chamber and figure 6.5B in a 250 μm high chamber.

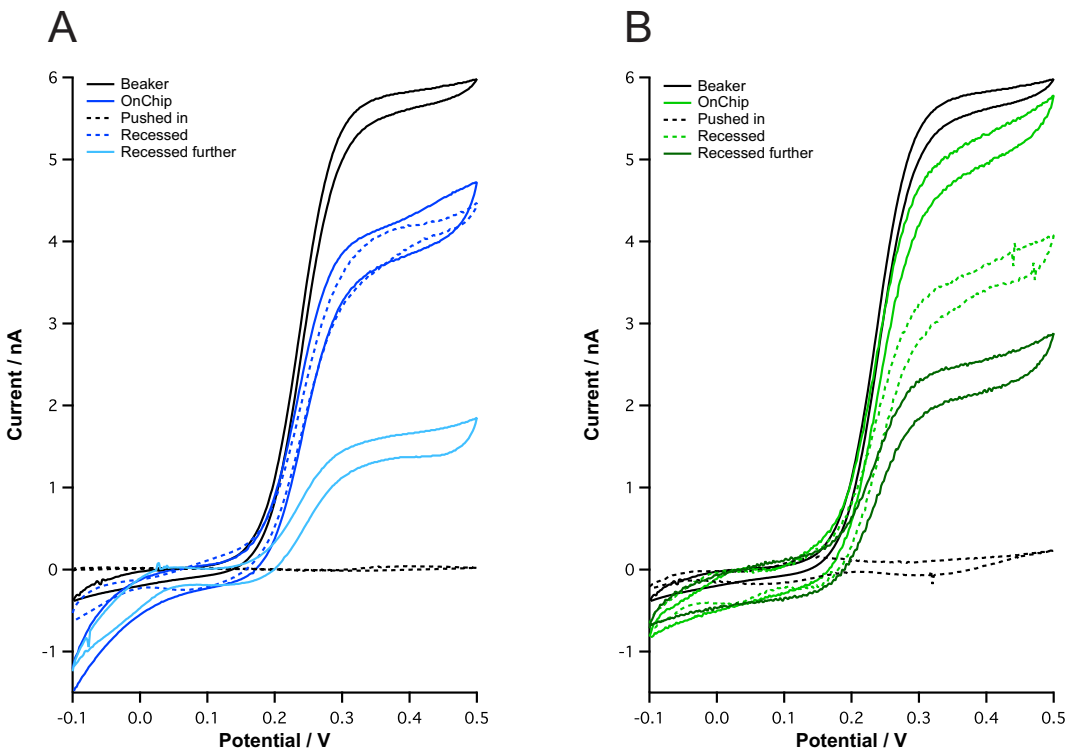


Figure 6.5: On-chip CVs at different heights in a 100 μm and 250 μm high chambers 1.5 mM Fc. Continuous flow 1 μLmin^{-1}. Scan rate 10 mVs^{-1}. 30G integrated needle. 25 μm platinum working electrode. A: 100 μm B: 250 μm.

The electrode is introduced to the chamber by pushing it through the PDMS via a hole punched during fabrication. Ideally it should be placed close to the ceiling without being recessed, but as it is placed by eye, this positioning can be variable. When placed by eye the resulting CVs (OnChip traces) are seen, figure 6.5. The electrode was then pushed until it was felt to touch the floor of the chamber. Here, there is no CV as the surface of the electrode is not exposed to the solution, only the PDMS floor. The electrode was then pulled out so that it was visibly recessed, denoted Recessed in figure 6.5. The electrode was finally pulled up further and the CV recorded again.

From using two different heights of channel, the electrode is more accurately placed by eye in a 250 μm high chamber i.e. the CV looks the closest to that in a beaker. The CV in 100 μm high chamber placed by eye, is similar to the CV of the visibly recessed electrode. Therefore, to maximise the response of the biosensors on-chip, a larger chamber should be used. This, however, increases the sample size, which may not be desired. The method of electrode placement could be made more accurate, for example by using a microscope.

6.2.2 Electrochemistry in Different Flow Regimes

Disc electrodes of diameter 25 μm were also investigated using cyclic voltammetry on-chip, and Fc was used as the redox couple. The CVs in continuous and droplet flow were again compared to that seen in a beaker, figure 6.6. The placement of the electrode on-chip is better with less reduction of the limiting current from the CV produced in a beaker. There is a difference in the observed currents recorded using these electrodes under continuous and droplet flow, but the CV produced in droplet flow was still highly acceptable.

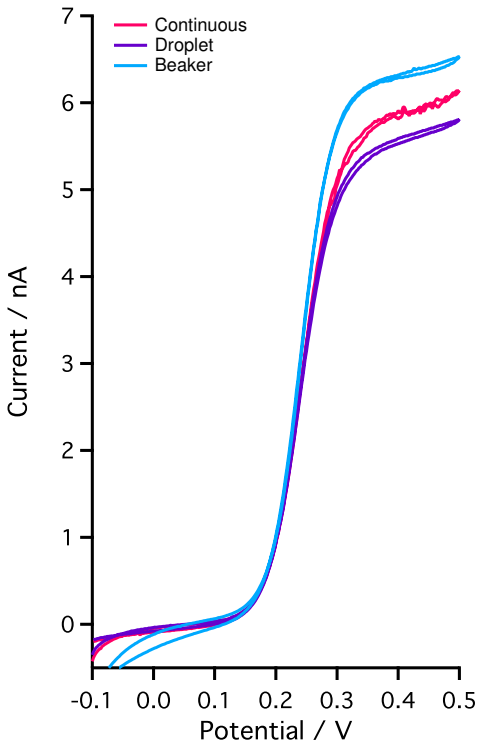


Figure 6.6: CVs in different flow regimes using ferrocene monocarboxylate
On-chip CVs of a 25 μm disc electrode in 1.5 mM Fc in a beaker (blue trace), continuous flow (1 μLmin^{-1}, pink trace) and droplet flow (Fc flow rate at 1 μLmin^{-1} and oil flow rate at 2 μLmin^{-1}) Scan rate 1 mVs^{-1}, potentials versus integrated Ag|AgCl reference, chip channel height 100 μm.

The decrease in the limiting current seen in the different flow regimes, is not due to a difference in the positioning of the electrode and could be due to two reasons. One, the Fc might partition into the oil changing the concentration within the aqueous droplets and two, the electrode may be fouled by the oil because the chamber does not work immediately.

The shake-flask method was used to investigate partitioning effects. A CV was recorded in Fc in a beaker. Oil was added to the beaker with a volume ratio equal to the flow rate ratio used to create droplets. The beaker was shaken to disperse the Fc into the oil. A CV was recorded again and the limiting current assessed. The beaker was then shaken for longer and CV was recorded for the third time in the Fc. Figure 6.7A shows the resulting CVs at the three stages. Comparing the CVs, it can be concluded that the Fc does not partition into the oil, as all the CVs are identical.

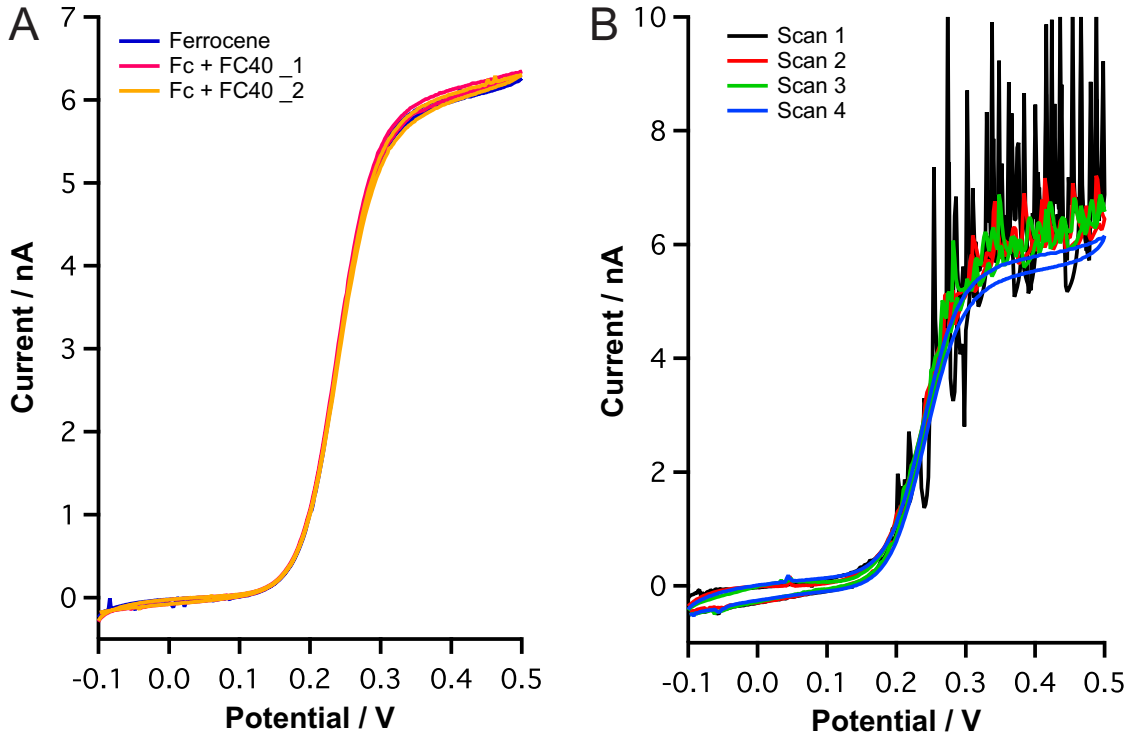


Figure 6.7: CVs looking at ferrocene monocarboxylate and oil
A: Shake-flask method; 1.5 mM Fc. FC40 Oil. Scan rate 1 mVs^{-1}. 30G integrated electrode. 25μm platinum working electrode. Blue line indicates the CV in ferrocene, the pink line after one shake, the orange line after a second shake. B: CVs run as the oil flow is switched on; 1.5 mM Fc. Scan rate 10 mVs^{-1}. Aqueous flow rate 2 $\mu Lmin^{-1}$, oil flow rate 5 $\mu Lmin^{-1}$. 30G integrated electrode with a 25 μm diameter platinum working electrode.

To assess potential fouling of the electrode by the oil, a clean electrode was assessed in continuous flow. Multiple CVs were run on-chip as the oil pump was turned on to generate droplets. To record multiple CVs as the oil is introduced, the scan rate was increased from 1 mVs^{-1} to 10 mVs^{-1}. Looking at these CVs, shown in figure 6.7B, it can be seen that the chamber does not start working straight away and the droplets passing straight through the chamber are seen as noise in the scan (black line: scan1). After three scans the CV is smooth and shows no noise (blue line), indicating that the chamber is now collecting the aqueous droplets and removing the oil effectively, however the limiting current has been lowered. The scans are equivalent to six minutes and indicate that during this time, the surface of the electrode has been affected slightly. However, once the chamber is working correctly, the CV is still acceptable and the electrode can still be used for droplet analysis.

6.3 Dispersion in Continuous and Droplet Flows

Taylor dispersion in continuous flow is a problem for online microdialysis as dynamic changes of an analyte in the brain are smeared as the dialysate passes down a long connection tubing (79). Continuous flow in a circular tubing, is laminar and develops a velocity profile, which is not uniform across the cross section. The fluid near the walls moves slower than the fluid at the centre of the tubing due to friction. This discrepancy in velocity distorts the distribution as shown in figure 6.8A. Diffusion then acts to reduce the sharp change in concentration, which leads to a smearing effect, figure 6.8B. The changes in the detected signal of the step change in concentration is shown in figure 6.8C. This section will investigate the effect of segmenting the dialysate into droplets upon dispersion using both optical and electrochemical methods.

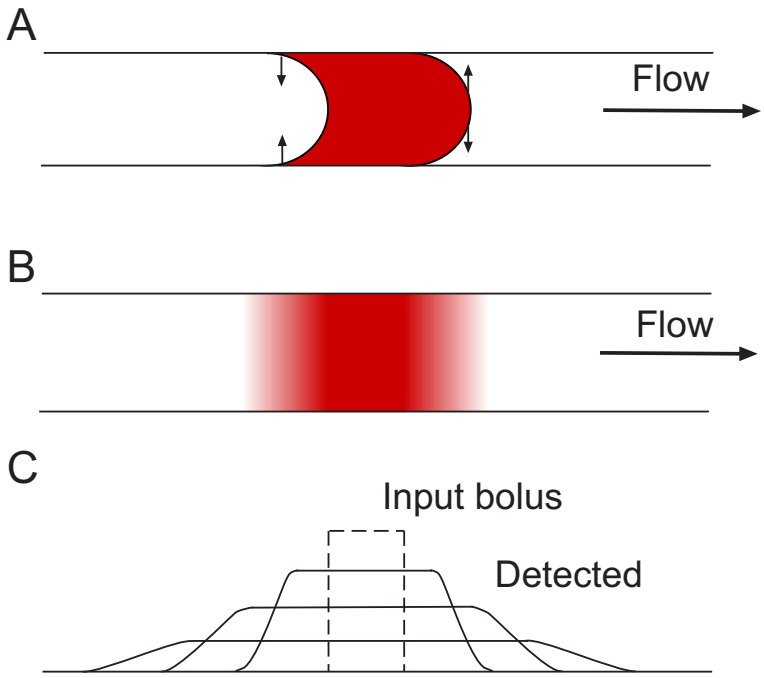


Figure 6.8: Taylor dispersion in continuous flow
A: A step change in concentration is indicated by the red bolus. Flow down the tubing is from left to right, B: diffusion causes smearing to equalise the concentration across the tubing, C: Initially the change in concentration of the input bolus is fast and the signal large, as indicated by the dotted line. However as the bolus travels down the tubing, the signal height decreases and the time course lengthens. This is shown by the solid lines

6.3.1 Optical Measurement

To simulate clinical microdialysis conditions, a step change in concentration was transported over 1 m of low volume connection tubing in both the continuous and droplet flow regimes at a flow rate of 4 μLmin^{-1}. Differences in droplet colour, created by the addition of food dye, were used for optical measurements. The change in concentration was created on-chip by turning on and off pumps and documented using the high speed camera. The resulting videos were analysed in ImageJ using grayscale as a function of concentration over time. Results are shown in figure 6.9A.

The continuous flow regime has a 90% response time, T_{90}, of 19.1 s. However, in droplet flow, when the change is measured at the point where the droplet coalesces, the T_{90} is dramatically reduced to <<16 ms, the frame rate of the video analysed. This is a >100-fold increase in time resolution, which provides a paradigm shift for microdialysis users by allowing the measurement of small sharp changes in the concentration on a sub-second timescale. Figure 6.9B shows the measurement 30 μm into the chamber and here the T_{90} has increased to 200 ms. Therefore dispersion is already having an effect on the time resolution over this small distance.

Using the high speed videos, detailed images of the droplet coalescence were collected. A video of droplets joining the aqueous solution in the analysis chamber, with a frame every 2 ms, was analysed. Figure 6.10 shows three consecutive frames from this video. In figure 6.10A the incoming droplet looks to be touching the solution held in the chamber. In figure 6.10B the camera has captured two states. One the same as A where the droplet is separate and also where the incoming droplet has merged with the solution in the chamber. Figure 6.10C shows that the droplet had joined and the oil is being filtered out. Coalescence of aqueous droplets therefore occurs in under 2 ms as figure 6.10B shows an intermediate picture where the interfaces are seen as both separate and joined together.

Therefore, close to the point of coalescence there is a cliff-like change in concentration. As the droplets coalesce in under 2 ms, diffusion has no effect. As the droplet is pushed into the chamber over a longer time period, diffusion can occur and the concentration change is altered by dispersion. Hence, the position of the electrode within the chamber is important and to improve time resolution the sensor should be placed as close as possible to the point of coalescence.

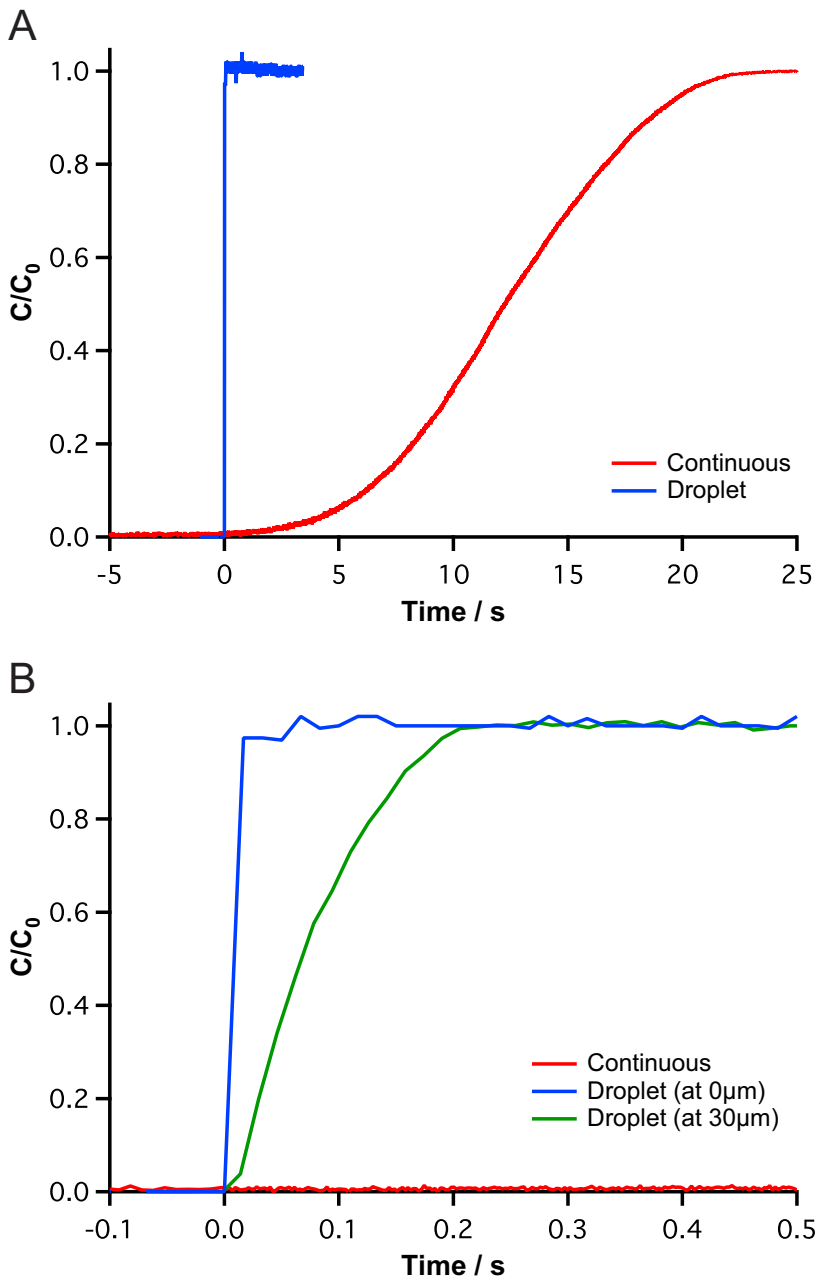


Figure 6.9: Optical comparison of continuous and droplet flow regimes upon dispersion over 1 m tubing

Data was collected from high speed videos. Total flow rate 4 μLmin^{-1}. Continuous flow indicated by a red line, the blue line indicates data collected from just inside the meniscus. In B droplet data collected at different positions in the channel is compared where the green line indicates the recording 30 μm into the chamber.

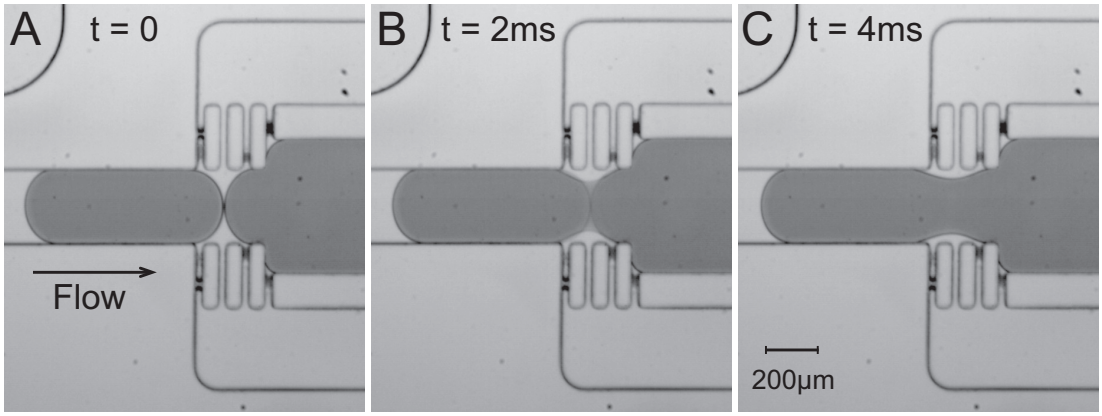


Figure 6.10: Coalescence of droplets
Frames every 2 ms from a high speed video. A: The incoming droplet touches the aqueous solution in the chamber. B: An intermediate image indicating that the coalescence of droplets occurs in under 2 ms. C: The aqueous solutions have joined together and the oil is being filtered through the pillars into the side channels.

6.3.2 Electrochemical Measurement

Dispersion over the 1 m connection tubing was also investigated using electrochemistry with electrodes placed on-chip. The results were compared to the optical measurement, shown again for easy comparison in figure 6.11A. Initially a redox couple was used with a bare platinum electrode. A step change from 0 mM to 1.5 mM Fc was created on-chip in continuous flow. The solution was passed through 1 m of low volume connection tubing at 2 μLmin^{-1}, to an analysis chip containing a clean 50 μm platinum working electrode. The experiment was repeated in droplet flow and the results are shown in figure 6.11B. The experiment was then repeated using a biosensor. A glucose sensor was fabricated using a 50 μm platinum disc electrode (as previously discussed in chapter 4) and placed on-chip. A step change in concentration from 0 mM to 1 mM glucose, was created in continuous flow and transported over 1m of connection tubing at a flow rate of 1 μLmin^{-1}. The experiment was repeated in droplet flow and the responses are shown in figure 6.11C.

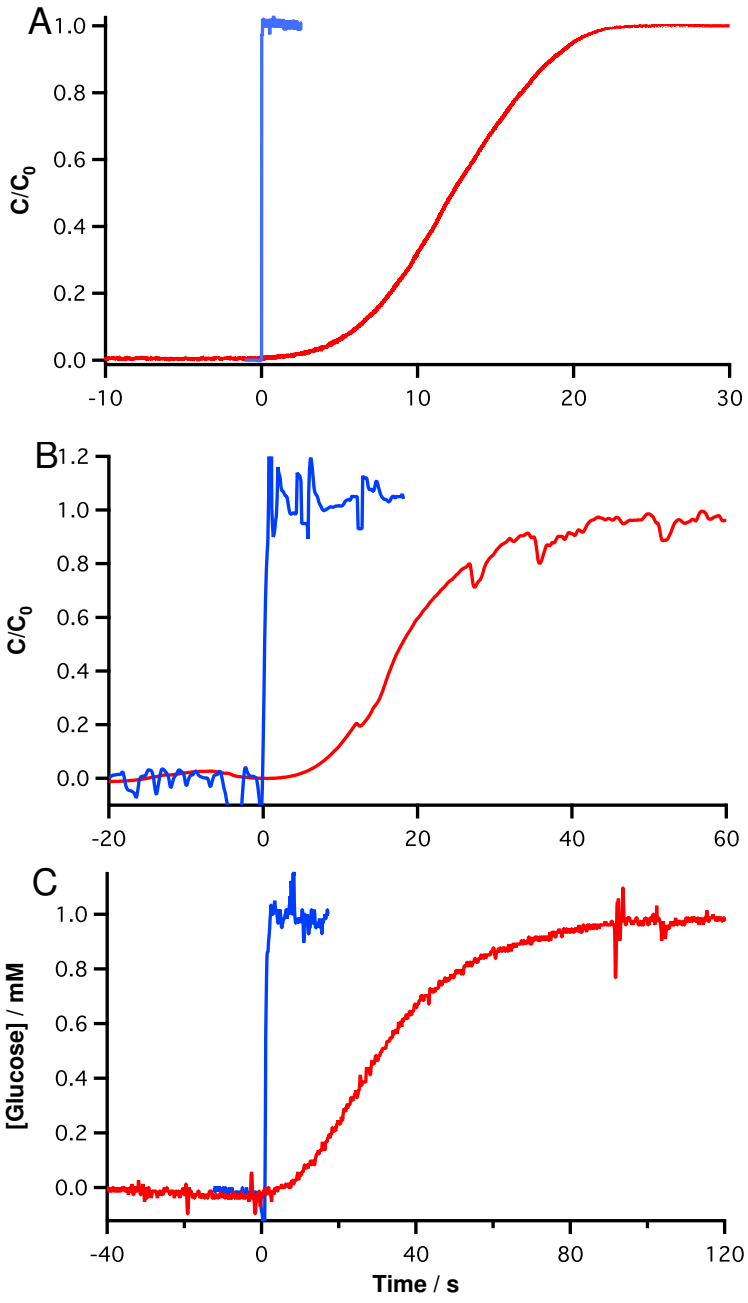


Figure 6.11: Comparison of continuous and droplet flow regimes upon dispersion over a 1 m tubing using different analysis techniques

A: Optical detection of a change in colour in droplet flow (blue) and continuous flow (red). Flow rate 4 μLmin^{-1}. B: Electrochemical measurement using a 50 μm platinum electrode detecting a change in concentration of Fc in droplet and continuous flow regimes. Flow rate 2 μLmin^{-1}. C: A glucose biosensor, fabricated on a 50 μm combined electrode, detects a change in concentration of glucose in both flow regimes. Flow rate 1 μLmin^{-1}.

Table 6.1 summarises the results from all three experiments, in terms of flow rate, and the 90% response times. The response times vary with flow rate and are comparable. As the flow rate is halved, the relative response time approximately doubles. The glucose biosensor has a slightly longer response time because diffusion to the electrode surface is reduced due to the poly(phenol) film used to entrap the enzyme.

Table 6.1: Dispersion over 1 m connection tubing: continuous and droplet flows

Method	Flow rate / μLmin^{-1}	T_{90} Continuous / s	T_{90} Droplet / s
Optical	4	19	0.2
Fc + bare electrode	2	32	0.5
Glucose + sensor	1	69	1.4

It is very apparent that digital microfluidics has the great effect of eliminating Taylor dispersion. This is due to the compartmentalisation of solutions into discrete droplets, which do not interact with each other until they reach the analysis chamber. Applied to microdialysis systems, this will have a large effect, as a long connection tubing from the probe to analysis is a necessary component in both animal and clinical procedures.

6.4 Placement of Electrodes Along the Length of the Chamber

This section will describe a detailed analysis of the chamber to find the optimal position of the electrode within the chamber to maximise the sensitivity and reliability of the recordings. Optical methods were used to compare flow dynamics in the chamber to a mathematical model.

6.4.1 Optical Analysis

Optical analysis was used to assess the droplets merging in the chamber and hence find the optimal positioning of the electrodes. This involved creating a sequence of alternating droplets, four dark (water with a dye moiety) and four light (water), using a robotic head. These droplets were then introduced to the analysis chamber where a CCD camera (Phantom V) recorded the chamber as the droplets passed through. The setup is shown in figure 5.4 (minus the laser setup). The videos were analysed in ImageJ, as shown in figure 6.12.

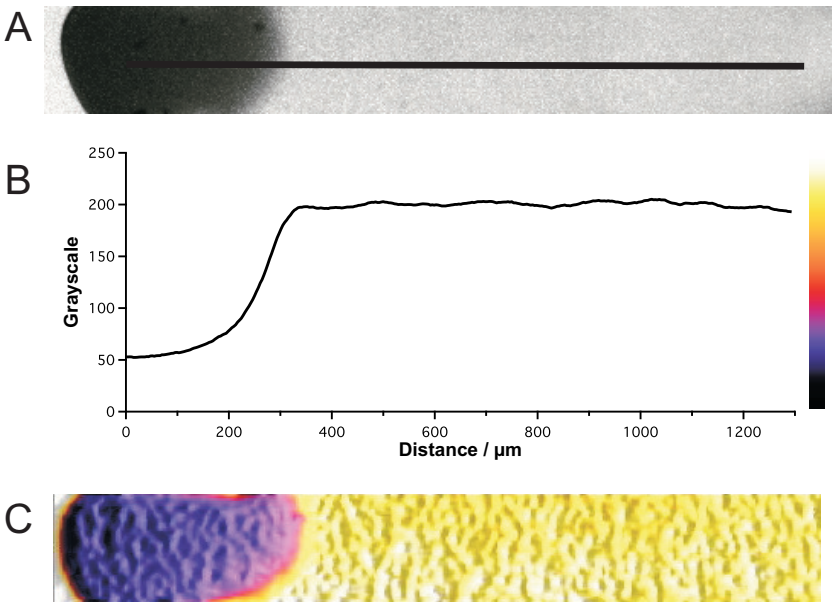


Figure 6.12: Processing of high speed videos
A: A single frame of a high speed video of the microfluidic chamber where droplets coalesce. An analysis line was drawn with ImageJ and the greyscale values measured (using 8-bit conversion). Distance measured from 0 μm to 1360 μm, left to right. B: Plot profile of the grayscale values measured along the line. C: For some images the grayscale was converted to false colour images (generated by ImageJ).

A line was drawn through the centre of the chamber within ImageJ, along which the grayscale was analysed at every pixel. The complete length of the chamber was analysed (1360 μm). The midline of the chamber was analysed to avoid the effects of flow complexities (such as corner flow), which occur due to the oil wetting the PDMS surface. The midline was analysed at different time points, which allowed the same change in concentration to be observed as it moved through the chamber. Figure 6.13 shows frames (in false colour) from a video (Video 7 on the associated DVD) of a dark droplet entering a white filled chamber.

Figure 6.14 displays the change from a light filled chamber to a dark filled chamber, with the midline analysed every 50 ms. The change is clearly seen at the entrance of the chamber by the decrease from 1 to 0.1 and occurs over 121 μm. 0.75 s later, the same step change in concentration occurs over 740 μm. Dispersion is affecting the time resolution by smearing out the step change in concentration, as each new droplet enters the chamber, displayed here as the change in the gradient of the rising slope. Before the arrival of the next droplet, the oil is being removed and the solution in the chamber is stationary. This is seen as overlapping traces. Here, the gradient does not change indicating that there is no mixing whilst the solution is stationary.

6.4.2 Mathematical Model of the Chamber

A mathematical model of the chamber was designed by Professor Kim Parker, to help determine the best position to place analysis electrodes. In developing a model, it was assumed that the chamber is rectangular and that the concentration of the dye inside the inlet droplet was uniform at the entrance of the chamber (where x = 0). It was also assumed that inertial effects are so small that the velocity profile within the chamber was either zero when the oil was being removed or instantaneously fully developed when the approaching droplet first coalesced. It also assumed that the pattern of dark and light droplets is symmetrical. The Reynolds (Re) number of the aqueous solution in the microfluidic channels was calculated, using equation 6.1, to be 0.4, placing the fluid flow in the laminar regime.

$$Re = \frac{vL}{\nu} \tag{6.1}$$

where v is the velocity, L is the length travelled and ν is the viscosity.

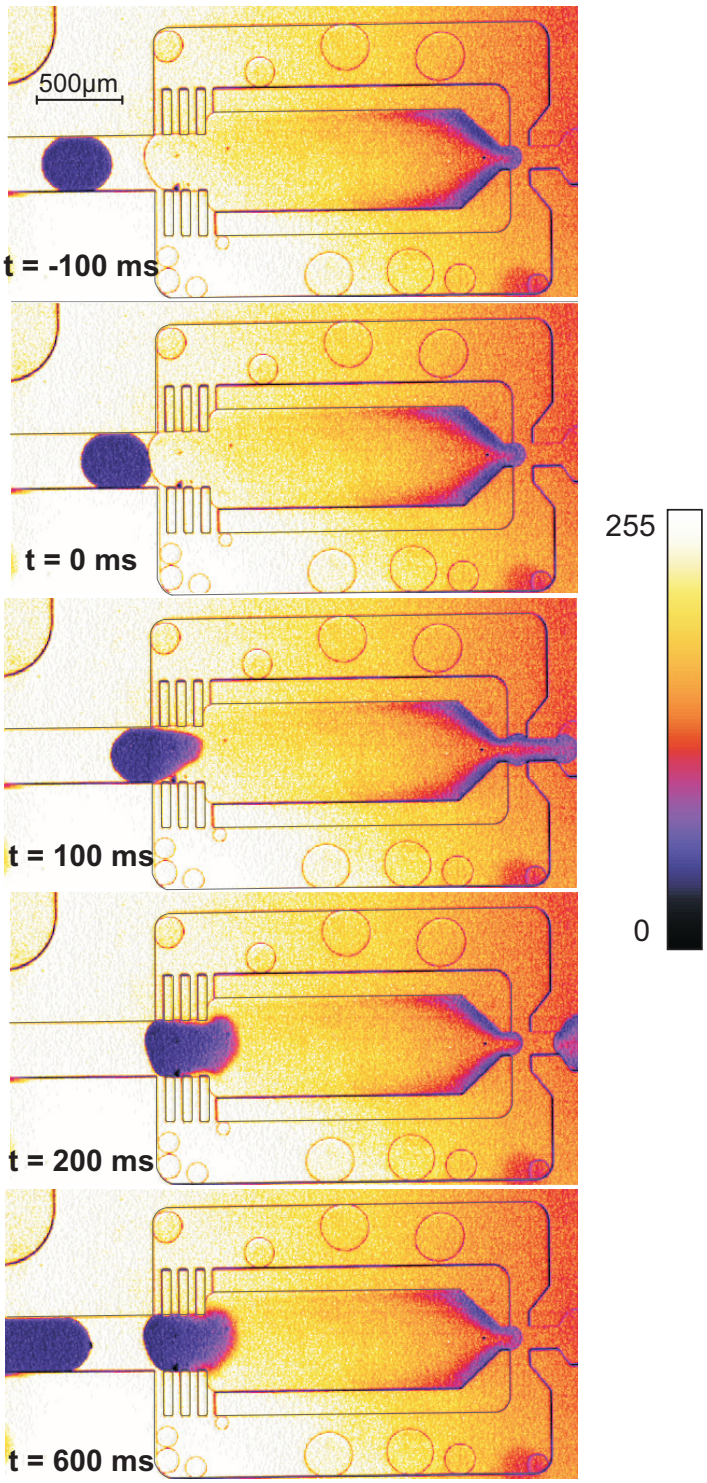


Figure 6.13: Frames of a video of the aqueous solution entering the analysis chamber The frames are in false colour for effect and show a progression of a dark droplet joining the light coloured aqueous solution held in the chamber.

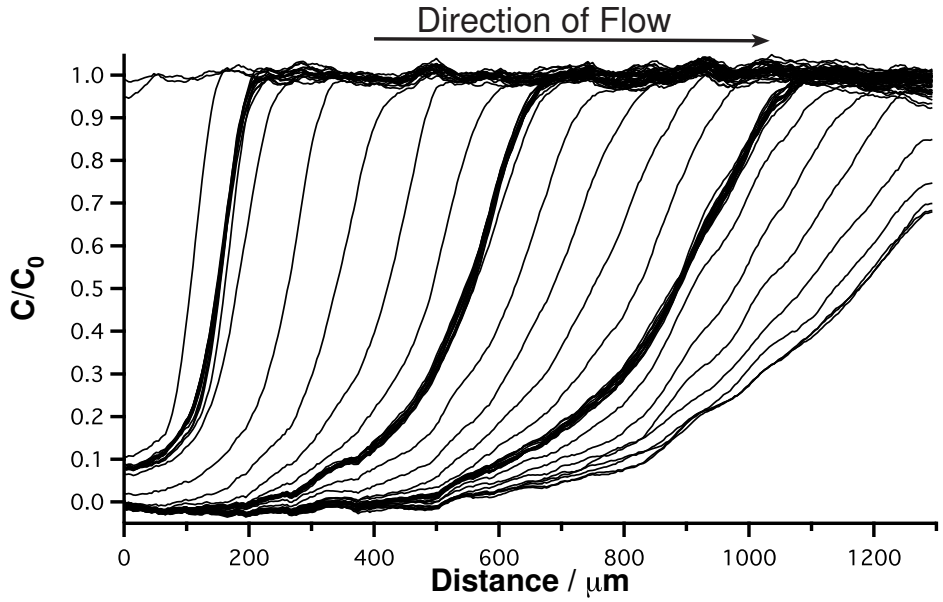


Figure 6.14: Experimental data of dark and light droplets in the chamber
Initially the chamber was filled with light drops, giving the horizontal lines at $C/C_0 = 1$. At 0 s, a dark droplet starts to enter the chamber. 50 ms later, C/C_0 was evaluated at all points along the midline giving the curve on the left hand side of the figure. This was repeated every 50 ms to give the complete figure. Thicker curves are due to the flow being stationary before the next dark droplet enters the chamber. Note that the coalescence of incoming droplets is not synchronised to the data collection rate, hence the spacing is not always even.

This also allows us to estimate the entrance length, x_L, for the establishment of a steady-state flow profile using equation 6.2 (200, 212).

$$x_L/2h = 0.04R_e + 0.5 \tag{6.2}$$

where h = height. For our system x_L is 100 μm, which can be compared with the droplet length of 600 μm in figure 6.13. The analysis uses the general solution for Poiseuille flow in a rectangular chamber given by Mortensen et al. (2005) (213). The channel has a width w with $y = [-\frac{w}{2}, \frac{w}{2}]$ and height h with $z = [0, h]$.

The distance along the channel is x. The velocity distribution across the (y, z) cross-section is given in equation 6.3.

$$u(y,z) = \frac{4h^2\Delta p}{\pi^3 L} \sum_{n=1,3,\ldots}^{\infty} \frac{1}{n^3} \left(1 - \frac{\cosh\left(\frac{n\pi x}{2}\right)}{\cosh\left(\frac{n\pi w}{2h}\right)}\right) \sin\left(\frac{n\pi y}{h}\right) \tag{6.3}$$

where $\frac{\Delta p}{L}$ is the pressure gradient along the channel and η is the coefficient of viscosity of the fluid. The velocity distribution is expressed either in terms of the maximum velocity, u_0, which occurs in the centre of the channel and is shown in equation 6.4,

$$u_0 = u(0, \frac{h}{2}) = \frac{4h^2\Delta p}{\pi^3 L} \sum_{n=1,3,\ldots}^{\infty} \frac{(-1)^{\frac{n-1}{2}}}{n^3} \left(1 - \frac{1}{\cosh\left(\frac{n\pi w}{2h}\right)}\right) \tag{6.4}$$

or the mean velocity U, which is shown in equation 6.5.

$$\begin{aligned} U &= \frac{1}{wh} \int_{-w/2}^{w/2} \int_{0}^{h} u(y,z) dz dy \\ &= \frac{4h^2\Delta p}{\pi^3 L} \frac{2}{\pi} \sum_{n=1,3,\ldots}^{\infty} \frac{1}{n^4} \left(1 - \frac{2h}{n\pi w} \tanh\left(\frac{n\pi w}{2h}\right)\right) \end{aligned} \tag{6.5}$$

The ratio of the maximum velocity and the mean velocity is given by equation 6.6.

$$\frac{u_0}{U} = \frac{\pi \sum_{n=1,3,\ldots}^{\infty} \frac{(-1)^{\frac{n-1}{2}}}{n^3} \left(1 - \frac{1}{\cosh\left(\frac{n\pi w}{2h}\right)}\right)}{2 \sum_{n=1,3,\ldots}^{\infty} \frac{1}{n^4} \left(1 - \frac{2h}{n\pi w} \tanh\left(\frac{n\pi w}{2h}\right)\right)} \tag{6.6}$$

This is shown in Figure 6.15 as a function of the aspect ratio of the cross-sectional area $\gamma = \frac{w}{h}$. For Poiseuille flow in a circular tube, this ratio is 2 and in 2D channel flow ($\gamma \to \infty$), the ratio is 3/2. For the aspect ratio of the microfluidic channels used, $\gamma = 2$, the ratio is very close to 2. This is a factor which should be considered when connecting square channels to circular tubing to achieve a smooth connection.

The velocity profile for Poiseuille flow in a channel is parabolic and comparison of the centre line profiles for finite aspect ratios shows that the centre line velocity profile is very close to parabolic for γ as small as 2, figure 6.16. The effect of the aspect ratio is predominantly on u_0, not the shape of the centre-line profile.

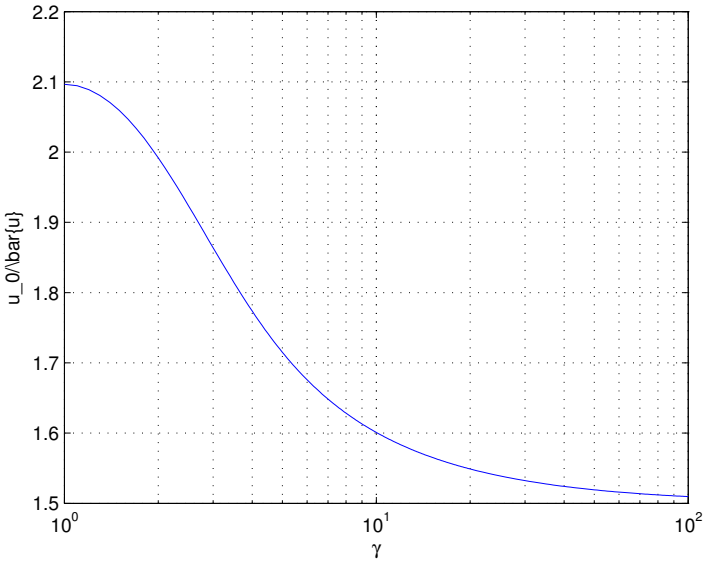


Figure 6.15: Velocity ratio
The ratio of centre-line velocity u_0 to mean velocity U as a function of the aspect ratio of the rectangular channel γ.

6.4.3 Flow Dynamics in the Droplets and the Chamber

The main difference between the flow in a droplet approaching the chamber and the flow in the chamber, is the effect of surface tension in the meniscus at the front and back of the droplet. At the interfaces between the oil, water and wall, the surface tension dominates the viscous forces that lead to the no-slip condition in single phase flow. Within the droplet, the no-slip condition holds at the walls whereas at the interfaces, the velocity at the wall is equal to the convective velocity of the droplet. This difference in boundary conditions results in a flux of fluid away from the wall at the back of the droplet and towards the wall at the front. This establishes a strong circulatory, secondary flow within the droplet which results in rapid mixing within the drop and homogeneous concentration profiles. Once the front meniscus of a drop coalesces with the meniscus at the front of the chamber, the no-slip condition requires that the velocity at the top and the bottom of the chamber is zero. The resulting velocity profile causes convective dispersion. The vertical dispersion on the centre line of the chamber is illustrated in Figure 6.17.

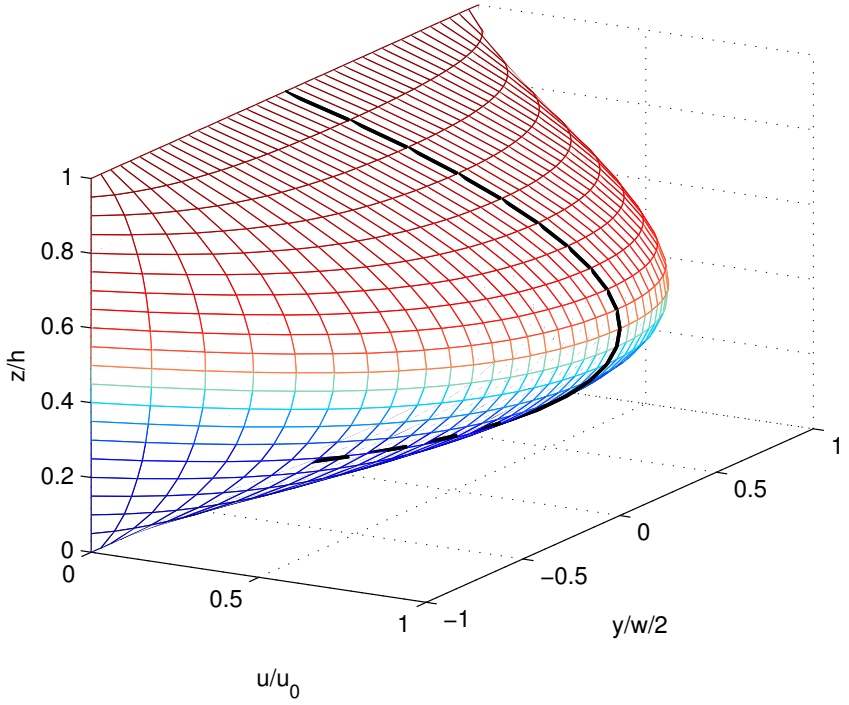


Figure 6.16: Velocity distribution
The velocity distribution u/u_0 in a rectangular channel with $\gamma = 2$. The black line indicates the velocity profile in the centre of the channel across which the concentration of tracer was measured.

The concentration measured in these optical experiments is the average concentration across the depth of the chamber. It is clear that the average concentration will vary with time along the length of the chamber in a way that is rather complex. Close to the inlet of the chamber, the concentration will change rapidly as the bands of tracer are predominantly vertical. Further from the inlet the bands become more angled and the fronts of tracer become more diffuse. Close to the ceiling and the floor of the chamber, the bands are nearly horizontal and the contribution of these bands to the average concentration provides a history effect. Close to the wall there is some tracer from all of the droplets that have preceded the current droplet. Over time, this leads to Taylor dispersion where the concentration gradients in the vertical direction due to the nearly horizontal bands becomes important leading to diffusive dispersion in the vertical direction. In the limit this dispersion, coupled with the parabolic velocity profile, leads to an axial concentration gradient that is approximately Gaussian.

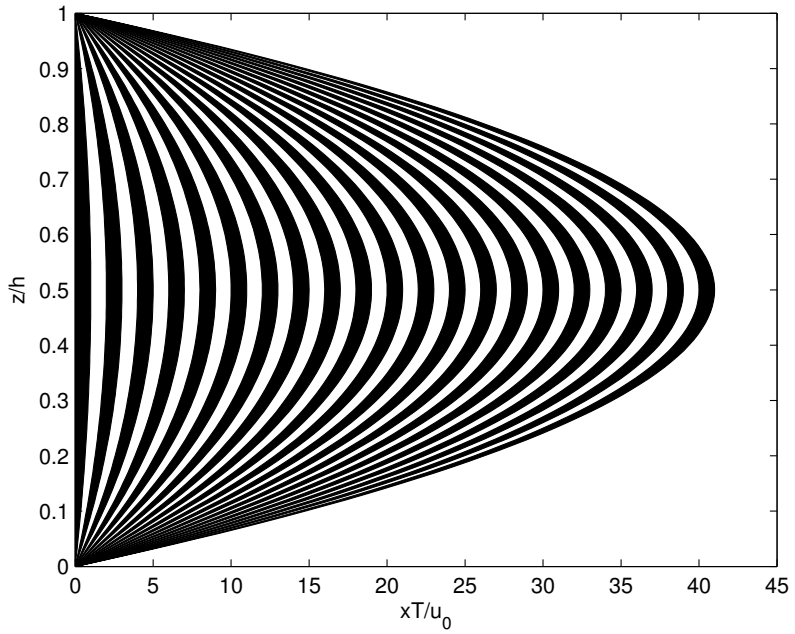


Figure 6.17: Simulated dispersion within the chamber
This figure shows a simulation of the dispersion along the centreline of the coalescence chamber as a function of z, the vertical axis, due to the parabolic flow profile. It is assumed that the droplets are well mixed due to the meniscus at the back of the droplet until it merges with the meniscus at the origin of the chamber, $x = 0$. When there is convection in the chamber, the no-slip condition at the top and bottom walls applies and the flow profile is parabolic. The sequence of droplets alternates between four dark and four light.

In a microfluidic device, the easiest and the most common place to fabricate an integrated electrode, is on the wall of the channel. We also discuss in section 6.13, that the wall is best for needle electrode on simple diffusion field arguments. Figure 6.17 shows that wall placement is not ideal due to the build up of previous droplets creating a history effect.

Therefore in this analysis chamber, the optimal position of the needle electrodes is as close as possible to the point of coalescence, where the bands are vertical. This is at the entrance of the chamber, and figure 6.18 displays this clearly. A high speed video, with a frame rate of 2 ms, of the joining of a droplet in false colour can be found on the associated DVD (Video 8).

Further away from the point of coalescence, the bands (seen in figure 6.17) become increasingly horizontal, lowering the sensitivity of the assay. This is shown in figure 6.19. Different coloured droplets were recorded as they passed through the chamber. The change from a light to dark was analysed in ImageJ. Figure 6.19A

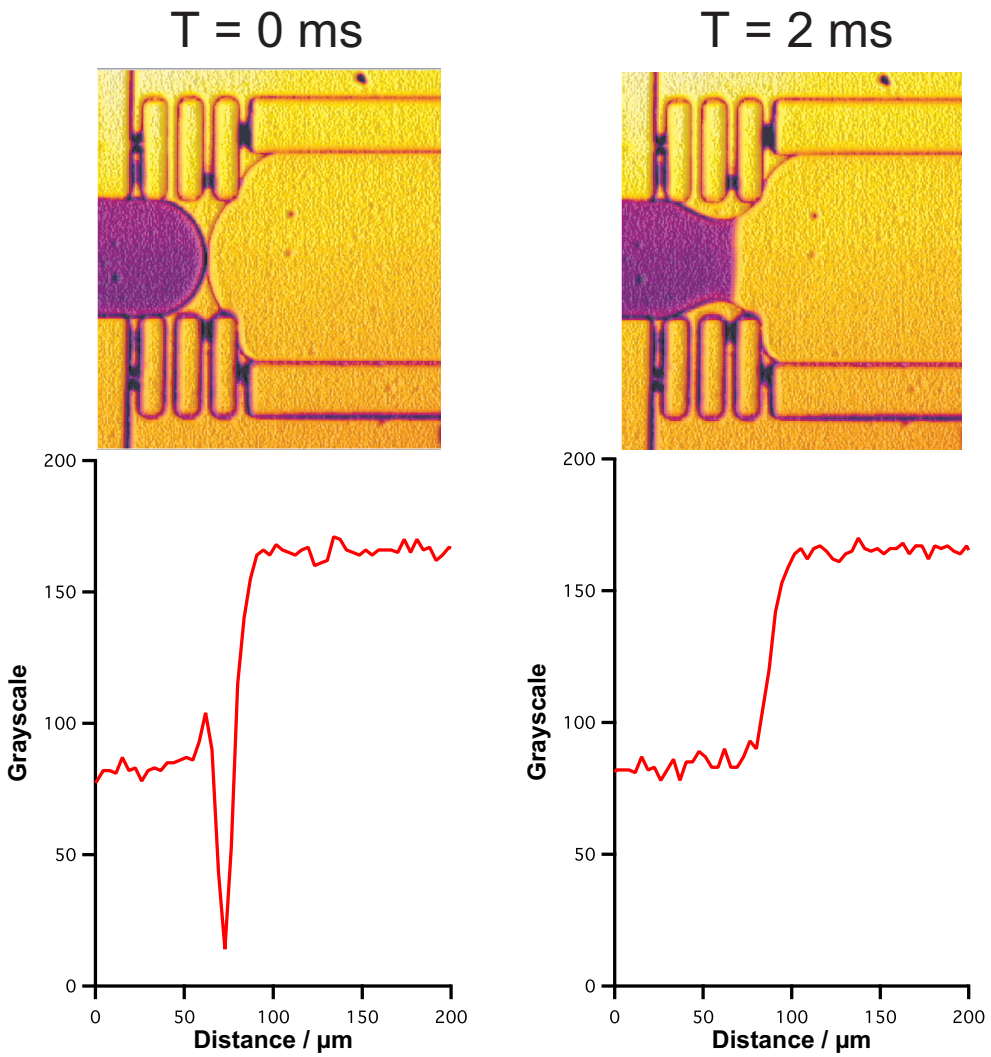


Figure 6.18: Coalescence at the entrance of the chamber
The chamber is filled with light solution. The interface when a dark droplet enters has been investigated using a high speed camera. The frames are 2 ms apart and are false colour. The graphs show the grayscale analysis of each frame.

shows the whole chamber. There is a shadow over the chip but the solution within the chamber is clear. The black indicates the dark droplets and the yellow indicates the light coloured droplet. The beginning of the chamber the change between the two coloured solutions is much sharper than towards the end. This is seen more clearly in figure 6.19B, which is a cut-out of the solution within the chamber. Figure 6.19C analyses the change from light to dark at the beginning of the chamber and a sharp cliff is seen. Whereas figure 6.19D shows the change at the end of the chamber where the change occurs over a longer distance indicating the smearing effect.

In summary, the microelectrodes should be located in the middle of the chamber, away from the walls, as here the bands are vertical and less of the history effect is seen. The electrode should also be placed close to the point of coalescence of the incoming droplet to take full advantage of the cliff-like change in concentration. Also here, the bands are more vertical and so the position of the electrode in the channel (in terms of position floor to ceiling) is less crucial. If, however, the no-slip condition at the wall was broken or baffles were introduced to the walls, convective mixing within the chamber would occur and stop the bands from forming. Positioning the needle electrode in the middle of the channel would also potentially disrupt the flow, resulting in the same effect.

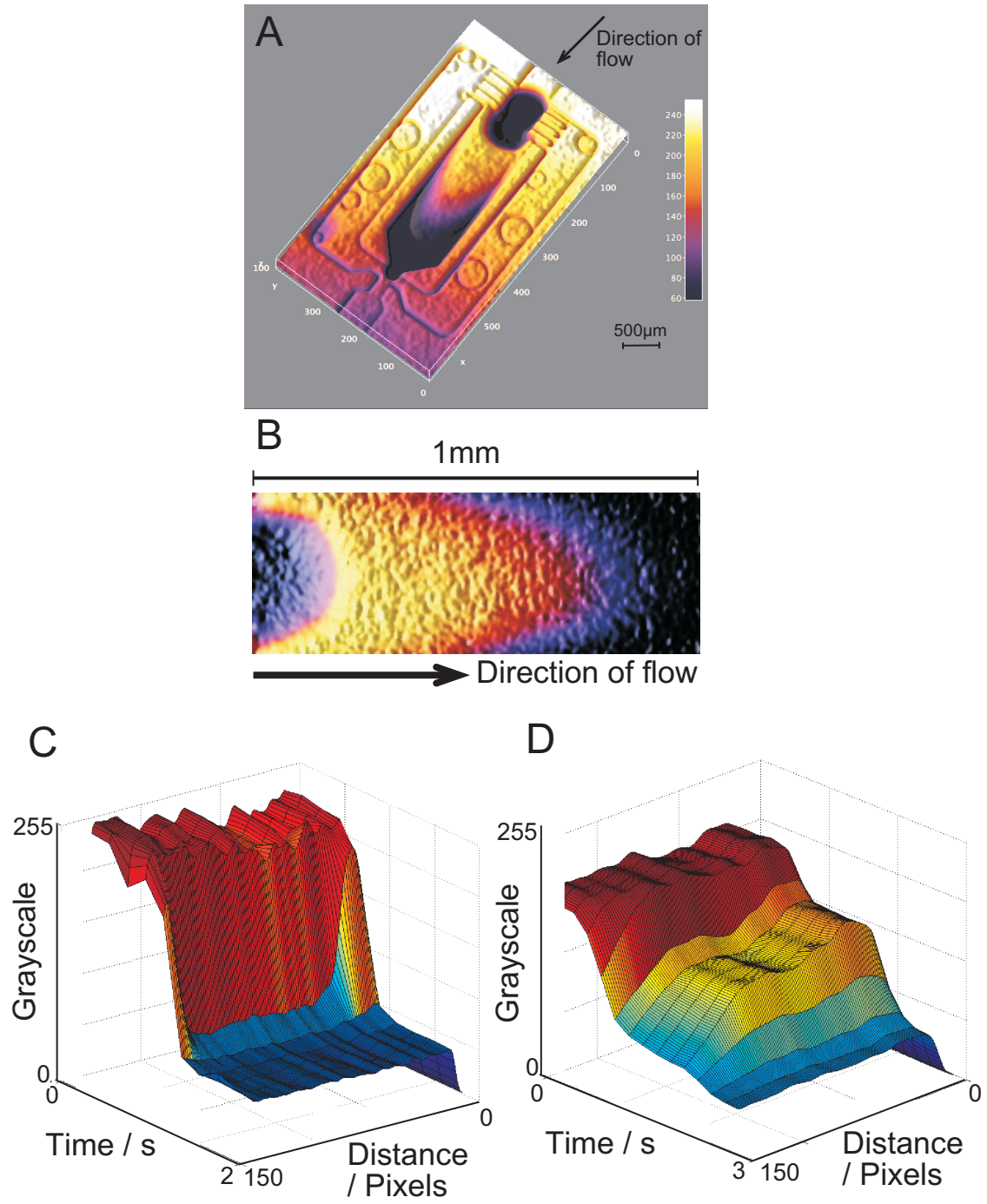


Figure 6.19: False colour frames of different coloured droplets within the chamber A: The chamber is filled with dark solution. Four light colour droplets have entered the chamber followed by one dark coloured droplet. B: displays a closer look at the solution within the chamber. C: Analysis conducted in ImageJ of the change in grayscale at the entrance of the chamber. D: Analysis of the change from light to dark droplets in grayscale at the end of the chamber.

6.5 Dual Electrode Orientation

The dual electrodes were developed for use either as a sensor and sentinel combination or for multi-analyte analysis. It has previously been discussed that the dual electrodes exhibit a degree of cross-talk when placed in a beaker of Fc (chapter 3). The dual electrodes were also investigated under flow conditions in a similar experiment. One electrode of the pair was held at a constant potential of 0 V, as the other had the applied potential scanned. As the potential increased, the classic cyclic voltammogram is seen as Fc is oxidised to Fc^+. Cross-talk is seen if the diffusion fields overlap and the constant potential electrode reduces this product back to Fc. This is seen as a negative peak. The collection efficiency is the percentage of product seen at the other electrode.

The orientation of the two working electrodes when placed on-chip will affect the collection efficiency as now there is a directional flow of solution introducing convection. Figure 6.20 shows schematics of the two extreme scenarios in which the electrodes can be placed.

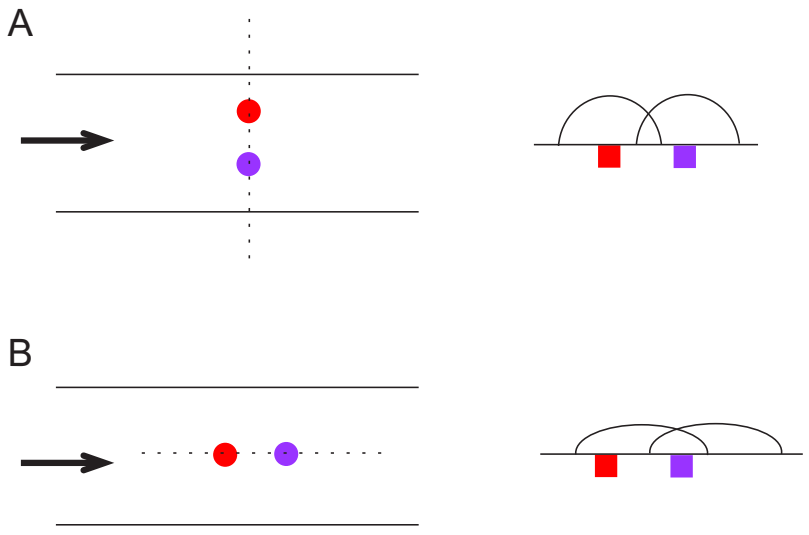


Figure 6.20: Schematic of dual electrodes under flow conditions
Flow direction is indicated by the arrows. The dual electrodes are shown within a chamber. A: the electrodes are positioned across the direction of flow. The dotted lines indicate the cross section taken to view the diffusion fields (schematic on the right) B: The electrodes are positioned in-line with the direction of flow.

On the right of each orientation a schematic indicates the likely geometry of the diffusion fields. When placed across the flow, figure 6.20A, the diffusion fields overlap, depending on the relative spacing of the electrodes within the hypodermic

needle. However, when placed in-line with the flow, figure 6.20B, there is now an added factor of convection. This distorts the diffusion fields by flattening and elongating them. Hence, more products formed at the upstream electrode will now be detected at the downstream electrode than vice versa.

The orientation of the dual electrodes was assessed by marking the relative positions of the electrodes on the needles using a microscope and placing them on-chip, both across and in-line with the flow. As an example, CVs produced at electrode D4 are shown in figure 6.21.

A summary of the results from all dual electrodes is shown in table 6.2. Note that D1 was broken and therefore no longer included. The collection efficiencies are shown as a percentage and were calculated from the limiting currents of the CVs. The electrodes used here correspond to the photographs shown in figure 3.16.

Table 6.2: Collection efficiencies on-chip

Electrode	Across		In Line	
	A_{Scan}:$B_{Collect}$	B_{Scan}:$A_{Collect}$	A_{Scan}:$B_{Collect}$	B_{Scan}:$A_{Collect}$
D2	1.13	1.03	2.11	9.33
D3	0.95	0.96	0.69	15.9
D4	13.75	15.02	17.12	8.93
D5	0.71	0.57	1.64	0.64
D6	7.55	5.87	23.62	3.04
D7	9.06	9.03	1.53	11.59

When placed across the direction of flow, the collection efficiencies of the dual electrodes are very similar at both electrodes. The cross-talk on-chip is much smaller than the cross-talk of the same dual needle electrode in a beaker (Table 3.8). This is due to the convection created by the flow carrying some products away from the collection electrode.

However, when the dual electrodes are placed in-line with the flow, the collection efficiency depends upon whether the collection electrode is upstream or downstream of the generating electrode. The downstream electrode will detect more products that are produced at the upstream electrode than vice versa, again due to the convection added by the flow.

The majority of dual electrodes are close together and display high levels of cross-talk. Electrode D5 has the most inter-distance between electrodes and under flow, it produces the smallest amount of cross-talk. The fabrication of electrodes to produce dual electrodes, which exhibit zero cross-talk should be developed.

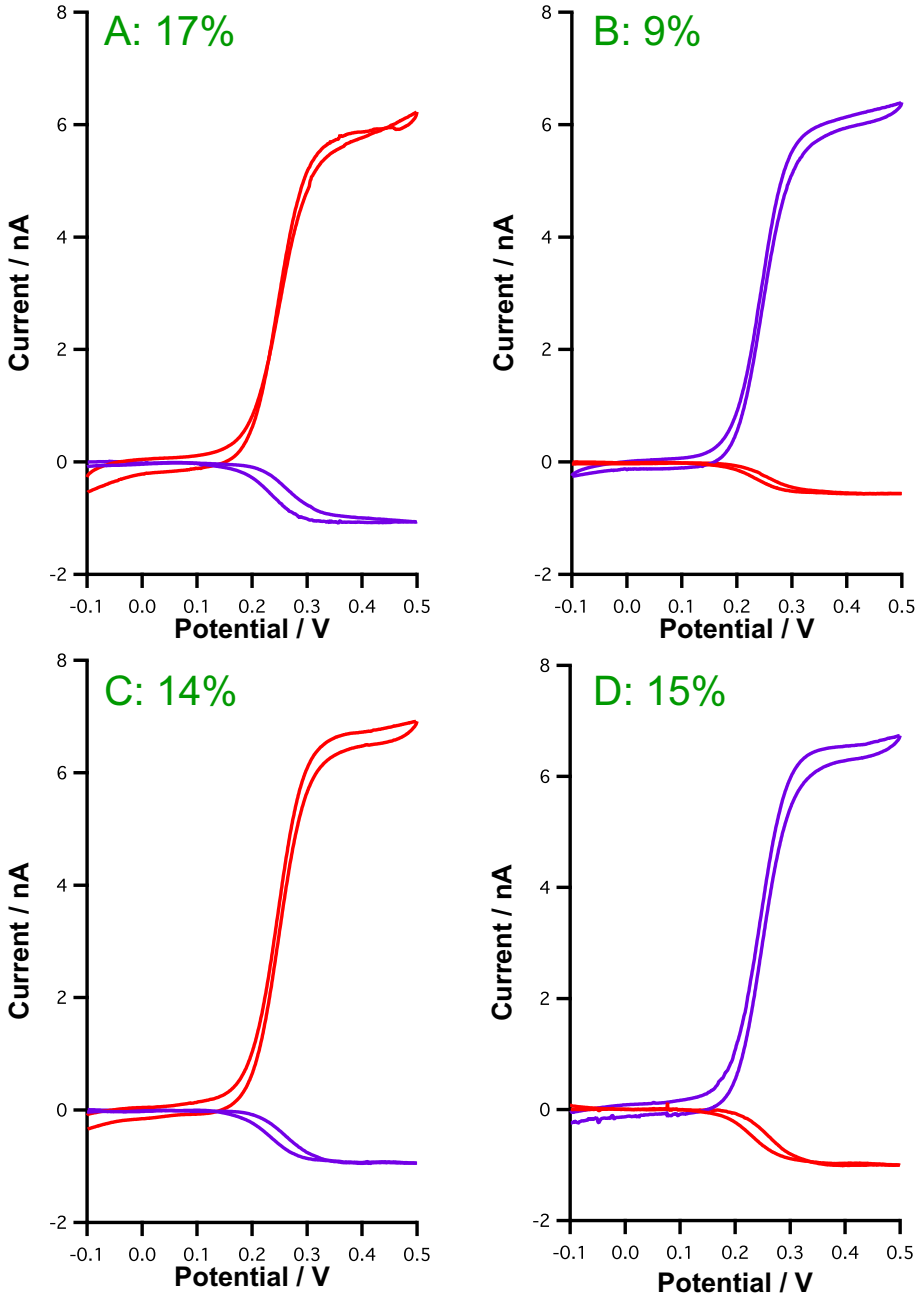


Figure 6.21: CVs showing the collection efficiencies of electrode D4 when placed in different orientations on-chip

1.5 mM Fc. Continuous flow 2 μLmin^{-1}. Scan rate 10 mVs^{-1}. 30G integrated needle. 2 x 25 μm platinum working electrode. The percentages indicate the collection efficiency. A and B show the response in line with the flow where the red electrode is upstream. C and D show the responses perpendicular to the flow. Positive CVs are scanning whereas negative traces are produced from the electrodes held at 0 V.

Due to the cross-talk, two different analytes cannot be measured. However, the chamber is large enough to house two separate hypodermic needles. In this arrangement, one electrode will be upstream of the other, and the cross talk between working electrodes was tested using the same experimental protocol. Figure 6.22 shows the CVs produced and cross talk was found to be 0.1 % between separate needles. Here, there is an approximate distance of 500 μm between electrodes.

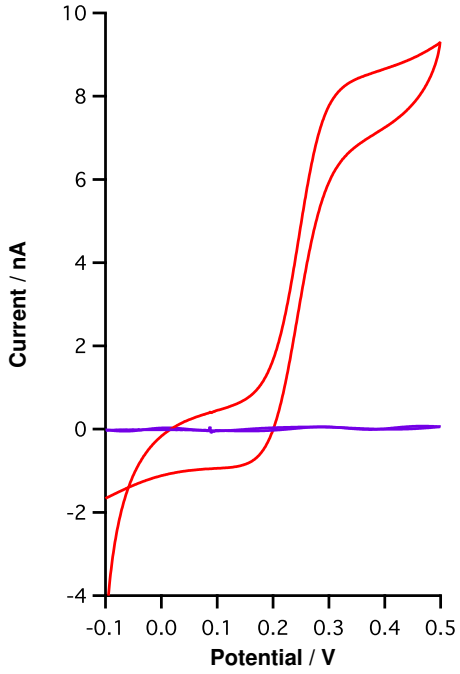


Figure 6.22: CVs of separate needle electrodes in the chamber
Continuous flow of 1.5 mM Fc perfused at 2 μLmin^{-1}. Scan rate 50 mVs^{-1}. 2 x 50 μm platinum working electrode. Electrodes are in line with the flow with the red electrode upstream. Red CV is scanning whereas negative the purple trace is held at 0 V. Collection efficiency is 0.1 %.

In summary, the amount of cross-talk on the dual electrodes, on-chip, depends upon the orientation of the two electrodes compared to the direction of flow. Therefore, dual electrodes in this format cannot be used to create a multi-analyte sensor. Two needle electrodes can be placed in the same chamber and run simultaneously with no crosstalk between the sensors. However, the response of the down stream electrode is compromised by being further away from the point of coalescence. An alternative solution may be smaller detection chambers placed in series, rather than expanding one chamber to house multiple sensors, as each microelectrode can be positioned at the optimal location at the point of coalescence within each chamber to achieve the highest time resolution and sensitivity.

6.6 Biosensors On-Chip

The glucose and lactate biosensors described in chapter 4 were placed on-chip for assessment. They were placed within the analysis chamber and initially tested in continuous flow. Solutions of varying concentrations of glucose and lactate were introduced on-chip and the responses characterised. The sensors were then assessed in droplet flow. Both glucose and lactate are considered hydrophilic and have partition coefficients (LogP values) of -2.84 and -0.62 respectively (214, 215). The glucose will not partition into the oil and will stay within the aqueous droplet ensuring an accurate measurement. The partition coefficient of lactate suggests that it may partition into the oil. However, lactate has a pKa value of 3.86 (216), meaning that less than 0.1 % will be in the correct state to partition into the oil. Finally the two different sensors were placed on-chip together, within the same analysis chamber, and solutions alternated between glucose and lactate.

The main problem of calibrating the sensors on-chip was found to be the alternation of solutions to produce a reproducible step change in concentration. A syringe switcher was initially tested but the change in pressure caused by the switching caused the solutions to jump. This was especially apparent in droplet flow and the droplet generation was greatly affected. Syringe pumps were then employed and the solutions alternated by stopping and starting the pumps. The solutions were fed into different channels on-chip. Whilst this was more reproducible the pumps were very slow in stopping and starting causing a variable flow rate, which affected the signal recorded at the flow-rate sensitive sensors. Figure 6.23 shows the speed of the pumps stopping and starting by use of integrated flow sensors. The time to change from 7 μLmin^{-1} to the flow in the system to stop moving is approximately 40 seconds. Finally, syringe taps were tested to divert the flow directly from the syringe. In this setup the pumps were continuously running. The diversion of fluids using syringe taps proved to be the most reliable method; however sometimes the switching did cause a change in flow rate, which can sometimes be seen as peaks.

6.6.1 Glucose

Continuous Flow

The glucose biosensors were placed on-chip within the analysis chamber. Solutions of varying concentrations were perfused through the chip. Solutions were controlled using a syringe pump (Harvard) and syringe taps were used to divert

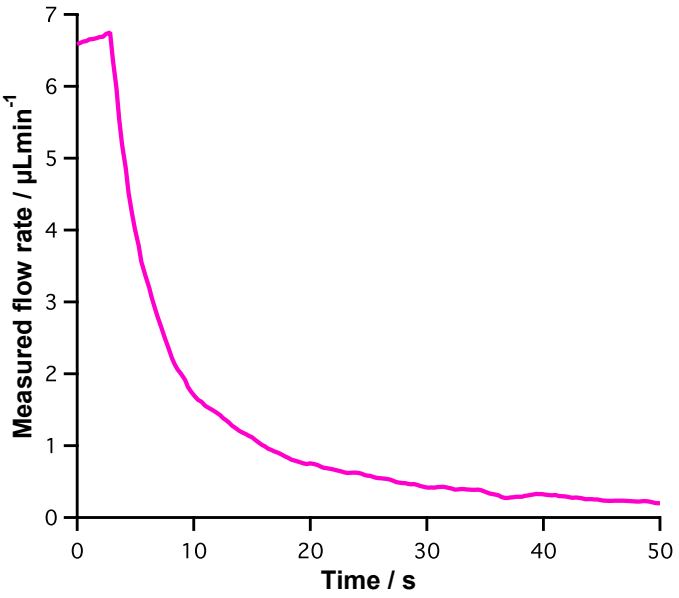


Figure 6.23: Syringe pump flow rate measured with flow sensors
Flow sensors, in-line with the flow from a syringe pump, record the change in flow rate as the syringe pump is turned from on at 7 μLmin^{-1} to off. It takes approximately 40 s for the flow rate to reach zero.

flows when required. The flow rate through the microfluidic chip was 2 μLmin^{-1} for all solutions. The solutions were switched between PBS, 1 mM and 0.25 mM glucose and the change in current at the electrode recorded. The results for a 50 μm disc glucose biosensor is shown in figure 6.24. The sensor responds clearly to changes in the glucose level and the majority of noise comes from changes in the flow rate as the syringe taps are turned and the solutions are alternated.

Two different sizes of glucose biosensors were placed on-chip, 50 μm and 25 μm. This was due to the 125 μm electrodes being housed in a larger syringe electrode, which did not easily fit in the analysis chamber. Table 6.3 summarises the results found. Comparing this to the glucose biosensors characterised in a beaker (Table 4.7) the sensitivity seems to be enhanced. This is due to mass transport of the analyte to the biosensors created by the flow. Overall, the response times are slower, but this is probably due to the placement of the sensors on-chip in relation to the ceiling height. Recessed electrodes will have a longer response time and the approximately 3-5 times larger standard deviations seen in the on-chip response times are probably due to positioning of the sensors on-chip.

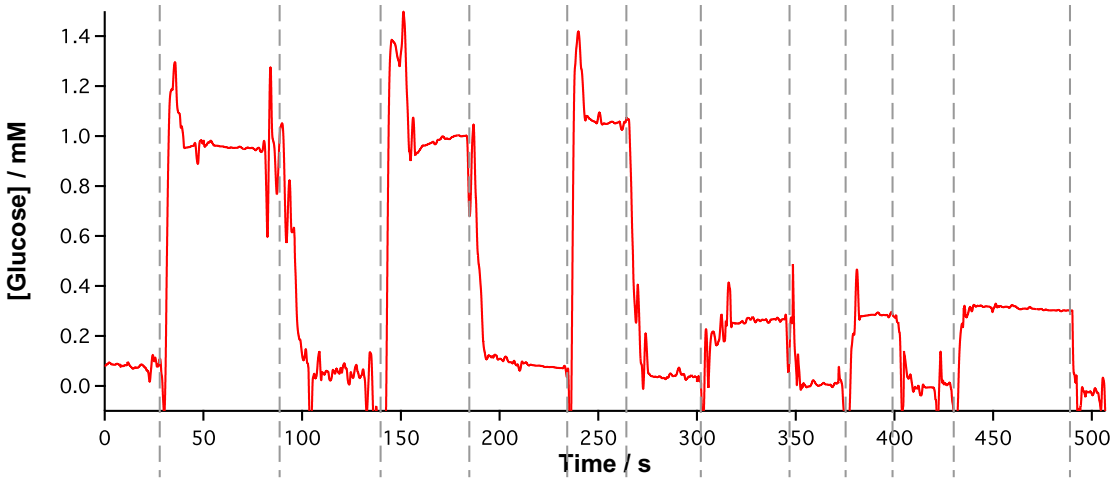


Figure 6.24: A glucose biosensor on-chip: calibration
Glucose biosensor: 50 μm diameter. Electrode held at a constant potential of 0.75 V. Solutions were alternated between PBS and 1 mM glucose at a flow rate of 2 μLmin^{-1}. The solutions then alternated between PBS and 250 μM glucose at a flow rate of 2 μLmin^{-1}. Grey dotted lines indicated when the solutions were switched.

This process needs further work to make it more accurate and reproducible. The LOD of the sensors is still within the same range as that seen in a beaker (a few μM).

Table 6.3: Continuous flow on-chip glucose biosensors at 2 μLmin^{-1}

Electrode size (μm)	Sensitivity (nAmM^{-1}cm^{-2})	T_{90} (s)
50 (n=13)	8.9 ± 0.9 x 10^3	14.3 ± 5.5
25 (n=7)	8.4 ± 2 x 10^3	15.4 ± 12.9

Droplet Flow

The sensors were placed on-chip and droplets of PBS and 1 mM glucose were alternated. Figure 6.25 shows the importance of correct positioning on-chip. Here the sensor is pushing on the PDMS design and distorting the geometry of the chip and the chamber is not catching the aqueous droplets but letting them pass straight through. Both the oil and the aqueous droplets are passing straight through the chamber, which is clearly seen as noise when 1 mM glucose droplets are running. The T_{90} of this sensor is 28.1 s.

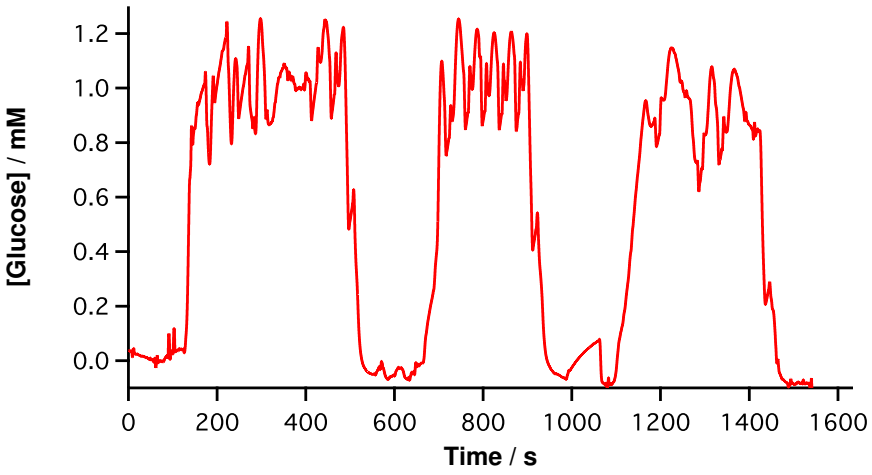


Figure 6.25: A glucose biosensor on-chip in droplet flow: chamber not working
Glucose biosensor: 50 μm diameter. Electrode held at a constant potential of 0.75 V. Solutions were alternated between PBS and 1 mM glucose at a flow rate of 2 μLmin^{-1} aqueous and 5 μLmin^{-1} oil.

Figure 6.26 shows a glucose biosensor in droplet flow, when it is correctly placed on-chip. Here the chamber is working correctly and is catching the aqueous droplets and filtering the oil through the side channels. The aqueous solutions were switched as before and the change in signal is much easier to see due to lower noise. The LOD is 12 μM glucose and the T_{90} of this sensor is 0.6 s. This shows the potential of the on-chip glucose sensors for monitoring online microdialysate in the intensive care ward.

However, table 6.4 displays the average sensitivity and response time of 50 and 25 μm glucose biosensors placed on-chip under the droplet flow regime. These figures are only for particular aqueous and oil flow rate (2 and 5 μLmin^{-1} respectively). The characteristics were investigated using these flow rates as it was found in section 5.8.1 that this was the optimal flow rate for functioning of the analysis chamber. We put the variability down to the electrode position within the length of the channel (not a problem for continuous flow) and with respect to the ceiling. Also problems with correct punching of electrode holes so that the chamber functions with electrodes in place.

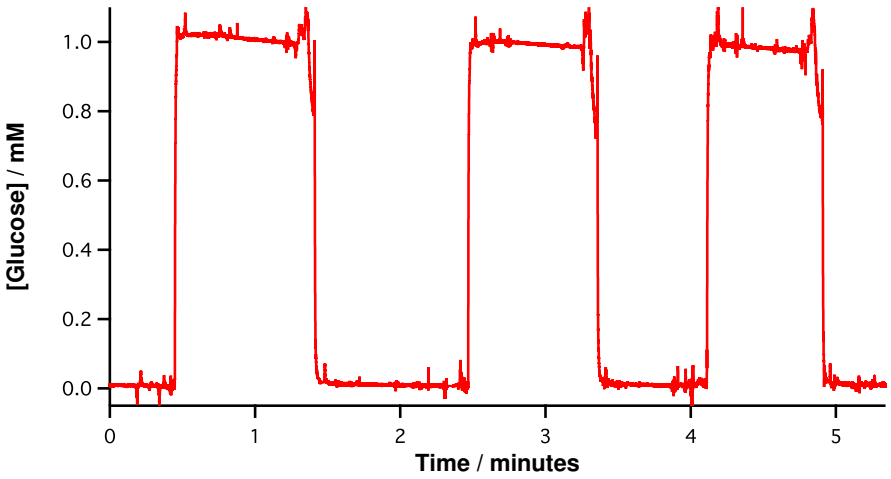


Figure 6.26: A glucose biosensor on-chip in droplet flow
Glucose biosensor: 50 μm diameter. Electrode held at a constant potential of 0.75 V. Solutions were alternated between PBS to 1 mM glucose and PBS to 0.5 mM glucose, at a flow rate of 2 μLmin^{-1} aqueous and 5 μLmin^{-1} oil.

Table 6.4: Droplet flow on-chip glucose biosensors at 2 and 5 μLmin^{-1}

Electrode size (μm)	Sensitivity (nAmM^{-1}cm^{-2})	T_{90} (s)
50 (n=3)	5.7 $\pm$ 1.7 x 10^3	34.3 $\pm$ 39.7
25 (n=7)	8.4 $\pm$ 2 x 10^3	13.2 $\pm$ 10.6

Overview

The glucose biosensors have been assessed in a beaker and on-chip in both continuous and droplet flow regimes. Table 6.5 assesses the sensors in terms of electrode size. The key factors are investigated and awarded ticks. Overall the 50 μm had a good sensitivity, LOD, T_{90} and it is the easiest to work on-chip. Therefore a 50 μm glucose biosensor will be validated in an *in vivo* study discussed in chapter 7.

Table 6.5: Assessment of glucose biosensors on-chip

Electrode size	Sensitivity	LOD	T_{90}	Feasibility on-chip
50	✓✓✓	✓✓	✓✓	✓✓✓
25	✓✓✓	✓	✓✓	✓✓

6.6.2 Lactate

Continuous Flow

Lactate sensors were also placed on-chip and characterised in the same way as the glucose sensors. Figure 6.27 shows the response from a 125 μm disc electrode fabricated as a lactate biosensor. The flow rate is 2 μLmin^{-1} and solutions were alternated between PBS and 1mM lactate. The large spike, as the solutions are changed back to PBS, is likely to be due to a change in flow rate.

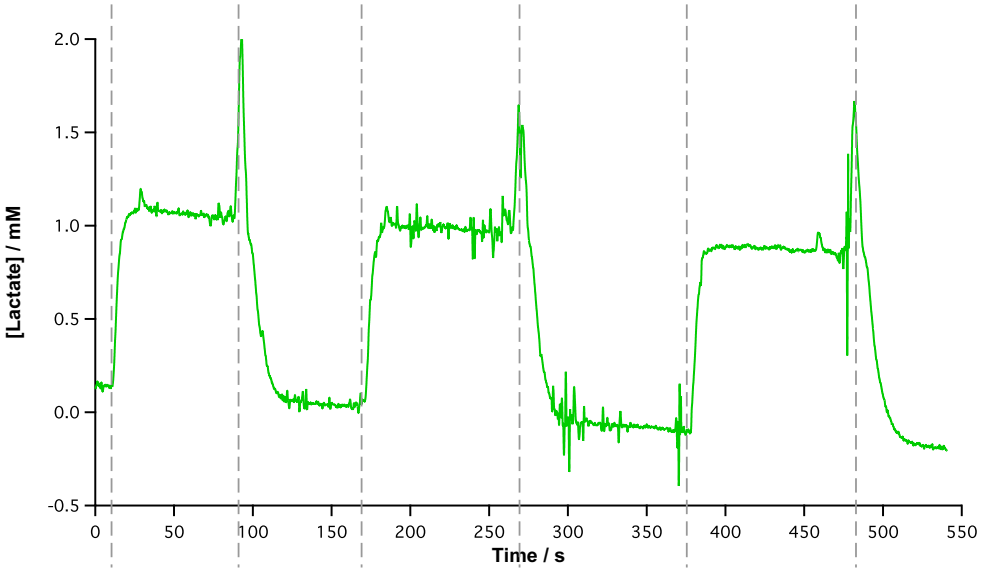


Figure 6.27: A lactate biosensor on-chip: calibration
Lactate biosensor: 125 μm diameter. Electrode held at a constant potential of 0.75 V. Solutions were alternated between PBS and 1 mM lactate at a flow rate of 2 μLmin^{-1}. Grey dotted lines indicated when the solutions were switched.

Table 6.6 gives a summary of the sensitivity and the 90 % response time for various sizes of electrodes, on-chip at a flow rate of 2 μLmin^{-1}. A few 25 μm diameter disc electrodes were fabricated into lactate sensors and placed directly on-chip. These too are included in table 6.6. The sensitivity of the 50 μm sensor is lower to that of the 50 μm glucose sensor (see table 6.3), likely due to the activity per gram as previously discussed. There seems to be more variation between sensors. This could be due to the low number of repeats. The response time is much longer on-chip, but when in a beaker the sensors responded in under 10 seconds. Therefore the placement on the chip was not correct and more repeats would possibly show a faster response time.

Table 6.6: Continuous flow on-chip lactate biosensors at 2 μLmin^{-1}

Electrode size (μm)	Sensitivity (nAmM^{-1}cm^{-2})	T_{90} (s)
125 (n=7)	1.3 ± 0.4 x 10^3	15.2 ± 8.2
50 (n=3)	6.5 ± 4.5 x 10^3	32.7 ± 13.2
25 (n=6)	3.9 ± 2.5 x 10^3	30.5 ± 11.7

Two different lactate sensors on-chip were placed in the same analysis chamber and their responses recorded simultaneously. A 50 μm lactate biosensor was placed upstream of a 125 μm lactate biosensor within the same analysis chamber. The solutions were changed between PBS and 500 μM lactate. Both sensors respond to the change in lactate and the downstream electrode responds 2.4 seconds later than the upstream sensor. This is due to the time delay for the solution to move between the sensors within the analysis chamber.

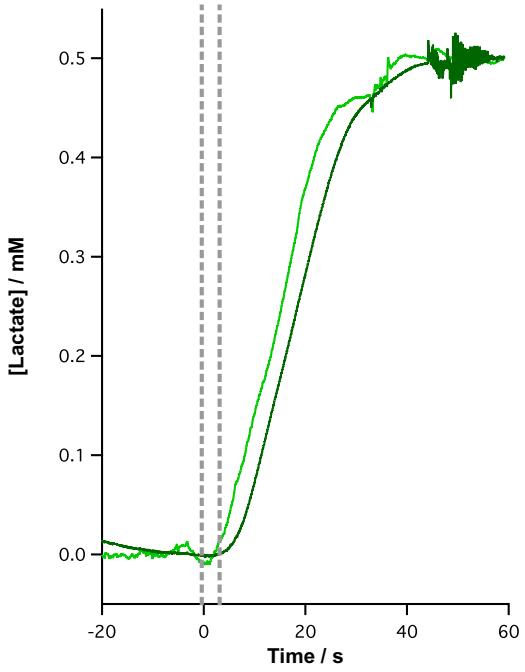


Figure 6.28: Two lactate biosensors on-chip: calibration
Electrodes were held at a constant potential of 0.75 V. Light green trace: 50 μm glucose biosensor. Dark green trace: 125 μm glucose biosensor. Solutions were alternated between PBS and 0.5 mM lactate at a flow rate of 2 μLmin^{-1}. The 50 μm lactate biosensor is upstream in the analysis chamber of the 125 μm biosensor. The time between the responses is 2.4 seconds.

Droplet Flow

The 25 μm diameter disc electrode were fabricated into lactate biosensors and tested in droplet flow on-chip. Figure 6.29 shows an example of the trace seen during this period. The on-chip flow rates were 2 μLmin^{-1} aqueous and 4 μLmin^{-1} oil. Droplets were alternated between 1 mM lactate and PBS. The T_{90} of this on-chip lactate sensor was 96 seconds. Whilst this seems very slow, it was since found that the positioning of the electrode within the PDMS chip is very important and so may be an limiting factor. The LOD (found by calculating 3 standard deviations of the baseline) was 62 μM and the sensitivity was 4.41 x 10^3 nAmM^{-1}cm^{-2}. The average sensitivity and T_{90} using 25 μm electrodes, on-chip in droplet flow, was 3.3 $\pm$ 1.5 x 10^3 and 20.8 $\pm$ 3.1 respectively (n=3). Due to further work investigating the properties of lactate sensors previously discussed, they were not tried again in droplet flow.

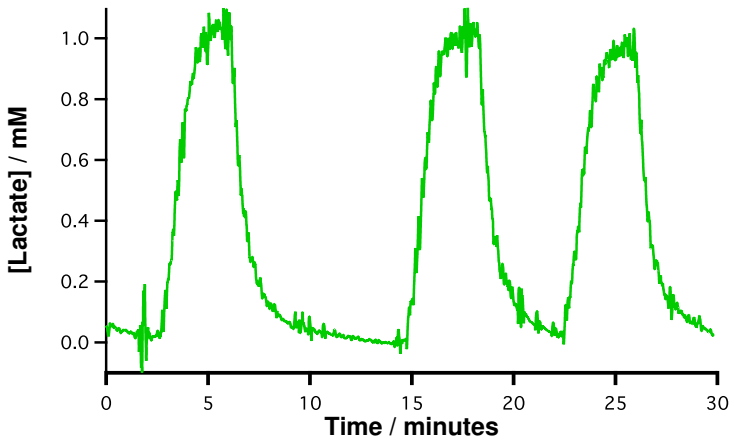


Figure 6.29: A lactate biosensor on-chip: calibration in droplet flow
Lactate biosensor: 25 μm diameter. Electrode held at a constant potential of 0.75 V. Solutions were alternated between PBS and 1 mM lactate at a flow rate of 2 μLmin^{-1}. Oil flow rate was 4 μLmin^{-1}.

Overview

The lactate biosensors have been assessed in a beaker and on-chip in continuous and droplet flow regimes. Due to the need for further optimisation only one size was used in droplet flow and so no comparison between sizes can be made in the droplet flow regime. However, the results from the beaker and continuous flow look promising and with further optimisation would be ready for use in droplet flow.

6.6.3 Multi-Analyte

A glucose and a lactate sensor were tested on-chip. They were made on two separate needle electrodes due to the cross talk previously discussed. The glucose biosensor was fabricated on a 50 μm disc electrode and the lactate on a 125 μm disc electrode. The analysis chip was connected to a syringe pump, which alternated solutions of 1 mM glucose and 1 mM lactate at 2 μLmin^{-1} via syringe taps. The results of the initial experiments are shown in figure 6.30. Initially it seems as though both sensors are a glucose sensor. The change in current at the larger lactate sensor is approximately 20 pA and at the smaller glucose sensor, approximately 65 pA. The syringe containing 1 mM glucose was removed from the pump and replaced with one containing PBS. The solutions were alternated between PBS and 1 mM lactate. Now only the lactate sensor responds. The response to a change of 1 mM lactate is 17 pA.

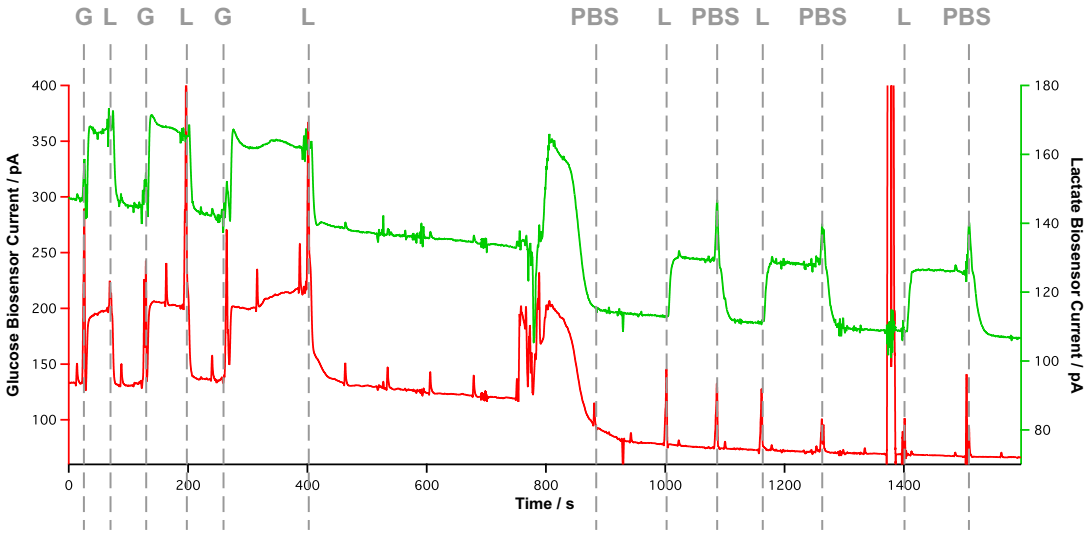


Figure 6.30: A glucose and lactate biosensor on-chip: contamination
Glucose (red) biosensor: 50 μm diameter. Lactate (green) biosensor: 125 μm diameter. Electrodes were held at a constant potential of 0.75 V. Solutions were initially alternated between 1 mM glucose (G) and 1 mM lactate (L) at a flow rate of 2 μLmin^{-1}. The 1 mM glucose syringe was then changed to one containing PBS and the solutions alternated between PBS and 1 mM lactate (L).

It was concluded that the lactate biosensor was somehow contaminated with glucose oxidase. New integrated electrodes should be fabricated and used only as lactate biosensors. A further study should look at whether the sensitivity of the lactate sensors change as a result and both a glucose and a lactate sensor should be tested together on-chip.

6.7 Conclusion

This chapter discussed the integration of electrodes onto the microfluidic platform. It was shown optically and electrochemically, that digital microfluidics eliminates Taylor dispersion, a phenomena seen in continuous flows that acts to smear out fast concentration changes. Within the microfluidic analysis chamber, a step change in concentration at the point of coalescence, had a T_{90} of < 2 ms, which is the time taken for the interfaces to join together. Further into the analysis chamber, the response time increased, indicating that the electrode must be as close as possible to the coalescence point to take full advantage of this effect. All measurements gave a huge increase in the time resolution, dramatically improving the potential of microdialysis to measure small, fast changes.

It was found that the punching of electrode hole was crucial to the functioning of the analysis chamber. The PDMS wall was easily lost if the hole was incorrectly punched and if too close to the walls or positioned at an angle, the large and rigid electrode could deform the chamber design, rendering the chamber useless. However, needle electrodes were successfully incorporated on-chip, and the electrodes were first tested using redox couples and electrochemistry. Glucose and lactate sensors were then fabricated and placed on-chip and the responses compared to that seen in a beaker. There were large variations in the response of the sensors, even in continuous flow. By simple diffusion field arguments, it was thought that the optimal position of the electrode was flush to the ceiling of the chamber. However, analysis of the flow dynamics within the chamber suggests that this is not the case, due to a memory effect caused by the build up of previous droplets horizontally along the chamber wall. The electrode should therefore be positioned in the middle of the chamber, where the bands are vertical. The needle electrode in this position would also disrupt the flow inducing convective mixing and stop the bands from forming. Introducing baffles on the wall of the chamber would also have the same effect. Positioning the electrode close to the point of coalescence has the added advantage that the bands here are more vertical, making the positioning of the electrode in the middle less crucial (an advantage as currently this is very difficult). Parts of the work discussed in this chapter has been published in the journal, Physical Chemistry Chemical Physics.

Dual electrodes were also assessed on-chip, and it was shown that the flow added a convective component to the diffusion field geometry. As expected, cross-talk occurred within the dual electrode, however two separate needle electrodes held within the same chamber eliminated the effect. This will compromise the response

of the downstream electrode by being further away from the point of coalescence but it does allow for multi-analyte detection. An alternative solution for multiple sensors could be to have several smaller detection chambers placed in series. In this way, each microelectrode can be positioned at the optimal location, the chamber size can be reduced to house only one electrode and as the droplet stream is re-formed after each chamber, the inherent time resolution of digital microfluidics is conserved between each analysis.

Chapter 7

On-Line Analysis of Microdialysate, *in vivo*

7.1 Introduction

7.1.1 Clinical Background

Traumatic brain injury (TBI) has been described by The Lancet Neurology as a silent epidemic (29) as around the world, TBI is a major cause of death and disability. Alarmingly, the UK incidence of TBI (238 - 458 / 100,000 population) is higher than that of breast cancer (120 / 100,000 population) (217). Public awareness of TBI remains low, and no new treatment has been approved in the past 30 years. The primary injury often causes a focal injury site, such as a haemorrhage. This causes local ischemia. This lack of blood flow starves the local region of oxygen and glucose, leading to changes in metabolism. Over several days, the injured area may increase in size, called secondary injury. Secondary injury is a subject of much clinical research. Patient outcome is hugely variable, as the occurrence of secondary injury is very unpredictable and a conservative wait-and-see approach is taken whilst the patient is being monitored in intensive care. Here, the patient is put in a drug induced coma to switch of brain activity and decrease the energy requirements in the injured areas. The classical covariates used to determine the outcome of TBI are age, motor score, pupil abnormalities, hypoxia, hypotension and the Marshall CT scale. However, the IMPACT study by Murray et al showed that these commonly used covariates only explain 30% of the variance in TBI outcome (52).

Spreading depolarisations (SDs) were first observed in the human brain by the Boutelle/Strong collaboration (40) and have subsequently been shown to occur fre-

quently in the injured brain (41). The mass depolarisation of cells, first described by Leao in 1944 (36), propagates like a wave over the cortex, leading to failure of ion homeostasis and disruption of cortical function. The depression of the electrical signal coincides with a large increase in extracellular potassium as the neuronal cells depolarise, an increase in blood flow and changes in metabolism due to the high demand of energy presumably to re-polarise the cells (37, 38).

These waves have been characterised using rapid sampling microdialysis, to give a chemical signature of an SD waves in patients (53). Notably, glucose levels are seen to decrease and lactate levels increase as the waves pass (57). It has previously been shown using microdialysis that SD waves are potentially harmful and may cycle around the site of injury, explaining the repetition at regular intervals seen in some patients (218). This repetition can drive down the local glucose concentration, possibly to a level where the tissue is no longer viable (53).

7.1.2 Translational Studies

Ischemia leads to a decreased energy production, which results in neuron depolarisation. Animal models of ischemia tend to reduce the levels of oxygen and glucose in the brain (56, 57). The pathophysiological outcomes are dependent upon the severity, location and duration of the ischemia within the brain (219).

Animal models have used a wide range of species, initially with gyrencephalic brains (folded cortex like a human brain) but more recently rats and mice. Rats have a small brain size allowing ease of fixation for sections and histology, commonly used after brain infarction. However, the brain of a rat is not folded and has less supporting glial cells than a human brain.

A successful study of SD waves, needs to have a method of initiating the wave, either an injury model leading to spontaneous SD waves, or a means acutely stimulating them. Both require a method to detect and monitor the wave progression. There are several models used in the literature and in this thesis, which are now discussed.

Acute Stimulation: Middle Cerebral Artery Occlusion

Middle cerebral artery occlusion (MCAO) is a technique used to model the effects of stroke. There are several variations of this technique but all produce a heterogeneous tissue state. A necrotic core is at the centre, surrounded by a penumbral, at-risk, area. This stroke model provides a highly useful approximation of ischemia in humans (220). The SD waves are spontaneous and one variation used

with microdialysis is where the artery is clipped, shutting off blood flow (56). Other variations involve the injection of an artificial sphere (or blood clots) into the cerebral circulation. Spheres that are approximately 300 μm tend to cause blockages in the proximal middle cerebral artery (MCA), whereas spheres approximately 50 μm in diameter causes blockages in distal regions.

Acute Stimulation: Spreading Depolarisations

There are several methods of evoking a depolarisation event. The micro injection of potassium chloride into the cortex was used by Hashemi et al (57). Cotton buds infused with KCl can also be placed on the cortex, triggering SD's. Similarly, pricking the cortex with a needle tip or pin, will elicit the same response. Both the cotton bud and needle prick methods are used in this thesis.

Imagining Techniques

There are many ways of imaging the propagation of SD waves. Optically intrinsic imaging was used to measure depolarisation's (221, 222) and with the use of voltage sensitive dyes (223, 224). Depolarisation's are associated with an increased light reflectance and was used to record changes in the extracellular space.

Fluorescence imaging was used by Hopwood et al (56) to monitor changes associated with the reduction of the NAD/H couple, as described by Strong et al (225), and monitor the propagation of depolarisation's over the cortex.

Another technique, laser speckle flowmetry (LSF), is a time-varying imaging technique that is used in biological applications to measure moving objects, such as red blood cells. Speckle is a phenomena, which is observed when a highly coherent light beam is diffusively reflected from a rough surface, producing a random interference pattern. It only came into prominence with the invention of the laser in the 1960s as it is can easily be observed when a laser beam hits a rough surface such as white paper. Speckle patterns result from the interference of many wavefronts of the same frequency but each have different magnitudes and phases. When added together, the intensity of the light seems to vary at random, however it was soon discovered that these patterns carry information about the surface deformations. When the particle moves, a time-varying speckle pattern is produced at each pixel of the captured image and when the fluctuations are rapid the pattern becomes blurred (226). Quantifying the blurring of the speckles allows a two dimensional map of blood flow to be formed.

Real time measurement of cerebral blood flow (CBF) using LSF, has been used to study SD propagation under both normal (57) and ischemic (49, 57) conditions. It has been shown to be a good tracker of depolarisation waves (49, 226) and is a semi-quantitative measure of dynamic CBF (227). LSF has high spatial and temporal resolution (10 to 25 μm and 10 to 50 ms respectively) providing a high resolution map of the evolution of cerebral blood flow (226).

7.1.3 Testing of the Microfluidic System for the Clinic

Before the new microfluidic system can be incorporated onto a clinical ward, it must be thoroughly tested. During my PhD I had the opportunity to spend two weeks at the Max Plank Institute (MPI) for Neurological Research in Cologne. Animal studies using rats, tested the microfluidic system. The dialysate was analysed using microelectrodes fabricated into glucose biosensors and was validated by rsMD (our gold standard). A potassium ion selective electrode (ISE) was also included (developed by Ms Chi Leng Leong) to give a clear chemical time point for the beginning of the depolarisation wave.

7.2 Animal Studies

To assess the microelectrodes in a flow system, before clinical use, a pilot study was conducted in rats comparing the performance to rsMD analysis. The microfluidic lab equipment and the sensors were transferred to the Max Plank Institute for Neurological Research in Cologne, Germany for two weeks. During this time, several models of ischemia were tested in collaboration with Dr Delphine Feuerstein and Dr Rudolf Graf.

7.2.1 Methods and Setup

The procedure for all animal studies is set out below, followed by the methods for the models used in this study.

Anaesthesia

All animal procedures were carried out in accordance with the German Laws for Animal Protection and institutional guidelines. For all experiments, rats (Male, Wistar) were anaesthetised with 5 % isoflurane delivered in air at 3.0 Lmin^{-1} for 2 minutes. Anaesthesia was maintained between 2 and 3 % isoflurane delivered in air at 0.5 Lmin^{-1}. Throughout the procedures, rectal temperature was maintained at 37.5 °C with a thermostatically controlled heating pad. Exclusion criteria include normality of blood gases, glucose, potassium levels and blood pressure, normality of MD basal levels of glucose and potassium, consistent basal value of cerebral blood flow and normality of SD propagation rate.

Imaging

In all experiments, the skull was thinned and the cortex illuminated with a laser diode (DL7140-201, 785 nm, 70 mW, Sanyo, Japan) to produce a speckle pattern. The speckle was captured using a CCD camera (A602f-2 BASLER, Ahrensburg, Germany) using Speckle Contrast Imaging Software. The region of interest (ROI) 1 is defined as 1 mm from the probe towards bregma, and ROI2 is 1 mm away from bregma.

Probe and sensor placement

An animal microdialysis probe (MAB 6.14.2) was implanted 4.5 mm posterior and 3.5 mm lateral from Bregma through a small durectomy, at a rate of 5 $\mu\mathrm{ms}^{-1}$ using a piezoelectric motor, whilst perfusing with aCSF at 1.6 $\mu\mathrm{Lmin}^{-1}$. The probe was inserted acutely to the full membrane length (2 mm). A parenchymal potassium

electrode was also implanted into the brain (4 mm posterior and 3.5 mm lateral from Bregma), which was fabricated by Dr Delphine Feuerstein.

Droplet flow

A microfluidic T junction was connected to the MD probe outlet. Oil could then be pushed through the system when required, by turning on the syringe pump to create droplets of microdialysate. The droplets were transferred to an analysis chip containing a glucose biosensor and a potassium ISE, fabricated by Ms Chi Leng Leong.

Continuous flow

The MD probe outlet was connected directly to a microfluidic analysis chip containing a glucose biosensor and a potassium ISE. The dialysate stream was then fed to the rsMD valve for FIA measurements of glucose and lactate. A photograph of the full setup is shown in figure 7.1. A close up of the probes positioned in the brain is shown in figure 7.2.

Equipment and Sensors

The glucose biosensors used in this chapter are combined needle electrodes of either 25 μm or 50 μm in diameter. The fabrication and characterisation is described in chapter 4 and on-chip in chapter 6. This chapter also refers to a potassium ISE, which was developed and fabricated by PhD student Ms Chi Leng Leong. A photograph of the sensors on-chip within an in-house faraday box is shown in figure 7.3. The rsMD system used in the animal procedures, is described in chapter 2. It is a system, which resides in Cologne for neurochemical analysis of brain injury and stroke patients in the hospital.

Euthanasia

By law, euthanasia is the end point of all procedures used in this study. Euthanasia was induced by the intravenous injection of a high concentration of potassium chloride (3M KCl).

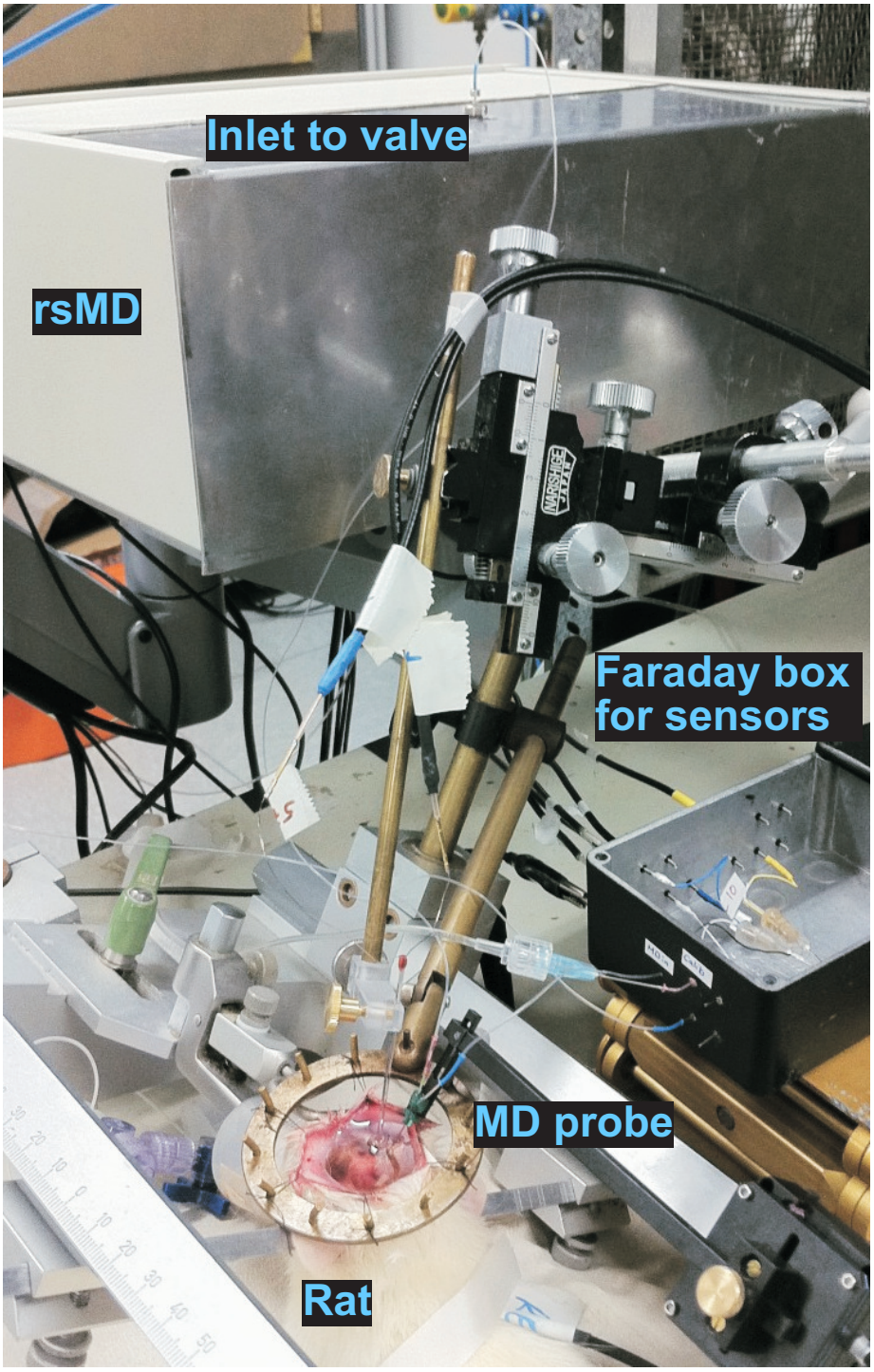


Figure 7.1: Setup for animal experiments in MPI, Cologne
The rat is facing top left. The skull has been exposed and thinned. A MD probe and a K^+ electrode, has been positioned into the cortex and the outlet is connected to the microfluidic chip containing different sensors. The microfluidic chip and sensors are housed in a purpose built faraday box. The outlet of the chip is connected to rsMD.

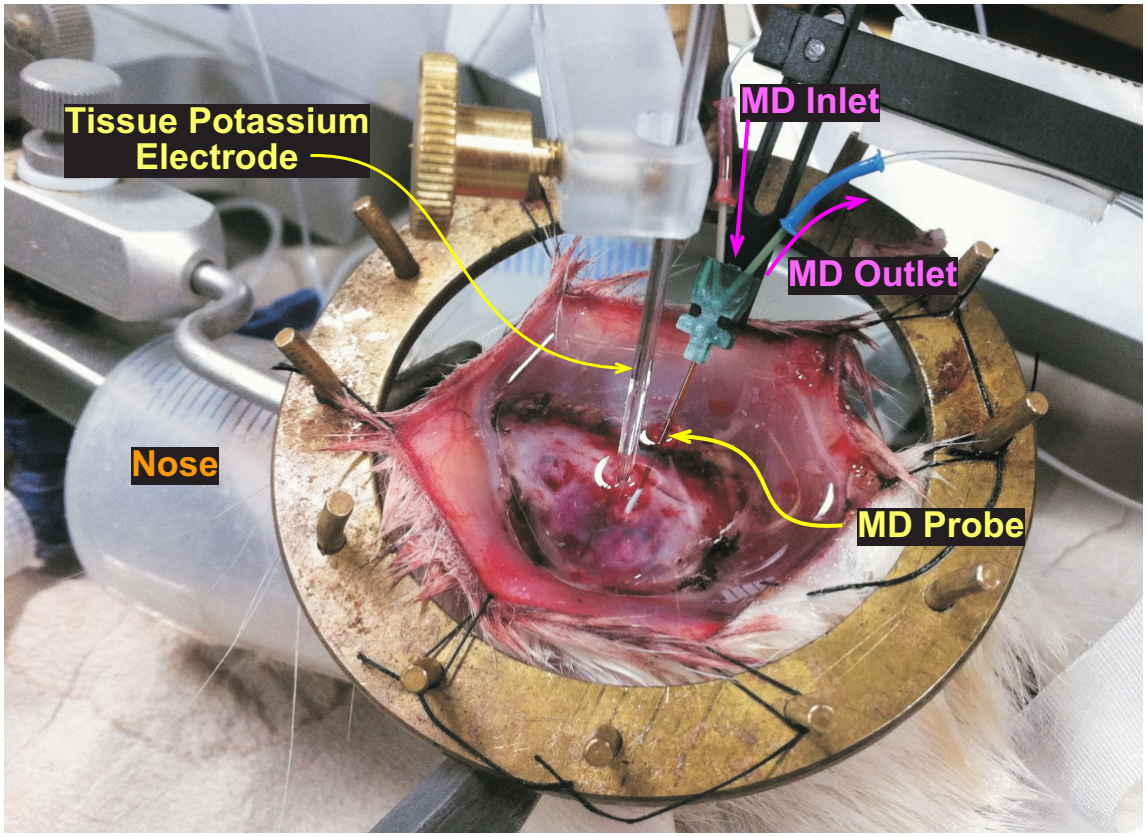


Figure 7.2: Close view of setup of probes in the rat in MPI, Cologne
The rat is facing top left. The skull has been exposed and thinned. A MD probe and a K^+ electrode, has been positioned into the cortex and the outlet is connected to the microfluidic chip containing different sensors. The skull is covered with protective oil. The microfluidic chip and sensors are housed in an in-house faraday box. The outlet of the chip is connected to rsMD.

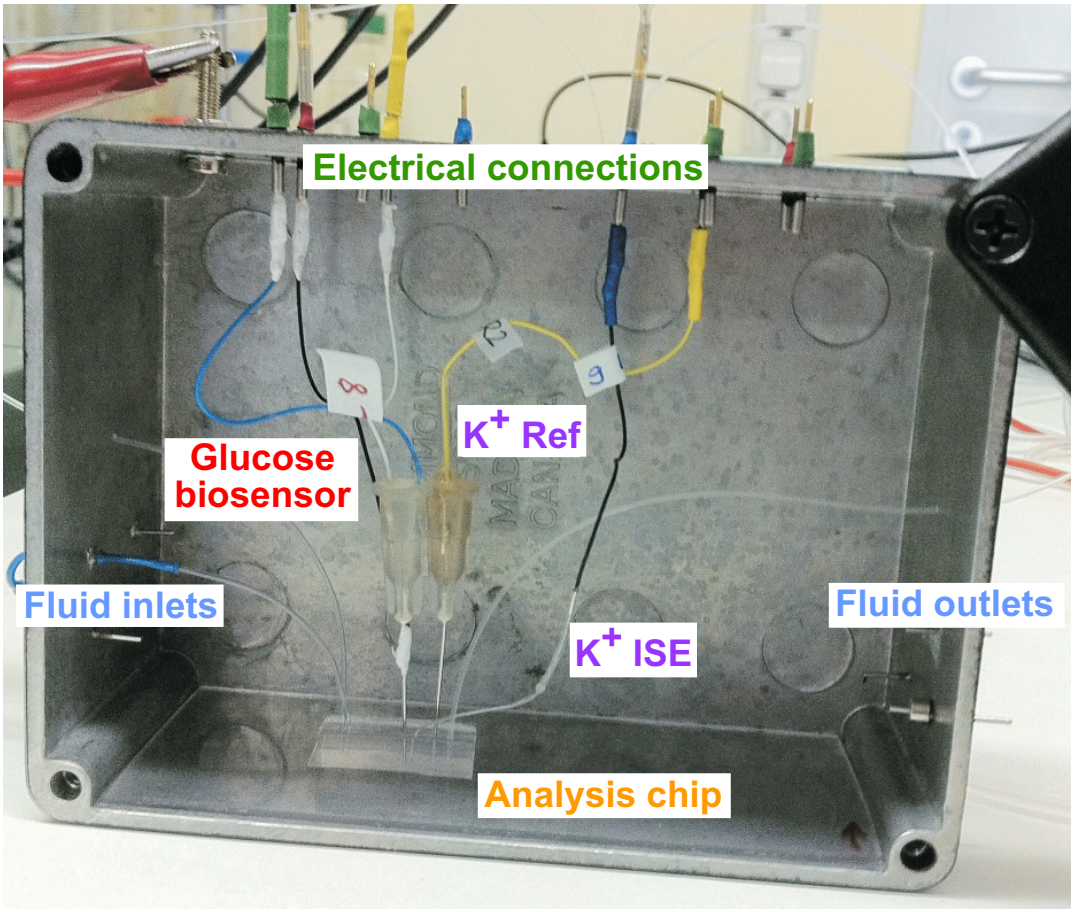


Figure 7.3: Close view of the sensors in an analysis chip in a faraday box
The fluid inlets and outlets are on the sides and the electrical connections are on the top face. A combined electrode has been fabricated into a glucose biosensor. A potassium ISE has a separate reference electrode in a side arm of the microfluidic chip.

Middle Cerebral Artery Occlusion

A TiO_2 macrosphere (diameter 0.315 - 0.355 mm, BRACE, Alzenau, Germany) was injected in to the circulatory system with the intention to block the MCA and emulate a stroke. One macrosphere was slowly injected with ∼0.2 mL of heparinised saline into the internal carotid artery (ICA) via a catheter (PE-50). The macrosphere location was determined by post-mortem examination, where the brains are removed from the skull and the cerebral arteries visually inspected.

SD Stimulation

SDs were induced via the application of a KCl (3M) infused cotton bud to the thinned skull. The cotton bud was in place for 30 minutes after which it was removed. The application of the cotton bud can evoke SDs, which circle over the dura. The circling of SD waves is sometimes seen in human patients where it can drive down the local glucose concentration if the tissue does not have enough time to fully recover before the next wave hits (53).

The needle prick (NP) model causes focal ischemia by stimulating a precise area of the cortex. A single needle prick on the cortex reliably induces a SD (228). The needle prick model has been successfully used to investigate SDs (229) and has been used in this thesis to study the potassium, glucose and blood flow changes during an event. The needle prick model was used to provide a larger stimulus than the cotton buds, which will hopefully be recorded on the rsMD glucose. Then the on-chip biosensor can be properly assessed.

In this model two different locations were stimulated and it was found that an ischemic event could be induced each time. The rat was given time to rest in between subsequent needle pricks so that a baseline of normal state could be recorded before each stimulus. Figure 7.4 indicates the relative locations of the probes and stimuli used in this thesis. The first trauma location was approximately 0.5 mm anterior and 3.5 mm lateral and the second location was approximately 3.5 mm posterior and 6 mm lateral from Bregma.

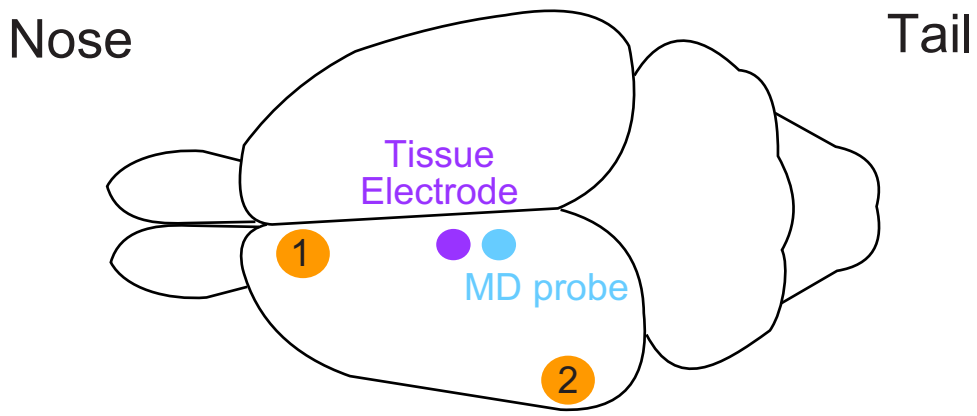


Figure 7.4: Depiction of relative positions of probes and stimuli on the rat cortex
The blue circle and purple circle indicates the position of the MD probe and the parenchymal electrode (if used) respectively. The orange circles indicate trauma sites. The cotton bud and needle prick were stimulated in position one. A second needle prick was also conducted at position two. In this diagram, the nose of the rat is towards the left and the tail towards the right.

Data presentation

All data shown in this thesis has been time aligned so that the events are synchronised between analysis techniques. Figure 7.5 shows the overall setup for the animal procedures. At t_0 the microdialysis samples the ECF during the event. It then takes time t_1 for the sample to reach the on-chip sensors. This is approximately 1 minute in droplet and 3 to 4 minutes in continuous flow. There is then a time, t_2, which is the delay of transferring the same sample to the rsMD analysis system. This is typically 8 to 10 minutes. Initially the on-chip sensors and rsMD were calibrated individually and the time delays calculated from the lengths of connection tubing. This made time aligning the datasets difficult as the PDMS chip swelled and the tubing connections had some dead volume. Therefore there was no clear event to accurately calculate the time delays created by transferring the solutions.

During the second opportunity to conduct these experiments, this was addressed and a calibration solution was passed through the chip via a side channel, also shown in figure 7.5. The solution therefore passed through the analysis chamber and calibrated the on-chip sensors and an accurate time delay (t_2) can be found between the sensors and rsMD. Also a recovery protocol was introduced, where the MD probe was transferred to a solution of glucose and potassium. This not only checked that the MD probe was working, but gave a recording of t_1 and a confirmation of t_2.

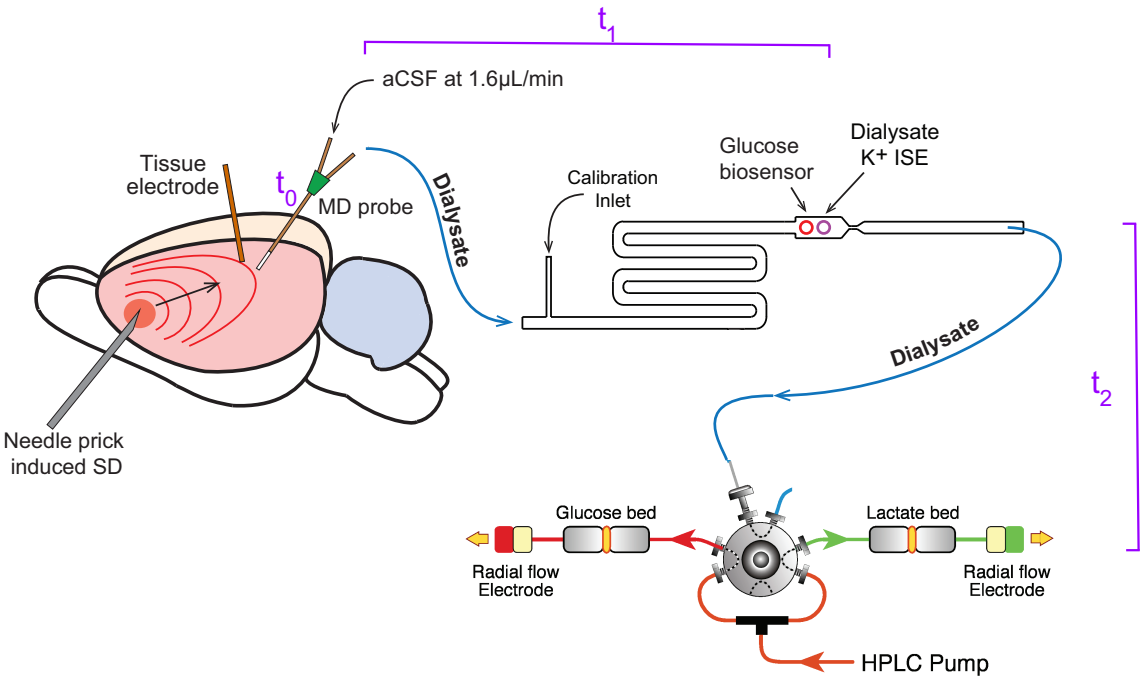


Figure 7.5: Schematic of animal set-up

Schematic shows event for a needle prick experiment in continuous flow. The needle prick initiates a SD waves that travels over the cortex (imaged by laser speckle). At t_0 the event is sampled by the MD probe. There is then a time t_1 until the sample is analysed by the on-chip sensors. The sample is then transferred to rsMD via connection tubing creating a time delay of t_2. Not to scale.

7.2.2 Results: Droplet Flow

The digital microfluidic set-up was tested. During the experiment, the on-chip potassium ISE failed and so the only measurements recorded on-chip was from the glucose biosensor. The parenchymal electrode, measuring tissue potassium, EEG and DC potential, was also used. However, due to no reliable way of removing a continuous stream from the analysis chip, the dialysate was not passed through rsMD for comparison. Figure 7.6 shows the events during droplet flow and all data is time aligned.

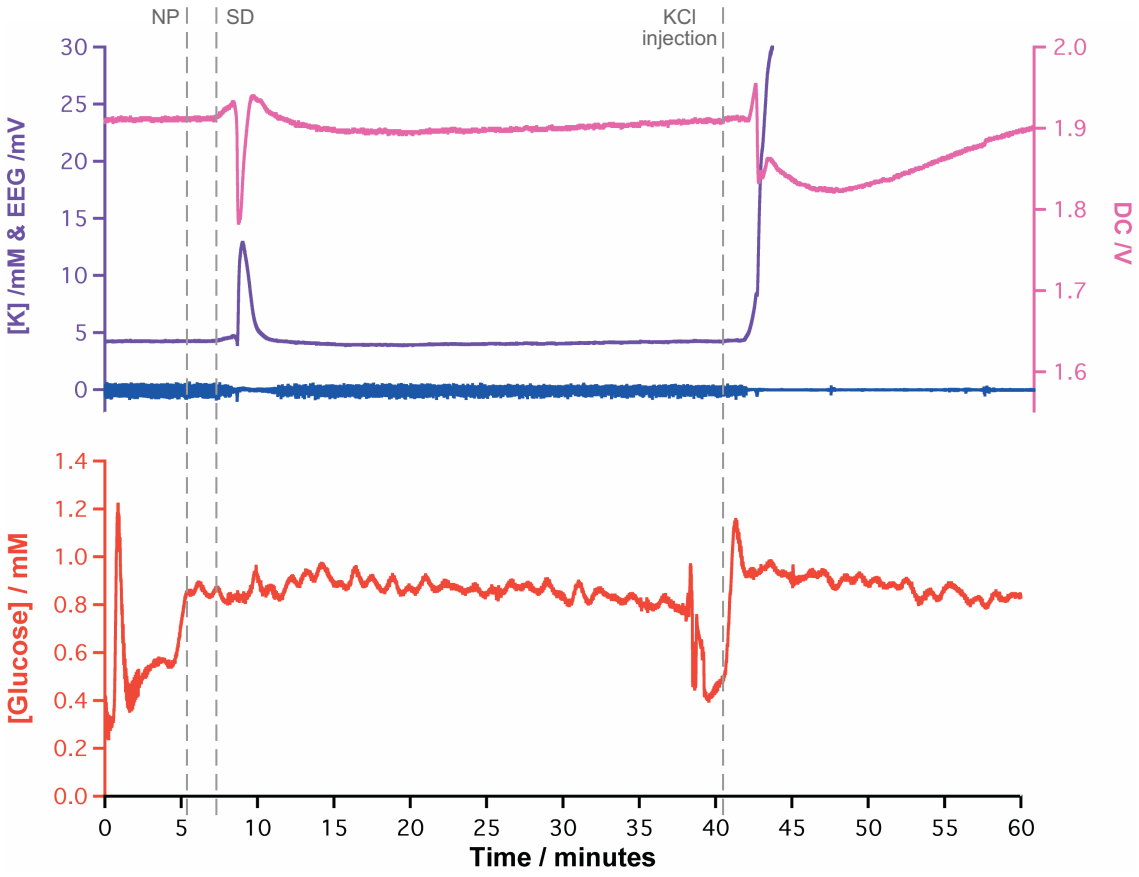


Figure 7.6: Needle prick and cardiac arrest in droplet flow
DC (pink), tissue K^+ (purple) and EEG (blue) shown in top graph. Glucose (red) is shown in the bottom graph. Digital microfluidics was run at a dialysate flow rate of 1.6 μLmin^{-1} and FC-40 oil flow rate of 8.4 μLmin^{-1}. Oil pump is turned on at time zero. Grey dotted lines indicate external events. NP = needle prick SD = spreading depolarisation wave.

A needle prick (NP) at site one was conducted as indicated by the first grey line. This evoked a SD wave, which was in the area of the implanted tissue electrode at a time indicated by the second grey line. At this point, the DC potential decreases sharply, the local potassium increases suddenly and the EEG is seen to flatten.

Unfortunately the SD caused by the NP was seen to pass just below the MD probe on the laser speckle video and the biosensor did not show any evidence of a SD. The tissue electrode was in a slightly different position to the MD probe and therefore does detect the SD wave passing. After the needle prick, the glucose biosensor was quite noisy. It is thought that perhaps the chamber was not functioning 100 % and some oil was passing through the chamber. This would create noise in the trace seen by the biosensor and cause the on-chip potassium ISE to fail (which indeed it did).

After 30 minutes the rat was euthanised by a 3 M intravenous KCl injection. This is clearly seen in the parenchymal electrodes, where there is a large increase in potassium, a permanent flattening of the EEG signal and a decrease in the DC potential. There is some disturbance of the glucose signal seen as the rat is prepared for injection and the glucose levels returned to higher than before the injection. In this experiment, lots of things were not working. The level of glucose recorded by the biosensor is higher than past levels of microdialysis brain glucose. There was no change during the needle prick in the dialysate but there was a clear SD wave passing the nearby tissue electrode. This could be due to the biosensor used on that day not functioning as well as previous sensors, or it could be working well and representing the glucose changes. Without a method of comparing the biosensor to a gold standard no conclusion can be made about this data set. Therefore, the experiments following were conducted in continuous flow, where the dialysate could be passed to rsMD for confirmation of glucose levels. Also, this allows successful recording from the on-chip potassium ISE. Connection tubing from the MD probe to the on-chip sensors was reduced to the smallest length to reduce dispersion.

7.2.3 Biosensor Validation

To validate the biosensor performance, continuous flow was used in the following experiments. This allows a chemical marker of the SD in the dialysate (on-chip potassium ISE) and further analysis of glucose and lactate levels via rsMD. To ensure that the microelectrodes were capable of detecting biologically relevant concentrations of glucose, the results from the glucose biosensor within the microfluidic chip were compared to the results from rsMD. This section will look in more detail to the levels of glucose recorded by both analysis techniques.

A glucose biosensor was fabricated on a 50 μm Pt disc integrated electrode and placed on-chip, where it was calibrated before being transferred to the animal room. The rsMD system was calibrated in the usual way.

Figure 7.7 shows a time course of the experiment with recordings from both rsMD (red) and the biosensor (orange). Time zero is the marker used to time align the two different analysis techniques (in this case the first needle prick). There is a large range of concentration from approximately 0.4 mM to 1 mM over the course of the experiment. This was one of the sets of data used to investigate how well the two analysis techniques correlated.

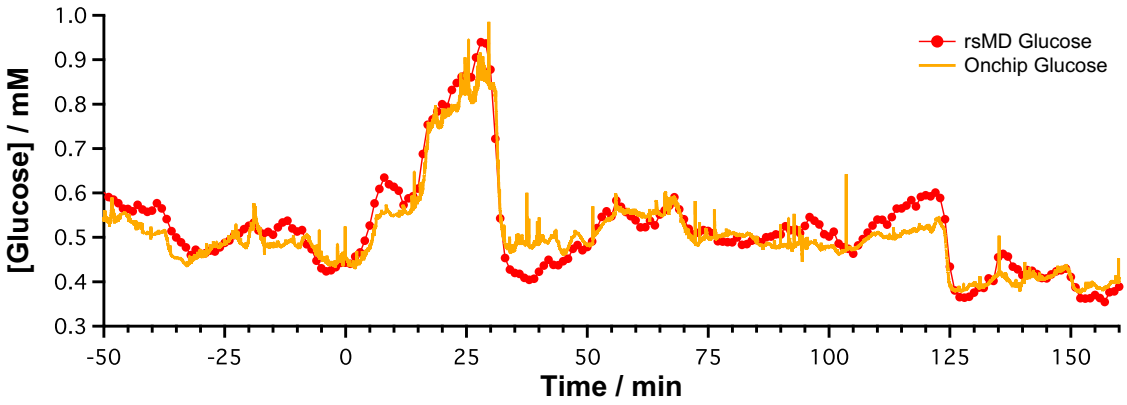


Figure 7.7: Glucose biosensor versus rsMD
A full experiment of over 200 minutes, comparing the online rsMD glucose levels in red and the on-chip glucose biosensor in orange. Levels have been converted to concentration after individual calibrations and the two traces have been time aligned.

The Clarke error grid was devised in 1987 to quantify the clinical accuracy of devices for the monitoring of blood glucose in diabetic patients (230). Figure 7.8 shows the on-chip biosensor and rsMD glucose comparison with a Clarkes grid laid over the top. The majority of points lie within the A band. This is the 95 % accuracy bracket. The other regions are most relevant to comparing sensor performance to the blood glucose, and indicate the outcome of using the device (inappropriate or unnecessary treatment, B and C, or failure to detect hypoglycemia or hyperglycemia, D, or confusion between hyper- and hypoglycemia, E).

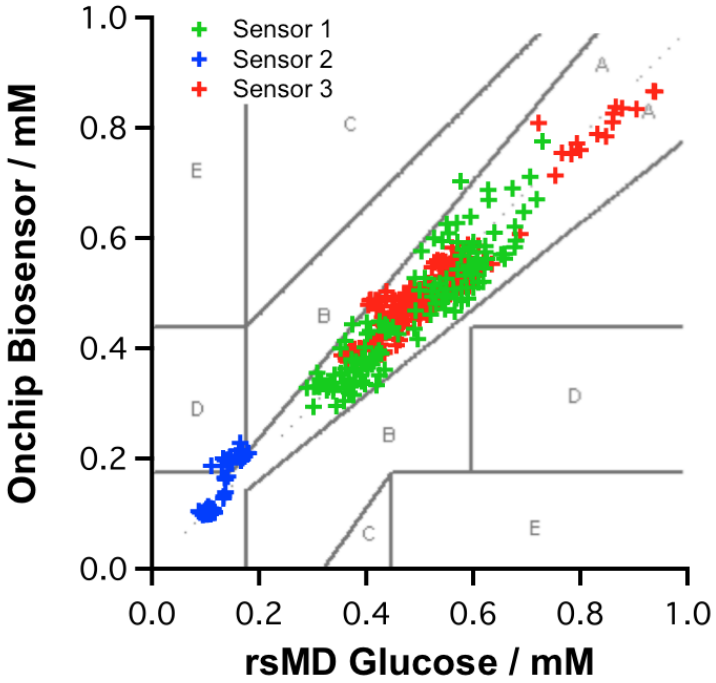


Figure 7.8: Glucose biosensor validation with Clarkes grid
Glucose biosensor readings versus the concentration detected by rsMD. Three biosensors individually fabricated and tested on different days are shown. The Clarkes error grid is overlaid in grey. The majority of points lay within the A banding.

Whilst error grids provide accuracy for paired static data, they do not account for the timing of paired results, which in continuous glucose monitoring is an important factor (231). Therefore the mean difference provides a better estimation of a continuous sensor performance and for the biosensor assessed here, this is shown in figure 7.9. Looking across the spread of this data, the standard deviation of this combined data is 40 μM. This includes error from both the biosensor and rsMD. The estimated error in rsMD is approximately 8 - 20 μM alone (53, 91).

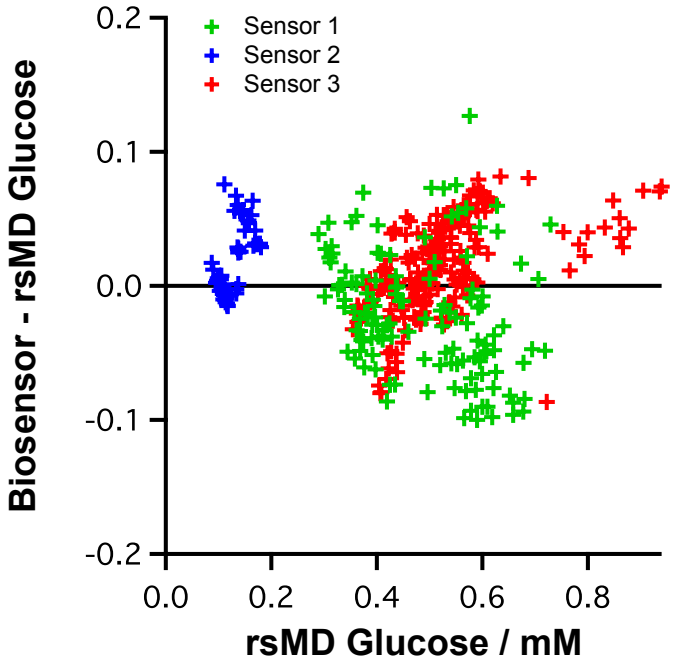


Figure 7.9: Glucose biosensor validation
A more stringent test of validation, comparing the difference in the two analysis techniques to the gold standard rsMD glucose concentrations.

Each animal model used in the pilot study, compares the glucose biosensor to the rsMD glucose analysis. To analyse the data and assess the biosensor, the raw data was individually calibrated and converted into concentration. The two data sets were then time aligned and the glucose levels compared. The results from each of these will now be discussed.

7.2.4 Results: Insertion of the Microdialysis Probe

A novel procedure was used, to implant the microdialysis probe, which allows for the first time to see the dynamic effects of insertion upon the tissue. The MD probe was implanted using a piezo-electric motor at a rate of 5 μms^{-1}, whilst being perfused with aCSF at a rate of 1.6 μLmin^{-1}. Cerebral blood flow increases during the implantation of the probe. This is shown in figure 7.10, which shows the laser speckle images and in Video 9 on the associated DVD. The areas of red indicate that there is higher blood flow in that region. This increased blood flow is easily seen in the surrounding area of the probe and is seen to radiate from the implantation site. This is characteristic of an SD wave.

Looking at the data of the online biosensor, during the implantation of a MD probe, the level in glucose increases. Figure 7.11 shows the raw data from the glucose biosensor and the corresponding data from rsMD. Again, this data has been time aligned to take account of time delay in analysis. Before implanting the MD probe, both analysis techniques are sampling aCSF only. For rsMD this gives zero peaks, but in the biosensor there is some background current generated.

The act of implanting a probe or an electrode into the brain causes localised stress to the tissue (75). In fact, the act of implanting a MD probe or tissue electrode is not dissimilar to a needle prick. A piezo-electric motor was used to try and reduce some of this stress by implanting the probe at a slow and constant rate. The glucose concentration increases slowly due to the sampling length of the membrane increasing as it is implanted. During this period the steady state is being set-up. At the peak recording, the concentration is approximately 1 mM and 900 μM for the rsMD and on-chip biosensor respectively. The act of implantation causes an increase in blood flow and hence an increase in glucose delivery. The SD wave will cause a decrease in glucose. However, the probe membrane length within the tissue is increasing as the probe is implanted and therefore it is not clear, which one of these factors is dominating the reading of glucose. After implantation when the full membrane length is inserted in the cortex and steady state has been reached, the glucose level has reached a constant concentration of approximately 500 μM and 400 μM for the rsMD and on-chip biosensor respectively. This difference between readings does disappear during the stabilisation period, which is where the rat is monitored for at least 30 minutes before the any stimulation.

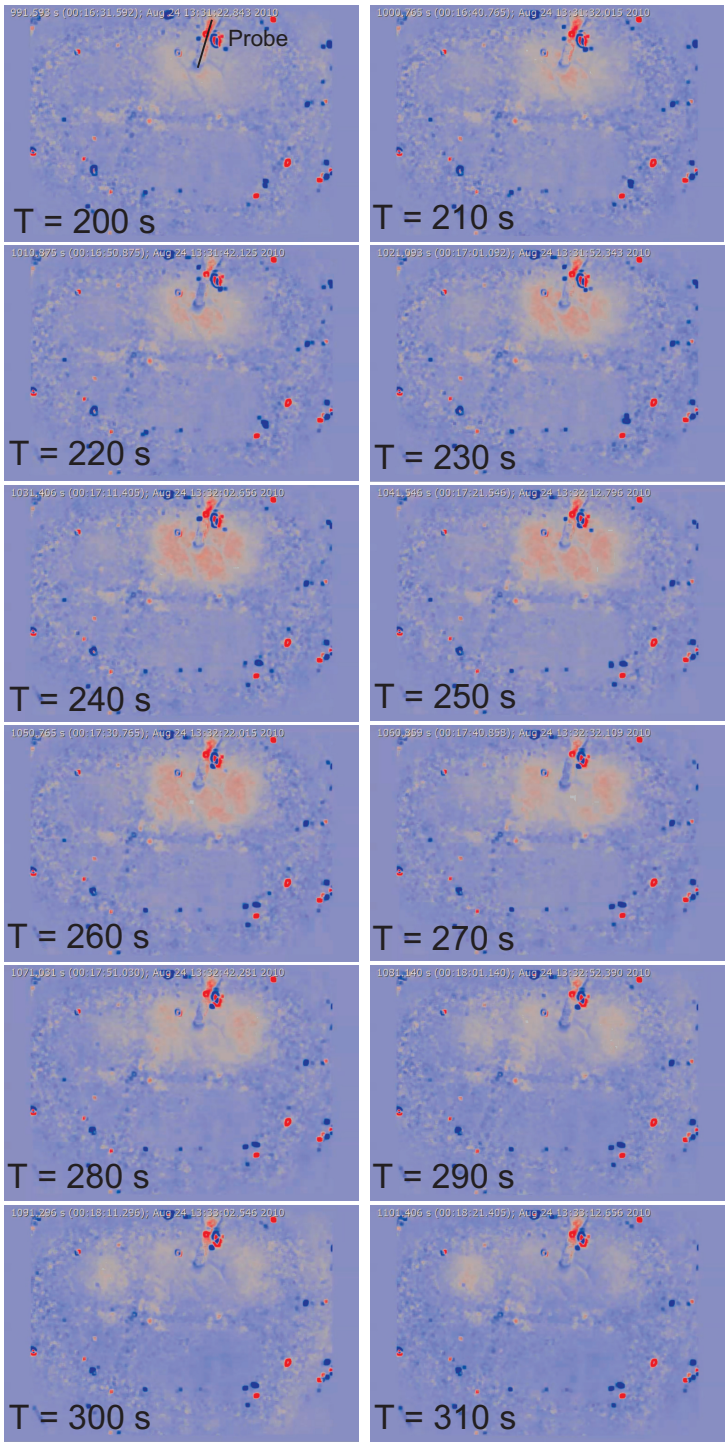


Figure 7.10: Laser speckle images of a MD probe insertion
Increased blood flow is seen as a change in colour from blue to red. T = 0 when the MD probe insertion began. The position of the probe is indicated on the first image where T = 200 s. During the course of the implantation, blood flow to the local area increases and an SD wave is induced. The insertion of the MD probe finishes at T = 400 s.

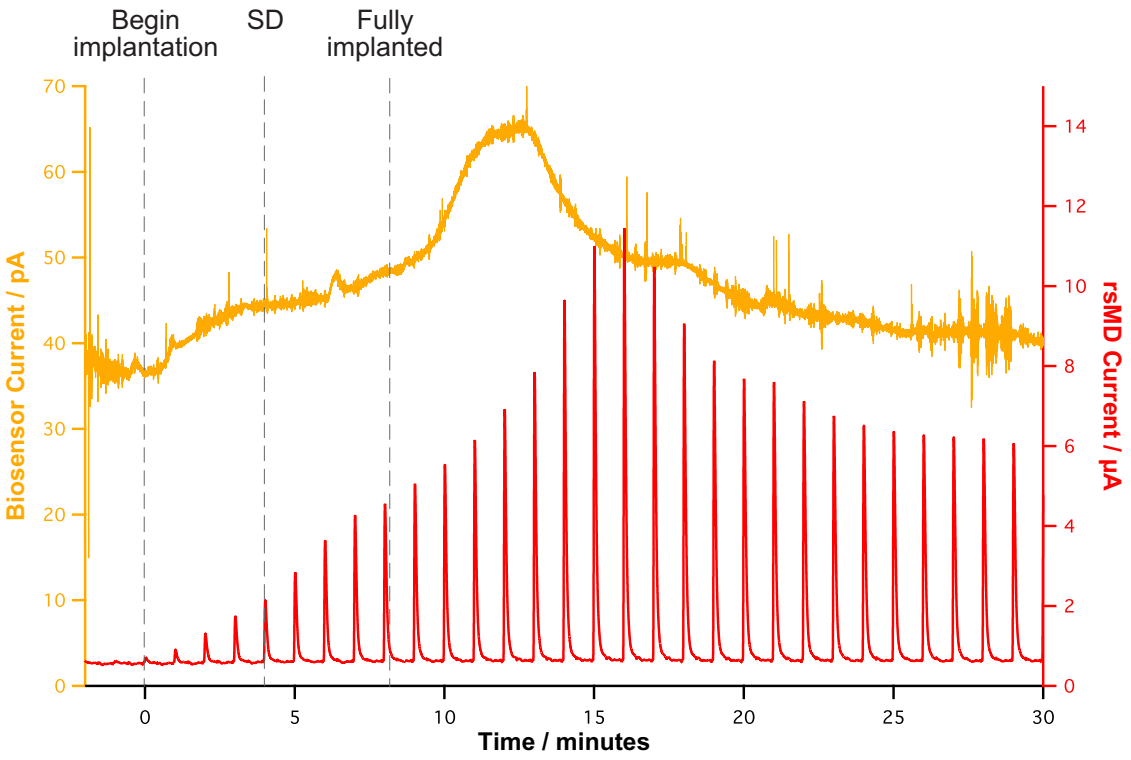


Figure 7.11: Biosensor and rsMD glucose raw data during a MD probe insertion
On-chip glucose biosensor in yellow, rsMD glucose in red where the peak height represents the level of glucose. Implantation of the probe begins at T = 0. An SD is seen on the laser speckle during implantation as indicated.

7.2.5 Result: Euthanasia

By law, the end point of all procedures was euthanasia induced by the intravenous injection of a high concentration of potassium chloride (3 M KCl). To ensure full use of the procedure, this too was studied in terms of glucose concentration. Laser speckle confirms that euthanasia has occurred by changing to a dark blue as seen in figure 7.12 and Video 10 on the associated DVD. This happens very quickly, over a few seconds.

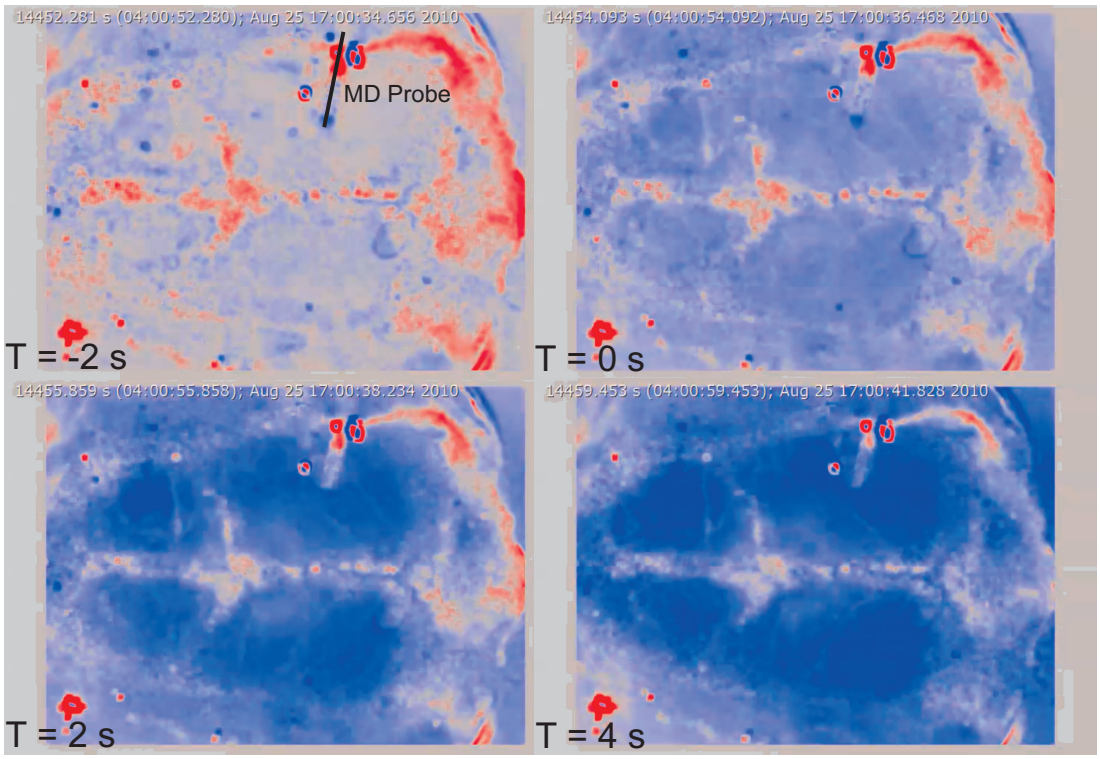


Figure 7.12: Laser speckle images of a KCl injection
The position of the MD probe is indicated in the first slide at T = -2 s. At T = 0 s the rat was injected with 3 M KCl. The speckle image turns a dark blue within a couple of seconds, indicating that there is no blood flow and hence no delivery of glucose or oxygen to the brain.

The changes of glucose throughout this period were recorded using both the on-chip glucose biosensor and the gold standard, rsMD. Figure 7.13 compares the levels of glucose as seen by the two techniques before and after an injection of KCl. Both analysis methods were individually calibrated and were converted into concentration before being time-aligned and compared. Out of the 8 animals, 5 procedures showed a change in glucose similar to that seen in figure 7.13. When the injection was administered (illustrated by the dotted line in figure 7.13) it caused noise in the

glucose biosensor, seen as a large spike in current. This is due to the sensors being very close to the animal and so may of been knocked during the procedure. The level of glucose falls below zero but this is likely to be mis-representative due to a change in baseline after the spike. Not all traces show this spike, but it is also sometimes noticed when blood gases are taken during the procedure and therefore is most likely to be noise. Both analysis methods are in good agreement with each other, in terms of the concentration before and after the injection, and the change in glucose is approximately 400 μM.

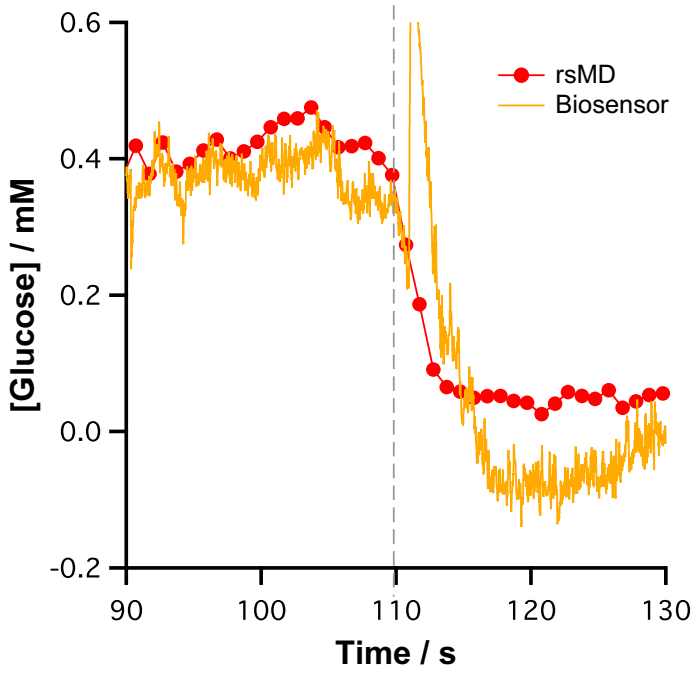


Figure 7.13: Euthanasia induced by KCl injection
The grey dotted line indicates the time point when the injection of KCl occurred. rsMD glucose is shown in red, and the glucose biosensor in orange.

Figure 7.14 shows another example of data, recorded over the duration of euthanasia and 2 of the 8 procedures show this story over the course of euthanasia. Blood flow is shown in the top graph, on-chip recordings of glucose and potassium in the centre graph and rsMD glucose and lactate levels in the bottom graph. During the course of the day the rat suffered from respiratory problems that resulted in large changes in glucose and potassium concentration, seen easily on-chip. These changes can only be seen in the chemical data, as the blood flow data is steady.

Cardiac arrest is seen as a clear drop in blood flow and glucose rsMD levels fall and lactate rsMD levels rise as expected. The on-chip sensors show a more detailed, complicated story. The delayed rise in potassium and fall in glucose could reflect consumption of astrocytic glycogen stores. Only when these stores run out, do the cells depolarise releasing potassium. When the potassium levels begin to increase, the glucose biosensor shows the level of glucose falling. There is a slight mismatch in the timing of the two glucose recordings, likely to be due to the PDMS swelling and therefore changing the volume of solution between the two analysis systems. This delayed fall in glucose (in comparison to lactate) has been noted previously in the literature (44).

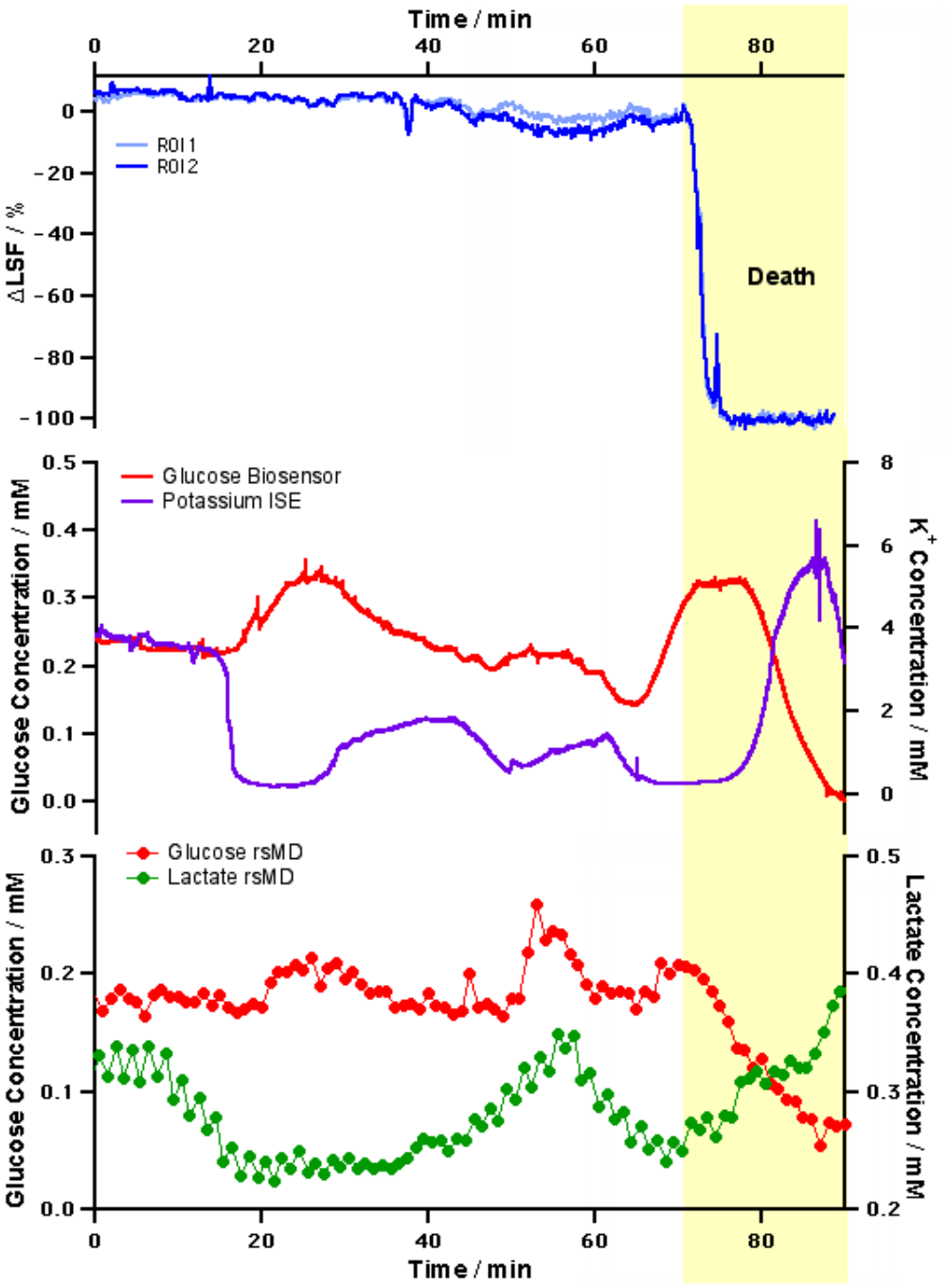


Figure 7.14: Changes during euthanasia

Blue lines = Blood flow changes taken from Laser Speckle data. Solid red line = On-chip glucose biosensor. Solid purple = On-chip potassium ISE. Dotted red and green = rsMD glucose and lactate respectively. The yellow colouring indicates the timing of the intravenous injection of KCl.

7.2.6 Results: Stroke model

The stroke model is widely used at the Max Plank Institute, Cologne, and it was decided to be used in this pilot study, as it induces a smaller change in glucose than cardiac arrest and so is a harder test for the glucose biosensor to pass. The method used to emulate a stroke in a rat, was a middle cerebral artery occlusion (MCAO).

Upon inspection of the brain post-mortem, it was found that the macrosphere had become lodged in the posterior communicating artery as opposed to the intended MCA. This is shown in figure 7.15. The macrosphere was contralateral to the MD probe and the blockage resulted in only a small change in blood flow. This is due to the macrosphere affecting flow to the brain and the change is only small, due to the ability of collateral flow to compensate for minor alterations.

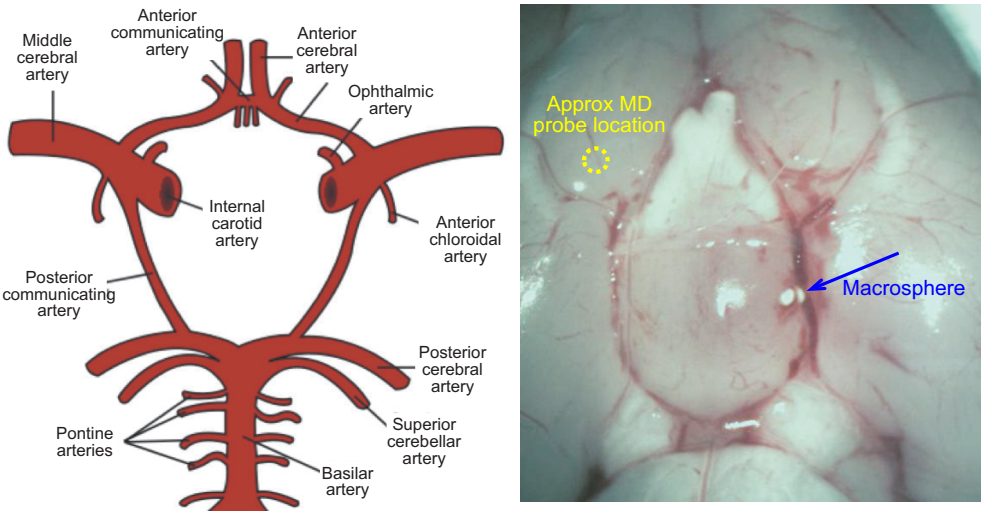


Figure 7.15: Visual inspection of the location of the injected macrosphere
On the left is a diagram of the major blood vessels taken from http://neurology-cases.blogspot.com/2011_03_01_archive.html On the right, is a photograph of the ventral view of the rat brain. Approximate position of MD probe on the dorsal side and the macrosphere placement is indicated.

Figure 7.16 shows the changes in blood flow and glucose levels as recorded by both the on-chip glucose biosensor and rsMD. The laser speckle video can be viewed on the associated DVD (Video 11). The levels of glucose correlate very well between the two analysis methods. Upon injection of the macrosphere, the glucose levels fall by approximately 200 μM and blood flow transiently decreases by approximately 10 %. Also contributing to the small change in blood flow is the positioning of the probe, relative to the connecting artery blockage.

The probe is in the penumbral region of the occlusion. The decrease in the level of glucose is likely to be due to the reduced blood flow causing a lower deliverance of glucose. The good agreement of rsMD and the on-chip biosensor indicate that the sensor is a viable option for measuring neurochemical changes in brain injury patients.

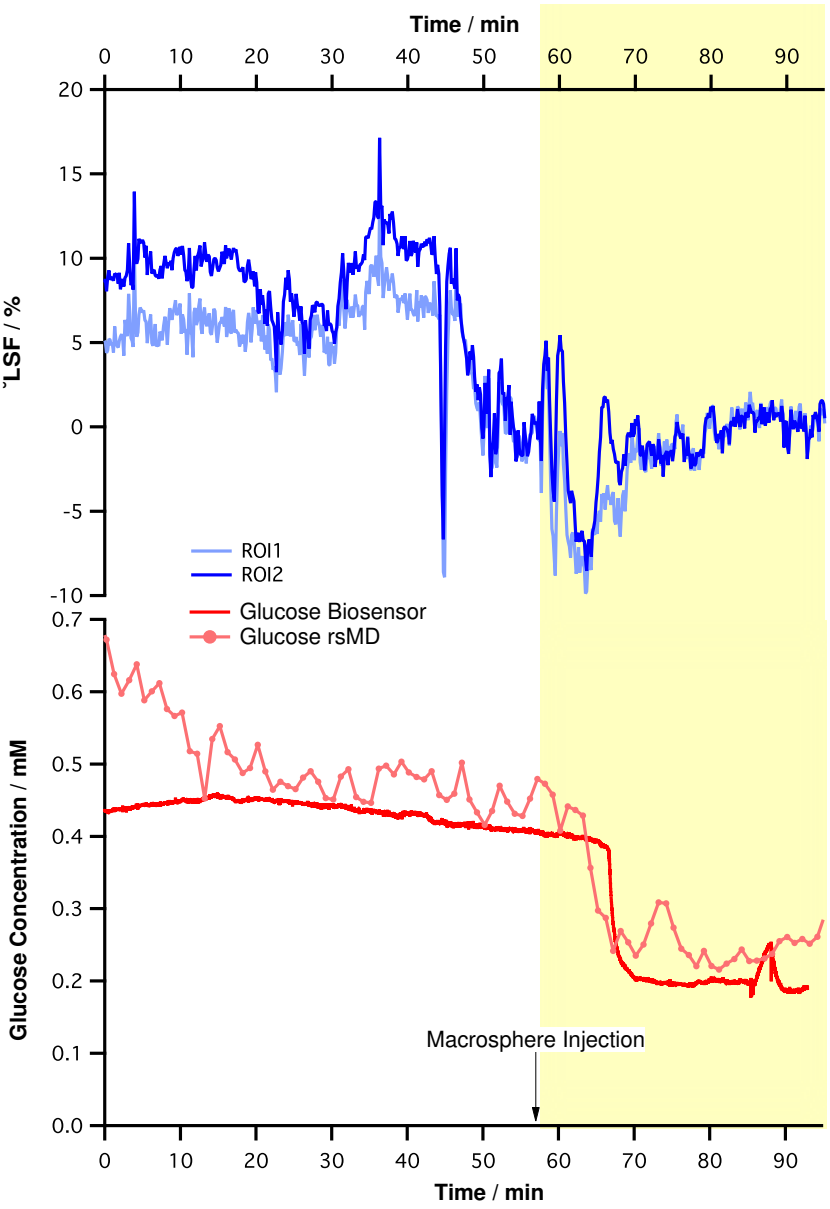


Figure 7.16: Changes upon injection of a macrosphere into the connecting artery. Blood flow changes taken from Laser Speckle data and shown in the top graph in blue. The solid red line indicates the glucose biosensor on chip and the dotted red line indicates the level of rsMD glucose.

7.2.7 Results: Spreading Depolarisation's

SD waves have been shown to occur in the injured human brain with possible detrimental effects. Within the animal brain, the events provide a tough test for the sensors to pass as often the concentration changes are small. SD waves can be caused by a variety of models. Here two such models are discussed, the cotton bud stimulation and the needle prick model.

1: Cotton Bud Stimulation

Figure 7.17 shows a section of laser speckle images during a cotton bud stimulation. The MD probe and cotton bud location is indicated on the first image. This figure only shows one SD wave (shown as areas of red) moving from the area where the cotton bud is placed towards the MD probe, as indicated by the small black arrows. In fact, during this particular stimulation, five SD waves were seen, which can be seen in Video 12 on the associated DVD. This is a feature of cotton bud model that repeated waves occur.

Figure 7.18 shows the chemical data collected during a cotton bud stimulation. SDs are seen as transient hyperaemia's in the speckle data (shown in blue) and coincident with these, the 25 μm disc electrode glucose biosensor (red trace) and the K^+ ISE (shown in purple) show opposing changes. Looking more closely at the raw data of rsMD (the bottom trace), the glucose decreases can also been seen, however with much more difficulty due to a sample rate of once a minute. The changes in glucose concentration are approximately 15 μM. These changes are very small, which is a very hard test for glucose biosensor. Although you can see the downward perturbations more clearly in the biosensor than the rsMD. If the blood flow or potassium data were absent, it would be very difficult to distinguish from noise.

Overall, the glucose biosensor has performed well, indicating the clear advantage of continuous analysis. Whilst the sensor is sensitive enough to see SDs, the small magnitude and rapid repetition of the waves in the cotton bud model, make it difficult to use a biosensor alone. A multi-analyte system is therefore the best option. To get an ambiguous of the biosensor during an SD wave, a second model of SDs was used, which is reported to give a bigger single SD wave, that can be seen on rsMD.

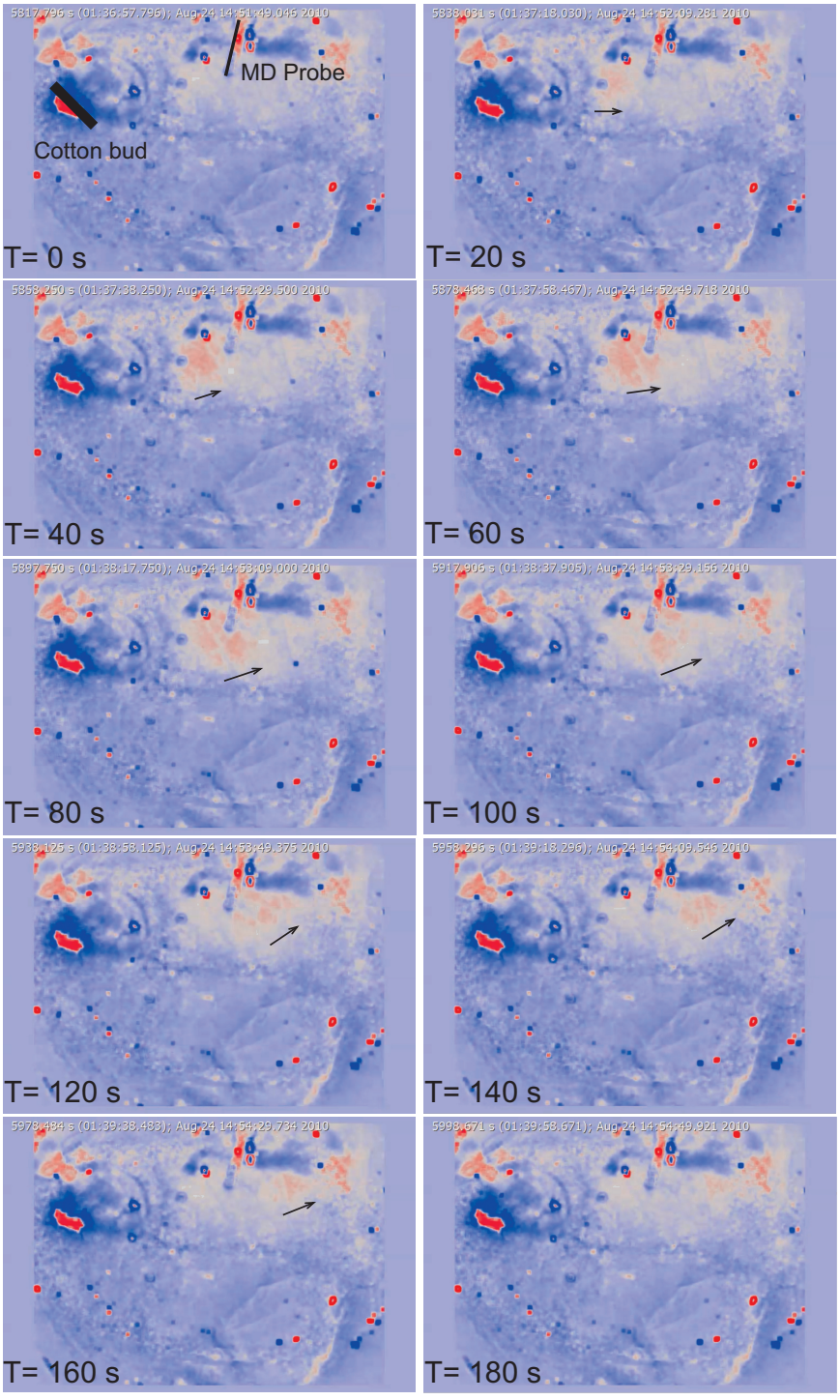


Figure 7.17: Laser speckle images of a cotton bud induced SD
An SD wave is seen as a red patch (area of increased blood flow) moving past the MD probe. Arrows help to indicate the wave and show the direction in which the wave is moving. During the placement of this cotton bud 5 SD waves were produced although only one is shown here.

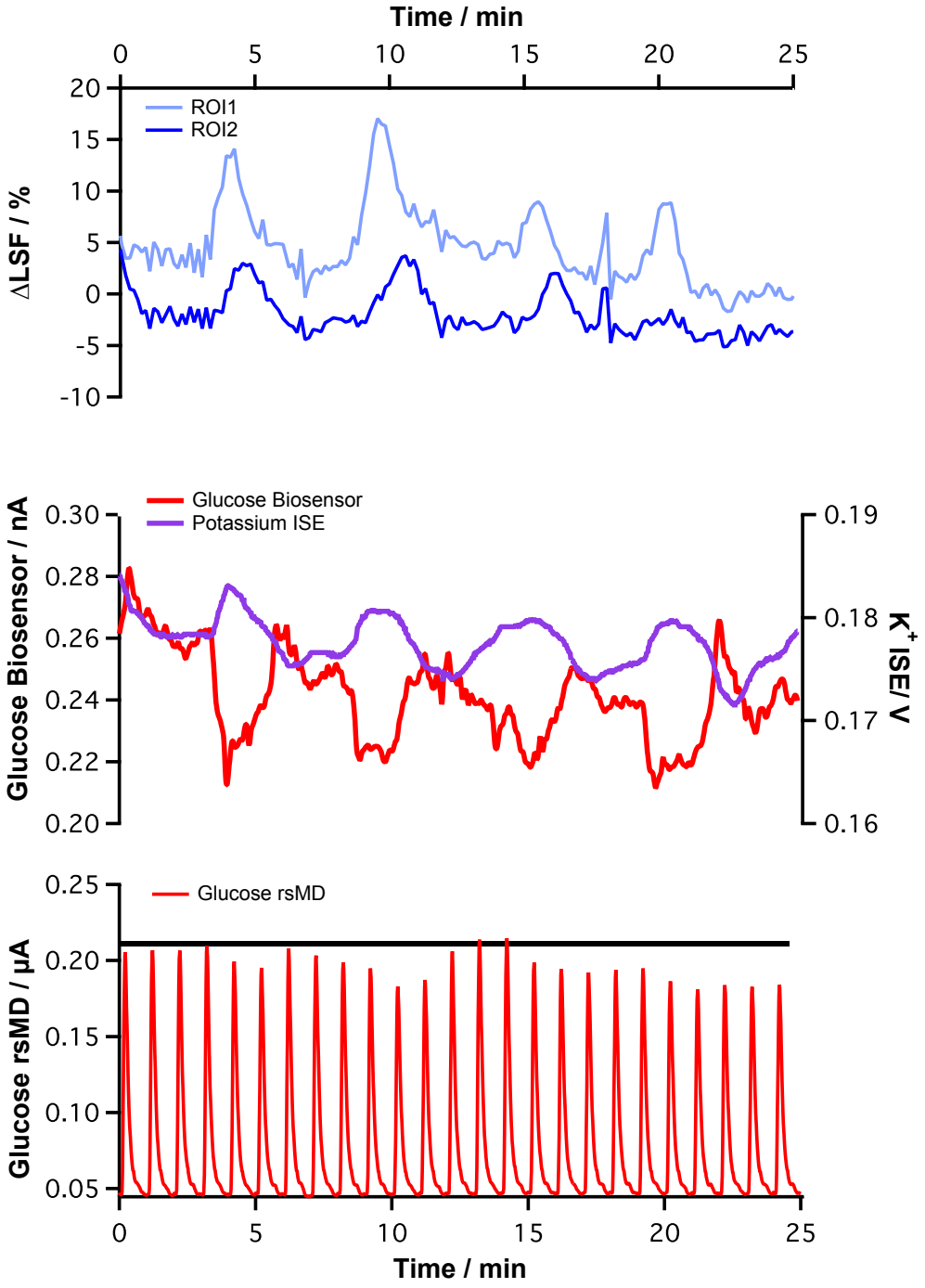


Figure 7.18: Changes upon application of a cotton bud.
Blood flow changes taken from Laser Speckle data shown in blue. The raw data of glucose biosensor (red), potassium ISE (purple) are displayed in the middle graph. The raw data of rsMD glucose is shown in the bottom graph and the height of the peaks indicates the concentration level.

2: Needle Prick Model

Figure 7.19 shows an overview of the measurements recorded from the probes in the brain tissue, during a needle prick. All the recordings were individually calibrated and time aligned, where time zero is the time that the needle prick occurred. The speckle video can be found on the associated DVD (Video 13).

The top graph displays the recordings from the DC electrode and the EEG. During an SD, there is a sudden and large decrease in the DC potential and a narrowing of the EEG trace, characteristic of cellular depolarisation.

The second graph compares the tissue potassium electrode and the on-chip MD potassium ISE. Potassium levels are much higher in the tissue than in the dialysate due to the dialysis sampling of the extracellular space. The shape of the transient measured at the on-chip sensor is stretched over time and this is due to Taylor dispersion in the connection tubing. The mismatch in timing of the beginning of the increase between the two recordings is due to slightly different positions of the tissue potassium electrode and the MD probe. During an SD a clear increase in the potassium levels is seen at both electrodes. The height of the peak at both electrodes is different, due to the tissue electrode sensing the full potassium signal. The MD probe however is a sampling technique dependent upon diffusion across the probe membrane, and the recovery of the probe is not 100%. Therefore, the full concentration will not be collected in the time it takes for the event to pass.

The glucose levels are compared in the third graph in figure 7.19 and show rsMD in red and the biosensor in orange. The concentrations correlate very well before and during the SD and there is a slight discrepancy after the SD has occurred. However, the two data sets do return to matching very closely not long after. During the SD, the concentration of glucose decreases by 12 μM in both data sets.

The rsMD data is shown in the bottom graph, where glucose is shown again in red for easy comparison to the lactate levels (shown in green), which increase during the SD. Both metabolites return to baseline after the event.

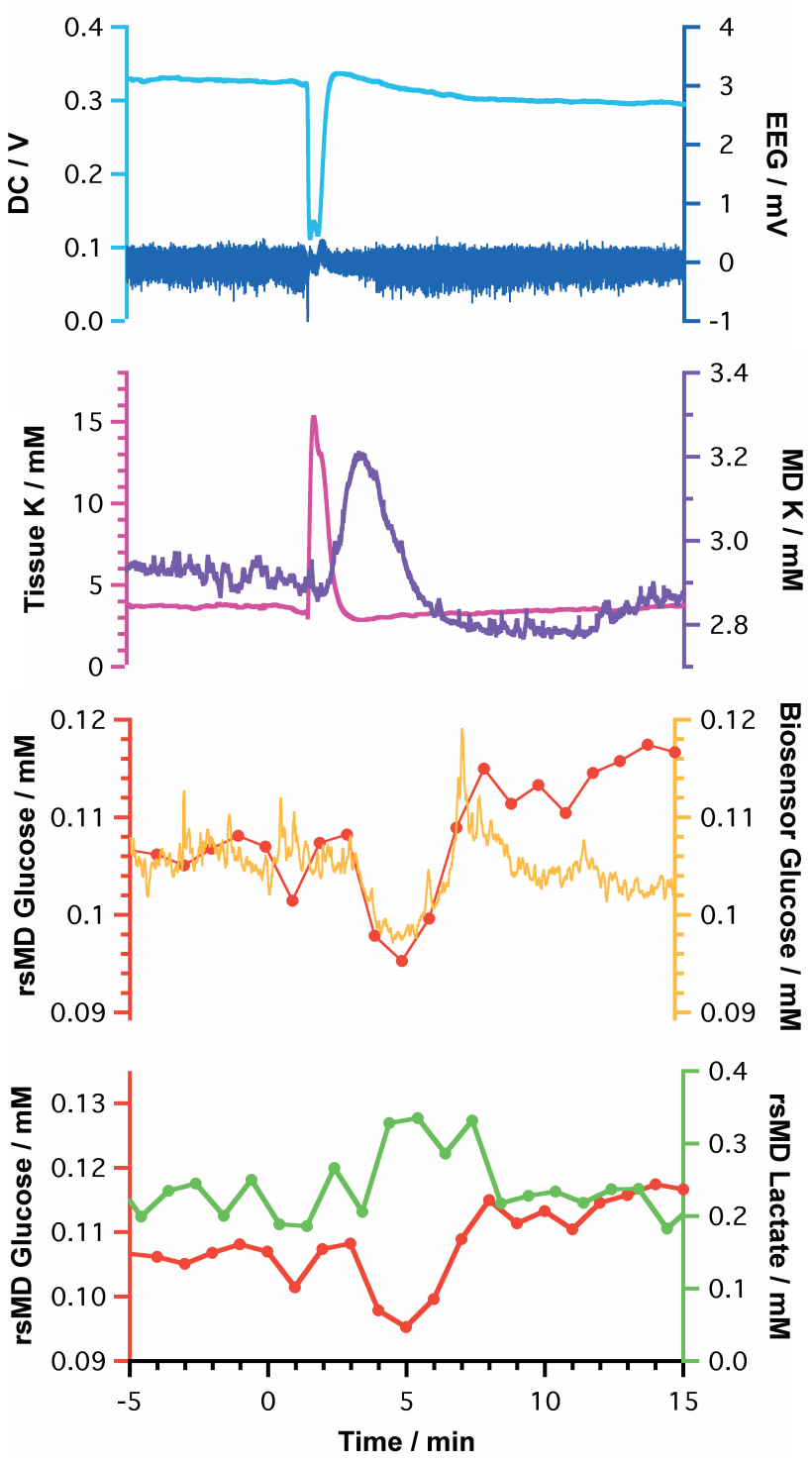


Figure 7.19: Needle prick: probe measurements
From top to bottom: DC potential (light blue) and EEG (dark blue) show transients characteristic of cellular depolarisation; Comparing tissue potassium (purple) and on-chip potassium (dark purple); The on-chip glucose biosensor (orange) and rsMD glucose measurement (red) show good correlation; rsMD data: glucose in red and lactate in green.

Figure 7.20 shows four NPs data sets, which show clear potassium and glucose changes, with the associated blood flow changes. Figure 7.20A is a laser speckle image, which indicates the position of the MD probe, approximate sites for the NP and the location of the ROI's used to analyse the blood flow. The colour of the circle indicates the trace seen in the blood flow graphs. Figure 7.20B-E show the four NP data sets.

Analysis from laser speckle reveals that the hyperaemia, during an SD wave, coincides with the increase in extracellular potassium. Once the hyperaemia has passed, the cells are re-polarising as indicated by the fall in potassium levels. For this, the cells require more energy, and therefore the local demand for glucose increases. However at this point, there is no longer an increase in blood flow and hence no increase in the supply of energy resources. A decrease in the local glucose concentration is then observed. It can be concluded that the energy demand of the tissue was not being met due to a lack of supply of glucose from the blood. This is true for all four NP data sets.

Table 7.1 gives a summary of the glucose changes, recorded from the microdialysate, during a needle prick and compares the glucose response of the 50 μm disc electrode biosensor to that of the rsMD system. The changes in the glucose concentration, observed as the SD wave passes the MD probe, are very similar in both analytical techniques. The average difference between the two recordings, was -6.5 $\pm$ 10 μM (n=6). The biosensor, therefore gives reliable recordings of the glucose level at low levels and during small changes. Whilst the two measurements were in agreement, the needle prick did not necessarily give a larger change in glucose than the cotton buds. Half of the successful needle pricks gave a change in glucose similar to that seen during the cotton bud stimulation, whereas the other half were indeed larger changes.

Table 7.1: Changes in glucose concentration caused by needle pricks

Biosensor / μM	rsMD / μM	(Biosensor - rsMD) / μM
-12	-12	0
-38	-52	14
-77	-85	8
-10	-3	-7
-40	-61	21
-10	-13	3

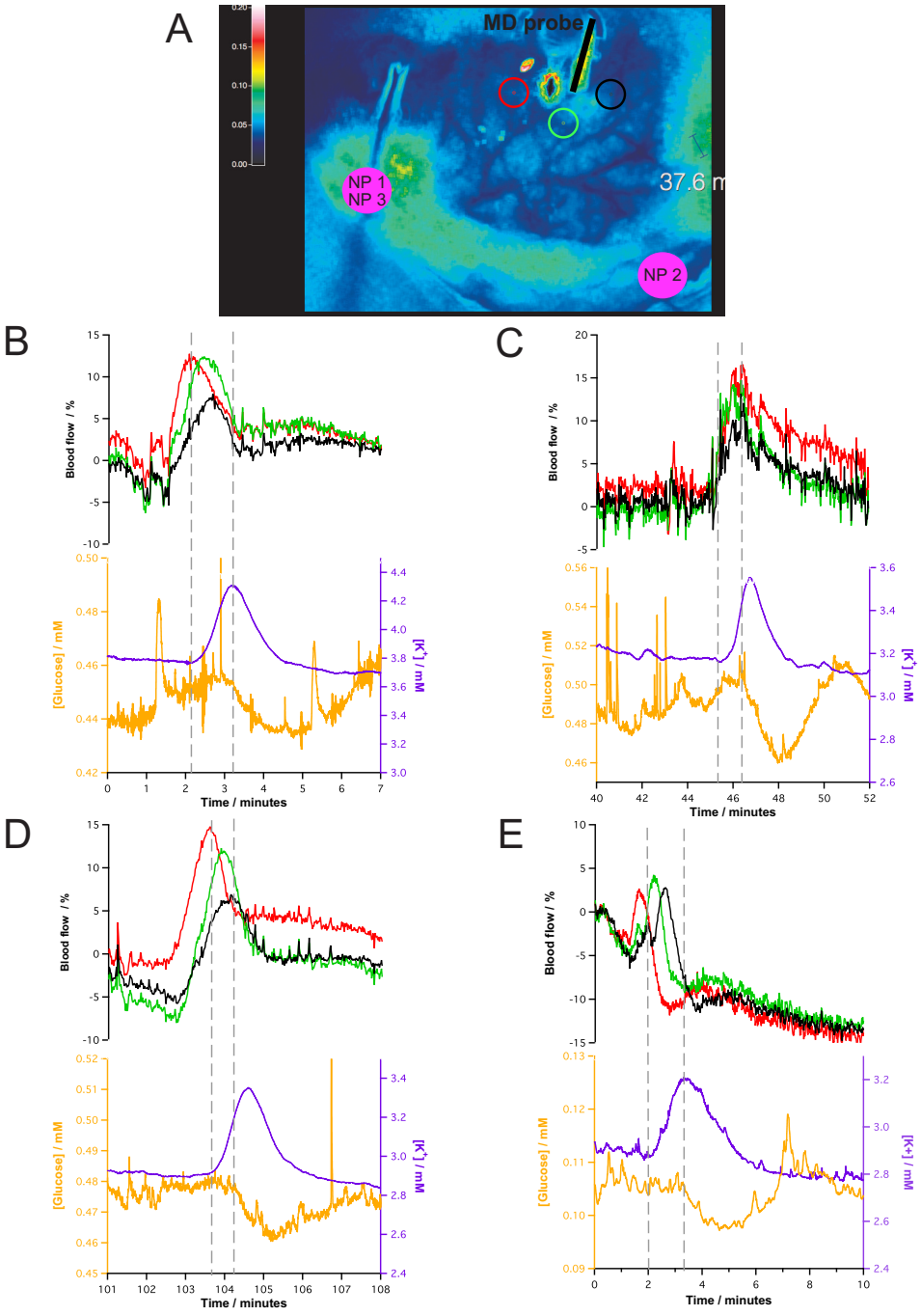


Figure 7.20: Needle prick: on-chip glucose, potassium and blood flow
A: Speckle image indicates the positions of the MD probe and approximate locations of NP sites. The coloured circles indicate the three ROI used to generate the blood flow data. The blood flow data is shown in corresponding colours in the data graphs. B to E show the results of the laser speckle analysis and the on-chip glucose biosensor (orange) and potassium ISE (purple) data. The dotted lines indicates the increase of potassium and the decrease in glucose.

The on-chip data from the needle pricks were analysed more closely. This is shown in figure 7.21. All changes in potassium and glucose concentration were aligned by allocating the point of change in potassium as 0,0. Therefore, the background is removed and the relative changes and timings can be closer assessed. In shades of purple, all of the potassium changes are overlaid. Clearly there is an increase as the cells depolarise. The potassium levels all return back to baseline and the release and uptake rates of all needle pricks are very similar. In variations of red, are the glucose concentration changes for the same four needle pricks. The changes are all small, all negative from the baseline and all delayed from time zero. Measuring potassium gives a chemical time point for the onset of depolarisation within the microdialysate, as any dispersion that occurs, affects both the potassium and the glucose. Previously, the glucose was aligned to other data (such as ECoG) by approximation.

All four needle pricks show some delay in the decrease of local concentration compared to potassium. Note, that the glucose biosensor is always upstream of the potassium sensor and in calibrations, the biosensor responded to the change in concentrations first. Therefore we can rule out this delay being due to mass transport effects. Table 7.2 shows the timings of the glucose and potassium responses. There seems to be no correlation between the duration of the glucose or potassium concentration changes and the delay in the glucose onset.

Table 7.2: Glucose and potassium changes during a NP

NP	Delay in response / s	Duration of K change / s	Duration of G change / s
1	68	150	216
2	60	174	197
3	30	175	192
4	90	267	320

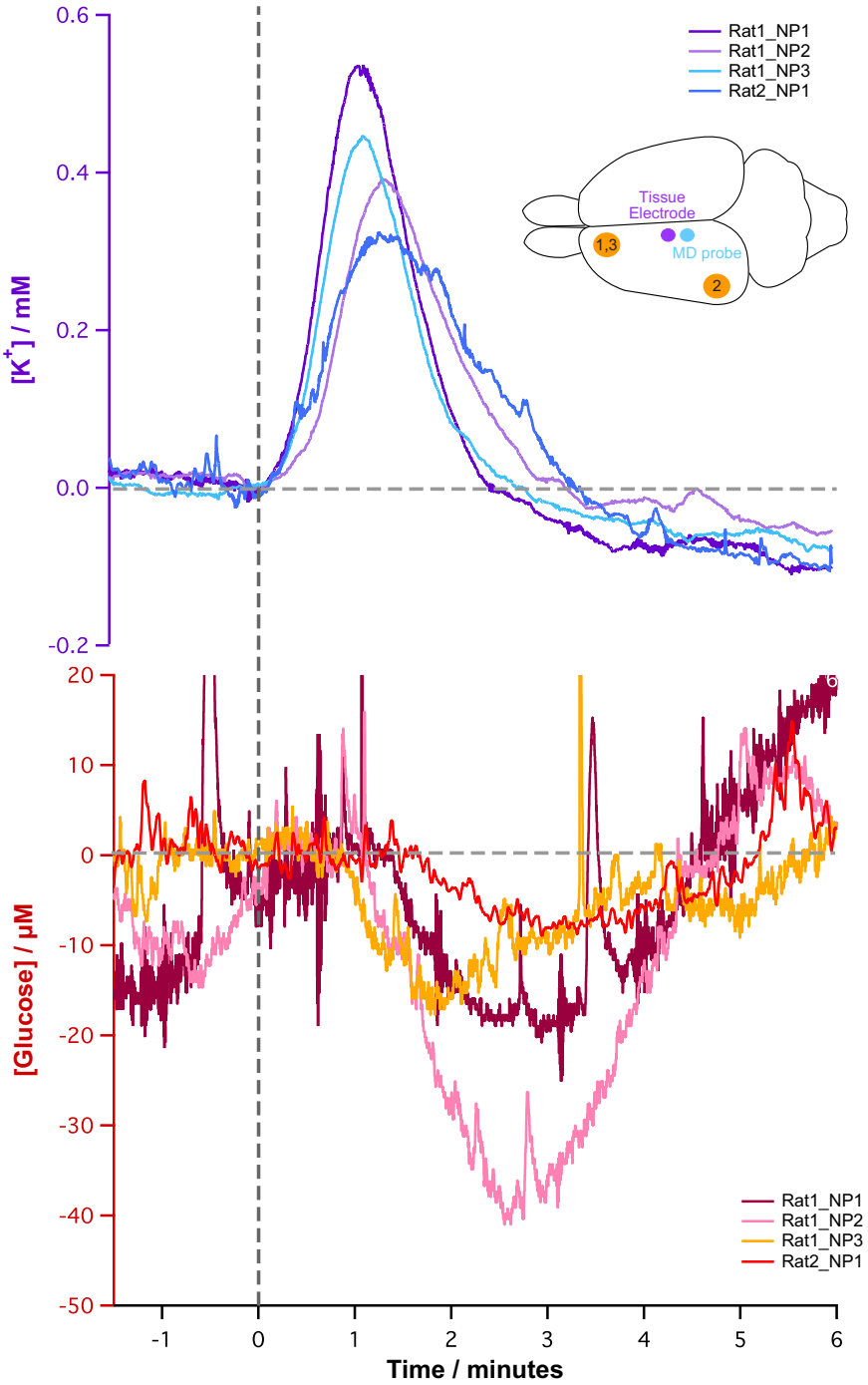


Figure 7.21: Assessment of glucose and potassium changes after a needle prick
Traces are aligned by allocating the point of potassium change as 0,0. In variations of blue and purple are an overview of the potassium changes as recorded by the on-chip potassium ISE. In variations of red and orange are an overview of the glucose changes as recorded from the on-chip glucose biosensor. The inset shows a reminder of the probe locations and NP sites.

7.3 Human Studies in the Intensive Care Ward

I had the opportunity to incorporate the microfluidic platform into the clinical monitoring system in two hospitals: at King College Hospital in London and in the MPI in Cologne. This section will now discuss the results from both locations.

7.3.1 Equipment Setup

The microfluidic analysis chip was tested in two hospitals and in two flow regimes. At both locations a glucose biosensor and potassium ion selective electrode were placed within the analysis chamber as previously done with the animal procedures. Initially, the microfluidic platform was run in continuous flow to reduce complications. Digital microfluidics was tested on one patient at the Max Plank Institute in Cologne. The set-ups in the two locations will now be described.

Kings College Hospital, London

The microfluidic set-up was transferred to King College Hospital (KCH) in London. Here, rsMD monitors brain injury patients. Once surgery has been conducted and the MD probe and ECoG strip electrodes implanted, the patient was moved onto the intensive care ward. The MD probe was perfused with sterile aCSF at 2 μLmin^{-1} and the rsMD is usually attached to the MD probe outlet via 1 m low volume FEP connection tubing. When applying the microfluidic platform and on-chip sensors, the microfluidic box (identical to the one used in the animal experiments, see figure 7.3) is placed in between the MD probe outlet and the inlet of rsMD. A 25 μm disc electrode glucose biosensor and a potassium ISE can be placed within the microfluidic analysis chip, which was contained within the microfluidic box that acts as a faraday cage. A photograph of the equipment at Kings College Hospital whilst monitoring a patient is shown in figure 7.22.

Max Plank Institute, Cologne

Whilst at the MPI in Cologne, conducting the pilot study in rats as previously discussed, a stroke patient was admitted who presented a case for rsMD monitoring. Therefore, the rsMD system (which was being used in the animal study) was transferred back to the clinic for patient monitoring. The staff allowed the microfluidic system to be tested on the patient and the sensor box was inserted between the MD probe outlet and the rsMD system as described above. Whilst monitoring the patient in Cologne, droplet flow was also tested. This involved placing a microfluidic T junction chip, at the outlet of the MD probe, which was connected to an

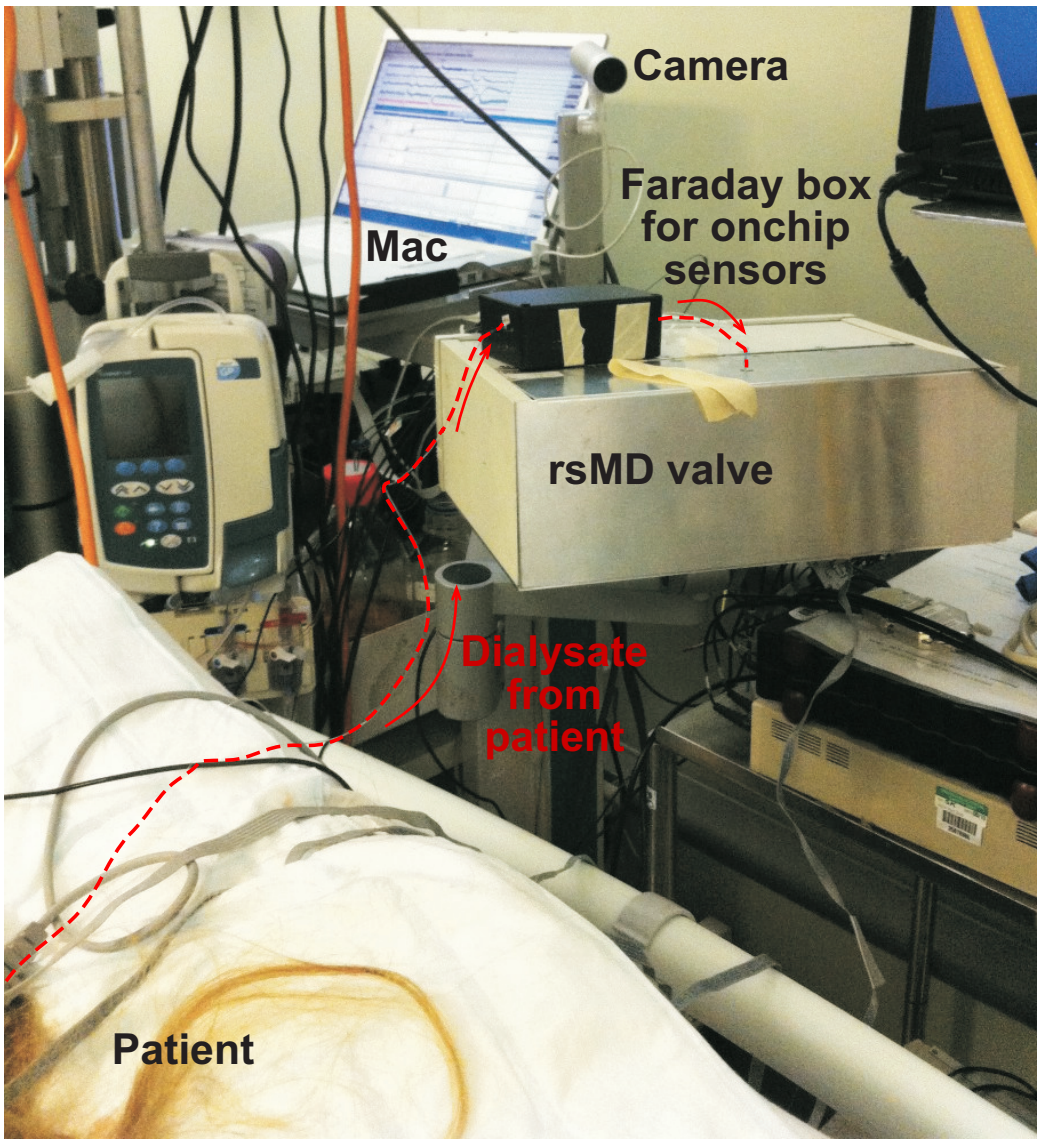


Figure 7.22: rsMD and microfluidic setup on the intensive care ward at KCH
Flow from the MD probe (patient out of shot bottom left) travels to the faraday box containing an analysis chip and on-chip sensors. The outlet of the microfluidic box is connected to the rsMD valve for glucose and lactate measurements.

open bottle of oil. When droplets were required a syringe pump was turned on that pushed the oil through the system at a flow rate of 8 μLmin^{-1}. A suction pump was also attached to the outlet of the system to pull the fluid through at a flow rate of 10 μLmin^{-1}. The droplets were transported to the analysis chip containing a 50 μm disc electrode glucose biosensor and the rsMD was disconnected to avoid oil contamination.

7.3.2 Patient Data

KCH Patient

The microfluidic platform was connected to the patient for 15 hours and data was collected from the on-chip glucose biosensor and rsMD. The levels of the glucose readings from both analysis techniques were individually calibrated, time aligned and compared. A 25 μm platinum disc electrode in a combined needle was used and fabricated into a biosensor the previous day prior to use on the clinical ward. Figure 7.23 shows the glucose biosensor and the rsMD glucose levels. Whilst they are both within the same concentration region, the rsMD shows more and larger fluctuations. It is possible that the biosensor was not sensitive enough to see these changes, as a 25 μm disc electrode was used. The apparent large dip in glucose concentration at about 2 hours, is due to nursing activity and the patient was turned to the left. The apparent change in rsMD glucose level is much larger, with a longer duration. The rsMD level then returns to a level approximately 200 μm higher than the microfluidic glucose biosensor. This is likely to be due to a kink in the connection tubing, affecting the flow. The effect of this kink on rsMD measurements, is that no sample is injected. However, the sensor is still held within the previous sample. Therefore it will continue to deplete the analyte. The change in current seen by the 25 μm disc diameter glucose biosensor, is only 7pA.

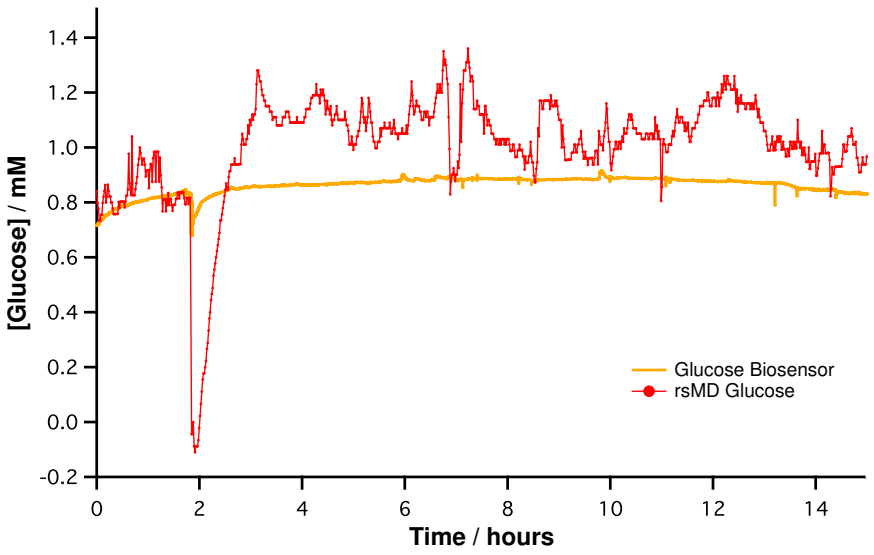


Figure 7.23: On-line glucose recordings from patient at KCH
The microdialysate was fed to the analysis chip in continuous flow. A 25 μm glucose biosensor (orange) and rsMD (red) analysed the glucose in the microdialysate.

MPI Patient

Figure 7.24A shows a period of almost 5 hours where the glucose biosensor and rsMD glucose were analysed simultaneously. The raw data is shown and the glucose biosensor had a negative offset that has been removed (adjusted by comparison of levels to rsMD and aCSF off-line levels). This negative offset was only seen when the sensor was connected to the microfluidic set-up on the clinical ward and grounding more equipment did not get rid of this offset. The apparent large changes seen after 3 hours is due to flow problems, associated with the microdialysis perfusion pump. These drops are analogous to the decrease seen in the Kings College patient. However, here they are more pronounced in the biosensor (approximately 20 pA), due to a larger electrode size used. Therefore when the flow stops, the larger electrode consumes more analyte in a given time. The glucose biosensor shows good correlation with rsMD with the levels fluctuating together. When converted into concentration the levels at the beginning of this monitoring period for the on-chip biosensor and rsMD were approximately 550 and 720 μM respectively. Both showed the glucose level increasing through the monitoring period, and levels at the end were approximately 700 and 1000 μM respectively. No events were recorded by the ECoG electrodes during this monitoring period.

Two days later, droplet flow was tested on the same patient. Oil was pumped at 8 μLmin^{-1} and a suction was applied to the end of the system at the total flow rate of 10 μLmin^{-1}. This was to reduce the pressure in the system and try to reduce flow problems created by the microdialysis perfusion pump. The result is shown in figure 7.24B and it is the world-first time digital microfluidics has been used on a patient. The trace is noisy as many people came to look at the system working in droplet flow, again indicating that there is a problem with grounding the system. The setup requires further improvement to reduce this noise. The levels of glucose are lower than that seen two days ago in continuous flow, which is normal for online microdialysis. The rsMD was recording a glucose level of approximately 600 μM before the droplet flow analysis had commenced and approximately 560 μM once the rsMD was reconnected after the droplet analysis. Again this is lower than the levels recorded in continuous flow but there is still a difference of a few 100 μM between analysis techniques.

In events of cause unknown, at approximately 16, 25 and 40 minutes in figure 7.24B, there are decreases in the glucose level over periods of 20 to 30 seconds, all corresponding to approximately 50 μM. This is after the dialysate has been transferred over 1m of tubing. In the continuous flow data (figure 7.24A), the changes

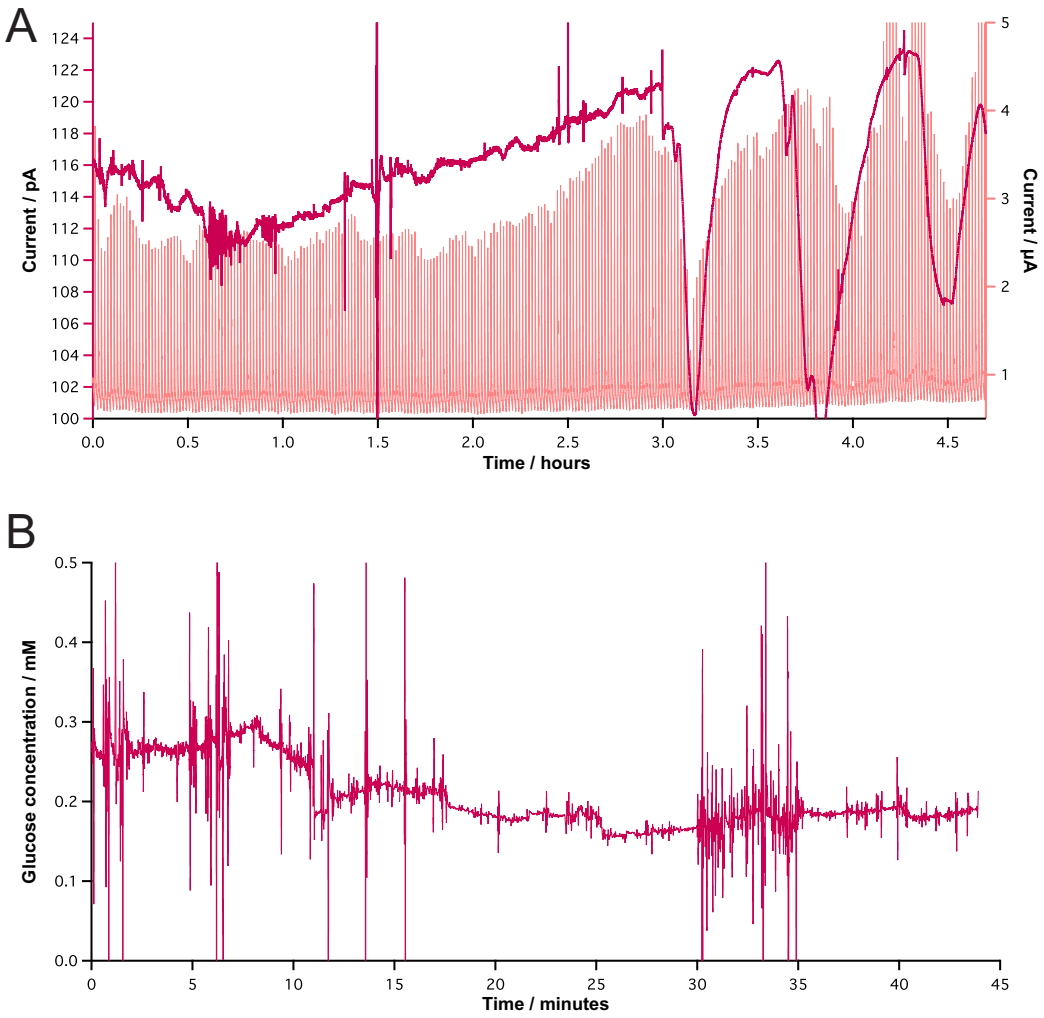


Figure 7.24: On-line glucose recordings from a stroke patient at MPI
A: MD probe was connected to the on-chip glucose biosensor (dark red) and the dialysate was then fed into rsMD (Light red). Raw data shown and the two traces are time-aligned. Peak height in the rsMD data corresponds to concentration. Note: large decreases are due to flow issues from the microdialysis perfusion pump. B: The dialysate was segmented into droplet flow at the probe outlet and fed to the analysis chip containing the glucose biosensor only. The oil flow rate was 8 μLmin^{-1} and suction was applied at the end of the system at 10 μLmin^{-1} to reduce pressure.

approximately 15 to 30 minutes into recording are approximately 50 to 90 μM and occur over approximately 120 seconds. These are of the same magnitude as that seen in droplet flow but possibly due to dispersion occur over a longer time period. Whilst the glucose changes in both sets of clinical data are not associated with SD events, it does show the possibility of measuring glucose levels in droplet flow.

All three opportunities to incorporate the microfluidic platform onto the clinical system has given great insight into the problems that need addressing. First, there is a problem with grounding as the sensors are more sensitive to noise and sometimes show an offset that is not seen off-line. Also all three cases have given a lower recording of the glucose level compared to the rsMD. This was not seen during the animal studies and is likely to be a background current, which we cannot control. One way of addressing this problem could be to introduce standard additions and therefore the background current can be taken into account. Despite this, the sensors show similar fluctuations with the rsMD and therefore with further optimisation, are suitable for monitoring on the intensive care ward.

7.4 Conclusion

The glucose biosensor and microfluidic platform was combined and tested *in vivo*. A pilot study was conducted in the Max-Plank Institute, Cologne, where several models of ischemia were used. The study was a multi-modal analysis of several focal ischemia models. Droplet flow was initially tested in the pilot rat study. Due to the lack of comparable glucose data (the rsMD could not be used), no on-chip potassium recording (due to oil incompatibility issues) and insufficient time to optimise the set-up in Cologne for droplet flow, the remaining procedures were carried out in the continuous flow regime. In continuous flow, the on-chip potassium ISE was used to detect the onset of depolarisation at the MD probe, and the glucose biosensor was assessed by comparison to rsMD glucose levels. It was concluded that the on-chip glucose biosensor is sufficient in sensitivity, time response and stability to analyse brain dialysate and assess the changes in glucose levels associated with ischemia.

During different stimuli, the local glucose levels in the dialysate were recorded by both a glucose biosensor and rsMD. During implantation of the microdialysis probe, an increase in glucose levels was seen by both. The glucose levels here are comparable with both seeing a change of approximately 400 μM. During euthanasia, glucose levels fell and were again comparable at both the on-chip glucose biosensor and rsMD. The concentration decreased for 5 out of 8 procedures.

A stroke model (MCAO) saw a change in glucose of approximately 200 μM. The two methods of glucose analysis again showed good correlation. The change in glucose levels was not as large as first expected. However, visual inspection of the macrosphere location showed that the occlusion occurred in the posterior communicating artery, as opposed to the intended middle cerebral artery. The occlusion also occurred on the opposite side of the brain to the sensors. This resulted in collateral flow compensating for blockage and therefore only a small change in blood flow and glucose levels were seen.

Spreading depolarisation's have been recorded in the injured human brain and these changes have been previously characterised by rsMD. It has been shown that SD waves are potentially harmful and can drive down the local glucose concentration by frequent repetition. This can harm and potentially kill the local tissue. Measuring the SD events using a glucose biosensor within the microfluidic platform was therefore investigated in the pilot study. The first method of initiating an SD event was a cotton bud stimulation. Here, multiple SD waves were produced from one application of the cotton bud. The changes produced in both the glucose and potassium levels were small and the on-chip glucose biosensor performance could

not be assessed using rsMD due to inadequate resolution of a sample a minute. Due to the repeatable nature of the SDs stimulated using this method, it was hard to distinguish the responses from noise. The use of multi-modal recording allowed the identification of the small glucose changes. Hence a second model, the needle prick, was used, to induce larger changes in glucose concentration and typically one single SD wave. Half of the changes in local glucose concentration were larger than those seen using the cotton bud model, however the rest were similar in magnitude. Again, the on-chip glucose biosensor performed well showing the same concentration of glucose as the rsMD. The needle pricks gave an insight, for the first time, into the relationship between glucose, potassium and blood flow during an SD event. The glucose concentration decrease is delayed from the onset of cellular depolarisation and coincides with the return of blood flow to baseline levels, i.e. the hyperaemia has passed but the cells are still re-polarising. Therefore, there is a high energy demand but no increase in supply and local glucose levels decrease.

The microfluidic analysis chip and glucose biosensors were preliminarily tested in the intensive care unit. Fifteen hours of monitoring in continuous flow was recorded at Kings College Hospital. Whilst in Cologne, there was the opportunity to assess the microfluidic system on a stoke patient. Five hours were recorded in continuous flow and droplet flow was also tested on this patient two days later. The glucose levels recorded, had a discrepancy of approximately 200 μM, between the biosensor and rsMD reading. Whilst no SD events were monitored, the data highlights the feasibility of implementing the digital microfluidic system at the bedside to monitor human patients.

Overall, the microfluidic platform with integrated glucose biosensor was highly successful. In continuous flow it was easily incorporated between the patient and rsMD analysis. Biosensor performance in all the ischemia models used in the pilot rat study was comparable to that of rsMD. In the clinic , for the first time, a microfluidic analysis system with integrated electrochemical biosensors, was incorporated at the bedside. This was conducted in both continuous and droplet based flows. The glucose biosensor was also more sensitive to noise and on occasion there was an offset that is not seen when run off-line. Further work to ground the equipment properly and optimise microfluidic system when incorporated into the intensive care unit is required. The next step is to test the system in the droplet flow regime.

Chapter 8

Discussion

8.1 Overview

The aim of this thesis was to develop a system capable of monitoring brain dialysate at the bedside in an intensive care unit. A microdialysis probe was used as a sampling method, as it is FDA approved and can therefore be placed within the human body, during surgery. Specifically, the concentrations of glucose and lactate within the dialysate, were desired using analysis in real-time, to give an insight into the health of injured brain tissue. I proposed the use of electrochemical biosensors, placed within a microfluidic manifold, to analyse the microdialysate continuously. The sensors needed to be highly sensitive and fast responding, as the events of interest (spreading depolarisations), are small concentration changes that occur relatively quickly. It has been suggested in the literature that a large number of SD waves, which occur frequently, can cause the deterioration of the brain tissue surrounding the focal injury site that is seen in 40% of patients.

The current rsMD system used at the clinic, dramatically improves upon the time resolution of traditional microdialysis. However, the system requires a long connection tubing (approximately 1 m) from patient to analysis, during both surgery and whilst monitoring at the bedside on the intensive care ward. At the typical microdialysis flow rate used during clinical monitoring (2 μLmin^{-1}), transport of the sample over 1 m of connection tubing takes approximately 10 minutes. If a real-time assessment of the health of the tissue was required (for example, if the system was used to alert clinicians of deterioration) then even a delay of 10 minutes may be too late for therapeutic action. In continuous flow, Taylor dispersion occurs. This smears out sharp concentration changes making it harder to analyse. Also, the clinical trolley on which the rsMD system is placed, is large and bulky, and

difficult to position close to the patient. Therefore a digital microfluidic system was proposed. Dispersion was eliminated due to the segmentation of flow and the microfabrication of devices dramatically reduces the size of the analysis system. The first step was to microfabricate a PDMS T junction using soft lithography and droplets of reproducible size were reliably formed.

The application of digital microfluidics, particularly the use of two phases, led to problems of analysis. A combined needle electrode was developed to house the working, reference and auxiliary electrodes, for placement within a microfabricated flow cell. The biosensors were successfully miniaturised and gave good results, with response times of a few seconds and a limit of detection in the low μM, but the placement in a two phase system was problematic. Firstly, the entire electrochemical cell must be contained within a single droplet for sufficient time for analysis of the droplets contents. Secondly, the oil fouled the electrode surface and blocked the aqueous signal from being recorded. An analysis chip was therefore designed to remove the oil and re-join the droplets together. This created an continually aqueous solution where the electrode could be placed without any interaction with the oil. Two designs were discussed in this thesis, both removing the oil using the geometry of the channels, with the separation occurring spontaneously via passive coalescence.

To assess the viability of the electrodes on-chip under a droplet flow regime, initially electrochemistry on bare electrodes was conducted with standard redox solutions. Cyclic voltammograms showed the sensors performing exceptionally well in the analysis chamber in both continuous and droplet flow. Dispersion in both flow regimes was assessed using optical and electrochemical methods. The T_{90} was reduced from 19 s in continuous flow to less than 16 ms in droplet flow. This 1000-fold increase in time resolution highlights the potential of using digital microfluidics for all microdialysis users, not only clinical monitoring on the intensive care ward as intended here, but in all microdialysis studies.

A translational study, conducted at the Max Plank Institute, Cologne, tested the microfluidic platform in a microdialysis study of SD waves. Here, the glucose biosensor, placed on-chip, was validated against rsMD glucose with excellent results. A potassium sensor, fabricated by Ms Chi Leng Leong, was also placed on-chip within the analysis chamber. This provided, for the first time, a chemical start point of the depolarisation in the microdialysate. Previously, the start of the depolarisation in the chemical data was estimated from the electrical signals seen on the ECoG. For the first time, this study has allowed an insight into the timing of events that occur during an SD wave. It was found that the characteristic hyperaemia was tightly

associated with the release of potassium as the cells depolarise. The decrease in glucose only occurred once the increased blood flow had returned to normal levels, and the cells were re-polarising, as indicated by the fall in potassium. Therefore the glucose signature was delayed by approximately one minute from the potassium and blood flow. It was concluded that whilst the cells were depolarising, the hyperaemia provided oxygen and glucose. However, once the hyperaemia passes and the cells begin to re-polarise, there is no additional supply of metabolic substrates by the blood and the local glucose concentration is seen to fall.

This study was conducted in continuous flow for several reasons. However, would the use of droplet flow help show more detail in the relationship between potassium and glucose? I would expect the transients to be sharper and quicker, due to the reduction of dispersion inherent in droplet flows. For example the potassium trace to be closer in shape to that seen by the tissue electrode (and presumably the glucose would be faster by the same extent). This is illustrated in figure 8.1. The empty boxes indicates the time period over which the transient occurred in continuous flow and the filled in boxes indicate the potential time period in droplet flow. This was based on the responses seen by the potassium tissue electrode and the on-chip potassium electrode in figure 7.19. In droplet flow, the time periods of the transients is likely to be approximately one minute. The time responses of the sensors therefore need to be fast enough and be able to distinguish the sharp transients from noise. The signal seen in droplet flow would not necessarily be greater in magnitude than that seen here in continuous flow, as this is dependent upon the recovery of the MD probe. However, digital microfluidics would allow the dialysate perfusion rate to be lowered, without compromising the transit time to analysis, and this would increase the recovery of analytes over the membrane and therefore give larger signal, which is easier to record.

This thesis also presented data conducted at the bedside, on a patient in the intensive care unit, using the microfluidic based analysis system. This is a first for the group and possibly world-wide. Continuous flow was initially used and over 15 hours were recorded at Kings College Hospital, using the glucose biosensor. Continuous and droplet flow were also tested on one patient at the Max Plank Institute in Cologne, which highlights the areas of improvements and shows the potential of combining digital microfluidics, electrochemical biosensors and microdialysis.

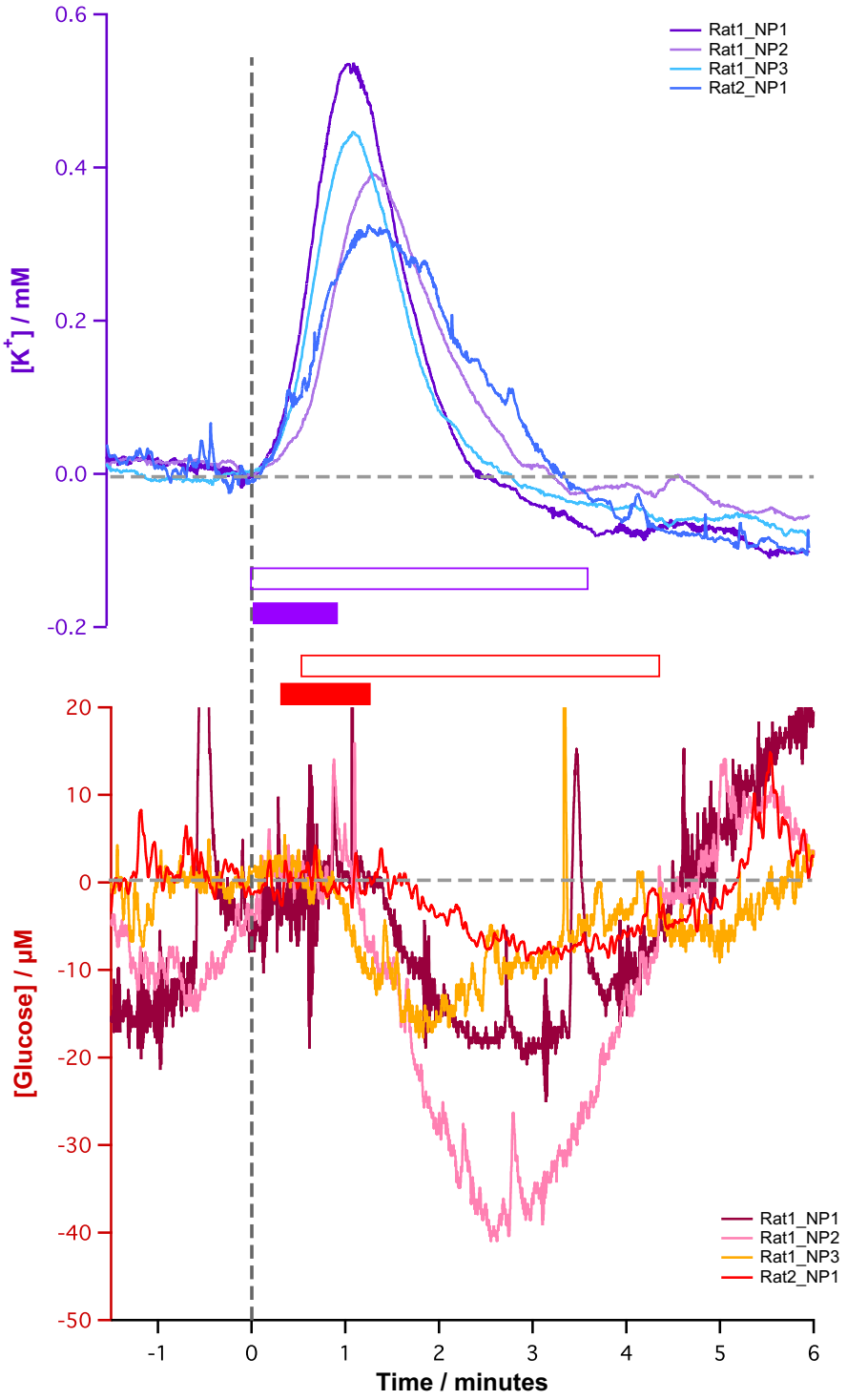


Figure 8.1: Glucose and potassium changes

Potassium changes shown in the top graph, Glucose on the bottom. The empty box shows the time responses seen (potassium purple, glucose red) and the filled boxes indicate the possible time responses if droplet flow was used.

8.2 Future Work

This section will discuss the future work required.

Electrodes and Sensors

The accurate placement of electrodes on-chip in relation to the chamber ceiling needs further work. This is the source of much variation in the biosensor performance and improvement in the method will greatly improve the success of the on-chip sensors. If it is not possible to accurately place the electrodes away from the walls, where the chemical history effect from previous droplets is less and the electrode will disrupt the formation of bands, then baffles could be introduced to enhance mixing and ensure accurate analysis of droplets. For multi-analyte analysis, the production of dual electrodes with better placement within the needle to eliminate cross talk would be desired. The second electrode could also be used as a sentinel electrode, which will help eliminate any questions about possible failings of the sensor overtime when run within the chamber. However, the size of the needle constricts the possibilities of eliminating crosstalk. Therefore, in my opinion, further optimisation of the design is required, with more than one analysis chamber. Optimisation of the geometry of the chamber, to house a single electrode, will allow multiple chambers to be placed concomitantly. As the droplet flow is reformed after each chamber, the high time resolution is retained. This will eliminate the cross talk seen in the system presently with the dual electrodes and does not compromise the time resolution by placing one electrode further from the point of coalescence.

Whilst the biosensors were shown to work well, the stability of stored glucose sensors is an area that could be improved. Whilst making fresh sensors for each experiment gives good results, it is not always practicable when dealing with patients. As brain injury patients are emergency cases, it is unknown when the next patient will be and therefore planning is very difficult. Sensors that are stable in storage will allow more flexibility. A higher enzyme loading to the electrode surface will help the biosensors fare better in storage. The lactate sensors also require further optimisation, the main objective being to be improve the sensitivity. This too will involve optimising the fabrication process to increase enzyme loading onto the electrode surface. The best way to increase enzyme loading would be using an electropolymerisation solution, which is low in volume and high in concentration.

Microfluidic Toolkit

The preliminary data from implementing digital microfluidics and microdialysis showed a possible enhancement of recoveries when the T junction was placed very close to the microdialysis membrane. Although very interesting, this was not investigated further due to the clinical microdialysis probes having a long outlet tubing. However, if there was the opportunity to redesign the microdialysis probe, incorporation of a T junction will allow segmentation of the dialysate as close as possible to the membrane. This could take advantage of the increased recovery rates (presumably due to the stop-start motion of the dialysate), which the preliminary data showed, but further investigations would be required. The incorporation of the T junction into the microdialysis probe will also increase the time resolution further, as it eliminates all continuous flow. The analysis of the flow through the chamber indicated that Poiseuille flow is established over a short distance and therefore dispersion would be reduced the closer the T junction was placed to the microdialysis membrane.

The first design of the microfluidic analysis chip separated the two phases into two channels. The second design was an improvement upon the first, by allowing symmetrical separation, about an analysis chamber. Whilst the second design of the analysis chip performs better than the first, it does not produce a continuous aqueous flow. This is desired for validation of the glucose biosensor in droplet flow. Initial studies show that the aqueous solution held within the chamber could be slowly drawn out without depleting the chamber for biosensor analysis. The solution could then be injected into rsMD for analysis and comparison. However, problems of suction through the valve, even when hard wired, disrupted the droplet flow and caused air to be drawn through the system. Further work to optimise this process would be extremely valuable.

The dosing of droplets holds much potential. Enzymes could be dosed in to eliminate high concentrations of interfering electro-active species (such as ascorbate oxidase) as well as enzymes for detection of analytes. Further investigations into the properties of the enzyme, the PDMS surface and use of oil surfactants need to be thoroughly investigated and optimised. A second advantage of dosing droplets, is to add standards at set intervals for auto-calibration. Auto-calibration is required for all hospital instrumentation and will be extremely beneficial, as the sensitivity of the sensors can be tracked throughout the course of monitoring, allowing for accurate interpretation of the recordings.

Implementation on the Intensive Care Ward

For successful implementation onto the intensive care ward, the system must first be validated in droplet flow. For this to happen, successful formation of a continuous aqueous flow of dialysate from the analysis chip to rsMD is required. Preliminary studies has shown that whilst in the intensive care unit, both at Kings College Hospital and the Max Plank Institute, the microfluidic system is subject to more noise and electrical offsets than seen either off-line in the lab or in the pilot animal studies. This needs to be address to reliably analyse the data.

References

[1] D.C. Johanson and B. Edgar. *From Lucy to language*. Simon and Schuster, 1996. 25

[2] K.S. Saladin. *Anatomy & physiology: the unity of form and function*. McGraw-Hill, 2007. 26

[3] J. Zhao, A.N. Moore, J.B. Redell, and P.K. Dash. **Enhancing expression of Nrf2-driven genes protects the blood–brain barrier after brain injury**. *The Journal of Neuroscience*, **27**(38):10240, 2007. 26

[4] N.J. Abbott, L. Ronnback, and E. Hansson. **Astrocyte-endothelial interactions at the blood–brain barrier**. *Nature Reviews Neuroscience*, **7**(1):41–53, 2006. 26

[5] J. Patlak and R. Gibbons. **Electrical Activity of Nerves**. *Aps in Nerve Cells*, 2000. 27

[6] S.G. Hormuzdi, M.A. Filippov, G. Mitropoulou, H. Monyer, and R. Bruzzone. **Electrical synapses: a dynamic signaling system that shapes the activity of neuronal networks**. *Biochimica et Biophysica Acta (BBA)-Biomembranes*, **1662**(1-2):113–137, 2004. 27

[7] C.J. Watson, B.J. Venton, and R.T. Kennedy. **In vivo measurements of neurotransmitters by microdialysis sampling**. *Analytical chemistry*, **78**(5):1391–1399, 2006. 28, 39, 40, 42, 43, 45

[8] E.R. Kandel and L.R. Squire. **Neuroscience: Breaking down scientific barriers to the study of brain and mind**. *Science*, **290**(5494):1113, 2000. 28

[9] D. Geduldig and D. Junge. **Sodium and calcium components of action potentials in Aplysia giant neurone**. *The Journal of Physiology*, **199**(2):347, 1968. 28

[10] M. Fillenz, JP Lowry, MG Boutelle, and AE Fray. **The role of astrocytes and noradrenaline in neuronal glucose metabolism**. *Acta physiologica scandinavica*, **167**(4):275–284, 1999. 29, 31

[11] M. Nedergaard, B. Ransom, and S.A. Goldman. **New roles for astrocytes: redefining the functional architecture of the brain**. *TRENDS in Neurosciences*, **26**(10):523–530, 2003. 29, 30

[12] P.J. Magistretti. **Low-cost travel in neurons**. *Science*, **325**(5946):1349, 2009. 29, 31

[13] LL Rubin and JM Staddon. **The cell biology of the blood-brain barrier**. *Annual review of neuroscience*, **22**(1):11–28, 1999. 29

[14] R.G. Shulman, D.L. Rothman, K.L. Behar, and F. Hyder. **Energetic basis of brain activity: implications for neuroimaging**. *TRENDS in Neurosciences*, **27**(8):489–495, 2004. 29

[15] G.A. Dienel and N.F. Cruz. **Astrocyte activation in working brain: energy supplied by minor substrates**. *Neurochemistry international*, **48**(6-7):586–595, 2006. 31

[16] LK Fellows, MG Boutelle, and M. Fillenz. **Physiological stimulation increases nonoxidative glucose metabolism in the brain of the freely moving rat**. *Journal of neurochemistry*, **60**(4):1258–1263, 1993. 31

[17] A. Schurr, R.S. Payne, J.J. Miller, and B.M. Rigor. **Brain lactate is an obligatory aerobic energy substrate for functional recovery after hypoxia: further in vitro validation**. *Journal of neurochemistry*, **69**(1):423–426, 1997. 31

[18] A. Schurr, R.S. Payne, J.J. Miller, and B.M. Rigor. **Brain lactate, not glucose, fuels the recovery of synaptic function from hypoxia upon reoxygenation: an in vitro study**. *Brain research*, **744**(1):105–111, 1997. 31

[19] ME Raichle. **The metabolic requirements of functional activity in the human brain: a positron emission tomography study.** *Advances in experimental medicine and biology*, **291**:1, 1991. 31

[20] H. McIlwain. **Substances which support respiration and metabolic response to electrical impulses in human cerebral tissues**. *Journal of Neurology, Neurosurgery & Psychiatry*, **16**(4):257, 1953. 31

[21] W. Walz and S. Mukerji. **Simulation of aspects of ischemia in cell culture: changes in lactate compartmentation**. *Glia*, **3**(6):522–528, 1990. 31

[22] GA Brooks. **Lactate: glycolytic product and oxidative substrate during sustained exercise in mammals–the lactate shuttle.**. *Comparative Physiology and Biochemistry: Current Topics and Trends*, pages 208–218, 1985. 31

[23] L. Pellerin and P.J. Magistretti. **Glutamate uptake into astrocytes stimulates aerobic glycolysis: a mechanism coupling neuronal activity to glucose utilization**. *Proceedings of the National Academy of Sciences*, **91**(22):10625, 1994. 31

[24] M.T. Wyss, R. Jolivet, A. Buck, P.J. Magistretti, and B. Weber. **In Vivo Evidence for Lactate as a Neuronal Energy Source**. *The Journal of Neuroscience*, **31**(20):7477, 2011. 31

[25] Y. Zilberter, T. Zilberter, and P. Bregestovski. **Neuronal activity in vitro and the in vivo reality: the role of energy homeostasis**. *Trends in pharmacological sciences*, 2010. 31

[26] L.B. Gladden. **Lactate metabolism: a new paradigm for the third millennium**. *The Journal of physiology*, **558**(1):5–30, 2004. 31

[27] J. Korf. **Is brain lactate metabolized immediately after neuronal activity through the oxidative pathway?** *Journal of Cerebral Blood Flow & Metabolism*, **26**(12):1584–1586, 2006. 31

[28] G.A. Dienel and N.F. Cruz. **Nutrition during brain activation: does cell-to-cell lactate shuttling contribute significantly to sweet and sour food for thought?** *Neurochemistry international*, **45**(2-3):321–351, 2004. 31

[29] **Traumatic brain injury: time to end the silence**. *The Lancet Neurology*, **9**(4):331, 2010. 32, 219

REFERENCES

[30] P.C. Whitfield, E.O. Thomas, M. Summers, F. Whyte, and P.J. Hutchinson. **Head injury: a multidisciplinary approach, volume 0**. 2009. 32

[31] J. Astrup, B.K. Siesjo, and L. Symon. **Thresholds in cerebral ischemia-the ischemic penumbra**. *Stroke*, **12**(6):723, 1981. 32

[32] M.E. Raichle. **The pathophysiology of brain ischemia**. *Annals of Neurology*, **13**(1):2–10, 1983. 32, 34

[33] C. Werner and K. Engelhard. **Pathophysiology of traumatic brain injury**. *British journal of anaesthesia*, **99**(1):4, 2007. 33

[34] B.O.K. SIESJ
"O, K.E.N.I. KATSURA, QI Zhao, J. FOLBERGROVÁ, K. PAHLMARK, P. SIESJ
"O, and M.A.J.L.I.S. SMITH. **Mechanisms of secondary brain damage in global and focal ischemia: a speculative synthesis**. *Journal of neurotrauma*, **12**(5):943–956, 1995. 33

[35] R.K. Narayan, M.E. Michel, B. Ansell, A. Baethmann, A. Biegon, M.B. Bracken, M.R. Bullock, S.C. Choi, G.L. Clifton, C.F. Contant, W.M. Coplin, W.D. Dietrich, J. Ghajar, S.M. Grady, R.G. Grossman, E.D. Hall, W. Heetderks, D.A. Hovda, J. Jallo, R.L. Katz, N. Knoller, P.M. Kochanek, A.I. Maas, J. Majde, D.W. Marion, A Marmarou, L.F. Marshall, T.K. McIntosh, E. Miller, N. Mohberg, J.P. Muizelaar, L.H. Pitts, P. Quinn, G. Riesenfeld, C.S. Robertson, K.I. Strauss, G. Teasdale, N. Temkin, R. Tuma, C. Wade, M.D. Walker, M. Weinrich, J. Whyte, J. Wilberger, A.B. Young, and L. Yurkewicz. **Clinical trials in head injury**. *Journal of neurotrauma*, **19**(5):503–557, 2002. 33

[36] A.A.P. Leao. **Spreading depression of activity in the cerebral cortex**. *J. of Neurophysiology*, **7**(6):359, 1944. 34, 220

[37] M. Lauritzen. **Pathophysiology of the migraine aura**. *Brain*, **117**(1):199, 1994. 34, 220

[38] H. Alle, A. Roth, and J.R.P. Geiger. **Energy-efficient action potentials in hippocampal mossy fibers**. *Science*, **325**(5946):1405, 2009. 34, 220

[39] J.P. Dreier. **The role of spreading depression, spreading depolarization and spreading ischemia in neurological disease**. *Nature Medicine*, **17**(4):439–447, 2011. 34, 35, 36

[40] A.J. Strong, M. Fabricius, M.G. Boutelle, S.J. Hibbins, S.E. Hopwood, R. Jones, M.C. Parkin, and M. Lauritzen. **Spreading and synchronous depressions of cortical activity in acutely injured human brain**. *Stroke*, **33**(12):2738, 2002. 34, 219

[41] M. Fabricius, S. Fuhr, R. Bhatia, M. Boutelle, P. Hashemi, A.J. Strong, and M. Lauritzen. **Cortical spreading depression and peri-infarct depolarization in acutely injured human cerebral cortex**. *Brain*, **129**(3):778, 2006. 34, 220

[42] J.P. Dreier, J. Woitzik, M. Fabricius, R. Bhatia, S. Major, C. Drenckhahn, T.N. Lehmann, A. Sarrafzadeh, L. Willumsen, J.A. Hartings, O.W. Sakowitz, J.H Seemann, A Thieme, M Lauritzen, and A.J. Strong. **Delayed ischaemic neurological deficits after subarachnoid haemorrhage are associated with clusters of spreading depolarizations**. *Brain*, **129**(12):3224, 2006. 34

[43] Y. Hu and G.S. Wilson. **A temporary local energy pool coupled to neuronal activity: Fluctuations of extracellular lactate levels in rat brain monitored with rapid-response enzyme-based sensor**. *Journal of neurochemistry*, **69**(4):1484–1490, 1997. 34, 42

[44] K. Caesar, P. Hashemi, A. Douhou, G. Bonvento, M.G. Boutelle, A.B. Walls, and M. Lauritzen. **Glutamate receptor-dependent increments in lactate, glucose and oxygen metabolism evoked in rat cerebellum in vivo**. *The Journal of physiology*, **586**(5):1337, 2008. 34, 38, 40, 241

[45] T. Back, M.D. Ginsberg, W.D. Dietrich, and B.D. Watson. **Induction of spreading depression in the ischemic hemisphere following experimental middle cerebral artery occlusion: effect on infarct morphology**. *Journal of Cerebral Blood Flow & Metabolism*, **16**(2):202–213, 1996. 34

[46] R.M. Dijkhuizen, J.P. Beekwilder, H.B. van der Worp, J.W. Berkelbach van der Sprenkel, K.A.F. Tulleken, and K. Nicolay. **Correlation between tissue depolarizations and damage in focal ischemic rat brain1**. *Brain research*, **840**(1-2):194–205, 1999. 34

[47] G. Mies. **Inhibition of protein synthesis during repetitive cortical spreading depression**. *Journal of neurochemistry*, **60**(1):360–363, 1993. 34

[48] J.P. Dreier, S. Major, A. Manning, J. Woitzik, C. Drenckhahn, J. Steinbrink, C. Tolias, A.I. Oliveira-Ferreira, M. Fabricius, J.A. Hartings, P. Vajkoczy, M. Lauritzen, U. Dirnagl, G. Bohner, and A.J. Strong. **Cortical spreading ischaemia is a novel process involved in ischaemic damage in patients with aneurysmal subarachnoid haemorrhage**. *Brain*, **132**(7):1866, 2009. 34

[49] A.J. Strong, P.J. Anderson, H.R. Watts, D.J. Virley, A. Lloyd, E.A. Irving, T. Nagafuji, M. Ninomiya, H. Nakamura, A.K. Dunn, and R. Graf. **Peri-infarct depolarizations lead to loss of perfusion in ischaemic gyrencephalic cerebral cortex**. *Brain*, **130**(4):995, 2007. 34, 222

[50] T. Kumagai, M. Walberer, H. Nakamura, H. Endepols, M. Sué, S. Vollmar, S. Adib, G. Mies, T. Yoshimine, M. Schroeter, and R. Graf. **Distinct spatiotemporal patterns of spreading depolarizations during early infarct evolution: evidence from real-time imaging**. *Journal of Cerebral Blood Flow & Metabolism*, 2010. 34

[51] L.Z. Leng, M.E. Fink, and C. Iadecola. **Spreading depolarization: a possible new culprit in the delayed cerebral ischemia of subarachnoid hemorrhage**. *Archives of neurology*, pages archneurol–2010, 2010. 34, 36

[52] G.D. Murray, I. Butcher, G.S. McHugh, J. Lu, N.A. Mushkudiani, A.I.R. Maas, A. Marmarou, and E.W. Steyerberg. **Multivariable prognostic analysis in traumatic brain injury: results from the IMPACT study**. *Journal of neurotrauma*, **24**(2):329–337, 2007. 34, 219

[53] D. Feuerstein, A. Manning, P. Hashemi, R. Bhatia, M. Fabricius, C. Tolias, C. Pahl, M. Ervine, A.J. Strong, and M.G. Boutelle. **Dynamic metabolic response to multiple spreading depolarizations in patients with acute brain injury: an online microdialysis study**. *J. Cereb. Blood Flow & Metab.*, **30**(7):1343–1355, 2010. 37, 38, 40, 220, 228, 234

[54] U. Ungerstedt and CH Pycock. **Functional correlates of dopamine neurotransmission.** *Bulletin der Schweizerischen Akademie der Medizinischen Wissenschaften*, **30**(1-3):44, 1974. 38

[55] L. Hillered, L. Persson, U. Ponten, and U. Ungerstedt. **Neurometabolic monitoring of the ischaemic human brain using microdialysis**. *Acta neurochirurgica*, **102**(3):91–97, 1990. 38

[56] S.E. Hopwood, M.C. Parkin, E.L. Bezzina, M.G. Boutelle, and A.J. Strong. **Transient changes in cortical glucose and lactate levels associated with peri-infarct depolarisations, studied with rapid-sampling microdialysis**. *Journal of Cerebral Blood Flow & Metabolism*, **25**(3):391–401, 2005. 38, 40, 220, 221

[57] P. Hashemi, R. Bhatia, H. Nakamura, J.P. Dreier, R. Graf, A.J. Strong, and M.G. Boutelle. **Persisting depletion of brain glucose following cortical spreading depression, despite apparent hyperaemia: evidence for risk of an adverse effect of Leao's spreading depression**. *J. Cereb. Blood Flow & Metab.*, **29**(1):166–175, 2008. 38, 40, 220, 221, 222

[58] J.A. Stenken, C.E. Lunte, M.Z. Southard, and L. Ståhle. **Factors that influence microdialysis recovery. Comparison of experimental and theoretical microdialysis recoveries in rat liver**. *Journal of pharmaceutical sciences*, **86**(8):958–966, 1997. 39

[59] B.H.C. Westerink and W. Timmerman. **Do neurotransmitters sampled by brain microdialysis reflect functional release?** *Analytica chimica acta*, **379**(3):263–274, 1999. 39

[60] K.C. Chen. **Evidence on extracellular dopamine level in rat striatum: implications for the validity of quantitative microdialysis**. *Journal of neurochemistry*, **92**(1):46–58, 2005. 39

[61] MG Boutelle and M. Fillenz. **Clinical microdialysis: the role of on-line measurement and quantitative microdialysis.** *Acta neurochirurgica. Supplement*, **67**:13, 1996. 40, 41

[62] J.P. Lowry, R.D. O'Neill, M.G. Boutelle, and M. Fillenz. **Continuous monitoring of extracellular glucose concentrations in the striatum of freely moving rats with an implanted glucose biosensor**. *Journal of neurochemistry*, **70**(1):391–396, 1998. 40, 42, 87

[63] DA Jones, MC Parkin, H. Langemann, H. Landolt, SE Hopwood, AJ Strong, and MG Boutelle. **On-line monitoring in neurointensive care* 1:: Enzyme-based electrochemical assay for simultaneous, continuous monitoring of glucose and lactate from critical care patients**. *Journal of Electroanalytical Chemistry*, **538**:243–252, 2002. 40

[64] G.S. Wilson and R. Gifford. **Biosensors for real-time in vivo measurements**. *Biosensors and Bioelectronics*, **20**(12):2388–2403, 2005. 40, 45

[65] M.K. Zachek, J. Park, P. Takmakov, R.M. Wightman, and G.S. McCarty. **Microfabricated FSCV-compatible microelectrode array for real-time monitoring of heterogeneous dopamine release**. *Analyst*, **135**(7):1556–1563, 2010. 42

[66] W.J. Albery, M.G. Boutelle, and P.T. Galley. **The dialysis electrodea new method for in vivo monitoring**. *J. Chem. Soc., Chem. Commun.*, (12):900–901, 1992. 42, 87

[67] J.J. Burmeister and G.A. Gerhardt. **Ceramic-based multisite microelectrode arrays for in vivo electrochemical recordings of glutamate and other neurochemicals**. *TrAC Trends in Analytical Chemistry*, **22**(8):498–502, 2003. 43, 94

[68] A. Jaquins-Gerstl and A.C. Michael. **Comparison of the brain penetration injury associated with microdialysis and voltammetry**. *Journal of neuroscience methods*, **183**(2):127–135, 2009. 43

[69] E.R. Hascup et al. **Histological studies of the effects of chronic implantation of ceramic-based microelectrode arrays and microdialysis probes in rat prefrontal cortex**. *Brain research*, **1291**:12–20, 2009. 43, 44

[70] AEG Cass, T. Cass, and F.S. Ligler. *Immobilized biomolecules in analysis: a practical approach*. Oxford University Press, USA, 1998. 44

[71] A.G. Gristina. **Biomaterial-centered infection: microbial adhesion versus tissue integration**. *Science*, **237**(4822):1588, 1987. 45

[72] R. Trouillon, C. Cheung, B.A. Patel, and D. O'Hare. **Electrochemical study of the intracellular transduction of vascular endothelial growth factor induced nitric oxide synthase activity using a multi-channel biocompatible microelectrode array**. *Biochimica et Biophysica Acta (BBA)-General Subjects*, **1800**(9):929–936, 2010. 45

[73] R.D. O'Neill, G. Rocchitta, C.P. McMahon, P.A. Serra, and J.P. Lowry. **Designing sensitive and selective polymer/enzyme composite biosensors for brain monitoring in vivo**. *TrAC Trends in Analytical Chemistry*, **27**(1):78–88, 2008. 45

[74] K.L. Clapp-Lilly, R.C. Roberts, L.K. Duffy, K.P. Irons, Y. Hu, and K.L. Drew. **An ultrastructural analysis of tissue surrounding a microdialysis probe**. *Journal of neuroscience methods*, **90**(2):129–142, 1999. 45

[75] A.S. Khan and A.C. Michael. **Invasive consequences of using micro-electrodes and microdialysis probes in the brain**. *TrAC Trends in Analytical Chemistry*, **22**(8):503–508, 2003. 45, 236

[76] K.T. Kishida, S.G. Sandberg, T. Lohrenz, Y.G. Comair, I. Sáez, P.E.M. Phillips, and P.R. Montague. **Sub-Second Dopamine Detection in Human Striatum**. *PloS one*, **6**(8):e23291, 2011. 46

[77] K.H. Lee, C.D. Blaha, P.A. Garris, P. Mohseni, A.E. Horne, K.E. Bennet, F. Agnesi, J.M. Bledsoe, D.B. Lester, C. Kimble, et al. **Evolution of deep brain stimulation: human electrometer and smart devices supporting the next generation of therapy**. *Neuromodulation: Technology at the Neural Interface*, **12**(2):85–103, 2009. 46

[78] M.L. Stephens, F. Pomerleau, P. Huettl, G.A. Gerhardt, and Z. Zhang. **Real-time glutamate measurements in the putamen of awake rhesus monkeys using an enzyme-based human microelectrode array prototype**. *Journal of neuroscience methods*, **185**(2):264–272, 2010. 46

[79] G. Taylor. **Dispersion of soluble matter in solvent flowing slowly through a tube**. *Proceedings of the Royal Society of London. Series A. Mathematical and Physical Sciences*, **219**(1137):186, 1953. 46, 186

[80] D.J. Harrison, K. Fluri, K. Seiler, Z. Fan, C.S. Effenhauser, and A. Manz. **Micromachining a miniaturized capillary electrophoresis-based chemical analysis system on a chip**. *Science*, **261**(5123):895, 1993. 47, 123

[81] H. Song and R.F. Ismagilov. **Millisecond kinetics on a microfluidic chip using nanoliters of reagents**. *J. Am. Chem. Soc*, **125**(47):14613–14619, 2003. 47

REFERENCES

[82] G.H. Seong, J. Heo, and R.M. Crooks. **Measurement of enzyme kinetics using a continuous-flow microfluidic system**. *Analytical chemistry*, **75**(13):3161–3167, 2003. 47

[83] Y. Schaerli, R.C. Wootton, T. Robinson, V. Stein, C. Dunsby, M.A.A. Neil, P.M.W. French, A.J. deMello, C. Abell, and F. Hollfelder. **Continuous-flow polymerase chain reaction of single-copy DNA in microfluidic microdroplets**. *Analytical Chemistry*, **81**(1):302–306, 2008. 47

[84] M.U. Kopp, A.J. Mello, and A. Manz. **Chemical amplification: continuous-flow PCR on a chip**. *Science*, **280**(5366):1046, 1998. 47, 123

[85] L. Chen, J. West, P.A. Auroux, A. Manz, and P.J.R. Day. **Ultrasensitive PCR and real-time detection from human genomic samples using a bidirectional flow microreactor**. *Analytical chemistry*, **79**(23):9185–9190, 2007. 47, 123

[86] G.M. Whitesides. **The origins and the future of microfluidics.** *Nature*, **442**(7101):368–373, 2006. 47

[87] A.E. Herr, A.V. Hatch, D.J. Throckmorton, H.M. Tran, J.S. Brennan, W.V. Giannobile, and A.K. Singh. **Microfluidic immunoassays as rapid saliva-based clinical diagnostics**. *Proceedings of the National Academy of Sciences*, **104**(13):5268, 2007. 47

[88] A. Huebner, M. Srisa-Art, D. Holt, C. Abell, F. Hollfelder, AJ Demello, and JB Edel. **Quantitative detection of protein expression in single cells using droplet microfluidics**. *Chem. Comm.*, **2007**(12):1218–1220, 2007. 47

[89] A. Tourovskaia, X. Figueroa-Masot, and A. Folch. **Differentiation-on-a-chip: a microfluidic platform for long-term cell culture studies**. *Lab Chip*, **5**(1):14–19, 2004. 47

[90] N. Belhadj Tahar, R. Abdelhédi, and A. Savall. **Electrochemical polymerisation of phenol in aqueous solution on a Ta/PbO 2 anode**. *Journal of applied electrochemistry*, **39**(5):663–669, 2009. 51, 52

[91] D. Feuerstein, K.H. Parker, and M.G. Boutelle. **Practical Methods for Noise Removal: Applications to Spikes, Nonstationary Quasi-Periodic Noise, and Baseline Drift**. *Analytical chemistry*, **81**(12):4987–4994, 2009. 55, 234

[92] J.L. Ponchon, R. Cespuglio, F. Gonon, M. Jouvet, and J.F. Pujol. **Normal pulse polarography with carbon fiber electrodes for in vitro and in vivo determination of catecholamines**. *Analytical Chemistry*, **51**(9):1483–1486, 1979. 61

[93] RM Wightman, JA Jankowski, RT Kennedy, KT Kawagoe, TJ Schroeder, DJ Leszczyszyn, JA Near, EJ Diliberto, and OH Viveros. **Temporally resolved catecholamine spikes correspond to single vesicle release from individual chromaffin cells**. *Proceedings of the National Academy of Sciences of the United States of America*, **88**(23):10754, 1991. 61

[94] M.L.A.V. Heien, A.S. Khan, J.L. Ariansen, J.F. Cheer, P.E.M. Phillips, K.M. Wassum, and R.M. Wightman. **Real-time measurement of dopamine fluctuations after cocaine in the brain of behaving rats**. *Proceedings of the National Academy of Sciences of the United States of America*, **102**(29):10023, 2005. 61

[95] S.B. Hall, E.A. Khudaish, and A.L. Hart. **Electrochemical oxidation of hydrogen peroxide at platinum electrodes. Part 1. An adsorption-controlled mechanism**. *Electrochimica acta*, **43**(5-6):579–588, 1997. 62, 64

[96] PN Bartlett and KFE Pratt. **A study of the kinetics of the reaction between ferrocene monocarboxylic acid and glucose oxidase using the rotating-disc electrode**. *Journal of electroanalytical chemistry*, **397**(1-2):53–60, 1995. 65

[97] C. Beriet and D. Pletcher. **A further microelectrode study of the influence of electrolyte concentration on the kinetics of redox couples**. *Journal of Electroanalytical Chemistry*, **375**(1-2):213–218, 1994. 65

[98] T. Henzler and E. Steudle. **Transport and metabolic degradation of hydrogen peroxide in Chara coralline: model calculations and measurements with the pressure probe suggest transport of H2O2 across water channels**. *Journal of experimental botany*, **51**(353):2053, 2000. 65

[99] B.A. Patel, M. Rogers, T. Wieder, D. O'Hare, and M.G. Boutelle. **ATP microelectrode biosensor for stable long-term in vitro monitoring from gastrointestinal tissue**. *Biosensors and Bioelectronics*, 2010. 73

[100] N.V. Kulagina, L. Shankar, and A.C. Michael. **Monitoring glutamate and ascorbate in the extracellular space of brain tissue with electrochemical microsensors**. *Analytical chemistry*, **71**(22):5093–5100, 1999. 87

[101] A.I. Schepartz and M.H. Subers. **The glucose oxidase of honey I. Purification and some general properties of the enzyme**. *Biochimica et Biophysica Acta (BBA)-Specialized Section on Enzymological Subjects*, **85**(2):228–237, 1964. 88

[102] R. Wilson and A.P.F. Turner. **Glucose oxidase: an ideal enzyme**. *Biosensors and Bioelectronics*, **7**(3):165–185, 1992. 88, 95, 100

[103] G. Wohlfahrt, S. Witt, J. Hendle, D. Schomburg, H.M. Kalisz, and H.J. Hecht. **1.8 and 1.9 A resolution structures of the Penicillium amagasakiense and Aspergillus niger glucose oxidases as a basis for modelling substrate complexes**. *Acta Crystallographica Section D: Biological Crystallography*, **55**(5):969–977, 1999. 88

[104] C.M. Wong, K.H. Wong, and X.D. Chen. **Glucose oxidase: natural occurrence, function, properties and industrial applications**. *Applied microbiology and biotechnology*, **78**(6):927–938, 2008. 88

[105] S. NAKAMURA and Y. OGURA. **Action mechanism of glucose oxidase of Aspergillus niger**. *Journal of Biochemistry*, **63**(3):308, 1968. 88

[106] A.E.G. Cass, G. Davis, G.D. Francis, H.A.O. Hill, W.J. Aston, I.J. Higgins, E.V. Plotkin, L.D.L. Scott, and A.P.F. Turner. **Ferrocene-mediated enzyme electrode for amperometric determination of glucose**. *Analytical Chemistry*, **56**(4):667–671, 1984. 89

[107] N.C. Foulds and C.R. Lowe. **Enzyme entrapment in electrically conducting polymers. Immobilisation of glucose oxidase in polypyrrole and its application in amperometric glucose sensors**. *J. Chem. Soc., Faraday Trans. 1*, **82**(4):1259–1264, 1986. 89

[108] M. Furuichi, N. Suzuki, B. Dhakshnamoorhty, H. Minagawa, R. Yamagishi, Y. Watanabe, Y. Goto, H. Kaneko, Y. Yoshida, H. Yagi, I. Waga, P.K. Kumar, and H. Mizuno. **X-ray Structures of Aerococcus viridans Lactate Oxidase and Its Complex with d-Lactate at pH 4.5 Show an [alpha]-Hydroxyacid Oxidation Mechanism**. *Journal of molecular biology*, **378**(2):436–446, 2008. 89

[109] I. Leiros, E. Wang, T. Rasmussen, E. Oksanen, H. Repo, S.B. Petersen, P. Heikinheimo, and E. Hough. **The 2.1 A structure of Aerococcus viridans L-lactate oxidase (LOX)**. *Acta Crystallographica Section F: Structural Biology and Crystallization Communications*, **62**(12):1185–1190, 2006. 89

[110] K. Sirkar, A. Revzin, and M.V. Pishko. **Glucose and lactate biosensors based on redox polymer/oxidoreductase nanocomposite thin films**. *Analytical chemistry*, **72**(13):2930–2936, 2000. 89

[111] K. Maeda-Yorita, K. Aki, H. Sagai, H. Misaki, and V. Massey. **L-Lactate oxidase and L-lactate monooxygenase: Mechanistic variations on a common structural theme**. *Biochimie*, **77**(7-8):631–642, 1995. 90

[112] G.I. Berglund, G.H. Carlsson, A.T. Smith, H. Sz "oke, A. Henriksen, and J. Hajdu. **The catalytic pathway of horseradish peroxidase at high resolution**. *Nature*, **417**(6887):463–468, 2002. 90

[113] V. Sanz, S. de Marcos, J.R. Castillo, and J. Galbán. **Application of molecular absorption properties of horseradish peroxidase for self-indicating enzymatic interactions and analytical methods**. *Journal of the American Chemical Society*, **127**(3):1038–1048, 2005. 91

[114] TA Steitz, M. Shoham, and WS Bennett. **Structural dynamics of yeast hexokinase during catalysis**. *Philosophical Transactions of the Royal Society of London. Series B, Biological Sciences*, **293**(1063):43–52, 1981. 91

[115] R.C. Alkire, D.M. Kolb, and J. Lipkowski. *Chemically modified electrodes*, **11**. Wiley-VCH, 2009. 93

[116] C.F. Blanford, C.E. Foster, R.S. Heath, and F.A. Armstrong. **Efficient electrocatalytic oxygen reduction by the bluecopper oxidase, laccase, directly attached to chemically modified carbons**. *Faraday Discuss.*, **140**:319–335, 2008. 93

[117] Y.C. Tsai, S.C. Li, and J.M. Chen. **Cast thin film biosensor design based on a nafion backbone, a multiwalled carbon nanotube conduit, and a glucose oxidase function**. *Langmuir*, **21**(8):3653–3658, 2005. 93

[118] K.M. Mitchell. **Acetylcholine and choline amperometric enzyme sensors characterized in vitro and in vivo**. *Analytical chemistry*, **76**(4):1098–1106, 2004. 94, 95

[119] H. Liu, T. Ying, K. Sun, H. Li, and D. Qi. **Reagentless amperometric biosensors highly sensitive to hydrogen peroxide, glucose and lactose based on N-methyl phenazine methosulfate incorporated in a Nafion film as an electron transfer mediator between horseradish peroxidase and an electrode**. *Analytica chimica acta*, **344**(3):187–199, 1997. 94

[120] N. Dale, S. Hatz, F. Tian, and E. Llaudet. **Listening to the brain: microelectrode biosensors for neurochemicals**. *TRENDS in Biotechnology*, **23**(8):420–428, 2005. 94

[121] A. De Mello. **Plastic fantastic?** *Lab on a Chip*, **2**(2):31N, 2002. 94

[122] S. Cosnier. **Biomolecule immobilization on electrode surfaces by entrapment or attachment to electrochemically polymerized films. A review**. *Biosensors and Bioelectronics*, **14**(5):443–456, 1999. 94

[123] A. Guerrieri, GE De Benedetto, F. Palmisano, and PG Zambonin. **Electrosynthesized non-conducting polymers as permselective membranes in amperometric enzyme electrodes: a glucose biosensor based on a cocrosslinked glucose oxidase/overoxidized polypyrrole bilayer**. *Biosensors and Bioelectronics*, **13**(1):103–112, 1998. 94

[124] J. Wang and M. Musameh. **Carbon-nanotubes doped polypyrrole glucose biosensor**. *Analytica chimica acta*, **539**(1-2):209–213, 2005. 94

[125] Y. NAKABAYASHI, M. WAKUDA, and H. IMAI. **Amperometric glucose sensors fabricated by electrochemical polymerization of phenols on carbon paste electrodes containing ferrocene as an electron transfer mediator**. *Analytical sciences*, **14**(6):1069–1076, 1998. 94, 95, 110

[126] J.C. Vidal, E. García, S. Méndez, P. Yarnoz, and J.R. Castillo. **Three approaches to the development of selective bilayer amperometric biosensors for glucose by in situ electropolymerization**. *Analyst*, **124**(3):319–324, 1999. 94, 95

[127] C. Malitesta, F. Palmisano, L. Torsi, and P.G. Zambonin. **Glucose fast-response amperometric sensor based on glucose oxidase immobilized in an electropolymerized poly (o-phenylenediamine) film**. *Analytical chemistry*, **62**(24):2735–2740, 1990. 94, 95

[128] P.N. Bartlett and D.J. Caruana. **Electrochemical immobilization of enzymes. Part VI. Microelectrodes for the detection of L-lactate based on flavocytochrome b2 immobilized in a poly (phenol) film**. *Analyst*, **119**(2):175–180, 1994. 94, 95

[129] C.P. McMahon, S.J. Killoran, and R.D. O'Neill. **Design variations of a polymer-enzyme composite biosensor for glucose: Enhanced analyte sensitivity without increased oxygen dependence**. *Journal of Electroanalytical Chemistry*, **580**(2):193–202, 2005. 95

[130] H. Zhou, H. Chen, S. Luo, J. Chen, W. Wei, and Y. Kuang. **Preparation and bioelectrochemical responses of the poly (m-phenylenediamine) glucose oxidase electrode**. *Sensors and Actuators B: Chemical*, **101**(1-2):224–230, 2004. 95

[131] H. Zhou, H. Chen, S. Luo, J. Chen, W. Wei, and Y. Kuang. **Glucose biosensor based on platinum microparticles dispersed in nano-fibrous polyaniline**. *Biosensors and Bioelectronics*, **20**(7):1305–1311, 2005. 95

[132] MM Rhemrev-Boom, MA Jonker, K. Venema, G. Jobst, R. Tiessen, and J. Korf. **On-line continuous monitoring of glucose or lactate by ultraslow microdialysis combined with a flow-through nanoliter biosensor based on poly (m-phenylenediamine) ultra-thin polymer membrane as enzyme electrode**. *Analyst*, **126**(7):1073–1079, 2001. 95

[133] P.N. Bartlett and D.J. Caruana. **Electrochemical immobilization of enzymes. Part V. Microelectrodes for the detection of glucose based on glucose oxidase immobilized in a poly (phenol) film**. *Analyst*, **117**(8):1287–1292, 1992. 95

REFERENCES

[134] DWM Arrigan and PN Bartlett. **A scanning force microscopy study of poly (phenol) films containing immobilized glucose oxidase**. *Biosensors and Bioelectronics*, **13**(3-4):293–304, 1998. 95, 105

[135] S. Hrapovic and J.H.T. Luong. **Picoamperometric detection of glucose at ultrasmall platinum-based biosensors: preparation and characterization**. *Analytical chemistry*, **75**(14):3308–3315, 2003. 95, 110

[136] Q.H. Gibson, B.E.P. Swoboda, and V. Massey. **Kinetics and mechanism of action of glucose oxidase**. *Journal of Biological Chemistry*, **239**(11):3927, 1964. 95, 100

[137] S. Nakamura, S. Hayashi, and K. Koga. **Effect of periodate oxidation on the structure and properties of glucose oxidase**. *Biochimica et Biophysica Acta (BBA)-Enzymology*, **445**(2):294–308, 1976. 95, 100

[138] D.G. Georganopoulou, R. Carley, D.A. Jones, and M.G. Boutelle. **Development and comparison of biosensors for in-vivo applications**. *Faraday Discuss.*, **116**:291–303, 2000. 97, 110

[139] IA Borisov, AV Lobanov, AN Reshetilov, and BI Kurganov. **Quantitative analysis of the calibration dependences for biosensors**. *Applied Biochemistry and Microbiology*, **36**(3):215–220, 2000. 97

[140] C.A. Anastassiou, B.A. Patel, M. Arundell, M.S. Yeoman, K.H. Parker, and D. O'Hare. **Subsecond voltammetric separation between dopamine and serotonin in the presence of ascorbate**. *Analytical chemistry*, **78**(19):6990–6998, 2006. 102

[141] S.A. Rothwell, M.E. Kinsella, Z.M. Zain, P.A. Serra, G. Rocchitta, J.P. Lowry, and R.D. ONeill. **Contributions by a novel edge effect to the permselectivity of an electrosynthesized polymer for microbiosensor applications**. *Analytical chemistry*, **81**(10):3911–3918, 2009. 105

[142] PN Barlett and JM Cooper. **A review of the immobilization of enzymes in electropolymerized films**. *Journal of Electroanalytical Chemistry*, **362**(1-2):1–12, 1993. 105

[143] D. Compagnone and G.G. Guilbault. **Glucose oxidase/hexokinase electrode for the determination of ATP* 1**. *Analytica chimica acta*, **340**(1-3):109–113, 1997. 119, 120

[144] A. Kueng, C. Kranz, and B. Mizaikoff. **Amperometric ATP biosensor based on polymer entrapped enzymes**. *Biosensors and Bioelectronics*, **19**(10):1301–1307, 2004. 119, 120

[145] J.F. Masson, C. Kranz, B. Mizaikoff, and E.B. Gauda. **Amperometric ATP microbiosensors for the analysis of chemosensitivity at rat carotid bodies**. *Analytical chemistry*, **80**(11):3991–3998, 2008. 119

[146] F. Scheller and D. Pfeiffer. **Glucose oxidase–hexokinase bienzyme electrode sensor for adenosine triphosphate**. *Analytica Chimica Acta*, **117**:383–386, 1980. 120

[147] S. Liu and Y. Sun. **Co-immobilization of glucose oxidase and hexokinase on silicate hybrid sol-gel membrane for glucose and ATP detections**. *Biosensors and Bioelectronics*, **22**(6):905–911, 2007. 120

[148] OO Soldatkin, OM Schuvailo, S. Marinesco, R. Cespuglio, and AP Soldatkin. **Microbiosensor based on glucose oxidase and hexokinase co-immobilised on platinum microelectrode for selective ATP detection**. *Talanta*, **78**(3):1023–1028, 2009. 120

[149] XZ Niu, B. Zhang, RT Marszalek, O. Ces, JB Edel, and DR Klug. **Droplet-based compartmentalization of chemically separated components in two-dimensional separations**. *Chem. Commun.*, (41):6159–6161, 2009. 123

[150] X. Niu, S. Gulati, and J.B. Edel. **Pillar-induced droplet merging in microfluidic circuits**. *Lab Chip*, **8**(11):1837–1841, 2008. 124

[151] N. Bremond, A.R. Thiam, and J. Bibette. **Decompressing emulsion droplets favors coalescence**. *Physical review letters*, **100**(2):24501, 2008. 124, 158

[152] BJ Jin, YW Kim, Y. Lee, and JY Yoo. **Droplet merging in a straight microchannel using droplet size or viscosity difference**. *Journal of Micromechanics and Microengineering*, **20**:035003, 2010. 124

[153] H. Song, D.L. Chen, and R.F. Ismagilov. **Reactions in droplets in microfluidic channels**. *Angewandte Chemie (International ed. in English)*, **45**(44):7336, 2006. 124, 126

[154] M.R. Bringer, C.J. Gerdts, H. Song, J.D. Tice, and R.F. Ismagilov. **Microfluidic systems for chemical kinetics that rely on chaotic mixing in droplets**. *Philosophical Transactions of the Royal Society of London. Series A: Mathematical, Physical and Engineering Sciences*, **362**(1818):1087, 2004. 124, 163

[155] DR Link, S.L. Anna, DA Weitz, and HA Stone. **Geometrically mediated breakup of drops in microfluidic devices**. *Physical review letters*, **92**(5):54503, 2004. 124

[156] S.Y. Teh, R. Lin, L.H. Hung, and A.P. Lee. **Droplet microfluidics**. *Lab Chip*, **8**(2):198–220, 2008. 124

[157] X. Niu, M. Zhang, S. Peng, W. Wen, and P. Sheng. **Real-time detection, control, and sorting of microfluidic droplets**. *Biomicrofluidics*, **1**:044101, 2007. 124, 176

[158] J.C. Baret, O.J. Miller, V. Taly, M. Ryckelynck, A. El-Harrak, L. Frenz, C. Rick, M.L. Samuels, J.B. Hutchison, J.J. Agresti, D.R. Link, D.A. Weitz, and A.D. Griffiths. **Fluorescence-activated droplet sorting (FADS): efficient microfluidic cell sorting based on enzymatic activity**. *Lab Chip*, **9**(13):1850–1858, 2009. 124

[159] E. Brouzes, M. Medkova, N. Savenelli, D. Marran, M. Twardowski, J.B. Hutchison, J.M. Rothberg, D.R. Link, N. Perrimon, and M.L. Samuels. **Droplet microfluidic technology for single-cell high-throughput screening**. *Proceedings of the National Academy of Sciences*, **106**(34):14195, 2009. 124

[160] D. Chen, W. Du, Y. Liu, W. Liu, A. Kuznetsov, F.E. Mendez, L.H. Philipson, and R.F. Ismagilov. **The chemistrode: A droplet-based microfluidic device for stimulation and recording with high temporal, spatial, and chemical resolution**. *Proc. Nat. Acad. Sci.*, **105**(44):16843, 2008. 124

[161] G.T. Roman, M. Wang, K.N. Shultz, C. Jennings, and R.T. Kennedy. **Sampling and electrophoretic analysis of segmented flow streams using virtual walls in a microfluidic device**. *Analytical chemistry*, **80**(21):8231–8238, 2008. 124

[162] M.A. Unger, H.P. Chou, T. Thorsen, A. Scherer, and S.R. Quake. **Monolithic microfabricated valves and pumps by multilayer soft lithography**. *Science*, **288**(5463):113, 2000. 124

[163] M.O.M. Berners, M.G. Boutelle, and M. Fillenz. **On-line measurement of brain glutamate with an enzyme/polymer-coated tubular electrode**. *Analytical chemistry*, **66**(13):2017–2021, 1994. 124

[164] E. Dempsey, D. Diamond, M.R. Smyth, G. Urban, G. Jobst, I. Moser, E.M.J. Verpoorte, A. Manz, H. Michael Widmer, K. Rabenstein, et al. **Design and development of a miniaturised total chemical analysis system for on-line lactate and glucose monitoring in biological samples**. *Analytica chimica acta*, **346**(3):341–349, 1997. 124

[165] E. Zilkha, TP Obrenovitch, A. Koshy, H. Kusakabe, and HP Bennetto. **Extracellular glutamate: on-line monitoring using microdialysis coupled to enzyme-amperometric analysis**. *Journal of neuroscience methods*, **60**(1-2):1–9, 1995. 124

[166] K. Ohno, K. Tachikawa, and A. Manz. **Microfluidics: applications for analytical purposes in chemistry and biochemistry**. *Electrophoresis*, **29**(22):4443–4453, 2008. 124

[167] V. Srinivasan, V.K. Pamula, and R.B. Fair. **An integrated digital microfluidic lab-on-a-chip for clinical diagnostics on human physiological fluids**. *Lab on a Chip*, **4**(4):310–315, 2004. 124

[168] T.H. Schulte, R.L. Bardell, and B.H. Weigl. **Microfluidic technologies in clinical diagnostics**. *Clinica Chimica Acta*, **321**(1-2):1–10, 2002. 124

[169] R.B. Lefkowitz, J.Y. Marciniak, C.M. Hu, G.W. Schmid-Schonbein, and M.J. Heller. **An electrophoretic method for the detection of chymotrypsin and trypsin activity directly in whole blood**. *Electrophoresis*, **31**(2):403–410, 2010. 124

[170] A. Huebner, S. Sharma, M. Srisa-Art, F. Hollfelder, and J.B. Edel. **Microdroplets: A sea of applications?** *Lab Chip*, **8**(8):1244–1254, 2008. 124, 126

[171] Meng Wang, Gregory T. Roman, Kristin Schultz, Colin Jennings, and Robert T. Kennedy. **Improved Temporal Resolution for in Vivo Microdialysis by Using Segmented Flow**. *Anal. Chem.*, **80**(14):5607–5615, 2008. PMID: 18547059. 125, 175

[172] Y. Xia and G.M. Whitesides. **Soft lithography**. *Annual review of materials science*, **28**(1):153–184, 1998. 125

[173] D. Bodas and C. Khan-Malek. **Formation of more stable hydrophilic surfaces of PDMS by plasma and chemical treatments**. *Microelectronic engineering*, **83**(4-9):1277–1279, 2006. 125

[174] E. Delamarche, H. Schmid, B. Michel, and H. Biebuyck. **Stability of molded polydimethylsiloxane microstructures**. *Advanced Materials*, **9**(9):741–746, 1997. 125

[175] D.T. Chiu, R.M. Lorenz, and G.D.M. Jeffries. **Droplets for Ultrasmall-Volume Analysis**. *Anal. Chem.*, **81**(13):5111–5118, 2009. 126

[176] S. Van der Graaf, MLJ Steegmans, RGM Van Der Sman, C. Schroën, and RM Boom. **Droplet formation in a T-shaped microchannel junction: A model system for membrane emulsification**. *Colloids and Surfaces A: Physicochemical and Engineering Aspects*, **266**(1-3):106–116, 2005. 126

[177] P. Garstecki, M.J. Fuerstman, H.A. Stone, and G.M. Whitesides. **Formation of droplets and bubbles in a microfluidic T-junctionscaling and mechanism of break-up**. *Lab on a Chip*, **6**(3):437–446, 2006. 126

[178] S.L. Anna, N. Bontoux, and H.A. Stone. **Formation of dispersions using flow focusing in microchannels**. *Appl. Phys. Lett.*, **82**:364, 2003. 126

[179] P. Garstecki, I. Gitlin, W. DiLuzio, G.M. Whitesides, E. Kumacheva, and H.A. Stone. **Formation of monodisperse bubbles in a microfluidic flow-focusing device**. *Appl. Phys. Lett*, **85**:2649, 2004. 126

[180] D.C. Duffy, J.C. McDonald, O.J.A. Schueller, and G.M. Whitesides. **Rapid prototyping of microfluidic systems in poly (dimethylsiloxane)**. *Analytical Chemistry*, **70**(23):4974–4984, 1998. 132

[181] J.R. Anderson, D.T. Chiu, R.J. Jackman, O. Cherniavskaya, J.C. McDonald, H. Wu, S.H. Whitesides, and G.M. Whitesides. **Fabrication of topologically complex three-dimensional microfluidic systems in PDMS by rapid prototyping**. *Analytical Chemistry*, **72**(14):3158–3164, 2000. 132

[182] H. Kanno, Y. Han, Y. Saito, and N. Shikazono. **Measurement of Liquid Film Thickness in Micro Tube Annular Flow**. ASME, 2010. 152

[183] HM Van Sonsbeek, H. De Blank, and J. Tramper. **Oxygen transfer in liquid-impelled loop reactors using perfluorocarbon liquids**. *Biotechnology and bioengineering*, **40**(6):713–718, 1992. 154

[184] JC Lotters, W. Olthuis, PH Veltink, and P. Bergveld. **The mechanical properties of the rubber elastic polymer polydimethylsiloxane for sensor applications**. *Journal of Micromechanics and Microengineering*, **7**:145, 1997. 154

[185] T. Henkel, T. Bermig, M. Kielpinski, A. Grodrian, J. Metze, and JM Kohler. **Chip modules for generation and manipulation of fluid segments for micro serial flow processes**. *Chemical Engineering Journal*, **101**(1-3):439–445, 2004. 163

[186] E.A. Mansur, M. Ye, Y. Wang, and Y. Dai. **A state-of-the-art review of mixing in microfluidic mixers**. *Chinese Journal of Chemical Engineering*, **16**(4):503–516, 2008. 163

[187] A. Goullet, I. Glasgow, and N. Aubry. **Effects of microchannel geometry on pulsed flow mixing**. *Mechanics Research Communications*, **33**(5):739–746, 2006. 163

[188] J. Sivasamy, Y.C. Chim, T.N. Wong, N.T. Nguyen, and L. Yobas. **Reliable addition of reagents into microfluidic droplets**. *Microfluidics and Nanofluidics*, **8**(3):409–416, 2010. 163, 165

[189] H. Song, J.D. Tice, and R.F. Ismagilov. **A microfluidic system for controlling reaction networks in time**. *Angewandte Chemie*, **115**(7):792–796, 2003. 163

[190] T. Hatakeyama, D.L. Chen, and R.F. Ismagilov. **Microgram-scale testing of reaction conditions in solution using nanoliter plugs in microfluidics with detection by MALDI-MS**. *Journal of the American Chemical Society*, **128**(8):2518–2519, 2006. 163

[191] H. Song, M.R. Bringer, J.D. Tice, C.J. Gerdts, and R.F. Ismagilov. **Experimental test of scaling of mixing by chaotic advection in droplets moving through microfluidic channels**. *Applied physics letters*, **83**(22):4664–4666, 2003. 166, 167

REFERENCES

[192] A.M. Leach, A.R. Wheeler, and R.N. Zare. **Flow injection analysis in a microfluidic format**. *Analytical chemistry*, **75**(4):967–972, 2003. 171

[193] R. Irawan, S.C. Tjin, X. Fang, and C.Y. Fu. **Integration of optical fiber light guide, fluorescence detection system, and multichannel disposable microfluidic chip**. *Biomedical Microdevices*, **9**(3):413–419, 2007. 175

[194] C. Liu, D. Cui, and X. Chen. **Development of an integrated direct-contacting optical-fiber microchip with light-emitting diode-induced fluorescence detection**. *Journal of Chromatography A*, **1170**(1-2):101–106, 2007. 175

[195] D.A. Chang-Yen and B.K. Gale. **Integrated optical glucose sensor fabricated using PDMS waveguides on a PDMS substrate**. In *Proc. SPIE–Int. Soc. Opt. Eng*, **5345**, pages 98–107, 2004. 175

[196] V. Srinivasan, V. Pamula, M. Pollack, and R. Fair. **A digital microfluidic biosensor for multianalyte detection**. In *Micro Electro Mechanical Systems, 2003. MEMS-03 Kyoto. IEEE The Sixteenth Annual International Conference on*, pages 327–330. IEEE, 2003. 175

[197] R.G. Compton and P.R. Unwin. **Channel and tubular electrodes**. *Journal of Electroanalytical Chemistry*, **205**(1-2):1–20, 1986. 175

[198] J.A. Cooper and R.G. Compton. **Channel electrodes-A review**. *Electroanalysis*, **10**(3):141–155, 1998. 175, 176

[199] N.P.C. Stevens, K.A. Gooch, and A.C. Fisher. **Computational Electrochemistry. Simulations of Homogeneous Chemical Reactions in the Confluence Reactor and Channel Flow Cell**. *J. Phys. Chem. B*, **104**(6):1241–1248, 2000. 176

[200] N.V. Rees, R.A.W. Dryfe, J.A. Cooper, B.A. Coles, R.G. Compton, S.G. Davies, and T.D. McCarthy. **Voltammetry under High Mass Transport Conditions. A High Speed Channel Electrode for the Study of Ultrafast Kinetics**. *The Journal of Physical Chemistry*, **99**(18):7096–7101, 1995. 176, 195

[201] N.V. Rees, J.A. Alden, R.A.W. Dryfe, B.A. Coles, and R.G. Compton. **Voltammetry Under High Mass Transport Conditions. The High Speed Channel Electrode and Heterogeneous Kinetics**. *The Journal of Physical Chemistry*, **99**(40):14813–14818, 1995. 176

[202] C. Amatore, N. Da Mota, C. Sella, and L. Thouin. **General concept of high-performance amperometric detector for microfluidic (bio) analytical chips**. *Anal. Chem.*, **80**(13):4976–4985, 2008. 176

[203] C. Amatore, O.V. Klymenko, and I. Svir. **In situ and Online Monitoring of Hydrodynamic Flow Profiles in Microfluidic Channels Based upon Microelectrochemistry: Optimization of Electrode Locations**. *ChemPhysChem*, **7**(2):482–487, 2006. 176

[204] C. Amatore, N. Da Mota, C. Sella, and L. Thouin. **Theory and Experiments of Transport at Channel Microband Electrodes Under Laminar Flow. 3. Electrochemical Detection at Electrode Arrays under Steady State**. *Anal. Chem.*, **82**(6):2434–2440, 2010. 176

[205] C. Amatore, O.V. Klymenko, A.I. Oleinick, and I. Svir. **Electrochemical Determination of Flow Velocity Profile in a Microfluidic Channel from Steady-State Currents: Numerical Approach and Optimization of Electrode Layout**. *Anal. Chem.*, **81**(18):7667–7676, 2009. 176

[206] M. Thompson and R.G. Compton. **Voltammetric monitoring of transient hydrodynamic flow profiles in microfluidic flow cells**. *Anal. Chem.*, **79**(2):626–631, 2007. 176

[207] S.M. MacDonald, J.D. Watkins, Y. Gu, K. Yunus, A.C. Fisher, G. Shul, M. Opallo, and F. Marken. **Electrochemical processes at a flowing organic solventaqueous electrolyte phase boundary**. *Electrochemistry Communications*, **9**(8):2105–2110, 2007. 176

[208] Y. Zhan, J. Wang, N. Bao, and C. Lu. **Electroporation of cells in microfluidic droplets**. *Anal. Chem.*, **81**(5):2027–2031, 2009. 176

[209] Z. Han, W. Li, Y. Huang, and B. Zheng. **Measuring Rapid Enzymatic Kinetics by Electrochemical Method in Droplet-Based Microfluidic Devices with Pneumatic Valves**. *Anal. Chem.*, **81**(14):5840–5845, 2009. 176

[210] M. Wang, G.T. Roman, M.L. Perry, and R.T. Kennedy. **Microfluidic Chip for High Efficiency Electrophoretic Analysis of Segmented Flow from a Microdialysis Probe and in Vivo Chemical Monitoring**. *Anal. Chem.*, **81**(21):9072–9078, 2009. 176

[211] I. Rubinstein. *Physical electrochemistry: principles, methods, and applications*, **7**. CRC, 1995. 177

[212] F.M. White. **Viscous Fluid Flow, 1974**. 195

[213] N.A. Mortensen, F. Okkels, and H. Bruus. **Reexamination of Hagen-Poiseuille flow: Shape dependence of the hydraulic resistance in microchannels**. *Physical Review E*, **71**(5):57301, 2005. 195

[214] M.F. Mazzobre, M.V. Roman, A.F. Mourelle, and H.R. Corti. **Octanol-water partition coefficient of glucose, sucrose, and trehalose**. *Carbohydrate research*, **340**(6):1207–1211, 2005. 207

[215] A. Leo, C. Hansch, and D. Elkins. **Partition coefficients and their uses**. *Chemical Reviews*, **71**(6):525–616, 1971. 207

[216] NV Narendranath, KC Thomas, and WM Ingledew. **Effects of acetic acid and lactic acid on the growth of Saccharomyces cerevisiae in a minimal medium**. *Journal of Industrial Microbiology and Biotechnology*, **26**(3):171–177, 2001. 207

[217] G. Critchley and A. Memon. **Head Injury: A Multidisciplinary Approach**. 2009. 219

[218] H. Nakamura, A.J. Strong, C. Dohmen, O.W. Sakowitz, S. Vollmar, M. Sué, L. Kracht, P. Hashemi, R. Bhatia, J.P. Yoshimine, T. Dreier, A.K. Dunn, and R. Graf. **Spreading depolarizations cycle around and enlarge focal ischaemic brain lesions**. *Brain*, **133**(7):1994, 2010. 220

[219] R.J. Traystman. **Animal models of focal and global cerebral ischemia**. *ILAR journal*, **44**(2):85–95, 2003. 220

[220] MD Ginsberg and R. Busto. **Rodent models of cerebral ischemia**. *Stroke*, **20**(12):1627, 1989. 220

[221] H. Ripps, L. Mehaffey, and IM Siegel. **" Rapid regeneration" in the cat retina: a case for spreading depression.** *The Journal of general physiology*, **77**(3):335, 1981. 221

[222] J.C. Chang, L.L. Shook, J. Biag, E.N. Nguyen, A.W. Toga, A.C. Charles, and K.C. Brennan. **Biphasic direct current shift, haemoglobin desaturation and neurovascular uncoupling in cortical spreading depression**. *Brain*, **133**(4):996, 2010. 221

[223] A. Grinvald, E. Lieke, R.D. Frostig, C.D. Gilbert, and T.N. Wiesel. **Functional architecture of cortex revealed by optical imaging of intrinsic signals**. 1986. 221

[224] A. Grinvald, E.E. Lieke, R.D. Frostig, and R. Hildesheim. **Cortical point-spread function and long-range lateral interactions revealed by real-time optical imaging of macaque monkey primary visual cortex**. *The Journal of neuroscience*, **14**(5):2545, 1994. 221

[225] AJ Strong, SP Harland, BS Meldrum, and DJ Whittington. **The use of in vivo fluorescence image sequences to indicate the occurrence and propagation of transient focal depolarizations in cerebral ischemia**. *Journal of Cerebral Blood Flow & Metabolism*, **16**(3):367–377, 1996. 221

[226] A.K. Dunn, H. Bolay, M.A. Moskowitz, and D.A. Boas. **Dynamic imaging of cerebral blood flow using laser speckle**. *Journal of Cerebral Blood Flow & Metabolism*, **21**(3):195–201, 2001. 221, 222

[227] AJ Strong, SE Hopwood, MG Boutelle, MC Parkin, L. Bezzina, S. Yih-Huei, and AK Dunn. **Measuring dynamic changes in perfusion in the penumbra with high spatial and temporal resolution using laser speckle imaging: comparison with indicator clearance**. *J Cereb Blood Flow Metab*, **23**(1):300, 2003. 222

[228] F. Richter, S. Rupprecht, A. Lehmenk "uhler, and H.G. Schaible. **Spreading depression can be elicited in brain stem of immature but not adult rats**. *Journal of neurophysiology*, **90**(4):2163, 2003. 228

[229] F. Richter, A. Ebersberger, and H.G. Schaible. **Blockade of voltage-gated calcium channels in rat inhibits repetitive cortical spreading depression**. *Neuroscience letters*, **334**(2):123–126, 2002. 228

[230] W.L. Clarke, D. Cox, L.A. Gonder-Frederick, W. Carter, and S.L. Pohl. **Evaluating clinical accuracy of systems for self-monitoring of blood glucose.** *Diabetes care*, **10**(5):622, 1987. 234

[231] NS Oliver, C. Toumazou, AEG Cass, and DG Johnston. **Glucose sensors: a review of current and emerging technology**. *Diabetic Medicine*, **26**(3):197–210, 2009. 234